Beyond Carbon: Permeance, Rejection and Scalability of Novel Nanotube Membranes

Casanova, Serena

Award date:
2020

Awarding institution:
University of Bath

Beyond Carbon: Permeance, Rejection and Scalability of Novel Nanotube Membranes

Casanova, Serena

Award date:
2020

Awarding institution:
University of Bath

Beyond Carbon: Permeance, Rejection and Scalability of Novel Nanotube Membranes

submitted by

Serena Casanova

for the degree of Doctor of Philosophy

of the

University of Bath

Department of Chemical Engineering

December 2019

Acknowledgements

I would like to thank my supervisors, Professor Davide Mattia and Professor Y.M. John Chew for their support and teachings during these past three years. Davide and John have been constantly engaged with my work. They have been willing to share ideas and expertise, and have supervised and facilitated the safe execution of my experiments in the lab. Specifically, Davide has always helped me strive to see the bigger picture, feeling secure of my achievements and research with purpose. John has aided me to be more structured in the presentation of my work and write with the reader in mind. Thus, I am deeply indebted to them not only for the technical knowledge I acquired in these years, but also for their guidance through my personal and professional growth. Their input and corrections have been crucial to the drawing up of this thesis and the research articles that have resulted from it.

I am also very grateful to my supervisors for having always encouraged me to collaborate with great researchers from other centres in the UK. I would particularly like to give credit to Dr. Matthew K. Borg, who has been a wonderful person to collaborate with, and of whom I sincerely appreciate the attention to detail and rigorousness in the scientific pursuit. A special mention should be given also to Sritay Mistry, Dr. TianYin Liu, Dr. Jerome Meng, Halan Mohammed and Prof. Andrew G. Livingston. I thank Dr. Hannah Leese whose excellent thesis has constituted a solid background for my work.

I have been lucky to have the chance to work with inspiring and amiable people during my PhD. A special thanks goes to "my postdocs" Jing, whose thoroughness and precision I admire, and Saeed, who is hard working and always inquisitive. I also loved working with Thais, Zac, Luz, Abouther, Nick, Yen, James, Alysson, David, Ejaz, Ekanem and Caitlin. I express my gratitude to Faye, Fraser and Sahand, who worked

with me for their undergraduate research projects.

This thesis would not have been possible without the help of Philip, Diana and Ursula from the MAS suit, Daniel Morgan for XPS and Duncan Muir for FESEM in Cardiff. Thank you Daniel Fonseca for teaching me the basics of Blender. I would also like to give a special thank to Emma Cliffe for support on Latex, the IT services for support and the amazing Chemical Engineering technical team, who makes our research possible. I deeply thank Dr. Daniel Wolverson for allowing me the use of his Raman spectroscopy setup and for sharing his knowledge and passion for the equipment. I thank the UK Engineering and Physical Sciences Research Council for supporting this research under the SynFabFun grant.

The PhD is a challenging experience and the support of my friends has been very important during this period. Thank you Robi for your warnings, Rojin for your free spirit, Horia for playing boardgames with me, Kseno & Stu for philosophy, Tobias for dubious tech and Cecilia for being a marvellous friend. My most important and big thank you goes to Sam, who has walked with me the steps of this journey, and made me smile every day: I would not have been able to complete my PhD without your precious support, you are a truly beautiful person.

Dedico questa tesi di dottorato ai miei genitori Sandra e Diego e a mio fratello Elio: è grazie al vostro affetto, incoraggiamento e supporto se sono riuscita a raggiungere questo traguardo. Grazie per aver creato lo spazio per costruire la mia strada e per avermene dato i mezzi, per rispettare le mie scelte, per esserci sempre per me e per la vostra infinita pazienza.

Summary

The present work investigates novel nanotube materials for application in the field of membrane technology, with the aim of going beyond the well-investigated carbon, by studying nanotubes made of carbon nitride, boron nitride and polystyrene.

Carbon nanotubes (CNTs) have long held the promise to revolutionise filtration technology, with orders of magnitude higher fluxes compared to commercial membranes. Nevertheless, during the introduction of CNTs in current membrane technology, several issues were encountered, amongst which the poorly understood dependence of water flow enhancement on the nanotubes' atomic structure, limited rejection potential and difficulties in scaling up.

In this thesis, the independent effect of nanotube surface chemistry and structure on the flow of water under nanoscale confinement is first demonstrated via the synthesis of carbon nitride nanotube (CNNT) membranes. Using a combination of experiments and molecular dynamics (MD) simulations, it is shown here that the hydrophilisation of the sp2 carbon structure, induced by the presence of the C-N bonds, decreases the pure water permeance in CNNTs, when compared with CNTs with different degree of defects. The effect on permeance is explained in terms of solid-liquid interactions with increased water viscosity and decreased surface diffusion near the CNNT wall, when compared to CNTs. The effect that different surface properties have on flow enhancement was also studied in polystyrene nanotubes membranes, with polystyrene being one of the commonly used polymers in membrane science. This was achieved by means of a one-factor-at-a-time optimisation of key parameters impacting the formation of nanotubes with well-defined geometries.

Moreover, it was previously found that CNTs can only reject particles and ions wider

than their internal diameter. Per contra, this work reports the fabrication of aligned boron nitride nanotube (BNNT) membranes, with a 45% higher permeate flow rate than CNT membranes with similar rejection. The increased permeance is due to a charge-based rejection mechanism in addition to the size-based one, enabled by the BNNT surface structure and chemistry and elucidated here with molecular dynamics and CFD simulations. This phenomena allows using nanotubes with larger diameters and also addresses challenges in the manufacturing of sub-nanometer CNTs in large quantities.

Following the aforementioned fundamental studies of nanotubes' permeance and rejection behaviours, the embedment of nanotubes in commercial nanofiltration membranes was investigated. A novel thin film nanocomposite (TFN) membrane was obtained by incorporating BNNTs in a polyamide (PA) thin selective layer prepared via interfacial polymerisation. The addition of just 0.02 wt% of BNNTs led to a 4-fold increase in pure water permeance with no loss in rejection for divalent salts, methylene blue and humic acid compared to the pure PA membrane. Fouling tests with humic acid showed a flux recovery ratio of $> 95\%$ with 40-50% lower flux loss during the fouling cycle compared to the polyamide only membrane. These values represent a significant improvement for both commercial PA membranes but also TFN using CNTs.

The work presented in this thesis investigates novel nanomaterials for membrane technology opening the way to tailoring surface chemistry and structure inside nanotube membranes for a wide variety of processes. These range from enhanced transport to improved targeted rejection, in ceramic and polymeric membranes.

Contents

List of Figures

List of Tables

Nomenclature

Acronyms

FRR Flux Recovery Ratio (-)

AAM Anodic Alumina Membranes

ASEM Analytical Scanning Electron Microscope

BNNTs Boron Nitride Nanotubes

BSA Bovine Serum Albumine

C_xN_y Carbon Nitride

CC Cyanuric Chloride

CNNTs Carbon Nitride Nanotubes

CNTs Carbon Nanotubes

CVD Chemical Vapour Deposition

DETA Diethylenetriamine

DSC Differential Scanning Calorimetry

EDX Electron Diffraction Spectroscopy

EELS Electron Energy Loss Spectroscopy

FESEM Field Emission Scanning Electron Microscope

FTIR-ATR Fourier Transform Infrared Spectroscopy with Attenuated Total Reflection

g-C_3N_4 Graphitic Carbon Nitride

h-BN Hexagonal Boron Nitride

HEPA High Efficiency Particulate Absorbing

IP Interfacial Polymerisation

LJ Lennard-Jones

MD Molecular Dynamics

MFC Mass Flow Controllers

MOFs Metal Organic Frameworks

MPD M-Phenylenediamine

MW-BNNTs Multi Walled Boron Nitride Nanotubes

MWCO Molecular Weight Cut Off

NF Nanofiltration

OCA Optical Contact Angle

PA Polyamide

PEI Polyethylenimine

PIP Piperazine

PMMA Polymethyl Metacrylate

POSS Polyhedral Oligomeric Silsesquioxane

PS Polystyrene

PVDF Polyvinylidene Fluoride

RA Risk Assessment

RO Reverse Osmosis

SC Spreading Coefficient (J m^{-2})

SEM Scanning Electron Microscope

TEM Transmission Electron Microscope

TEPA Tetraethylenepentamine

TETA Triethylenetetramine

TFN Thin Film Nanocomposites

TMC Trimesoyl Chloride

UF Ultrafiltration

VA-CNTs Vertically Aligned Carbon Nanotubes

VLS Vapor Liquid Solid

XPS X-Ray Photoelectron Spectroscopy

XRD X-Ray Diffraction

Greek Symbols

α	Effective Hydrodynamic Diameter of one Water Molecule (Å)
α_K	Supersaturation Ratio of Adsorbed Atoms (-)
δ	Thickness of the Low Viscosity Annular Region near the Nanotube Wall (m)
ϵ	Flow Enhancement (-)
ϵ_{ij}	Van der Waals Interaction Energy between a Pair of Interacting Atoms (i,j) (J)
ϵ_0	Vacuum Permittivity (F/m)
ϵ_r	Dielectric Constant (-)
ι	Randomly Generated Number (-)
κ	Inverse Debye Length (1/m)
λ_D	Debye Length (m)
μ	Fluid Viscosity
μ_B	Bulk Viscosity (Pa s)
μ_W	Annular Region Low Viscosity (Pa s)
ϕ	Membrane Porosity (-)
ρ_{n}	Number Density
σ	Surface Energy (J m^{-2})
σ_{ij}	Characteristic Length Scale (m)
τ	Tortuosity (-)
ζ_c	Particle Zeta Potential (mV)
ζ_m	Membrane Zeta Potential (mV)

Other Symbols

A	Constant (-)
c	Concentration (g L^{-1})
J_{BF}	Flux Before Fouling ($m^3m^{-2}s^{-1}$)
J_F	Flux During Fouling ($m^3m^{-2}s^{-1}$)
R_{ir}	Irreversible Fouling Resistance (m^{-1})
R_m	Intrinsic Membrane Resistance (m^{-1})
R_r	Reversible Fouling Resistance (m^{-1})
R_t	Total Fouling Resistance (m^{-1})
V	Volume (m^3)
ΔP	Transmembrane Pressure (Pa)
Δt	Time Step (s)
$\hat{y}_\mathrm{i}$	Predicted Adsorbance Value
$\langle\dot{\omega}\rangle$	Steady-State Average Mass Flow Rate (kg s^{-1})
μ_i	Chemical Potential (J)
ω_i	Mass (kg)
$\overline{x}$	Mean of the Concentration Values (g L^{-1})
$\overline{y_0}$	Mean of N Repeat Measurements of Absorbance (-)
$\overline{y}$	Mean of Absorbance Values (-)
$\mathbf{u}_p$	Particle Velocity Vector (m/s)
a	Particle Radius (m)
A_{mem}	Membrane Area (m^2)
Ad	Adsorption (%)
C	Nanotube Chirality Vector (m)
C_F	Feed Concentration of Nanoparticles (g L^{-1})

C_F Permeate Concentration of Nanoparticles (g L^{-1})

C_S Concentration of Nanoparticles Static Adsorption Tests (g L^{-1})

C_S Concentration of Nanoparticles Static Adsorption Tests Control (g L^{-1})

D_S Surface Diffusion (m^2/s)

dP/dz Pressure Gradient along Flow Direction (Pa/m)

F' Increase in Free Energy for the Formation of a Critical Nucleus (J)

F_B Brownian Force (N)

F_E Elecrostatic Force (N)

F_D Drag Force (N)

g System Steric Factor ($1/m^{-1}$)

h Distance between Particle and Membrane (m)

K Permeance (L $m^{-2}h^{-1}bar^{-1}$)

k_B Boltzmann Constant (m^2 kg s^{-2} K^{-1})

K_f Fluid Hydrodynamic Factor(-)

K_p Particle Hydrodynamic Factor (-)

Kn Knudsen Number (-)

L_s Slip Length (m)

m Graph Gradient

m_p Particle Mass (kg)

N Number of Repeats

n Number of Pores in a Membrane (-)

n_P Number of Paired Calibration Points

P_N Probability of Nuclei Formation

Q volumetric flow rate (m^3s^{-1})

q_{ij} Charge on one Atom (C)

R	Rejection (%)
r	Tube Radius Coordinate (m)
r_{ij}	Characteristic Length Scale (m)
R_N	Normalised Rejection ($\mathrm{m^{-1}}$)
R_t	Tube Radius (m)
R_a	Roughness Average
S	Tube Cross Section ($\mathrm{m^2}$)
T	Temperature (K)
$v_{(\mathrm{x,i})}$	x-Component Velocity ($\mathrm{m\ s^{-1}}$)
v_z	Cross Sectional Parabolic Velocity (m/s)
W_A	Work of Adhesion ($\mathrm{J/m^2}$)
x_{i}	Concentration ($\mathrm{g\ L^{-1}}$)
y_{i}	Adsorbance at a given concentration (-)
a_i	Nanotube Crystal Unit Vector (-)
m_i	Nanotube Crystal Structural Index (m)
p	Reactive Vapour Pressure (Pa)
$\mathrm{p}*$	Vapour Pressure (Pa)
p°	Equilibrium Vapour Pressure (Pa)

Achievements

Research Papers

Published

"*Surface-Controlled Water Flow in Nanotube Membranes*" Serena Casanova, Matthew K. Borg, Y. M. John Chew, and Davide Mattia in ACS Applied Materials and Interfaces in January 2019.

"*High Flux Thin-Film Nanocomposites with Embedded Boron Nitride Nanotubes for Nanofiltration*" Serena Casanova, TianYin Liu, Y. M. John Chew, Andrew G. Livingston and Davide Mattia in Journal of Membrane Science in December 2019.

"*The modelling and enhancement of water hydrodynamics: general discussion*" Baaden, M., Borthakur, M. P., Casanova, S., Coalson, R., Freger, V., Gonzalez, M., Gora, A., Hinds, B., Hirunpinyopas, W., Hummer, G., Kumar, M., Lynch, C., Murail, S., Noy, A., Sansom, M., Song, Q., Vashisth, H., and Vogele, M., in Faraday Discussions in September 2018.

"*Structure and function of natural proteins for water transport: general discussion*" Baaden, M., Barboiu, M., Bill, R. M., Casanova, S., Chen, C-L., Conner, M., Freger, V., Gong, B., Gora, A., Hinds, B., Horner, A., Hummer, G., Kumar, M., Lokesh, M., Mitra, S., Noy, A., Pohl, P., Sadet, A., Sansom, M. and Tornroth-Horsefield, S. in Faraday Discussions in September 2018.

Under Review

"*Enhanced Nanoparticle Rejection in Aligned Boron Nitride Nanotube Membranes*" Serena Casanova, Sritay Mistry, Saeed Mazinani, Matthew K. Borg, Y. M. John Chew and Davide Mattia.

"*Water Flow Enhancement in Polymer Nanotube Membranes*" Zheyi Meng, Serena Casanova, Halan Mohamed, Nidhi Kapil, Xiao Xiao, Yuheng Zhang, Marc-Olivier Coppens and Davide Mattia.

Presentation of Research

Oral

Dead Sea Water Workshop 2019 in Ein Gedi, Israel.

CVD Systems 2018 at Bath, UK.

Poster

Dead Sea Water Workshop 2019 in Ein Gedi, Israel.

Euromembrane 2018 in Valencia, Spain.

Artificial Water Channels Faraday Discussion 2018 in Glasgow, UK.

Chapter 1

Introduction

Membranes for water purification are semipermeable filters used to reject specific components in an aqueous mixture. In most cases, pressure is the driving force for the passage of clean water from the feed side to the permeate side of a membrane. This makes the processes particularly energy intensive and often dependent on fossil fuels [1]. However, the availability of cheaper, renewable, and more readily available energy has helped membrane technology to become predominant both in specific applications and in large growing markets such as desalination [2]. Currently, in order to further decrease the energy demand of the technology, membranes would benefit from the development of more mechanically, chemically and thermally durable materials, with higher water permeance and selectivity in specific applications and improved ability to resist fouling. Nanoengineered membrane materials have, in the past decades, been envisioned as a way to address these specific issues, via blending nanomaterials with new exceptional properties in the commercial membranes matrix [3].

Employing nanotubular structures in the membranes matrix sparked interest when the properties of carbon nanotubes (CNT) as fast transporters of water were discovered [4], thanks to the extraordinary behaviour of liquids in nanoconfined spaces [5]. This meant that the water flow per unit area at a specific applied pressure (called permeance) resulted in higher values in CNTs than what would have been expected by the classical Hagen Poiseuille theory for flow in a macroscopic channel. These findings were corroborated by experimental results and molecular dynamics, and sometimes also observed in polymeric nanochannels, however carbon nanotubes produced in different ways were found to be fast transporters of water to different degrees. In fact, several types of CNTs exist, each of them with different surface structure and chemistry. Additionally, there exist different types of membrane designs, all offering distinct advantages [6]. While CNTs could benefit membrane technology by providing improved water flow per unit area, the focus on new nanotube materials other than carbon alone has the potential to bring added functionalities such as pollutants rejection based on both size and charge [7, 8].

This work aims at discerning the effect that distinct types of nanotube structures and chemistries have on water flow through them to facilitate the selection of nanotube materials for specific applications. The scope of this research is then to investigate how different tubes surface charge properties can be used to target removal of specific pollutants. The findings of this work hope to direct future research towards the most promising nanotubes materials, by analysing different types and configurations of nanotube membranes.

Research on the synthesis of nanotubes membranes was first published in the late 90es

[9, 10], with arrays of nanotubes serving as the membrane transport-promoting phase. The basic concept of nanotube membrane is visualised in Figure 1-1. In this work, two types of nanotube membranes will be under analysis:

- Hybrid membranes, where nanotubes serve as the transport phase and a dense, rigid template provides structural support;
- Thin film nanocomposite membranes, where nanotubes are randomly embedded in a selective part of a layered membrane, located on top of a porous support.

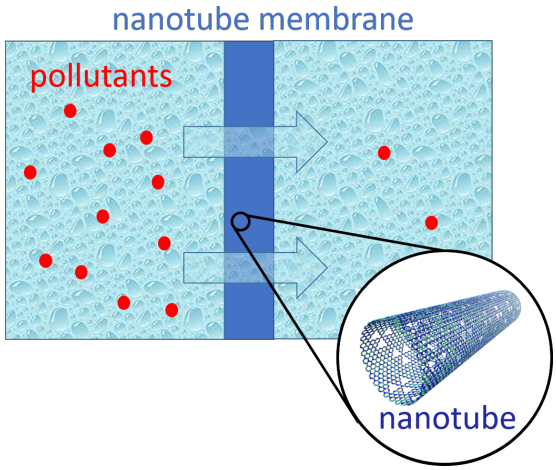

Figure 1-1: Simplified illustration of a nanotube membrane for water purification. The central blue rectangle is the representation of a membrane, where nanotubes are inserted. The feed on the left hand side contains a large amount of pollutants (represented by red dots), whilst the permeate side contains only few.

Hybrid membranes based on different materials will be used in this work for fundamental studies on permeance and rejection, and thin film nanocomposites for investigating application in commercial membranes.

Carbon nitride and boron nitride represent excellent candidates for the production of the next generation of nanotube membranes. Graphitic carbon nitride is a non-metallic visible light photocatalysit that could allow for integrated *in situ* degradation of pollutants or fouling break up [11] in a nanofiltration step. However, there is a gap in the literature studies of water flow through carbon nitride nanotubes. Boron nitride nanotubes (BNNTs) possess high chemical inertness and thermal stability, and are excellent candidates for application in targeted rejection [12]. Molecular dynamics (MD) studies have predicted higher salt rejection for BNNTs than CNTs [13], although experiments have shown slower transport than CNTs [14]. Thus, it is interesting to elucidate on rejection mechanisms in BNNTs.

Polymeric nanotubes are also of interest for fundamental research. Whilst a rich literature exists on transport in polymeric membranes, the permeability of a given material depends on its geometry, as well as its chemistry. Phase inversion, the method most widely used to produce membranes with pores in the nanometre-range, is a macroscopic process that leaves little to no ability to predict the shape of a membrane's pores. This means that we do not have reports that directly link water flow in polymeric nanochannels to their geometry, and thus do not know whether the choice of specific polymeric materials can allow for water flow enhancement.

Literature relevant to this work is discussed in Chapter 2. Firstly, the general concept of dual phase hybrid membranes is given in Section 2.1, alongside explaining their potential in membrane technology. Section 2.2 aims at presenting the theory behind water transport in nanotubes, supported by papers on experimental measurement and molecular dynamics modelling. Section 2.3 gives an elucidation on the interplay of the major forces that play a role on rejection in nanoporous materials. The state of the art research on boron nitride and carbon nitride nanotubes is discussed in Sections 2.4 and respectively, emphasising the interest in the materials, their structure and the investigated synthetic routes. Aims and objectives are summarized in Chapter 3. In Chapter 4, Materials and Methods include characterisation, synthesis, modelling and testing methods. Chapter 5 aims at separately describing the effect that a change in carbon nanotube structure with the introduction of defects and a change in chemistry with the introduction nitrogen has on water permeance by combining experimental results and molecular dynamics. Chapter 6 reports on improved nanoparticle rejection in boron nitride nanotubes membranes, due to the material ability to maintain a highly negative charge over a wide range of pH. The optimisation of polymeric nanotubes synthesis in anodic alumina membranes is reported in Chaper 7, together with the first attempts to measure water flux through polymeric nanotubes with a fixed geometry. The novel embedding of boron nitride nanotubes in membranes modules with facile up-scaling is investigated in Chapter 8. The main conclusions drawn from this research and a contemplation on future challenges are collected in Chapter 9.

Chapter 2

Literature Review

2.1 Dual Phase Hybrid Membranes

Nanotube membranes have been prepared in various configurations, each resulting from different synthesis paths and presenting remarkably specific challenges [6]. In the production of vertically aligned carbon nanotubes (VA-CNTs) membranes (Figure 2-1a and d), the tubes are grown by catalytic chemical vapour deposition (CVD) on a silicon substrate. CVD is a bottom-up, atom by atom technique, where the material to be deposited is first heated to sublimation and then allowed to deposit, directly or via a chemical reaction, on to a solid surface. The diameter of the tubes produced via this method is controlled by the chosen catalyst size [15]. A polymer is then spin coated [16] on top of the carbon nanotubes (CNTs) forest and the resulting membrane detached from the substrate by dissolving the latter in hydrofluoric acid. Plasma etching is then used to remove excess polymer from the top surface and open the tubes tips [17]. Although this method provides a route for the fabrication of aligned tubes with controllable size embedded in a durable membrane, it has not seen commercialisation in the decade since its discovery due to challenges in scalability and cost [6].

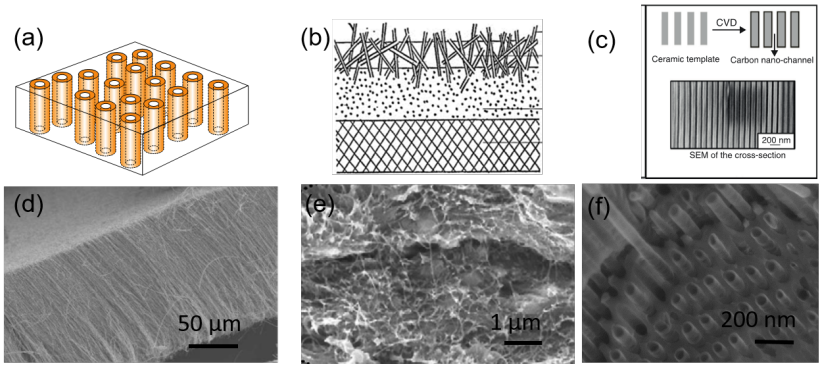

Figure 2-1: Different types of nanotube membranes reported in literature [6]: (a,d) VA-CNTs (adapted from [17]); (b,e) TFC and (c,f) templated CNTs (adapted from [18]).

A cheaper option has been envisioned in the embedding of nanotube fillers in the selective layers of thin film nanocomposites (TFCs) schematised in Figure2-1b,e which, although often promising [19, 20], results in randomly oriented tubes [21]. This depresses the maximum attainable improvement in permeance and renders the nanofiller addition rarely worthwhile [3].

The orientation question is completely bypassed when the nanotubes are directly deposited in the pores of ceramic anodic alumina membranes (AAM) as shown in Figure 2-1c and f [22]. In this case, however, the resulting membranes find little industrial

application due to their brittleness and cost. They nonetheless represent an excellent platform for fundamental studies, given the extremely well defined geometry and pore uniformity of the substrate [23, 18].

The AAM-nanotube membranes are dual-phase hybrid membranes, namely composites including two phases at the nanometre scale. A phase promoting transport is embedded in a phase that serves as support material (Figure 2-2). The transport phase creates a continuous channel across the membrane. In this configuration, the nanotubes are the only phase promoting transport, unlike in VA-CNTs and TFN where water can also flow through the porous polymeric support. This makes templated nanotubes an ideal mean for experimental studies of the nanotube performance, independent from its matrix.

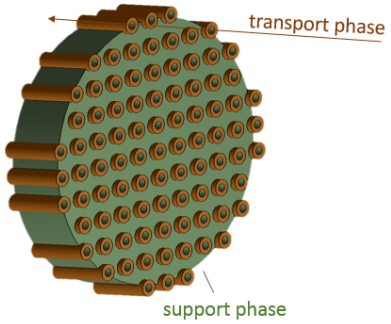

Figure 2-2: Schematic of a dual-phase hybrid membrane, where one phase favours transport and another solely serves as structural support.

2.2 Nanotubes as Fast Transporters of Water

This section will focus on water flow in nanotubes. This will include the concept and history of flow enhancement, molecular dynamics simulations and the nature of permeance in nanotubes based membranes.

2.2.1 Flow Enhancement

Navier-Stokes equations are used for the description of velocity profiles in laminar flow of Newtonian fluids, where the fluid is well approximated by a continuum. This latter condition is verified when $Kn \ll 1$, with Kn being the dimensionless Knudsen number, defined as the molecular mean free path over the characteristic physical length [24].

Equation 2.1 describes a parabolic fluid velocity profile in a tube with circular cross section and radius (r):

$$v_z(r) = \frac{dP}{dz}\frac{1}{2\mu}[(L_s + R_t)^2 - (R_t - r)^2] \tag{2.1}$$

The cross-sectional velocity (v_z) is a function of the pressure gradient along the flow direction (dP/dz), the dynamic fluid viscosity (μ), the tube radius (R_t) and the slip length (L_s). The slip length represents the depth in the solid wall of the tube where the velocity profile equals zero [25] as depicted in Figure 2-3.

When v_z is integrated over the cross sectional area along the length of the tube with length L on a cross section S, the volumetric flow rate can be expressed as:

$$Q_{L_s} = \int v_z dS = \frac{\pi(R_t^4 - 4R_t^3 L_s)}{8\mu}\frac{\Delta P}{L} \tag{2.2}$$

This equation can be rearranged in the Hagen Poiseuille equation for flow of an incompressible fluid at a constant velocity in a smooth, cylindrical pipe where L_s equals zero:

$$Q_{HP} = \int v_z dS = \frac{\pi R_t^4}{8\mu}\frac{\Delta P}{L} \tag{2.3}$$

When dealing with tubes in the nanoscale, the Haagen Poseuille equation can no longer be used with the classical Hagen-Poiseuille no-slip boundary condition (L_s=0) [27]. The observed slip lengths are often much larger than the tube radius and cannot, therefore, be neglected [28, 29, 6, 30, 31, 18].

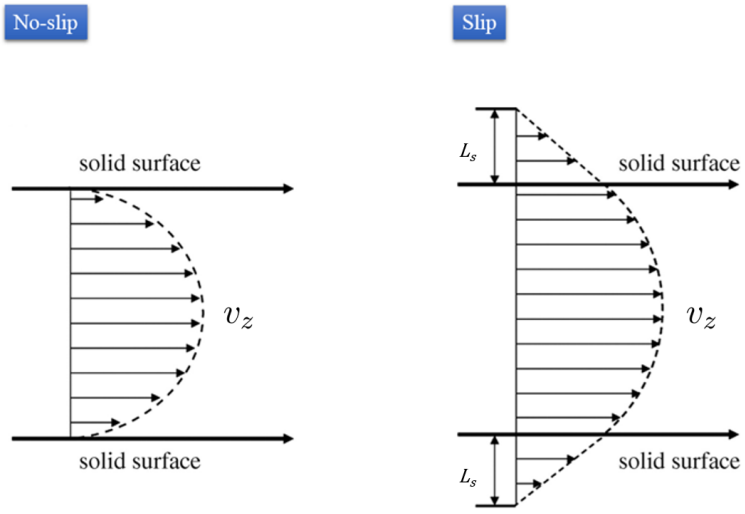

Figure 2-3: Schematics of the slip length (L_s) in a tube where the cross section of the parabolic velocity of the fluid is displayed as v_z in the two conditions of no-slip and slip. Image adapted from Dean et al. [26].

To describe the increased flow in nanotubes and other nanochannels [32], the concept of flow enhancement (ϵ) has been employed and analysed via molecular dynamics (MD) and experimental work:

$$\epsilon = \frac{Q_{L_s}}{Q_{HP}} = 1 + \frac{4L_s}{R_t} \tag{2.4}$$

2.2.2 Molecular Dynamics Studies

Hummer et al. [4] firstly modelled features of water transport in carbon nanotubes in 2001, acknowledging the possibility of the formation of a vapour layer between the nanotube wall and the bulk water in the centre of the nanotube. This was attributed to strong H-H bonding that would cause the water molecules to separate from the tube surface. This study concluded that water molecules would be transported in a pulse-like manner inside the tube. It was also found that increasing the water-tube interaction lead to an increased amount of water in the tube and vice versa, suggesting that CNTs could be used as unique fast water channels [4].

In 2008, Suk et al. [33] used non-equilibrium MD simulations to model the passage of water through polymethyl metacrylate (PMMA) membranes, CNTs and boron nitride nanotubes (BNNTs). Higher fluxes in both types of nanotubes in respect to PMMAs were explained with the use of a theoretical single file water molecules "hopping" model,

where groups of molecules arranged in a single file are transported as a series of discrete hopping events as shown in Figure 2-4 [33, 34].

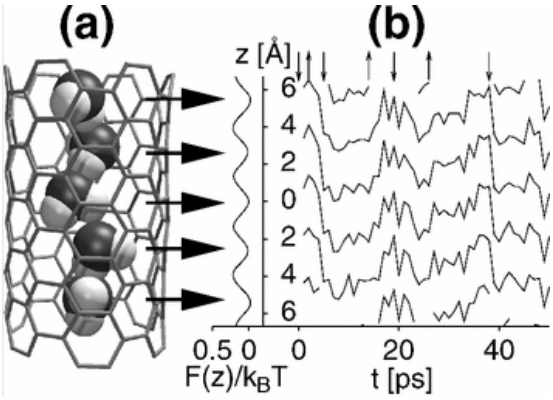

Figure 2-4: (a) Graphical representation of the theoretical single file water molecules "hopping" in a CNT. (b) Dimensionless free energy profile, function of the water density along the channel axis from MD simulations, with minima indicated by horizontal arrows. The trajectories of the molecules permeating the nanotube are plotted as a function of time in the right part of panel (b). Figure is adapted from Berezhkovskii et al. [35].

The assumption of joint hops of water molecules files through nanopores clarifies the disagreement of the results with classical solution-diffusion theory [36], which does not contemplate collective water molecules movement. Larger hopping rates for BNNT were explained from the lower energy barrier present at the pore entrance and in the pore interior. This difference in the energy profiles is due to stronger van der Waals interaction between BNNT and water than in CNTs.

In addition to the observation of the peculiar single-file flow path in the sub continuum, the flow of water in a nanotube varies also as a consequence of water-tube interaction. Figure 2-5 shows how the increase in attraction strength between nanotube and water makes it more likely for the nanotube to be filled. Per contra, when the attraction strength becomes too high, the tendency for water is to stick on the carbon nanotubes walls leading to a decrease in the water permeation. Garnier et al. performed MD studies on the physics behind water transport through the 2D counterparts of CNTs and BNNTs [37]. In this study as well, BN layers were shown to be more permeable than carbon layers, and this was attributed to the higher surface tension of the graphene monolayer (91.5 mN m^{-1}) in respect to the BN one (78 mN m^{-1}), i.e. a varied water-tube interaction resulting in a 60% higher water permeation. Additionally, in the subcontinuum, permeation is stongly related to the edges' atomic configuration and the energy requirements for single water molecules to enter the nanotubes [38].

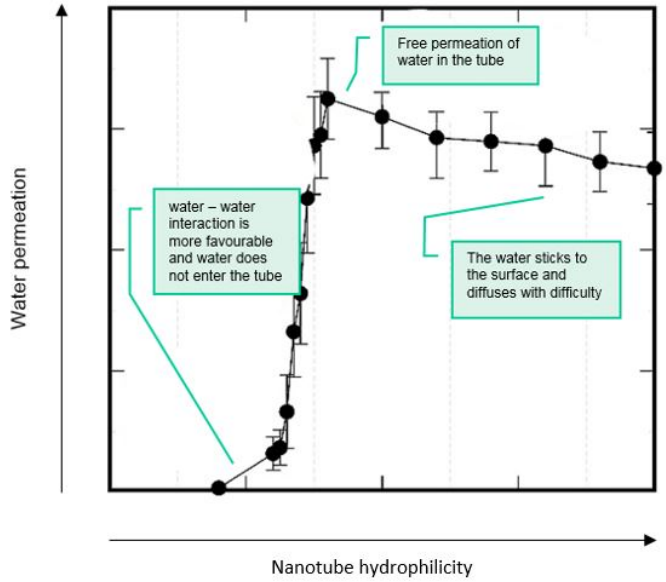

Figure 2-5: Dependence of the water passage through a carbon nanotube on the nanotube hydrophilicity. Figure adapted from Melillo et al. [35].

When the conditions of the continuum model are satisfied, for nanotubes with 2 nm diameter and above, the flow rate in CNTs was shown to be consistently higher than in BN and silicon carbide nanotubes [30]. This proved the direct proportionality between solid-liquid molecular interaction and flow enhancement, exemplified in this study through the use of the parameters D_S, surface diffusion on the nanotube material, and work of adhesion (W_A), function of the tube's wettability. The water inside the tubes was modelled as a two-fluid system, being that the fluid density decreased more toward the central annular region of the tubes for all the three materials analysed, showing a reduced-density corona of water adjacent to the wall. This phenomena was explained elsewhere in terms of friction as one of the main sources of dissipation in liquid water/solid interfaces and therefore as one of the major limits to water transport at nanoscale [39].

2.2.3 Experimental Studies

Experimentally, the importance of the nanotube radius in evaluating its permeance[14] could be shown, as simulating large radii is computationally expensive for MD. In the nanoscale (diameter $D \leq 100$ nm), the water permeability of CNTs is found to be considerably higher than for BNNTs, revealing unexpectedly large and radius-dependent

surface slippage in CNTs, and no slippage in BNNTs. This was explained by the electronic landscape on the walls of boron nitride nanotubes different from carbon nanotubes despite the similar structure and wetting behaviour [40]. A high slip length was also recorded for small CNTs radiuses, and this relates back to the hypothesis of enhanced permeability due to hydrodynamic slippage put forward in previous literature [25, 41–43].

A further advancement in term of nanofluidics devices was made when ion currents in single nanotubes were first measured [44]. The detection of flows for nanotubes with small radii still was earlier impeded by the insufficient sensitivity of available flow detecting systems. Subsequently, these challenges were overcame by recording the flow that a fluid jet entrains outside of a nanotube [14] and using the scaling properties of the jet hydrodynamics [45], opening up the way to test water flow in single BNNTs and CNTs.

Whilst water flux in single BNNTs was reported experimentally [14], difficulties into synthesizing a full-sized boron nitride nanotube membrane to date impeded obtaining data on the permeance of boron nitride nanotube membranes.

2.2.4 Permeance Model in AAMs

While numerous studies provided the evidence that water flow is higher in nanotubes than what predicted from the classical Hagen Poiseuille model, little has been done to relate such flow enhancement to nanotube permeance. This latter is a key parameter that allows one to state if a membrane is attractive to the water purification market. In contrast, extrapolating only flow enhancement for a nanotube membrane has little to no direct practical applications. The permeance of a membrane (K), often expressed in L $m^{-2}h^{-1}bar^{-1}$, is calculated by:

$$K = \frac{Q}{\Delta P A_{mem}} \tag{2.5}$$

where Q is the flow through the membrane, ΔP is the transmembrane pressure and A_{mem} is the membrane area. Traditionally, this term has been ambiguously called permeability in the literature on water filtration, while it has been addressed as permeance in gas permeation [46]. Permeability is a qualitative property and has the units L m $m^{-2}h^{-1}bar^{-1}$, equal to the permeance multiplied by the thickness of the membrane. It is therefore better to focus on permeance or flux instead of permeability, since one could make a very dense film and get a high permeability, however, the permeance

could be very low. The orders of magnitude improvements in flow in nanochannels do not necessarily translate to equal permeance increases and flow enhancement changes as a function of nanotubes radii and lengths, making the comparison of results from different publications a challenging task.

Testing the permeance of carbon nanotubes coated inside an AAM offers cylindrical, equally spaced pores with narrow size distribution, and allowed for the elaboration of a theoretical model for the prediction of permeance in nanotubes membranes[18]. AAMs are ideal for an easy definition of porosity (ϕ) as the pores area over the total membrane area can be defined as:

$$\phi = \frac{1}{A_{mem}} \sum_{i=1}^{n} \pi R_{t_i}^2 \equiv \frac{n\pi R_t^2}{A_{mem}}, \tag{2.6}$$

where n is the number of pores. A model for the flow enhancement as a function of the tube's geometry was built and validated [47] starting from the assumption of reduced liquid viscosity near the tube wall, supported by molecular dynamics simulations [31, 41]:

$$\epsilon = \left(\frac{R_t - \delta}{R_t}\right)^4 \left(1 - \frac{\mu_B}{\mu_W}\right) + \frac{\mu_B}{\mu_W} \left(1 + 8\mu_W \frac{L}{R_t^2} \frac{D_S}{W_A}\right), \tag{2.7}$$

where δ is the thickness of the low viscosity annular region near the nanotube wall. μ_W is the low viscosity in the annular region and μ_B is the higher bulk fluid viscosity. Equation 2.7 can be combined with Equations 2.4, multiplying Q_{HP} (Equation 2.3) by n to find an expression for the total Haagen Poiseuille flow in the n nanotubes of an AAM as follows:

$$Q_{exp} = \frac{\pi D^4 \Delta P}{128 \mu_B L} \left(1 + \frac{8L_s}{D}\right) \frac{4\phi A_{mem}}{\pi D^2} = \frac{\phi A_{mem} D^2 \Delta P}{32 \mu_B L} \left(1 + \frac{8L_s}{D}\right), \tag{2.8}$$

where D is the membrane diameter. Inserting this in Equation 2.5 yields an expression for permeance:

$$K = \frac{Q_{exp}}{\Delta P A_{mem}} = \frac{\phi R_t^2}{8\mu_B L} \left[\left(\frac{R - \delta}{R}\right)^4 \left(1 - \frac{\mu_B}{\mu_W}\right) + \frac{\mu_B}{\mu_W} \left(1 + 8\mu_W \frac{L}{R_t^2} \frac{D_S}{W_A}\right)\right] \tag{2.9}$$

The first term in the square brackets on the right hand side of the equation is negligible compared to the second term for pore sizes in the ultrafiltration range and below [18]. Additionally, $8\mu_W \frac{L}{R^2} \frac{D_S}{W_A} >> 1$ for the same domain, so Equation 2.9 can be simplified:

$$K \approx \phi \frac{D_S}{W_A} \tag{2.10}$$

Equation 2.10 was found to describe (R^2=0.70) the experimental results of Mattia et al. [18] for the permeance through CNT-AAMs quite well, as shown in Figure 2-6. W_A can be calculated knowing the contact angle of the material, while D_S is a product of molecular dynamics. The applicability of Equation 2.9 is not limited to CNT membranes and can in principle be also used for other AAMs [48].

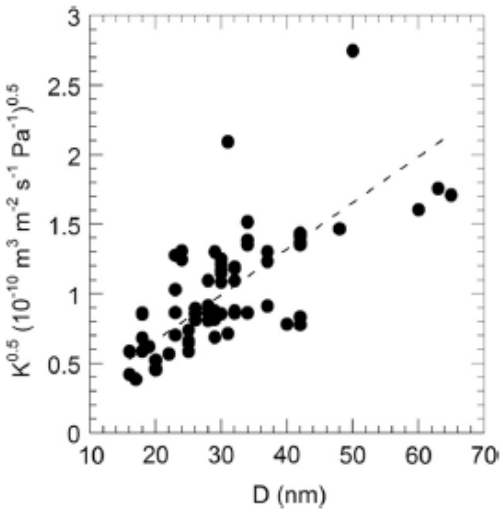

Figure 2-6: Square root of CNTs membranes' permeance, with full dots showing experimental value and a dotted line showing the values computed from the theoretical model in Eq. 2.10 (Figure adapted from Mattia et al. [18]).

Carbon nanotubes permeance results for this work and others in literature are displayed in Figure 2-7. The increase in term of permeance is less significant than what flow enhancement appeared to promise. While CNT-based membranes do not appear to outperform traditional polymeric membranes for reverse osmosis (RO), this changes in the nanofiltration (NF) and ultrafiltration (UF) range where CNT-based membranes show significant potential of improving performance.

In many configurations, nanotube membranes are penalised by tubes agglomeration and low porosities [49]. As it can be noted from Figure 2-7, there is a big variation in the reports of permeance in different carbon nanotube materials, and this picture might become even more complex once other nanotube materials are investigated.

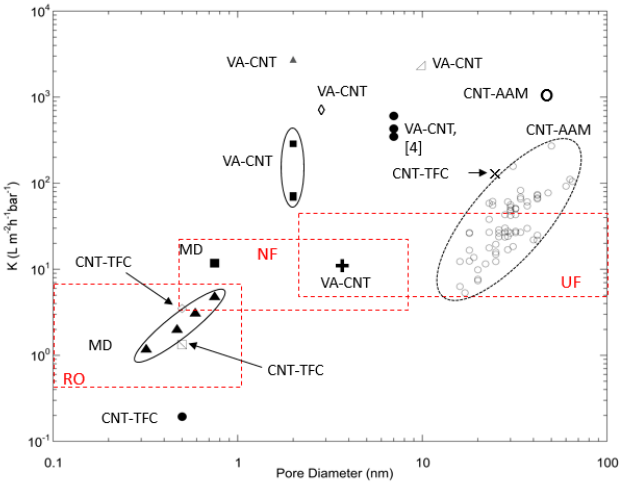

Figure 2-7: Figure that groups CNTs performances in terms of permeances as a function of the tubes diameters, in comparison to reference values for RO, NF and UF (Figure adapted from Mattia et al. [18]).

2.3 Charge Selective Transport

In nanotube membranes with pore sizes above 2 nm the transport of water is mainly controlled by the Hagen Poiseuille equation, as seen in Section 2.2. When particles are dispersed in the feed, the following equation describes the driving force along a tube acting on all components:

$$F = -\frac{d\mu_i}{dz}, \tag{2.11}$$

where μ_i is the chemical potential of the species i and z the tubes' axis direction. In the absence of charge on the particles filtered, the main mechanism for separation is due to the exclusion given by the narrow pore size of the membrane compared to the pollutants'.

Nanotube membrane permeance, as shown in Equations 2.8 and 2.9, is proportional to the square of the nanotube diameter D. It follows that achieving the same rejection with a membrane having a fractionally bigger nanotubes diameter could lead to a great advantage in terms of permeance, pushing research via achieving rejection towards mechanisms other than the size based one.

In fact, sieving is governed by the interplay of forces acting on feed particles [50]. Drag

(F_D), electrostatic (F_E) and Brownian (F_B) are reputed as the primary non negligible forces that should be analysed when pollutants size is comparable to membrane pore size [51]. It is possible to study the combined effect of such forces on particle trajectories in dead end and cross flow filtration by numerically integrating the Langevin equation [52], used to describe the stochastic motion of a particle subject to different forces:

$$m_p \frac{d\mathbf{u}_p}{dt} = \mathbf{F}_D + \mathbf{F}_E + \mathbf{F}_B. \tag{2.12}$$

In Eq. 2.12, the term $\mathbf{u}_p$ is the particle velocity vector and m_p its mass. The drag force arises from the friction induced by the relative velocity of the particle and fluid medium and is so expressed:

$$\mathbf{F}_D = 6\pi\mu a[K_p\mathbf{u}_p - K_f\mathbf{u}_f]. \tag{2.13}$$

$\mathbf{u}_f$ is the fluid velocity evaluated in absence of the particle, a is the particle radius, μ the fluid dynamic viscosity, and K_f and K_p hydrodynamic factors accounting for the hydrodynamic hindrance due to interactions between the particle and membrane surface.

An expression for F_E based on DLVO (Derjaguin, Landau, Verwey, and Overbeek) theory was introduced by Bowen et al. [53] as a function of the surface zeta potentials of the particle (ζ_c) and membrane (ζ_m). F_E is also dependant on the distance h between the particle centre and the membrane and the Debye length ($\lambda_D = 1/\kappa$):

$$\mathbf{F}_E = \frac{2\pi\kappa\epsilon_r\epsilon_0}{g}\left[\frac{2\zeta_c\zeta_m exp(\kappa[h-a]) - (\zeta_c^2 + \zeta_m^2)}{exp(2\kappa[h-a]) - 1}\right], \tag{2.14}$$

where ϵ_0 is the vacuum permittivity, ϵ_r is the dielectric constant and g is a steric factor linked to the specific geometry of the system [51].

The Brownian force is modelled on the basis of the Gaussian white noise method [54]:

$$\mathbf{F}_B = \iota\sqrt{\frac{12\pi a\mu k_B T}{\Delta t}} \tag{2.15}$$

where ι is a randomly generated number, Δt is a predetermined time-step, T is the temperature and k_B the Boltzmann constant. It is possible to solve this system of equations by computational fluid dynamics simulation as introduced by Zydney et al.

[51], who showed how the interplay of these forces dominated fouling in ultrafiltration membranes. Figure 2-8 shows the impact of the surface zeta potential on the ability of a charged particle to cross the membrane pore, stimulating future research on how this could work in nanotube membranes delivering high rejection and permeance.

Based on the system under analysis, rejection's dominating mechanism can either be steric, that is geometrical hyndrance to the pollutant's passage, or instead mainly controlled by surface-pollutant electrostatic interaction [55].

The rejection of salts in pristine, uncharged carbon nanotubes is mainly steric-based and almost solely depends on the energy barrier at the entrance of the pore, whilst the transport of molecules results almost frictionless, corresponding to $L_s \to \infty$, once ions have made it into the inside of the nonpolar CNTs interior [56].

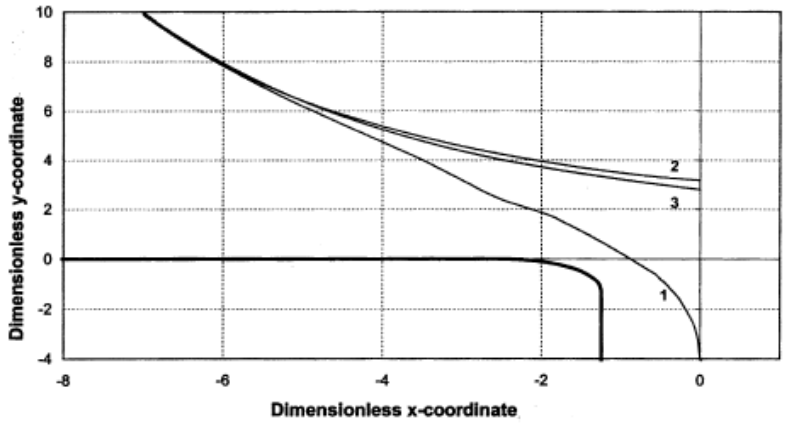

Figure 2-8: Particles in simulations with a membrane with ζ_m =-25.7 mV and $\mathbf{u}_f$ = 0.001 m/s and different forces acting upon them: (1) No electrostatic or hydrodynamic hindrance, (2) Electrostatic force only and (3) combined electrostatic force (Figure adapted from Zydney et al. [51]).

MD showed that the addition of charged groups at the entrance of nanotubes aided the effective rejection of ions in CNTs, moving from a steric based to a charge based type rejection [57, 58] and BNNTs [59]. Nanotube membrane rejection was studied experimentally in small CNTs (D = 1-2 nm) [60], finding that electrostatic interactions between functionalised ends and salts were a more dominant contribution than steric effects. In fact, pore entrance functionalisation with negativley charged carboxylate groups contributed to ionic exclusion, showing great dependence of the latter on solution pH and ions valency [60]. However, when values for flow enhancement were analysed in these membranes, a significant decline in water transport was recorded

[61, 57], highlighting that, as is often the case, the improved rejection in functionalised tubes is paid back with a decrease in permeance. A similar decline in permeance can be observed when comparing highly charged BNNTs and silicon carbide nanotubes to CNTs [30], however to a smaller extent, and investigating highly charged materials for enhanced rejection applications could benefit the technology with higher fluxes and no need for purification steps [13].

Tube type	Water flux	% Water flux	Na^+ flux	Cl^- flux	Na^+ rejection	Cl^- rejection
non func	107.8 ± 0.6	100%	0.22 ± 0.01	0.05 ± 0.01	28%	86%
$4COO^-$	35 ± 2	33%	0.10 ± 0.04	0.00 ± 0.03	32%	100%
$8COO^-$	14 ± 3	13%	0.00 ± 0.03	0.00 ± 0.03	100%	100%
$2NH^+_3$	60 ± 2	67%	0.03 ± 0.03	0.03 ± 0.03	86%	87%
$4NH^+_3$	22.1 ± 0.7	24%	0.00 ± 0.03	0.00 ± 0.03	100%	100%
$8NH^+_3$	18.9 ± 0.8	18%	0.00 ± 0.03	0.03 ± 0.03	100%	66%
$2NH^+_3$ $2COO^-$	46 ± 2	49%	0.03 ± 0.03	0.03 ± 0.03	82%	82%
$4NH^+_3$ $4COO^-$	18 ± 1	17%	0.03 ± 0.03	0.00 ± 0.03	55%	100%
4OH	70 ± 2	75%	0.30 ± 0.06	0.10 ± 0.06	−16%	61%
8OH	43 ± 2	47%	0.08 ± 0.04	0.00 ± 0.03	50%	100%
$4CONH_2$	59 ± 3	65%	0.13 ± 0.06	0.03 ± 0.03	41%	86%
$8CONH_2$	38 ± 2	42%	0.10 ± 0.04	0.00 ± 0.03	29%	100%
$3 \times (2NH^+_3)$	59 ± 1	66%	0.01 ± 0.01	0.02 ± 0.01	94%	92%
$3 \times (4NH^+_3)$	23 ± 1	25%	0.00 ± 0.01	0.00 ± 0.01	100%	100%

Figure 2-9: List of carbon nanotubes of various sizes (indicated by a number in the first column) and functionalised with different groups. Permeances and rejections of sodium and chloride ions are reported in comparison to a non-functionalised membrane (Figure adapted from Corry et al. [57]).

Surface charge dependant rejection was observed in silica nanopore membranes, where the strong rejection of dyes dependance on ion valency and pH was corroborated [7]. On the contrary, when no extra charge is present on the nanotube materials, the rejection of nanoparticles follow the classical size exclusion model [55]. In addition to promised higher rejection, materials with higher negative zeta potential can reduce foulant adhesion [62], therefore demonstrating themselves as promising.

2.4 Beyond Carbon Nanotubes

The ability to produce nanotubes membranes with enhanced water transport properties but with improved rejection and additional intrinsic antifouling and antibacterial functionalities promotes research beyond carbon by the investigation of new materials.

Soon after the discovery of carbon nanotubes in 1991 [63], attempts were made at altering these structures to tune performance by the addition of dopants. Boron and nitrogen stood out as feasible options [64], and explorations regarding their atomic structures eventually lead to the theorization of pure BNNTs [65]. C_xN_y structures and particularly graphite-like carbon nitride g-C_3N_4 have also attracted a lot of research and have proved an interesting option both in methanol electrooxidation [66] and as a metal-free photocatalyst. In fact when g-C_3N_4 and the most widely used photocatalyst P25 TiO_2 are compared, the g-C_3N_4 nanotubes show much higher photocatalytic activity [67]. However, P25 has a much larger BET surface area (about 50 m^2g^{-1}), and this is a key factor in increasing photocatalytic activity. This means that when the surface area increases, without changing the surface properties, the rate of reaction between e- and h+ with the substrate (which is proportional to the photocatalytic process efficiency) becomes faster due to the greater number of adsorbed molecules surrounding the pair e-/h+. Given this, it is particularly interesting to assess if the water permeance of carbon nitride nanotubes is as high as in CNTs in the prospective to integrate photocatalytic degradation of pollutants in a new generation of dual phase membranes for nanonofiltration. This analysis is eased by the recent simplification of bulk graphitic carbon nitride nanotubes (g-C_3N_4 NTs) synthesis routes [67].

BNNTs are interesting for their superior thermal and mechanical properties [68], optical characteristics [69], chemical stability and thermal conductivity [70]. BNNTs are isostructural and isolectronic of CNTs [71, 72]. They are semiconductors (bandgap $\sim$5.5 eV) and electrical insulators at room temperature [69] and have been considered for a variety of applications as a standalone material in nanodevices or to enhance the properties of mixed matrix materials [73, 71]. However, BNNTs are not found in nature and are hard to synthetically produce in large quantities. The most recurrent synthesis product consists of multi-walled boron nitride nanotubes (MW-BNNTs).

BN nanomaterials are today considered as one of the most promising inorganic nanosystems [12], particularly because of their ability to bind more strongly to polymers than carbon nanotubes [74]. Therefore, BNNTs are suitable candidates as the water transport phase of a hybrid membrane for desalination or for heavy metals removal, at the

same time providing the membrane composite with improved robustness and thermal resilience [75]. MD studies of tubes with diameters ≈ 0.8 nm predicted water fluxes one order of magnitude larger than in thin film composite membranes and rejections very close to 100% even for salt concentrations as high as 1M [33, 13].

2.4.1 Carbon Nitride Nanotubes Structure and Synthesis

Carbon nitride nanotubes (CNNTs) are formed by hexagonal structures assembled in triazine-like units to form the nanotube wall, similarly to carbon nanotubes [76] (Figure 2-10).

When the tubes are multiwalled, the layered structure involves weak Van der Waals interaction between layers. Whilst the ideal CNNTs stoichiometry is 1:1.33=C:N, this varies based on the synthetic route. Early experimental results reported a 1:1.25=C:N atomic ratio, with a 0.5 wt% hydrogen component [77]. Wang et al. later found a ratio of 1:1.07 [67], synthesizing carbon nitride nanotubes with 19.7% less nitrogen than theoretically expected. Occasionally carbon nanotubes doped with nitrogen (N ∼ 17%) have been produced with the aim of synthesizing carbon nitride nanotubes [78]. Theoretical studies prove that the synthesis of C_3N_4 can be achieved with smaller strain energies compared to CNTs, leading to a material with metallic properties irrespectively of their chirality [76]. In this work, we refer to graphitic carbon nitride nanotubes when the stoichiometry is very close to the theoretical C:N=0.75, and to nitrogen doped carbon nanotubes for N atomic % below 20%. The class of nanotubes which present high ratio of N:C, but lower than theoretically expected for C_3N_4 is named carbon nitride nanotubes (CNNTs).

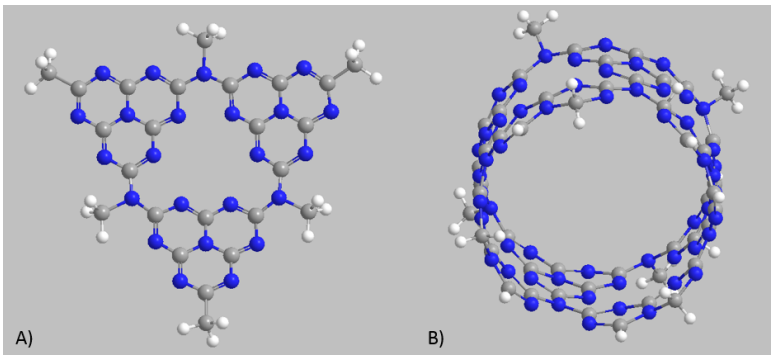

Figure 2-10: Chemical structure of (A) one g-C_3N_4 unit and a (B) CNNT. The nitrogen atoms are coloured blue and the carbon atoms are coloured in grey.

The reported synthesis routes of carbon nitride nanotubes can be grouped into solid [79,

80], liquid [66, 78, 81, 82] and gas synthesis [83]. All the synthesis methods described occur at relatively low temperature between 500 and 600 °C. A schematic summary of the synthesis routes listed in this Section is given by Figure 2-11.

Bulk synthesis

Amorphous CNNTs were successfully formed by metathesis reactions between cyanuric chloride and several solid nitrogen sources. g-C_3N_4 NTs were found in a mixture with tubes on a μm scale but contained Cl core impurities resulting from the precursors. It was found that the produced nanotubes could not be dispersed in water, weak acids or organic solvents [79].

The most notable advance in CNNTs synthesis was probably the discovery that these could be produced from melamine calcination, releasing NH_3 in the process. Melamine is a cheap, easy to source and non hazardous precursor. The proposed formation process for this route is by rolling up of graphitic carbon nitride 2D layers exfoliated from the melamine [67], procedure hypothesized to be aided by the NH_3 flow produced by melamine calcination in a specific pathway that would aid NTs formation [84]. Nanotubes thus manufactured present high photocatalytic activity, their synthesis proving repeatable and versatile [80, 11]. However, the aforementioned CNNTs were often short ($\approx$ 200 nm), presenting morphological inhomogeneities [67].

Templated synthesis

CNNTs have been synthesized in AAMs, however the use of toxic precursors and the inability to surpass N percentages of $\sim$30% hindered the widespread of the approach. The first liquid synthesis of nanotubes made of carbon and nitrogen started with the preparation of a sol gel precursor from $(CH_2NH_2)_2$ and CCl_4 and its subsequent infiltration inside the membranes pores with the aid of ultrasonication (Figure 2-12), followed by polymerisation reaction in a AAM template.

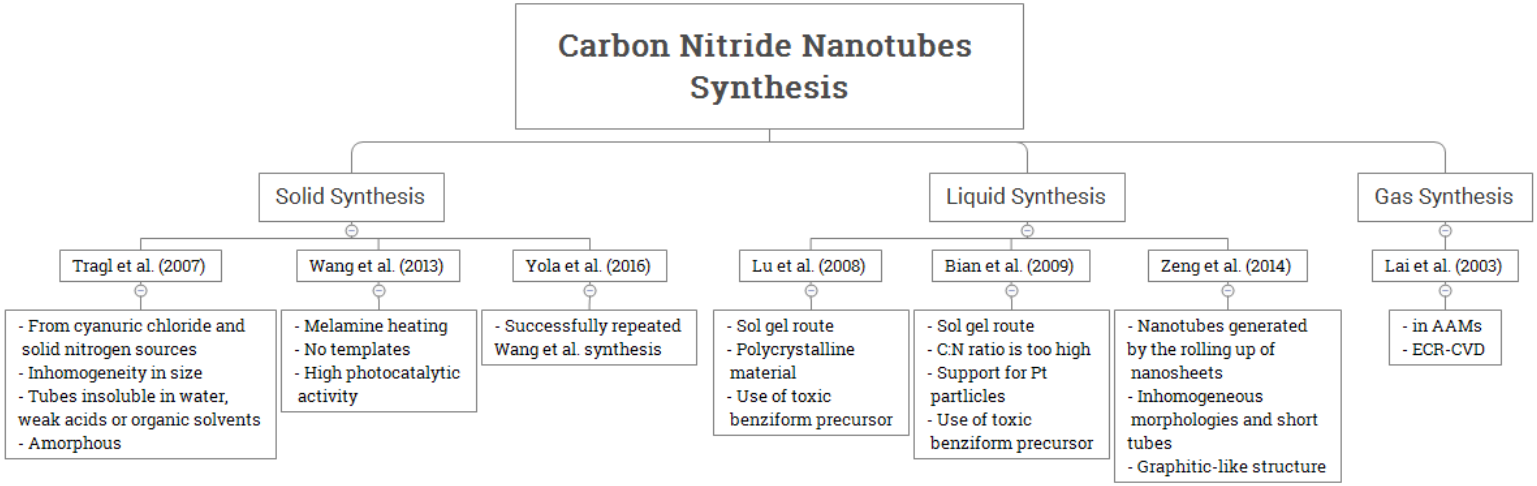

Figure 2-11: Key publications on template synthesis of C_3N_4[67, 80, 66, 78, 83, 79, 11].

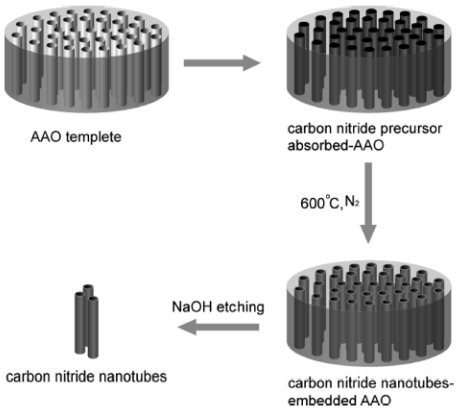

Figure 2-12: Schematics of the liquid synthesis of carbon nitride nanotubes in anodic alumina membranes [78].

The carbon-to-nitrogen ratio of the carbon nitride nanotubes was significantly higher than the theoretical value, making it more appropriate to call these tubes nitrogen doped carbon nanotubes. The choice of this synthesis, although efficient for Pt nanoparticles loading for use in catalysis [81], has the major drawback of using toxic benziform (CCl_4) as a precursor. Previously, carbon nitride nanotubes were uniformly deposited in the pores of AAMs by electron cyclotron resonance plasma CVD from a mixture of C_2H_2, but resulted in a disordered turbostratic (i.e. partly amorphous) structure and low nitrogen percentages (N $\sim$ 27%) [83].

2.4.2 Boron Nitride Nanotubes Structure and Synthesis

B and N molecules can assemble to form BNNTs in a hexagonal structure (Figure 2-13 A). This molecular architecture was calculated to be favourable thanks to the buckling effect of the boron-nitrogen bond that stabilizes the BN tubular structure. In the minimum energy construction, all the boron atoms are arranged in one cylinder, and all the nitrogen atoms in a minutely larger concentric one, the distance between the two cylinders being independent of the helicity of the tube. The buckled tubular structure forms a dipolar shell because of charge transfers from boron to nitrogen [71].

Each wall so formed consists of a single-BN layer, where boron and nitrogen atoms alternate in an hexagonal pattern. The spatial orientation that single walled nanotubes present can be defined with the aid of the so-called circumferential vector C, which circles the nanotube breadth on a plane perpendicular to its axis:

$$\boldsymbol{C} = n\boldsymbol{a_1} + m\boldsymbol{a_2} \tag{2.16}$$

The chirality C of a BNNT is defined with the help of crystal unit vectors (a_1, a_2) and structural indices (m_1, m_2).

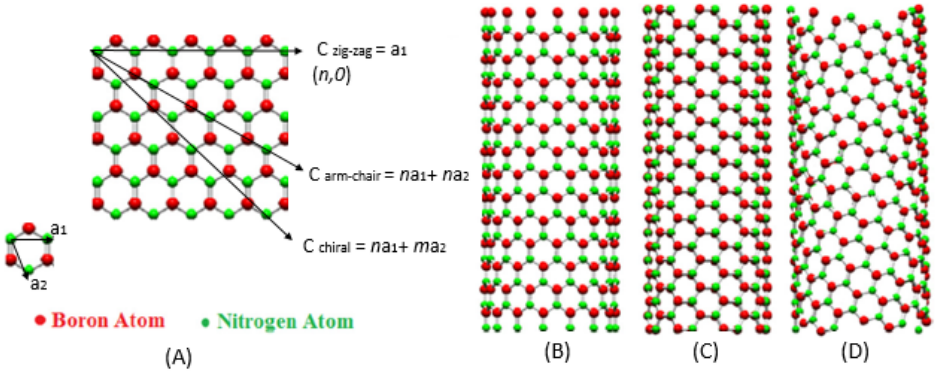

Figure 2-13: Circumferential vectors on a boron nitride nanosheet (BNNS) are displayed in (A) to define the spatial orientation of atoms in the nanotube zig-zag (B), arm chair (C) and chiral (D). This figure is adapted from Panchal et al. [85].

For the successful formation of BNNTs it is necessary that the hexagonal pattern displayed in Figure 2-13 A is maintained. It follows that it is possible to form only a few type of nanotube helicities, corresponding to integer combinations of the m_1 and m_2 indices. The feasible and most common BNNTs arrangements are presented in Figure 2-13 B (zig-zag), C (arm chair), D (chiral). Helicity, however, has not been found to be as crucial in determining properties such as mechanical integrity as it is for CNTs [86] . Additionally, while in CNTs all helicities are statistically equally probable, the majority of BNNTs observed so far displayed zig-zag or near zig-zag configurations with no strong dependence correlation on the synthesis method used [73]. Defects in BNNTs occur differently from CNTs, due to the B-B and N-N bonds being less energetically favourable and therefore more unlikely than B-N bonds. Consequently, squares or octagons can be found to replace the basic hexagonal structure, but pentagons and heptagons are very unlikely to occur [87, 88]. The hexagonal three-dimensional arrangement of the layers is not the only possible one, although it is the most frequent. Co-axial layers pile following two possible ways of stacking as displayed in Figure 2-14. This depends on whether the hexagons align on top of each other or if they are shifted [73].

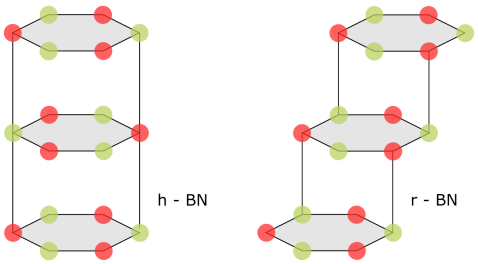

Figure 2-14: Schematic representation of two possible BN stacking in nanotubes: hexagonal (on the left hand side) and rhombohedral (on the right hand side). Boron and nitrogen atoms are depicted in red and green respectively.

The investigation into synthesis routes for BNNTs started in 1995 [89], and witnessed increasing activity in the past decade (Figure 2-15) with a focus on increasing purity and homogeneity of the products. In 2009, an appreciable production (200 mg per run) level was reached [90] but the purity and quality of the products, alongside the high cost of the technique, still remain crucial issues [91]. Methods tended to be categorised into high temperature and low temperature synthesis.

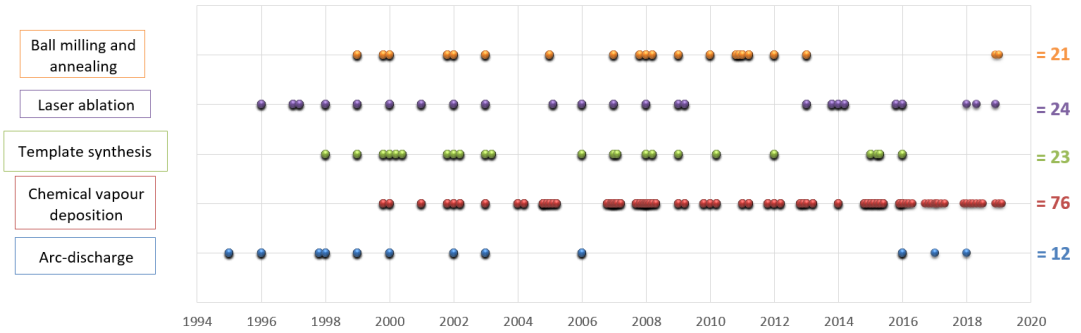

Figure 2-15: Number of publications found (right hand side) on the synthesis of BNNTs per method (listed on the left and associated to a colour) over the years.

Arc-discharge and laser ablation which are operated at temperatures higher than 2000 °C fit in the high temperature synthesis category. Ball milling and annealing, template-assisted synthesis, CVD and chemical synthesis paths often belong to the medium/low temperature synthesis methods and their choice assure temperatures below 2000 °C [72]. The lowest synthesis temperature for BNNTs recorded in literature so far (600 °C) was achieved by plasma-enhanced pulsed laser deposition [92]. Template synthesis and CVD mostly report temperatures betweeen 1000 °C and 1300 °C [93, 94]. This section aims at analysing in more depth prominent methodologies for BNNTs synthesis distinguishing them between a powder, bulk form and an arranged, templated form.

Bulk synthesis

CVD has been largely used for BNNTs production, and an extensive literature on this type of synthesis [95] has been reviewed for this work and is reported in Figure 2-15.

MW-BNNTs with lengths up to 5 μm were grown for the first time from nickel boride catalyst particles by CVD on a silicon layer at 1000 – 1100 °C using a borazine precursor. Despite the novelty of the goal achieved, the product still showed a wide range of tips formation and lacked homogeneity in the structure [96].

Other early investigations found lithium to be an effective catalyst for the growth of nanotubes on hexagonal and rombohedral boron nitride particles by thermal annealing at 1200 °C. The formation of BNNTs was not observed in absence of lithium vapor and therefore the metallic catalyst was considered key for the production of BNNTs. As a result of this synthesis, very short tubes between 50 and 250 nm in length protruded from the precursor particles [97].

Subsequently, MW-BNNTs started to be produced with several mg in yield with a catalysed route at medium temperature (1080 °C). This consisted of *in situ* generation of boron oxide (B_2O_2) gas from an iron oxide precursor following the reaction:

$$2Fe_2O_{3(s)} + 6B_{(s)} \longrightarrow 4Fe_{(g)} + 3B_2O_{2(g)}$$

The boron oxide intermediate reacted with the ammonia gas via *in situ* silica-assisted catalytic growth [98] yielding BNNTs [99], but with Si and Fe impurities and a large tube diameters distribution. After this successful synthesis, the use of different oxides as precursors was investigated, evaluating transition metals as good catalysts for the tubes growth [100, 101]. The choice of Ga_2O_3 led to BNNTs exhibiting a well-crystallized concentric structure with the excellent achievement of diameters below 30 nm, and no carbon contamination or defects. However, some of the produced BNNTs with larger diameters tended to show a number of defects [102].

Zhi et al. found FeO and MgO in a mixture with boron powder to be effective precursors for the large yield production of highly pure BNNTs (Figure 2-16) in a wide temperature range (1100 – 1700 °C) [103]. This is because FeO is a good catalyst for the reaction between boron oxide and ammonia and MgO is a good promotor for the formation of the boron oxide intermediate.

This method was further investigated by Lee et al., who proposed a vapor liquid solid

(VLS) type growth mechanism to explain why the trapping of vapours inside the test tube and the use of a partially covered combustion boat was enhancing the BNNTs growth [104]. This mechanism is the base of most CVD synthesis used today. Their reasoning followed theory on nucleation [105, 106], where the probability of nuclei formation P_N is given by the expressions in Eq.2.17.

$$P_N = Ae^{\frac{-F'}{k_B T}}, \tag{2.17}$$

where A is a constant and F' is the increase in free energy for the formation of a critical nucleus (Equation 2.18) so defined[107]:

$$F' = \frac{\sigma^2 \pi}{kTln\alpha_K}, \tag{2.18}$$

where α_K is the supersaturation ratio of adsorbed atoms and is defined as the ratio between p$*$ (vapour pressure) and p$^\circ$ (equilibrium vapour pressure of the condensed phase at temperature T). This means that at constant growth conditions and temperature and assuming a constant surface energy (σ) throughout the experiment, it is possible to enhance α and the nucleation probability of both the catalyst particles and BNNTs by trapping the reactive vapour pressure (p) to a critical level.

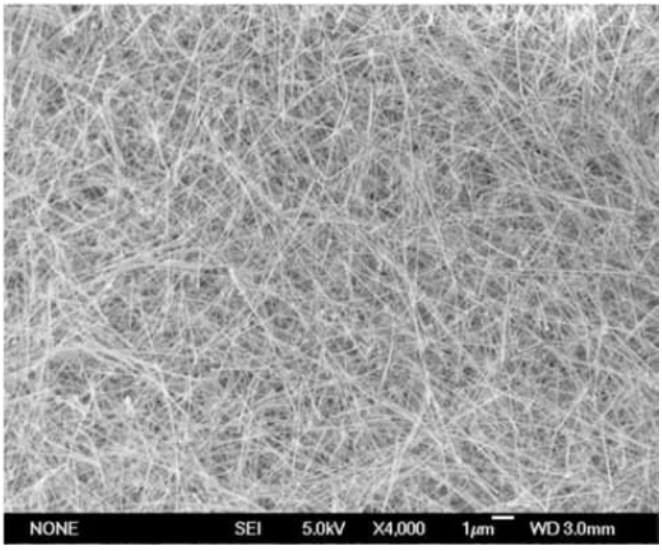

Figure 2-16: SEM image of as-grown BNNTs obtained at 1300°C by Zhi et al. [103] using iron and magnesium oxides precursors.

Therefore, the growth of BNNTs is favoured by vapour trapping. Several publications followed using close ended quartz tubes to contain the alumina boats so that the flow of the N-containing ammonia gas in the tube would not affect the growth mechanism

[104, 108–112]. A typical setup used to assist this growth path is displayed in Figure 2-17.

Additionally, substrates of several kinds were used to close the alumina boat to provide support for the BNNTs. It was found that choosing Si substrate would imply the loss of some of the catalysts properties. The substrates were therefore covered by an alumina buffer layers in which BNNTs were grown directly on Transmission Electron Microscope (TEM) grids covered with a patterned alumina layer [113]. Borazine was chosen as a precursor at low pressure as well, with a floating nickelocene catalyst that created high quality double-walled BNNTs in high volumes, although with varying morphology and showing catalytic contamination [114].

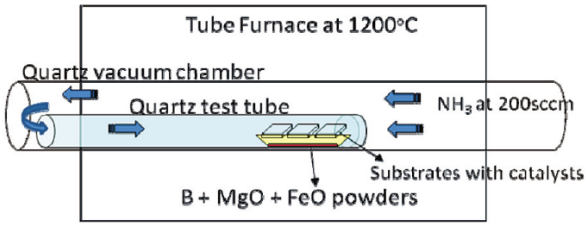

Figure 2-17: Figure adapted from Lee et al. [113] schematising a frequent choice of a set-up promoting boron nitride trapped vapour growth mechanism.

Lithium oxide was used for the growth of sub 10 nm pure boron nitride nanotubes in a vertical furnace, where the reactions of boron oxide formation and boron reaction with ammonia were ingeniously separated [110]. This catalyst was further investigated to observe that sufficiently high concentrations of lithium in the precursors led to the unzipping of boron nitride nanotubes and the formation of nanoribbons [115].

The influence that precursors concentration and temperature have on the products was studied in a comprehensive analysis of the method, finding that at a low content of metal oxide in ratios B:MgO:FeO = 1:1:1 lead to curly BN bundles, while when the oxide particles were in substantial excess, tubes with very large diameters were formed. Molar ratios of B:MgO:FeO = 2:1:1 repeatedly led to desirable products. When the temperature was increased from 1200 °C to 1400 °C, an increase in and a broader distribution of diameters could be observed [116].

Most recently, BNNTs forests were grown by CVD on a tugsten substrate moving away from the trapped vapour method catalysed by metal catalysts. Copper was used instead [117], thus reducing the number of catalysts used from the classical two (MgO and Fe_2O_3) to one and easing up the purification process.

The catalyst ball milling time prior to CVD was found to be a key variable to consider to ensure better structural homogeneity of the products. The need for precursor homogeneity is in line with findings stressing the imperfections brought by a too high or too low catalyst loading [116]. A narrow distribution of diameters (30 - 50 nm) was obtained by choosing a ball milling time of 6 hours and annealing the precursors mixture for 12 hours in an ammonia and nitrogen atmosphere [118]. The method goes beyond the good CVD control on tube diameters allowing for far more precise morphology control [119]. However, this often happens at the expense of yields, with only few mg attainable per run [120].

Arc discharge was one of the first methods explored [89], but continues to attract interest [121, 122], and over the years led to the synthesis of both multi- and single-walled nanotubes. The method was employed to produce macroscopic amounts of pure BNNTs, which however self-assembled into bundles or ropes [123]. In 2006 BNNTs were synthesized by arc jet plasma at high temperatures (5000-20000 K) with a good control on the nanotubes diameters. A mixture of h-BN and catalyst metal powders was used as the precursor, and a combination of argon and N_2 formed the plasma gas [124]. Due to its low yields, the metal impurities coming from the electrodes and the very high temperatures required, arc discharge soon left the stage to simpler methods.

Laser ablation is another widely chosen option [125–136]. This route was pioneered in 1996 and consisted in the second method of production of BNNTs reported [137]. For this technique, the use of catalyst is not imperative as BNNTs growth is recorded also in its absence [138, 139]. Initially, laser ablation was not very selective in terms of structure and formations different form nanotubes could be found as products [140]. Single walled BNNTs were first produced with a laser technique. However, the product still contained unwanted morphologies besides tubular structures [141]. Outstanding results were obtained with laser ablation in 2009, leading to over-mm large-yield productions of BNNTs fibrils [90]. This process happened mostly at high temperatures [142]. However, the synthesis of micro-scale boron nitride nanotubes at low substrate temperature (300 °C) could be used by employing a catalyst to reach the sought BNNT structure [136]. Most recently [143], a thermal plasma process with a 20 g/h output was developed, thanks to a link made between high yield growth and presence of hydrogen.

Templated synthesis

Template synthesis refers both to the production of BNNTs starting from a CNT and in the pores of AAMs. SiC [144], colemantite [145] and earth metals [111] were also

used for the template synthesis of BNNTs. To give an example, a SiC nanowire was used as a template and ammonia borane as the source for boron and nitrogen using the vapours produced by the decomposition of the former to form pure BNNTs [144]. However, template synthesis of BNNTs largely focuses on CNTs as starting material.

Carbothermal template synthesis was based on the idea of turning CNTs to BNNTs through the substitution of C atoms with B and N atoms. BNNTs were first produced from CNTs in 1998 through such substitution reaction at 1500°C in which the carbon nanotubes reacted with boron oxide and nitrogen with carbon monoxide as a side-product [146].

$$B_2O_3 + 3C(\text{nanotubes}) + N_2 \longrightarrow 2BN(\text{nanotubes}) + 3CO$$

The diameters and lengths obtained with this approach are very similar to the ones of the starting CNTs, even for single wall tubes in subsequent studies [147]. Predictably, the major drawback of the approach is the presence of unreacted carbon atoms residue in the tube when high BNNTs' purity is sought. However, it was demonstrated that C content in the product can be reduced by adding an oxidizing agent, for example MoO_3' to the system [148]. Additionally, unwanted morphologies could be found in the products depending on the degree of defects of the carbon nanotube templates.

This template synthesis approach was finely tuned until the reach of successful millimetre-scale production in 2015 [94]. After the substitution reaction at 900 °C, boron nitride single layers were chemically deposited on vertically aligned CNTs forests (Figure 2-18).

The carbon nanotubes were burnt away during annealing under air and vertically aligned BNNTs remained. The as-prepared materials presented good thermal properties with BNNTs stable up to 975 °C under air and high purities with about 1% C left in the final product. The tuning of the diameters in carbothermal template synthesis could be done very precisely by referring to the broad literature data available on VA-CNTs CVD [149, 150]. Key publications in the history of the template synthesis of BNNTs on CNTs are schematised in Figure 2-19 with a highlight on precursors, synthesis temperature, novelty and pushes for further research of the works presented.

BNNTs were firstly deposited in the pores of AAMs by pyrolysis at relatively low temperature (750 °C) [151]. Tubes produced were shorter than what achieved by the carbon synthesis. On the other hand, this method allowed for the synthesis of very well arranged tubes and for the precise control on the number of layers and their chemical composition and thickness.

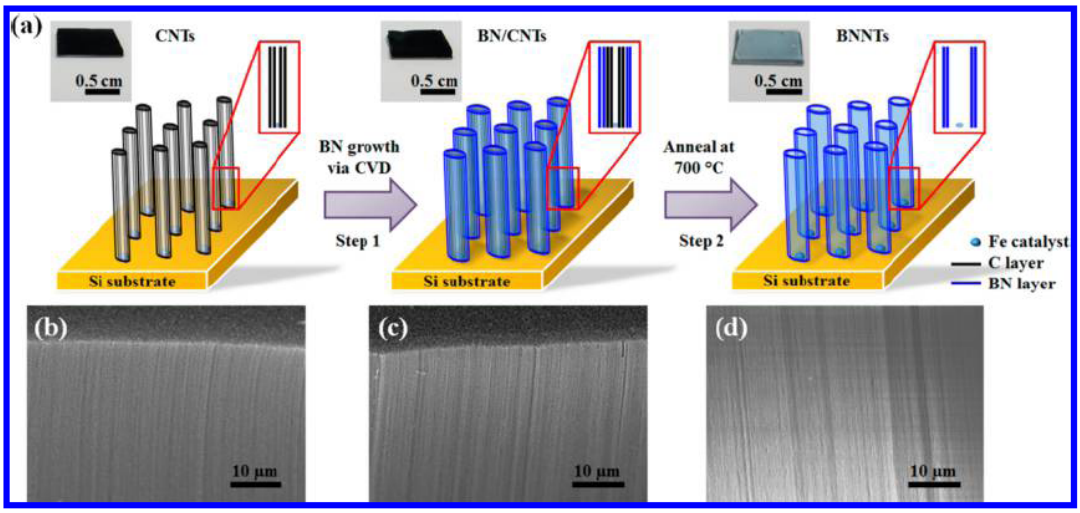

Figure 2-18: (a) Schematic illustration of the fabrication process of VA-BN/CNT and BNNT forests using CNT templates. The insets show the photographs of the respective as-grown VA-NTs on Si. BN layers are coated onto the CNTs by CVD in Step 1, and the CNT templates are removed by annealing in air in step 2. SEM images of (b) CNTs, (c) BN/CNTs, and (d) BNNTs displaying their vertically aligned structures. Figure adapted from Tay et al. [94].

Template synthesis combined with polymer thermolysis was performed starting from a similiar precursor [152]. Firstly, liquid polymeric borazine was synthetized. This was then infiltrated into an alumina membrane and a thermolysis of the polymer deposited in the 200 nm ordered nanochannels took place. Finally, template etching was performed to release as-formed boron nitride tubes. The highest temperature used during the synthesis was 1200°C but high temperature treatments were then performed to improve the crystallinity of the samples produced. Highly-ordered AAM based nanotube arrays have been synthesized subsequently by an hybrid microwave plasma-enhanced chemical vapour deposition below 520 °C. The product of this synthesis resulted amorphous in nature [153]. Atomic layer deposition has also been used for the deposition of boron nitride on the top surface of anodic alumina membranes, although not leading to the production of nanotubes [154].

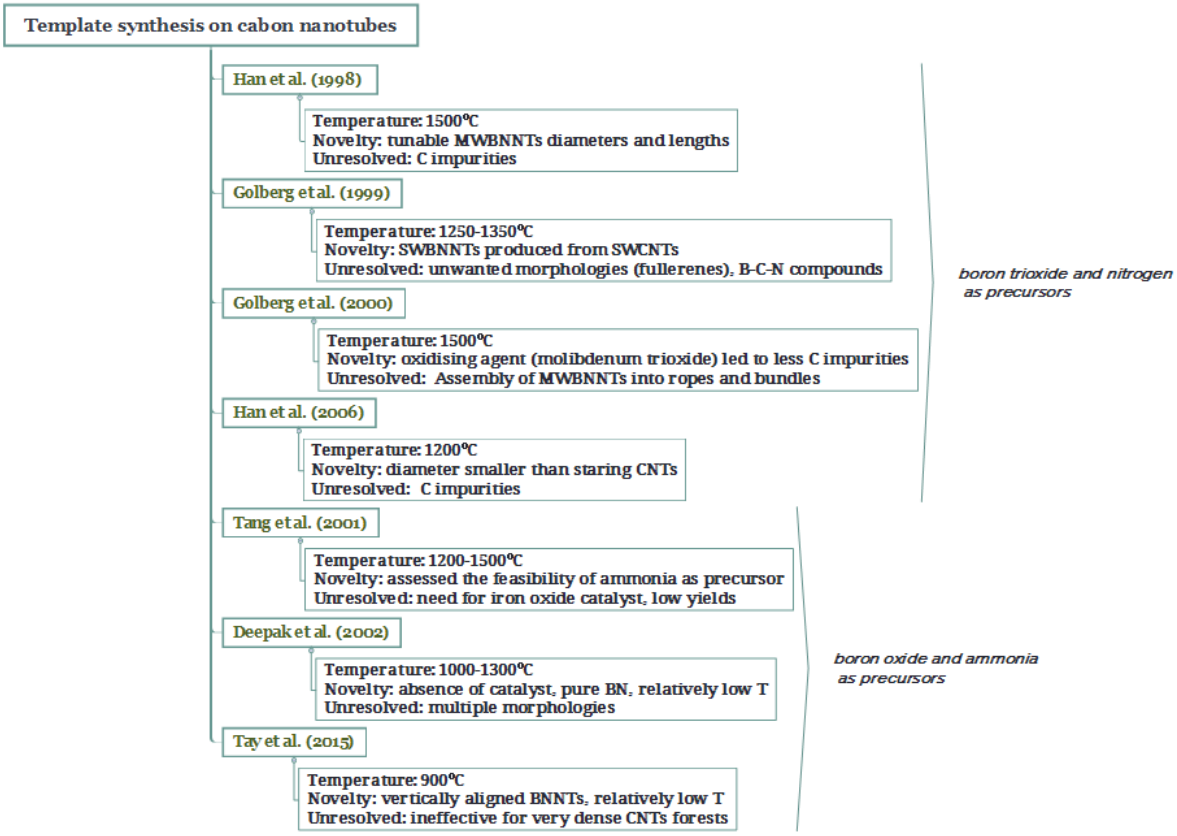

Figure 2-19: Key publications of template synthesis of BNNTs on CNTs templates [146–148, 155, 156, 93, 94].

Tubes in various conformations were produced by Wang et al. by using a porous alumina anodic membrane as a template, removed after the successful pyrolysis of liquid borazine [157]. Also in this case the specifications of the template could determine the properties of the obtained tubes, and the number of layers obtained depended on the number of deposition cycles. However, the handling of liquid borazine is a challanging synthesis step due to its high flammability and violent reactivity with moisture. More recent reports describe the CVD of h-BN films on Cu and Pt substrates [158, 159] starting from powder borazane, initiating a trend for application of this simple route to other substrates [160–162], although not yet on AAMs. In these processes, borazane (H_3NBH_3) is thermally decomposed to hydrogen, borazine, and polymeric amminoborane at 60-180 °C. Successively, borazine degrades at ∼1100 °C into h-BN and H_2, forming the sought BNNTs.

A summary of the key publications on the synthesis of AAMs is given in Figure 2-20 with a highlight on precursors, synthesis temperature, novelty and pushes for further research.

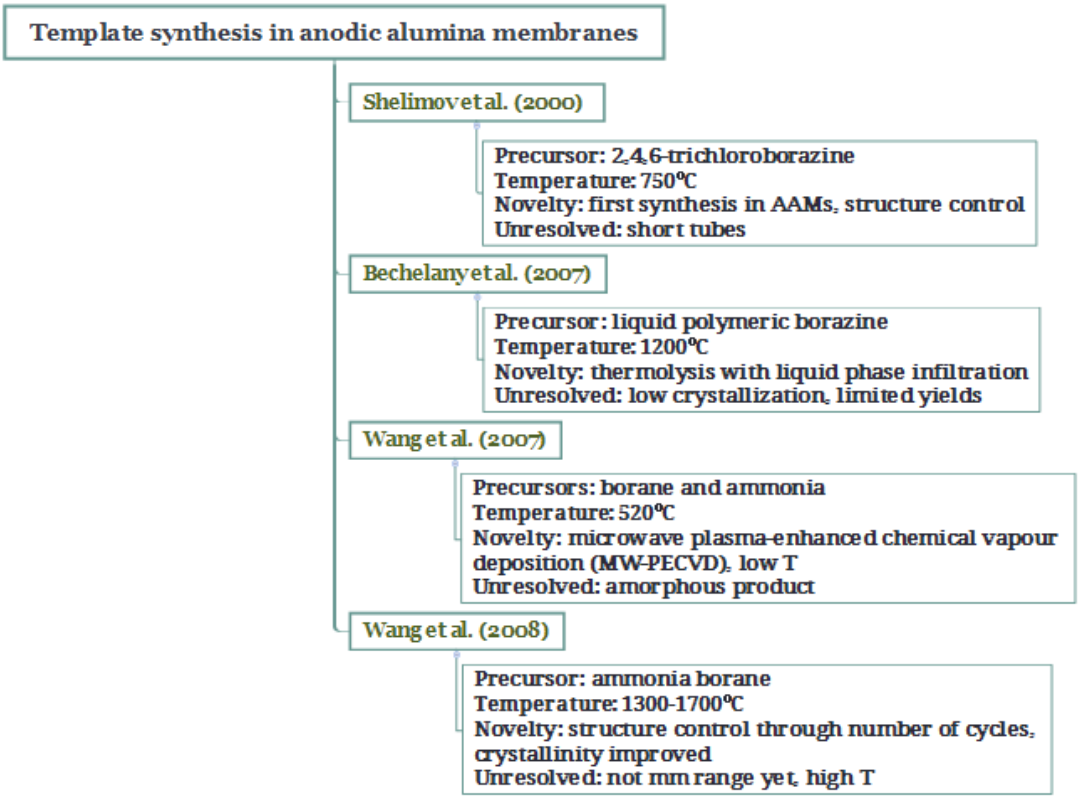

Figure 2-20: Key publications templated synthesis of BNNTs in AAMs templates [151–153, 157].

2.4.3 Polymeric Nanotubes Structure and Synthesis

If the classic Hagen Poiseuille (Eq. 2.3) is adapted for the more practical case where cylindrical membrane pores are not perfectly aligned we obtain:

$$Q_{HP} = \frac{\pi R^4}{8\mu\tau}\frac{\Delta P}{L}, \tag{2.19}$$

where the tortuosity τ is the ratio between the effective length of the pore and the shorter distance between its beginning and end. Given that higher tortuosities result in lower fluxes, membrane science attempts at bringing this value as close as possible to 1, by making sure this is done at affordable prices. The cheapest membrane materials in use today are polymers, and this explains a particular effort into looking at minimising τ in polymeric matrices. This has been done by copolymer self-assembly into isoporous membranes [163], also adopting an upscalable coating process. Block copolymerisation allows for a fine control on pore size and, indeed, tortuosity [164] even though not yet approaching perfectly cylindrical tubes fully across the membrane [165].

The precise experimental extrapolation of τ is complicated in polymeric membranes and this explains the gap in literature on the fundamental investigation of the eventual presence of enhanced water flow in polymeric nano-channels. With the advent of technologies that aim at the formation of highly porous, thin membranes with τ=1, it is interesting to obtain a basic understanding of the effect of material structure and chemistry on the water passage in said nanochannels. As expressed in Section 2.2.4, AAM-based nanotube membranes are ideal for this assignment. The synthesis of polymeric nanotubes made of a wide span of materials in the pores of the aforementioned membranes has been investigated, offering a promising, versatile approach for the next generation of nanotubes and potential incorporation of nanoparticles in the tube walls [166].

The geometrical properties of polymer nanotubes are determined by the template used, and their chemistry from the synthesis process and starting dope solution. Based on the monomers of choice and process conditions the polymerisation will lead to different polymers with varied degree of crystallinity, stiffness and application potential.

2.4.4 Templated Synthesis Routes

Polymers have been deposited in the pores of AAMs by the wetting method, where a polymer solution in an appropriate solvent wets the support and then penetrates the pores with the aim to create tubular structures by heating and annealing [167]. Polymethylmethacrylate (PMMA), polyvinylidene fluoride (PVDF), polystyrene (PS) and polyesters have been the polymers most investigated for the production of nanotubes by forming a layer on the pore wall of several nanometers [168]. When the polymer melt filled the nanopore completely, the polymer nanostructures formed are called nanorods. For all polymers used, the key issues related to this method regard the ability to obtain open tubes and clean membrane surfaces, as well as succeeding in depositing the polymer melt along the entire AAM length [166].

Polyvinylidene fluoride (PVDF) crystallysation in the nanotube walls was extensively investigated, due to its vast application in UF. In this work, annealing temperatures were accurately chosen to be $\sim$ 40 degrees above glass transition temperature, to allow for crystallisation. It was proven that the crystal growth in this semi-crystalline polymer could be directed along the nanotube axis, constituting a great advantage for nanotube design from polymer melts [168]. PVDF nanotubes were successfully produced, and phase transition was identified as the key parameter to control the tubes morphology (Figure 2-21) [168].

Zhang et al. studied the synthesis optimisation for nanotubes made of polystyrene (PS) looked into the limiting steps in their synthesis from polymer solutions [169]. Key factors were identified and independently examined: choice of solvent, polymer concentration, polymer molecular weight, support wetting, drying and crystallisation temperature. It was found that very low starting polymer concentration lead to unstable cylindrical structures, and only above predefined high concentrations could polymeric nanotubes be synthesized. Low molecular weight polymers resulted in the formation of nanorods rather than nanotubes [170]. Additionally, the complete wetting of the template can be facilitated by adjusting annealing temperature. This temperature is dependant on the polymer's glass transition temperature and thus its molecular weight. Nanotubes were obtained for annealing temperatures $\sim$ 100 °C above glass transition, in order to have sufficiently high polymer spreading on the template, related to a spreading coefficient SC which increases for the polymer with increasing temperature [171]. In addition to this, also the annealing time was found to have an impact on the hollowness of the nanotubes, as this needed to be optimised to 2 hours to avoid that the nanopores were fully filled by polymer melts [169].

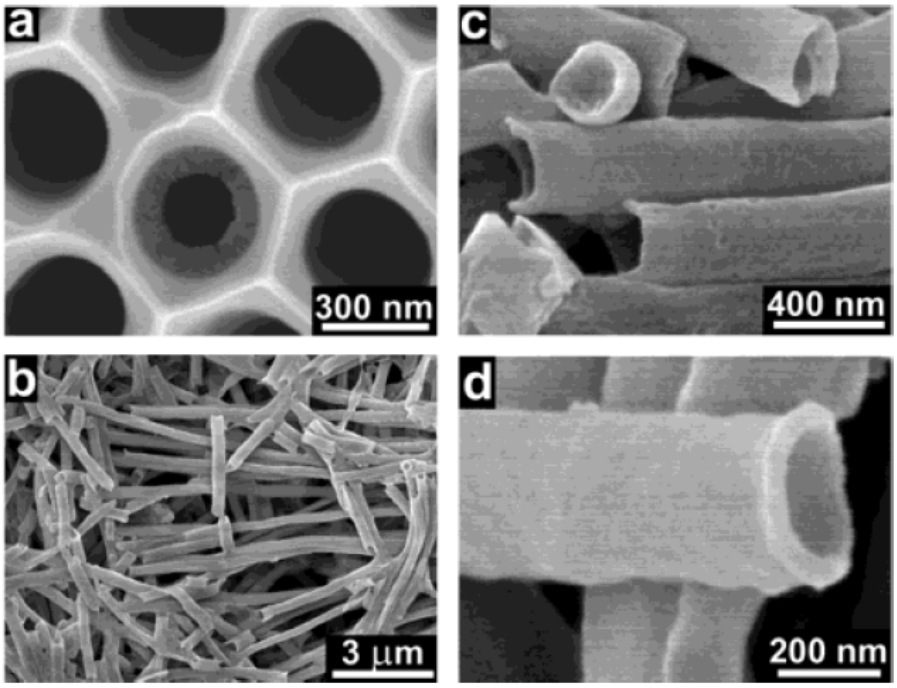

Figure 2-21: Scanning electron micrographs of PVDF nanotube sample showing (a) a pore opening partially covered by a nanotube wall, (b) nanotubes after the selective removal of the template and (c, d) detailed views of the openings of the nanotubes. This image is adapted from Steinhart et al. [168].

2.5 Nanotube Membrane Scale Up

However impressive the achievements of AAMs, only ease of production and processing can grant these nanotube membranes a place in the water treatment market. AAMs are brittle, expensive, non scalable and have low porosities, resulting in proportionally low permeance per unit membrane area.

To overcome these issues, nanotubes have been blended in the selective layer of thin film composite membranes as previously mentioned in Section 2.1. The success of this scaling up route strongly depends on nanotube stability in the solvents used, as agglomeration can heavily penalise the produced membranes in terms of permeance and rejection [172, 173]. Additionally, the lack of available routes to align nanotubes in a membrane matrix means that only the fraction of tubes randomly oriented in the direction of flow can contribute to flow enhancement.

Notwithstanding these limitations, interfacially polymerised CNTs membranes for nanofiltration have been successfully prepared [174, 175]. Additionally, performances could be improved when the nanofiller were cross-linked to the polymer matrix, so that no flow preferential pathways were created at the polymer/nanotube interface, thereby improving membrane rejection [176].

Despite recent achievements in terms of nanofiller dispersion and improved separation capabilities, actual scaling up of the technology involves more than just the ability of producing a polymeric-based membrane, but also, as an example, the proof of its good anti-fouling properties [177]. Compact module design and the ability to produce large sheets of membranes in continuous with consistent properties are also crucial features for commercialisation. Whilst this has been achieved for interfacially polymerised membranes industrially, the addition of a nanofiller complicates the process by adding many variables hard to control [3]. Recently, start-ups like NanoH_2O have incorporated nanomaterials in TFNs, achieving 8–12% lower energy consumption and 2-3 fold improvements in rejections [178].

2.6 Interfacially Polymerized Membranes with Nanofillers

Interfacial polymerisation (IP) is one of the key methodologies used for the production of NF and RO membranes. The technique was first developed in 1959 [179], and has since grown to be the vastly preferred method for the production of desalination membranes [180], which to date cover approximately 60% of the total desalination market [181].

The preparation process consists in the polymerisation of a very thin (normally $<5\mu$m) selective layer on top of an ultrafiltration structural support [182]. The synthesis occurs at the interface between two immiscible liquid phases. Normally, the support gets wetted by an aqueous phase, where a first monomer is dispersed. Then, a second monomer is dispersed in an organic phase which is poured on top of the wetted substrate. The resulting layer properties depend on a very long list of variables, from reaction times, monomer types, to substrate properties, monomers concentration, dispersant, curing and additives [183].

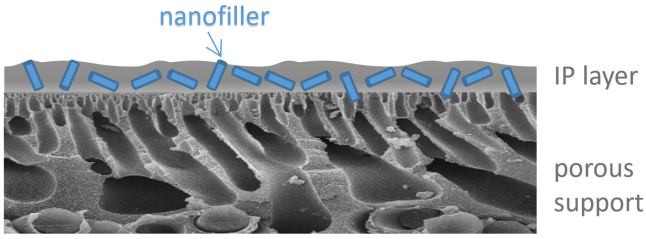

Figure 2-22: Conceptual illustration of interfacially polymerized membranes to form a TFN. The image is not drawn to scale.

Starting monomers for the TFN top layer space from amide, ester, urethane, urea, alkene, aniline, pyrrole and their derivatives, resulting in films applicable to many polymerisation mechanisms, from emulsion polymerisation to films for the membrane market, and shapes, from hollow to spherical and flat [184–188, 177, 189–192]. This versatility came to fruition in the membrane market providing high fluxes and wide pH tolerance [193].

The mechanism of formation of thin films allows for the embedment of nanostructures in the texture: when two immiscible phases get in contact, a gradient in chemical potential pushes the monomers dispersed into them to migrate at the interface where they polymerise and stabilise [187, 194]. This methods renders facile the addition of nanomaterials in the film matrix, simply by dispersing them in the aqueous phase

[195]. The choice of nanomaterials as additives to form TFN (concept schematised in Figure 2-22) addresses issues related to the membrane permeance-rejection compromise [196–201], as well as tailoring intrinsic chemical and physical features to improve, for example, antifouling potential [202, 203, 188, 204–206].

The extraordinary properties of nanotubes made of different materials can confer to the host membrane advanced capabilities, from enhanced rejection [207] to higher fluxes [208, 176]. One of the challenges of this strategy relates to one key step in the IP process, where a roller is commonly used to remove the excess aqueous solution from the impregnated membrane. However, in the case of added nanofiller, this procedure might result in its uneven distribution, uncertainty in assessing the exact amount added and partial loss [209]. Lastly, as already mentioned in Section 2.1, this membrane design pays for its cheaper synthesis route in terms of difficulty in controlling nanotube alignment and agglomeration.

Piperazine (PIP) and polyethylenimine (PEI) are amongst the most used monomers and better performing in the aqueous phase for the production of IP membranes, in concentrations spacing from 1 to 10 g/L [193]. Diethylenetriamine (DETA) [210], triethylenetetramine (TETA) [210], tetraethylenepentamine (TEPA) [210], bisphenol A [211], tannic acid [212] and m-phenylene diamine (MPD) [213] have also been investigated and compared to the previous options. It was found that monomer choice deeply affects morphology and network structure, and ultimately the membrane performance.

Trimesoyl chloride (TMC) is a common monomer of choice for the water-immiscible solution, mainly based on n-hexane. Cyanuric chloride (CC) was also found to be and advantageous choice, especially thanks to the absence of carbonyl groups which confer instability at extreme pH conditions [193].

Increase in flux of water was observed in polyhedral oligomeric silsesquioxane (POSS) [214], silicalite [215], metal organic frameworks (MOFs) [216, 217], Ag nanoparticles [218] and TiO_2 [219]. The introduction of nanofillers was shown to induce a clear increase in the film roughness and at times a spontaneous [218] and UV-induced [219] antibacterial effect, as well as improved permeation of organic solvents [217].

Amongst tubular nanofillers, carbon [176] and hallosyte [208] have been the most investigated materials. Their addition was motivated by the enhanced flow rates observed in nanotubes [4]. It was observed that when CNTs were functionalised with amino group, the polyamide selective layer would link at the tube wall and fully cover it. However, when the nanotubes were not functionalised or only presented -OH group, voids between the embedded tubes and the polymer would create, serving as preferen-

tial pathways for the water and salt molecules. Generally, this addition results in higher permeance because it creates a shorter pathway for water molecules, as schematized in Figure 2-23.

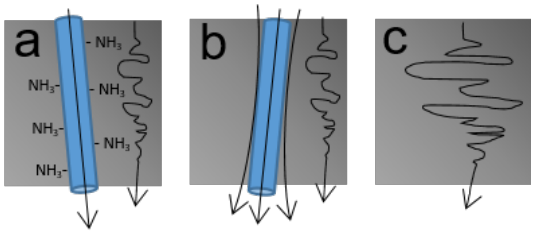

Figure 2-23: Conceptual illustration of possible flow pathways in IP selective layers: (a) functionalised nanotubes (b) non functionalised nanotubes and (c) selective layer only. The image is not drawn to scale.

The issue regarding the technical incompatibility of the widespread use of a roller in the production of nanofiller-based IP membranes was addressed by the use of vacuum filtration as an alternative (Figure 2-24)[209]. The support is in this procedure impregnated with a set amount of nanomaterial suspension under vacuum, followed by a PIP aqueous solution and then TMC in n-hexane. Contact times of each step were carefully controlled. This resulted into the uniform distribution of the graphene oxide nanosheets used in the study, significant improvement of water flux without compromising rejection and enhanced antifouling resistance for bovine serum albumine (BSA) [209].

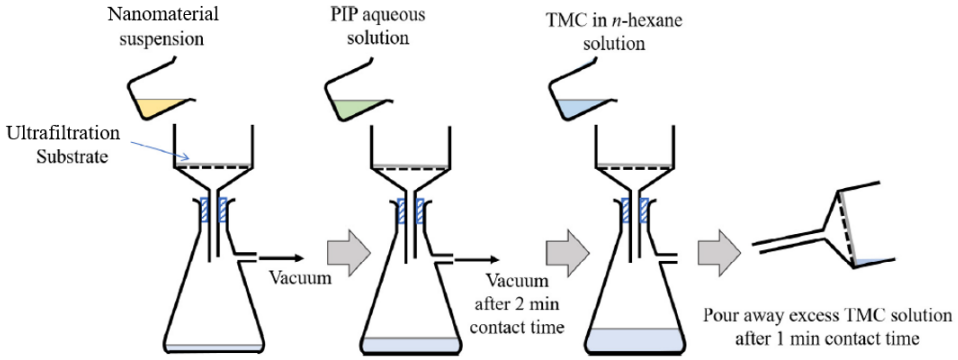

Figure 2-24: Conceptual illustration of interfacially polymerized membranes with nanofillers production. The image is adapted from the work of Lai et al. [209].

An analogous approach has been used repeatedly to exploit the ion gating and fast transport capability of biological protein channels, called aquaporins, by adding them in the IP aqueous phase in the form of nano-sized vescicles [220]. In order to avoid the

problematic use of a roller for the removal of excess aquaporin solution, compressed nitrogen gas is in these cases were used to remove eventual bubbles formed and assure an uniform distribution of the filler in the rejection layer [221]. Like in the case of nanotubes, the idea of embedding aquaporins in a membrane matrix came with great theoretical promises of two order of magnitude higher permeance than commercially available membranes with complete salt rejection [222]. However, like in the case of nanotubes, issues like proper immobilisation and defects hindered the widespread of the technology [223].

2.7 Environmental and Health Risks

As high aspect-ratio nanomaterials, nanotubes are classified as irritant for the respiratory track, cause of pulmonary inflammation and rapidly developing, persistent fibrosis [224]. As such, the materials have to be handled in ventilated areas provided with high efficiency particulate absorbing (HEPA) filters [225], limiting ease of operation, representing an occupational hazard and potentially a deterrent for application. Cytotoxicity (toxicity to living cells) was proved for BNNTs [226], CNTs [227] and CNNTs [228], and its degree depends in general on the type of nanotube (e.g. straight or curly, long or short) and the cell attacked.

Following from these health and safety considerations, a particular care should be taken to avoid dispersion of these materials in the environment, as this might be damaging to the fauna and be a source of pollution. Additionally, further research should look into the production of nanotubes in a less energy intensive way, in the prospect of large applications in a carbon neutral era.

Alongside insights into permeance and selectivity, it is fundamental that nanofiller leaching into water streams is investigated and understood prior to industrial application. Efforts are growing into defining standardised methods for nanomaterials risk assessments [229, 230]. A good approach to minimise risk was proved to be covalently bonding the nanotubes to polymer matrices through nanotube functionalisation [231]. Most importantly, it is vital to develop techniques for the assessment of leaching in thin film composites membranes and promote them as standard operations when analysing such systems [232].

2.8 Literature Review Summary

This section will offer some high level conclusions about the state of the art on nanotube synthesis, membranes, mechanisms of water transport and pollutants rejection, and identify gaps in the literature, which will serve as the theoretical framework for the research presented in this thesis.

It is well documented that precursor compaction plays an important role in the synthesis of CNNTs. This fact, in addition to an identified gap in literature, inspired our choice to attempt the templated synthesis of the material in the nanoconfined channels of AAMs. No synthesis routes showing facile formation of CNNTs in AAM with N% above 30% have been reported. Amongst the precursors investigated, melamine is the cheapest and least toxic, and synthesis reactions with this precursor were carried out at relatively low temperatures between 500 and 600 °C.

Attempts to synthesise BNNTs have been more numerous than for CNNTs, but the yields, purity and high costs have delayed its application [73]. The most successful synthesis in terms of yield was performed by laser ablation [90], but is not yet cost effective for large scale adoption. CVD is the most versatile, relatively cheap and investigated method for synthesis in bulk. However, it still suffers from product purity issues and low yields. Additionally, an ideal ratio of catalyst to precursors was identified, and it was found that deviating from this ratio would result in structural imperfections in the product [116]. This helped identifying pre-ball milling of the catalyst-precursors mix as a necessary step to assure local homogeneity of their ratio.

Research on AAM templated BNNTs accounts for a small fraction of the interest in BNNTs, but is of great importance for fundamental studies on permeance and rejection in this work. The most promising route was envisioned in the formation of an h-BN layer from borane-ammonia complex precursors, easily formed on Pt and Cu foils [158, 159]. This could be expanded to morphologically more complex substrates, like AAMs.

A great deal of the synthesis and optimisation of polymer nanotubes membranes regards polystyrene, with most parameters affecting successful synthesis scrutinised in the literature. The wetting method was identified as the most promised amongst the ones investigated so far [166], and will be utilised in this work for the synthesis of the first polymeric nanotubes membranes tested for water permeation.

The most desirable properties for the next generation of membranes, on general eco-

nomic and environmental principles as pointed out by some eminent reviews [3, 233], are:

(A) Durability, translatable into mechanical, chemical and thermal robustness, as well as resistance to fouling;

(B) Ease of production;

(C) Uniform molecular-size pores;

(D) High throughput, also translatable in high pore density and continuity;

(E) Ability to form defect-free films;

Many of the above features, namely (A), (C), and (D), have the potential to be achieved by densely packed, vertically aligned nanopores with uniform size, by identifying materials for targeted applications. Section 2.2 outlined this potential in terms of water transport, whilst Section 2.3 highlighted how specific nanotube properties can render them particularly favourable for targeted separations.

The ability to vertically align nanotubes in an inexpensive membrane has been one of the major shortfalls of the technology, and in parallel represents an obstacle for its fulfilment of condition (E) from the above, due to frequent nanomaterial agglomeration.

Even in the case of carbon nanotubes, where the nanomaterial production has become economically profitable on the large scale for specific applications, the membranes' ease of production does not yet fulfil the markets' demand.

In addition to this, the use of powder nanomaterial in industrial applications is sometimes discouraged, due to related difficulties in handling, health risks and environmental concerns due to nanomaterial leaching in the environment.

Large flow enhancements in carbon nanotubes have been reported numerous times, however this does not easily translate into a nanotube membrane's performance increase. A leap forward has been made by developing a theoretical model that links membranes' properties to their flow per unit area [18]. This model's effectiveness has been only experimentally shown for CNTs to date, but there is a gap in the literature on the experimental analysis of other materials, which could help the validation of a potent tool for nanotube membranes assessment.

Whilst carbon nanotube permeance can now be scrutinised in a relatively large number of publications, the literature on nanotube membranes rejection is extremely limited. MD and sometimes experimental work showed some interest in salt rejection for reverse

osmosis, unit operation where, however, the industry might not necessarily benefit from membranes with higher fluxes, given that the current technology already works close to the thermodynamic limit. Experimental work on non-carbon nanotubes membranes rejection at the nanoscale is very little to non-existent. The high surface charge that BNNTs can offer over a wide pH range, already deployed for the generation of osmotic current [44], could be used for targeted rejection of negatively charged nanopollutants in low concentrations [234]. A great attention is needed into understanding how nanotubes could reject particles for UF and NF, if we desire to exploit nanotubes' promise in terms of permeance for real case applications.

Moreover, BNNTs have been identified as the most promising alternative to carbon nanotubes in water application: they displayed tunable cation and anion selective properties [13], osmotic energy storage capabilities [44], improved membrane's thermal resistance and mechanical stability [235], and have recently seen a boost in mass production [90]. Additionally, when boron nitride nanosheets were recently embedded in mixed matrix membranes, they showed improved fouling resistance [236] and it is possible to hypothesize that the tubular counterparts might show a similar behaviour. However, to date, there has not been an experimental attempt at using them for the production of commercially deployable thin film composite membranes. Interfacially polymerised membranes based on nanomaterial have been successfully investigated in the literature, mainly starting from PEI and TMC precursors, and the same procedure could be employed for the production of BNNTs-based membranes.

Lastly, electrical field induced alignment has been achieved by teslaphoresis [237] by orienting carbon nanotubes along their axis. The extension of this alignment method to materials other than carbon could certainly be of interest for researchers that want to manipulate nanoscale, airbone objects.

Chapter 3

Aims and Objectives

Being able to improve current technologies for water purification will have positive scientific, social and economical implications. There is a strong need for low energy and less expensive filtration technologies in light of global warming and rapid population growth, as those exacerbate water scarcity issues. Industries spanning from agriculture to energy and environment are eager to step forward and benefit from superior water filtration methods.

For many years polymeric membranes have tried to meet the need for better water purification technology and have been used for desalination, dialysis, food processing and sterile filtration. Their advantage lies in low energy requirements, compact designs and simplicity of the process. However, they suffer from a selectivity-permeability trade off, as well as performance decay over time due to fouling, chlorine attack and membrane ageing. One direction that has been taken to tackle these issues is to have a very fine control over membrane geometry, structure and surface-pollutant interactions. Nano-engineered membranes have the potential to address these challenges that the water purification market poses today.

3.1 Aims

The present work investigates novel nanotube materials for application in membrane technology, with the aim of going beyond carbon, by studying nanotubes made of carbon nitride, boron nitride and polystyrene.

Core water transport properties of nanotubes made of different materials will be compared with their carbon homologous, exploring their link to the water-surface interplay. Furthermore, the steric- and charge-based selectivity mechanisms will be examined in nanotubes made of different materials, as fundamental investigations on rejection and permeance have the potential to demonstrate themselves a powerful tool for nanotube membrane evaluation. As the goals of this work intend to be application-oriented, the embedment of the studied nanomaterial in commercially exploited thin film composites membranes will also be researched.

3.2 Objectives

The goals of this investigation are simplified in Figure 3-1 and specifically consist of:

- Advancing the facile synthesis of aligned carbon nitride, boron nitride and polystyrene nanotubes in the pores of anodic alumina membranes;
- Fully characterising these hybrid membranes using advanced microscopy, spectroscopy and surface analysis;
- Testing pure water flow and rejection in a custom-made setup;
- Studying the effect of surface-liquid interaction on water transport in nanotubes made of carbon nitride, boron nitride and polystyrene and comparing them to carbon;
- Applying and validating a theoretical model from the literature that describes flow in nanotube membranes;
- Analysing charge and steric controlled rejection in nanotube membranes made of boron nitride and carbon;
- Focussing on nanotube membranes scaling up techniques, with the development of a novel boron nitride nanotubes-based interfacially polymerised membranes;
- Comparing the performance of these boron nitride nanotubes polyamide membranes to unloaded membranes as used in industry.

The attainment of these objectives will allow this thesis to meet its overall aim of studying permeance, rejection and scaling up potential of nanotube membranes based on materials other than carbon.

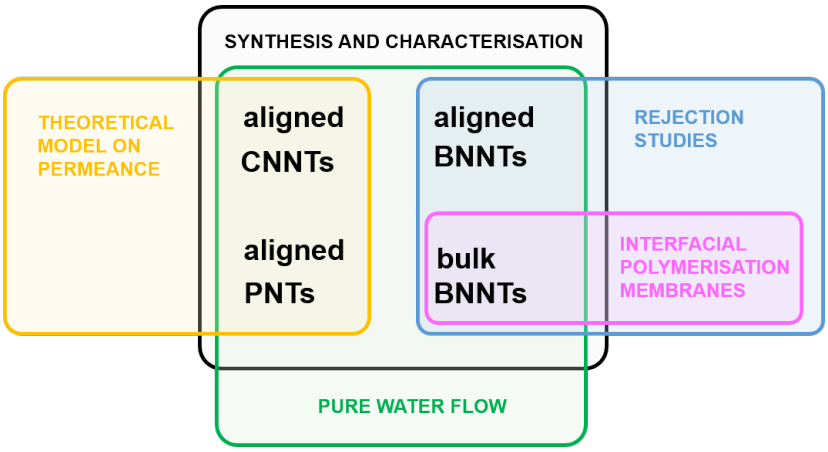

Figure 3-1: In this work, carbon nitride nanotubes (CNNTs), boron nitride nanotubes (BNNTs) and polymeric nanotubes (PNTs) are synthesised. Nanotubes can be produced in aligned and bulk form. Each of the material is used for different applications and tests.

Chapter 4

Materials and Methods

4.1 Synthesis

Material synthesis methodologies in this work can be defined as "templated" or "bulk". The former refer to the synthesis of nanotubes in the pores of symmetric AAMs. The latter refers to the production of nanotubes in powder form.

The characteristics of the membranes used as support are summarized in Table 4.1. Whatman™ Anodisc® were purchased from Sigma Aldrich while SmartPor were purchased by SmartMembranes GmbH. Synkera and InRedox Membranes were directly purchased by the companies of the same name. All membranes but InRedox membranes contained residual oxalic groups within the matrix, as their preparation process involved the use of oxalic acid.

Table 4.1: Characteristics of the 13 mm diameter membranes used in this work.

Membrane type	Porosity	Nominal Pore diameter	Thickness	Stable up to
SmartPor25-50	∼12%	25 nm	∼ 50 μm	1000 °C
SmartPor40-50	∼32%	40 nm	∼ 50 μm	1000 °C
Synkera18	∼12%	18 nm	∼ 50 μm	950 °C
Synkera35	∼20%	35 nm	∼ 50 μm	950 °C
Synkera50	∼25%	55 nm	∼ 50 μm	950 °C
InRedox10	∼10%	10 nm	50 μm	1150 °C
InRedox20	∼15%	20 nm	50 μm	1150 °C
Whatman™ Anodisc®	25-40%	200 nm	∼ 60μm	700 °C

4.1.1 Templated Carbon Nanotubes

CNTs membranes were prepared by CVD following an established method [18]. The AAMs were pre-annealed at 900 °C, which was reached with a ramp rate of 1 °C/min and then placed in the central zone of a horizontal TZF 12/38/850 type CARBOLITE tubular reactor where they were heated to 670 °C at 1 °C/min in argon atmosphere. Once the maximum temperature was reached, the feed was switched to 3:7 ethylene:argon (120 sccm total) and was maintained in these conditions for 4 hours. After synthesis, the membranes were left to cool naturally under a gentle argon flow.

When subjected to the curing procedure, the CNT membranes were treated at 800 °C for 2 hours under a 50 sccm flow of H_2 to increase their degree of graphitisation [238] and then left to cool in argon.

4.1.2 Templated Carbon Nitride Nanotubes

Commercial symmetric AAMs were purchased from Smartmembranes and Synkera and had diameters ranging from 18 nm to 100 nm. Prior to CNNTs synthesis (Figure 4-1), all AAMs underwent a 1 hour annealing process at 30 °C higher than the final synthesis temperature (520 °C) to increase their thermal resistance. The desired temperature was reached with a 1 °C/min ramp rate and the annealing was followed by natural cooling down.

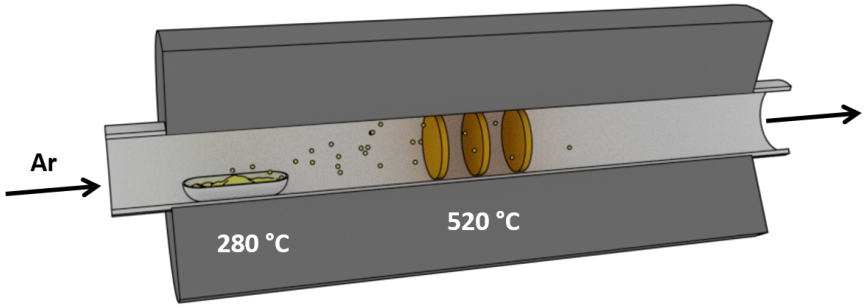

Figure 4-1: Schematics of the CNNTs membrane synthesis procedure in a model of a tubular furnace. The argon gas enters the furnace and carries along sublimated melamine ($C_3H_6N_6$), which degrades into solid carbon nitride (C_3N_4) and gaseous ammonia (NH_3). The schematics is not drawn to scale.

CNNTs were deposited using non-catalytic CVD in the pores of the AAMs using a melamine precursor $\geq$ 99% purity, purchased from Sigma Aldrich. The synthesis was carried out for 5 hours under a 200 sccm argon (Ar) flow in a quartz tube (ID 20 mm, OD 22 mm) heated up in the central section of a horizontal TZF 12/38/850 type CARBOLITE tubular furnace. Temperatures inside the furnace were monitored by external thermocouples. Gas flows were controlled with Omega FMAb5400A/5500A series mass flow controllers (MFCs) regulated by LabVIEW. Once the synthesis temperature of 520 °C with a ramp rate of 10 °C/min was reached, the melamine precursor was sublimated at 280 °C in the first section of the tubular furnace. At completion of the synthesis, the system was left to cool naturally under Ar flow, and the sublimation of melamine was stopped by switching off the heating in the first section of the furnace. After synthesis,

the CNNTs membranes were gently rinsed with deionised water. The dissolution of the alumina templates of the CNNTs membranes was performed by reflux of H_3PO_4 (85 wt% in water, purchased from Sigma Aldrich) at 80 °C.

4.1.3 Templated Boron Nitride Nanotubes

BN was deposited in the pores and on the surface of the AAMs by non-catalytic CVD, producing boron nitride nanotube membranes (BNNT-AAMs).

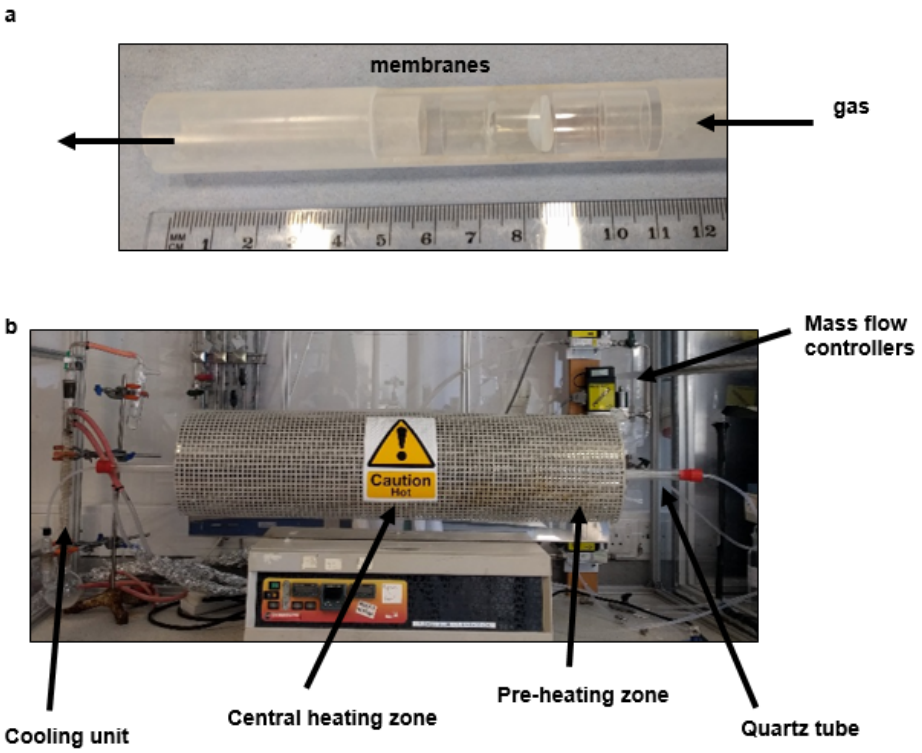

Figure 4-2: (a) Customised quartz membrane holder and (b) furnace setup where the gas is controlled by mass flow controllers, enters the quartz tube from the right hand side and is cooled at the outlet in a water cooled unit. The borazane precursor is preheated in a pre-heating zone where it degrades in polyiminoborane, $B_3H_6N_3$ and hydrogen.

Thermally treated symmetric AAMs templates with 13 mm diameter were purchased from InRedox, with pore diameters ranging from 10 nm to 30 nm. The membranes were assembled in a custom-made quartz membrane holder (Figure 4-2a) inside a quartz tube (ID 20 mm, OD 22 mm) to be inserted in the centre of a horizontal TZF 12/38/850

type CARBOLITE furnace (Figure 4-2b).

Gas flows to the furnace were controlled using Omega FMAb5400A/5500A mass flow controllers (MFCs) regulated by a LabVIEW program. Once the quartz tube was sealed, the temperature was ramped up at 10 °C/min under 150 sccm Ar flow to displace residual air left in the reactor. The precursor (borazane $\geq$ 97% purity, Sigma Aldrich) was sublimated at 80-100 °C in the reactor pre-heating zone. The synthesis was then carried out for 40 min under a 15:135 sccm H2:Ar flow with Reynolds number $\sim$ 1 at the synthesis temperature of 1000 °C. The gas carried along the products of the degradation of borazane, namely polyiminoborane, borazine and hydrogen [239]. Borazine degraded into BN and hydrogen at 1000 °C in the central section of the furnace, forming a BN layer onto the AAMs. After synthesis, the BNNTs membranes were left to cool down to room temperature and were gently rinsed with deionised (DI) water to remove any debris. As demonstrated in Figure 4-3, not all anodic alumina membranes are suitable for the synthesis of BNNTs. Since the synthesis happens in a reducing environment due to the presence of hydrogen gas, it is not advisable to choose alumina templates containing residual oxalic groups from the anodization process [23], as this might result in carbon impurities retained as carbonate or carboxyl groups after synthesis. This is why, in this work, only InRedox membranes (Table 4.1) that did not contain oxalic groups were used as substrates.

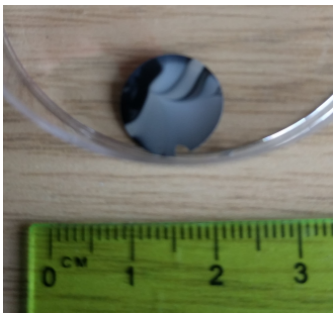

Figure 4-3: Anodic alumina result of a synthesis process on a membrane anodised with oxalic acid as electrolyte.

4.1.4 Templated Polymer Nanotubes

PS with molecular weight of 90 kDa and 200kDa (both analytical standard) were purchased from Sigma-Aldrich. Chloroform (99%) was purchased from VWR. Symmetric unsupported anodiscs with nominal pore diameter 200 nm, thickness 60 μm and diameter 13 mm were sourced from Sigma Aldrich. AAMs were soaked into 3-5 ml of

chloroform solution with PS (90 or 200kDa) for an hour at 40 °C in concentrations 1%, 3% and 7 wt%, and then dried in air on stainless steel support. The samples were then annealed at 220 °C for 2 or 12 hours in a tubular furnace with a protective argon flow of 600 mL/min (Figure 4-4). After synthesis, the membranes underwent plasma oxidation in a Henniker Plasma, HPT-10 for up to 10 minutes.

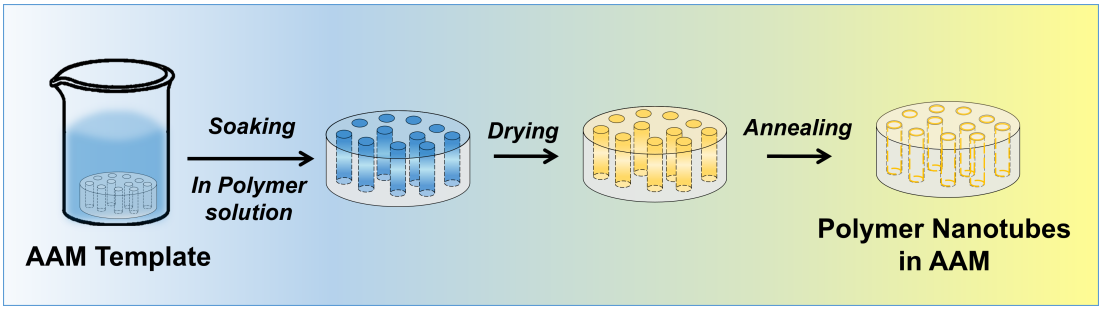

Figure 4-4: Schematic of the synthesis of PNT-AAMs via soaking method.

4.1.5 Bulk Boron Nitride Nanotubes

BNNTs synthesis with ammonia gas and boron powder precursors was catalysed by Fe_2O_3 and MgO catalysts with a molar ratio of B:MgO:Fe_2O_3=2:1:1. Boron (B, $\geq$ 95%), magnesium oxide (MgO, $\geq$ 99.99%), iron oxide (Fe2O3, $\geq$ 99.9%) and MgO nanopowder (average particle size $\leq$ 50 nm) were purchased from Sigma Aldrich. B, MgO and Fe_2O_3 were pre-mixed at 250 r.p.m. for 12 h in a Fritsch Pulverisette P6 planetary ball mill, half filling a 45 ml stainless steel grinding bowl with 2.2 g of B, MgO and Fe_2O_3 in an ethanol suspension and 18 grinding balls with 5 mm diameter. After ball milling, 5 ml of precursor was poured in a Coors^{TM} alumina combustion boat, which was then totally capped with a rightly sized silicon wafer substrate, P-type silicon wafers polished on one side were purchased by Agar Scientific and previously seeded with MgO nanopowder. The closed alumina boat was then placed in a 15 cm long quartz test tube (ID 18 mm, OD 19 mm) facing the gas inlet in the centre of a quartz tube reactor (H-Baumbach, ID 20 mm, OD 22 mm) in a three sections horizontal TZF 12/38/850 type CARBOLITE tubular furnace. Temperatures inside the furnaces were monitored by external thermocouples. Gas flows were controlled with Omega FMA 5400A/5500A series mass flow controllers (MFCs) regulated by a LabVIEW program. The tube reactor was abundantly flushed with Ar and then let ramp up at 10 °C/min up to 1100 °C under a 200 sccm Ar flow. Then, the gas flow was switched to 145 sccm NH_3 and the temperature increased to 1200 °C at the same rate. This maximum temperature was kept for 1 hour before letting the system cool down under

a 200 sccm Ar stream. The exhaust NH_3 gas was neutralized with a sulphuric acid scrubber, generating ammonium sulphate salts. The boron nitride nanotubes white powder was gently removed with a stainless steel spatula by scratching it from the silicon substrate and boat top and sides. The unreacted boron in the white collected powder was removed by heating in air at 700 °C for 2 hours, where it reacted to form boric anhydrite vapour, while BNNTs remained intact as they have high thermal stability and are resistant to oxidation up to 950 °C [94]. Catalysts were removed with a 3 hours 10% HCl (purity 36.5-38.0%, purchased from Sigma Aldrich) water cleaning at 40 °C, followed by washing of the products in DI water by vacuum filtration using a 0.45 μm Nylon membrane (Pall Corporation). The bulk BNNTs synthesis is simplified in a schematics in Figure 4-5.

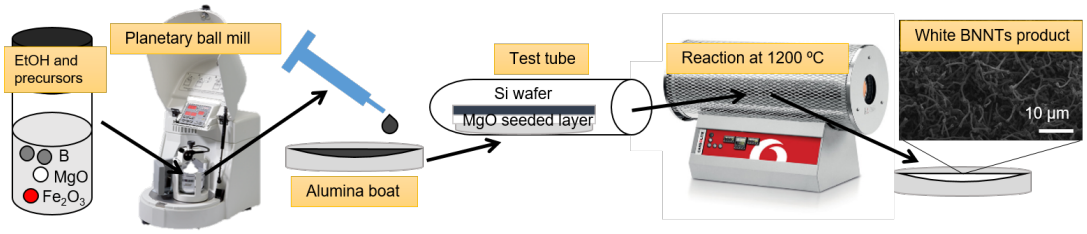

Figure 4-5: Schematics of the CVD synthesis of bulk boron nitride nanotubes production.

4.1.6 Interfacially Polymerised Membranes

The PA-BNNTs membranes were synthesized by interfacial polymerisation following an established vacuum filtration technique [193], which has been recently used for the fabrication of nanocomposite membranes [209]. Deionised (DI) water was used unless specified otherwise. Methanol (MeOH, anhydrous, 99.8%), Piperazine (PIP, 99%) ReagentPlus, with MW86, n-hexane (anhydrous, 95%) and trimesoyl chloride (TMC, 99%) were purchased from Sigma Aldrich. The PES support membrane (Microdyn Nadir PMUP010 with 10 kDa MWCO) was cut in discs with 5.5 cm in diameter, and then flushed by 20 ml of water in a filtration setup prior to synthesis. Then, 1 wt% PIP aqueous solution (MeOH:H2O 50:50 v/v%) solution was prepared by rapidly dissolving the PIP flakes. For PA-BNNT membranes, 0.01, 0.02 or 0.03 wt% BNNTs was dispersed in the amine solution by ultrasonication for 1 h (Table 4.2). Then, 25 ml amine solution or amine solution with dispersed BNNT was pumped through the support membrane until the entire amount of solution was filtered, but ensuring the membrane remained wet. Subsequently, any residual drop on the side of wetted membrane were

removed by using an air gun to avoid the formation of defects in the amine film. In the interfacial polymerisation, a 0.8 wt% TMC n-hexane solution statically contacted the amine-saturated support in the filtration setup. The reaction time was 3 min. The residual organic solution was discarded and the membrane was quenched with n-hexane for 1 min. After reaction, the membrane was left to dry at room temperature for 24 h. Similarly, a free-standing thin film was formed by contacting 1 ml PIP solution with 1 ml TMC solution, specifically for the analysis of a free standing film at the interface.

Membranes with different concentration of BNNTs in the starting solution were prepared, their nomenclature, PIP solution composition and the estimated weight of nanofiller deposited per unit area by filtering 25 ml of amine solution (calculated from the concentration of nanomaterial in the starting solution) can be found in Table 4.2. The concentrations to be investigated were chosen in a range where no obvious large agglomeration could be observed on the membrane top surface with the naked eye.

Membrane	PIP wt%	MeOH/H2O (wt%)	BNNTs (wt%)	$\mathbf{c_S}$ (mg/cm^2)
PA-BARE	1.00%	99.00%	0.00%	0.000
PA-BNNTs0.01	1.00%	98.99%	0.01%	0.096
PA-BNNTs0.01	1.00%	98.98%	0.02%	0.195
PA-BNNTs0.01	1.00%	98.97%	0.03%	0.283

Table 4.2: Composition of the PIP solutions in MeOH:H2O 50:50 v/v% for the PA-BNNTs membranes including surface coverage per unit area c_S.

It should be noted that there is a small degree of uncertainty in the estimation of the amount of BNNTs per unit area, due to the possibility that a minor fraction of nanomaterial could have filtered through the PES support.

4.2 Characterisation Methods

4.2.1 Field Emission Scanning Electron Microscope

The produced membranes were fractured in small pieces, coated with 5 nm of chromium and positioned on carbon tape for analysis with a JEOL JSM-6301F FESEM . High magnification (>90,000) images were taken with a Zeiss Sigma HD Field Emission Gun Analytical SEM (ASEM). The inner diameters of the tubes were calculated via statistical image analysis of FESEM micrographs using ImageJ by multiplying the obtained Feret's diameters by the circularity of the pores [18]. Bulk nanotubes were

scanned by dispersing them in EtOH and then depositing few drops of the suspension on mica.

4.2.2 Transmission Electron Microscope

JEOL JSM-2100Plus TEM samples were prepared following a similar procedure, finely grinding the membrane in an agate mortar prior to 1 hour and 20 minutes of dissolution in 1M NaOH. Each sample was then washed with vacuum filtration with a Nylon membrane (Pall Corporation) with 3 litres of water per AAM, suspended in 5 ml DI water and ultrasonicated in a VWR Ultrasonic Cleaner USC-T for 30 min. Two to five drops of the sample were then placed on a TEM window (Lacey carbon purchased from EM Resolutions) until a desirable concentration was reached. Analysis of structural features with ImageJ was done on a minimum of 10 measurements. Phillips CM200 TWIN TEM samples of BNNTs embedded in a free standing film were prepared by gently depositing a thin film on a TEM window and imaging it at 250 and 25k magnification.

4.2.3 Atomic Force Microscope

AFM data was acquired with a Nanosurf easyScan 2 Flex in dynamic mode, using a monolithic silicon AFM probe (Tap190Al-G, BudgetSensors, Bulgaria; spring constant: 48 N/m, resonant frequency: 190 kHz, a nominal tip radius: $\leq$10 nm), 1 s time/line and 250 points/line. Images were analysed with Gwyddion and always levelled to make the facets point upwards, aligned and corrected from horizontal scars and artefacts. Quantities such as the roughness average R_a were computed by the software.

4.2.4 Electron Energy Loss Spectroscopy

Before Electron Energy Loss Spectroscopy (EELS) analysis, the samples were finely grinded with mortar and pestle and then diluted in 5ml of DI water (18.2 MΩ). A JEM – ARM 200F was used, with 8C spot size 30 μm aperture, CL2 - 20 cm CL (JEOL ADF1) for imaging. The Gatan Spectrum Imaging Toolbox was used for data acquisition and processing. EELS settings were 6C; 40 μm CL2; 2.5 cm CL and 5 mm entrance aperture.

4.2.5 Electron Diffraction Spectroscopy

EDS scans on the Zeiss Sigma HD Field Emission Gun Analytical SEM were performed with 30 seconds livetime, 16 μs process time, all elements measured, normalised to 100% using 5kV and 60 μm aperture.

4.2.6 X-Ray Photoelectron Spectroscopy

X-Ray Photoelectron Spectroscopy (XPS) was performed on powdered samples using a Thermo Fisher Scientific K-alpha+ spectrometer. Samples were analysed using a micro-focused monochromatic Al x-ray source (72 W) over an area of approximately 400 microns. Data was recorded at pass energies of 150 eV for survey scans and 40 eV for high resolution scan with 1 eV and 0.1 eV step sizes respectively. Charge neutralisation of the sample was achieved using a combination of both low energy electrons and argon ions. Data analysis was performed in CasaXPS using a Shirley type background and Scofield cross sections, with an energy dependence of -0.6.

Sections of the polyamide membranes top surface measuring 1 cm $\times$ 1 cm were also analysed by XPS. The ratio O/N from the XPS analysis of the polyamide membranes was measured to assess the degree of crosslinking in relation to loading percentage.

This was calculated from:

$$crosslinking(\%) = \frac{(O/N)_{XPS} - (O/N)_{fullycrosslinked}}{(O/N)_{fullylinear} - (O/N)_{fullycrosslinked}}, \tag{4.1}$$

where $(O/N)_{XPS}$ is the oxigen to nitrogen ratio obtained experimentally, ignoring the 398 eV contribution of the h-BN nitrogen. $(O/N)_{fullylinear}$ and $(O/N)_{fullycrosslinked}$ are the ratios for a fully linear and fully crosslinked polyamide [240].

4.2.7 Raman Spectroscopy

Raman spectroscopy was performed on the as-produced CNNT membrane with UV light (wavelength 325 cm^{-1}) in a Renishaw InVia confocal Raman Microscope. On the BNNTs samples, Raman spectroscopy was carried out after pure water tests on a glass slide using a Renishaw Raman Microscope series 1000 with wavelength 244 cm^{-1} (5.08 eV), spectral resolution of 5 - 10 cm^{-1} and spatial resolution of about 5 μm.

4.2.8 Fourier Transform Infrared Spectroscopy

FTIR-ATR tests were carried out on the as-synthesized samples in a Perkin Elmer Frontier FTIR spectrometer setup with 16 scans per run between 600 and 4000 cm^{-1} and a spatial resolution of 2 cm^{-1}. The background was run in the absence of the sample.

4.2.9 X-Ray Diffraction

XRD tests of products of the synthesis were reduced into fine powders dispersed on a silicon wafer were carried on Bruker D8 Advance with Vantec detector with Cu kalpha radiation 2θ values of 10°–70°.

4.2.10 Contact Angle Measurement

Contact angle measurements were obtained from sessile water droplets on carbon nitride, carbon and boron nitride deposited on alumina discs via the same synthesis method described for the respective deposition inside the AAMs in Sections 4.1.1, 4.1.3 and 4.1.2. DI water was used as solvent for the sessile droplet method in air at 20 °C with 2.5 μl droplets. Images of the drop were obtained using a Dataphysics Optical Contact Angle (OCA) Measuring Device each minute for 10 minutes per measurement. The accuracy of the machine is ± 2°. The Young contact angle (θ_{Y}) on a flat smooth surface is related to the measured contact angle (θ_{W}) using the Wenzel model [241]:

$$cos\theta_{\mathrm{W}} = rcos\theta_{\mathrm{Y}}, \tag{4.2}$$

where r is the ratio between the coated alumina disc surface area and the projected area, obtained by AFM Nanosurf easyScan 2 Flex.

The Cassie-Baxter equation is used to compute the Young contact angle θ_Y of water on the PS nanotubes:

$$cos\theta_{\mathrm{CB}} = f(cos\theta_{\mathrm{Y}} + 1) - 1, \tag{4.3}$$

where θ_{CB} is the Cassie-Baxter measured contact angle and f the surface fraction of the solid on the selected area, corresponding to 1 - ϕ.

4.2.11 Differential Scanning Calorimetry

Differential Scanning Calorimetry (DSC) data were acquired on samples of 1.7 ± 0.1 mg with a DSC Q20 (TA INSTRUMENTS), ranging from -80 °C to 400 °C. Data analysis is performed by TA Universal Analysis 2000 software.

4.2.12 Porosimetry

N_{TM} porosimetry (Porolux^{TM} 1000) was employed to analyse pore size and distribution, giving an indication of the smaller pore diameter across the membrane thickness. Membranes were fully immersed in Porefil liquid (fluid tension 16 dyn/cm) for 5 minutes prior the test, and scanned in the pressure range 0 -20 bar, for 20 wet measurements.

4.2.13 Zeta Potential Measurement

Malvern Zetasizer NS (U.K.) was used to measure the membranes' surface and the particles' zeta potential. The tracer solution for surface zeta membrane potential measurements was prepared by adding a low concentration of 0.48 μm polystyrene microbeads (Polysciences, Inc.) in an aqueous solution of pH 6. Membranes were glued with superglue to a silicone sheet, left to dry overnight, and then cut into the size of the sample holder prior to measurement, to avoid breaking the membrane and accidentally covering the electrodes with glue. The membranes' zeta potential (ζ_m) was calculated by subtracting the measured zeta potential at zero displacement from the tracer potential [236]. The linear relationship between displacement and reported zeta potential was obtained from three repeats at four displacement locations and the zeta potential at zero displacement was obtained from this relationship. Hanna standard buffer solutions from Sigma Aldrich at pH 10.01 and 4.01 were used to adjust the tracer solutions pH. In the case of the colloidal suspensions, fixed concentrations of 0.08 g/L were ultrasonicated for 5 minutes prior to zeta potential tests.

Surface zeta potential of PA membranes with dimensions 2 cm x 1 cm or 1 cm x 1 cm was measured in a SurPASS electrokinetic analyser with adjustable gap cell in a pH range between 3 and 10. For each pH, the measurement was repeated four times.

4.2.14 UV-vis Measurement

An Agilent UV-vis Cary 100 setup was used to relate the concentration of nanoparticles in the water suspension to absorbance in the spectral region between 190 and 900 nm. Hellma quartz glass 1400 μl cuvettes with 10 mm optical path length were used for the UV-vis testing of all the standards and samples.

4.3 Templated Nanotube Membranes Flow Tests

Pure water permeation tests took place in a horizontal dead-end filtration setup (as shown in the schematic in Figure 4-6 with 13 mm diameter stainless steel membrane holders with a 4 mm, 5 mm or 10 mm inner diameter effective area. The membrane holder was connected to a fluid flow measurement apparatus acquiring data via a Labview program. Pressure transducers P1 and P2 in Figure 4-6 (Swagelok industrial standard, 5kPa error) recorded the transmembrane pressure. A thermocouple (Omega, Type T) recorded the temperature. Ultrapure water (Veolia, 18.2 MΩ at 25 °C) in a stainless steel syringe was driven by a pump (Nexus 6000) with a controllable flow rate. The rig was degassed with two valves positioned before and after the membrane holder (V1 and V2 in Figure 4-6). Each membrane was tested for at least one hour at stable transmembrane pressure. The water permeate was collected in a beaker pre-filled with a layer of silicone oil on a weighting scale (Mettler Toledo, MS304S/01, 0.1 mg sensitivity). For each membrane, the permeance $K = Q/\Delta P/A_{mem}$ was calculated as an average of four measurements at different syringe flow rates.

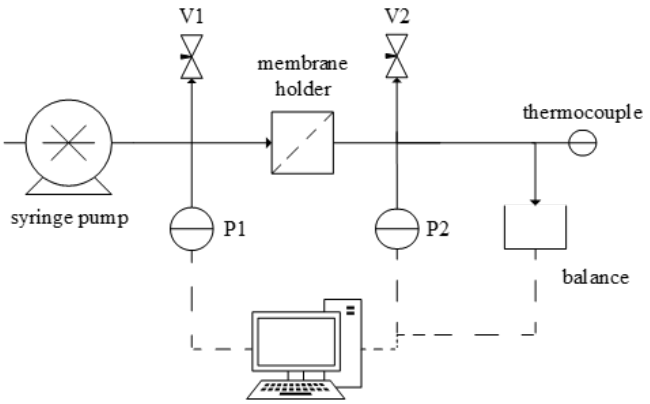

Figure 4-6: Schematic of the pressure-driven fluid flow measurement rig.

4.4 Templated Nanotube Membranes Rejection Methods

The rejection performance was tested in a custom-made crossflow setup, based on a bored-through tee in a dead-end flow cell as schematised in Figure 4-7. The feed approached the membrane normally at 0.01 ml/min and flowed radially outwards when it touched the membrane. The retentate was directed to the cell outlet by the side junction of the bored-through tee.

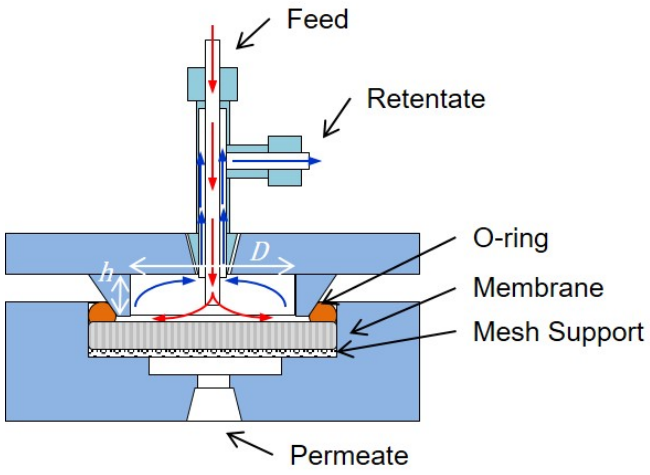

Figure 4-7: The dimensions for the water tangential flow in the feed side are 20 mm × 2 mm $D \times h$. Image courtesy of InRedox, www.inredox.com

The first permeating drops of permeate collected were analysed with UV-vis. Then the membranes were slowly backflushed after each rejection test for each particle. If backflushing caused the partial fracturing of the membrane under investigation, a silicone gasket was added on top of the membrane to prevent leakage through the fracture. Silica nanoparticles rejection tests were performed prior to the hematite nanoparticle tests for all membranes. Smaller nanoparticles were tested first. Rejection $R(\%)$ is calculated as:

$$R = \left(1 - \frac{C_P}{C_F}\right) \times 100, \tag{4.4}$$

with C_F and C_P being the concentration of nanoparticles in the feed and permeate streams respectively. The normalised rejection (R_N) is obtained by dividing R by the average pore diameter D_P. It is worth noticing that in the ceramic membranes studied deformation of the matrix does not take place during testing [2].

4.5 Static Adsorption Tests Methods

Static adsorption tests were performed in 20 ml glass vials containing an alumina disc or a BN coated alumina disc dipped in silica and hematite nanoparticle suspensions, with a control vial containing only the nanoparticle suspension. The solutions were gently shaken with an IKA KS 130 for 24 h at a temperature of 25 °C and with stirring at 80 rpm. The vials were capped to minimise evaporation. The supernatant of each test vial was then collected. The concentration of silica and hematite in the solutions was analysed by UV–Vis spectrophotometry. The concentration of nanoparticles in the vials containing alumina or BN-coated alumina is referred to as C_S, while the concentration of nanoparticles in the control vial containing the solution only is referred to as C_C. The adsorption $Ad(\%)$ of nanoparticles on membranes and gaskets was then calculated by:

$$Ad = \left(1 - \frac{C_S}{C_C}\right) \times 100, \tag{4.5}$$

4.6 Polyamide Membranes Performance

Pure water flux was tested in cross flow mode on a minimum of three membranes per composition, with 24 h of compaction at 7 bar and three days of testing at 3 bar. Dye and salts rejections were tested for 7 h with a 45 L h^{-1} pump flow rate. Salts (NaCl, $CaCl_2$ and $MgSO_4$), humic acid and dyes were purchased from Sigma Alderich. Rejection of Methylene Blue was assessed using a UV spectrophotometer (UV Cary 100, Agilent, U.K.), and the one of salts using an Orion Versastar ThermoScientific conductivity meter. The feed concentration for the dye tests was 0.01 g/L, whilst for salts rejection it ranged from 500 to 2000 ppm. Humic acid fouling tests were performed on pre-compacted membranes in cross flow mode. The 2.5 L feed of 1 g/L humic acid in water was prepared beforehand, and mixed with a magnetic stirrer for 24 hours before the test. The fouling test consisted in two fouling cycles of 15 hours and two physical cleaning cycles of one hour each. Flow rate was set as 175 ml/min (Reynold number, Re = 130) and 750 ml/min (Re = 550) for fouling and cleaning respectively. Flux recovery ratio (FRR) was measured before each cycle as follows:

$$FRR(\%) = \left(\frac{J_{AF}}{J_{BF}}\right) \times 100, \tag{4.6}$$

where J_{BF} and J_{AF} are the two fluxes before fouling and after cleaning, and are calculated for each cycle. The membrane total resistance R_t after 15 hours of fouling test was also calculated:

$$R_t = R_m + R_r + R_{ir}, \tag{4.7}$$

with R_m, R_r and R_{ir} being the intrinsic membrane resistance and the reversible and irreversible fouling resistance respectively. These are so calculated:

$$R_m = \frac{\Delta P}{\mu \times J_{BF}}; \tag{4.8}$$

$$R_{ir} = \frac{\Delta P}{\mu \times J_{AF}} - R_m; \tag{4.9}$$

$$R_r = \frac{\Delta P}{\mu \times J_F} - R_m - R_{ir}. \tag{4.10}$$

The transmembrane pressure is indicated with ΔP and the viscosity with μ, while J_F is the flux of humic acid after 15 hours of fouling. The first 10 ml of permeate were discarded in every test, to account for dead volume and permeate tubing. The mass balance for the rejection of component i is so calculated:

$$mass\,balance(\%) = \left(\frac{V_{P,i}c_{P,i} + V_{R,i}c_{R,i}}{V_{F,i}c_{F,i}}\right) \times 100, \tag{4.11}$$

where the subscripts P, R and F stand for permeate, feed and retentate respectively; V is the volume and c the concentration. Chlorine resistance tests were performed with 4 L feed water containing 2000 ppm NaOCl (technical solution, purchased from Fischer Scientific) and 2000 ppm $CaCl_2$. Rejection and permeance were monitored over a period of 5 hours and 30 minutes. The membranes are tested in cross flow mode with a pump velocity of 45 L h^{-1} at 3 bar. Membranes are always precompacted before rejection tests.

4.7 Computational Methodology for Water Flow Tests

The LAMMPS platform47 was used to perform high-fidelity MD simulations of water flows through double-wall CNNTs. A side view of a double-wall CNNT filled with water molecules is shown in Figure 4-8a. As a means of comparing MD flow results with previous experiments [18], we also simulate as benchmark cases flow through pristine double-wall CNTs (Figure 4-8b) and CNTs with 8.8% defects.

MD solves Newton's equations of motion for a system of molecules, which move deterministically in time and space, and interact together via potential energy functions; in this work we use the pair-wise Lennard-Jones (LJ) and electrostatic Coulombic potentials for all atoms in the flow simulations:

$$U_{ij} = 4\epsilon_{ij}\left[\left(\frac{\sigma_{ij}}{r_{ij}}\right)^{12} - \left(\frac{\sigma_{ij}}{r_{ij}}\right)^{6}\right] + \frac{1}{4\pi\epsilon_0}\frac{q_i q_j}{r_{ij}}, \tag{4.12}$$

where ϵ_{ij} is the van der Waals interaction energy between a pair of interacting atoms (i,j), σ_{ij} is the characteristic length scale, r_{ij} is the distance between the atoms, q_{ij} is the charge on one atom, and ϵ_0 is the vacuum permittivity.

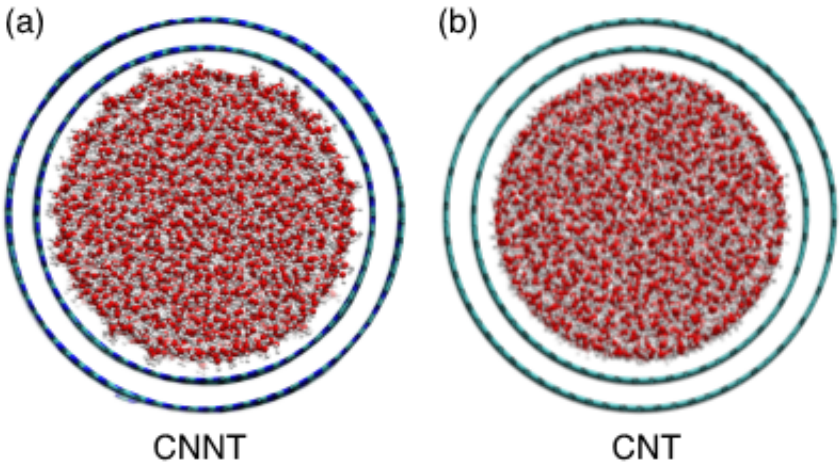

Figure 4-8: Cross-section of a MD simulation through (a) a CNNT and (b) a pristine CNT. The atoms are identified by the following colours: red = oxygen; white = hydrogen; cyan = carbon; blue = nitrogen.

The TIP4P/2005 model48 along with the SHAKE algorithm is used for modelling water molecules, which consist of two hydrogen (H) atoms (0.5564 e), one LJ oxygen (O) atom and one massless (M) site (-1.1128 e). The PPPM method is used to evaluate all long-range Columbic interactions, while all short-range LJ interactions are shifted and truncated by a cut-off of 1.3 nm. An NVT MD ensemble is used in all flow cases, with an integration time-step of 2 fs. In order to get the surface structure and chemistry in the MD simulation as close as possible to the experiment CNNTs, the surface was constructed with the same C:N and pyridinic:quaternary ratios as the experiments. The CNNT is constructed by initially considering a CNT of known radius and chirality. Nitrogen atoms replace carbon atoms on the CNT in a spatially alternating pattern (i.e. quaternary sites initially occupying the full nanotube) that gives a ratio of 50:50

C:N. Pyridinic rings in various templates (sizes and orientations) are then generated, with number calculated from the above pyridinic:quaternary ratio, and are distributed randomly across the surface, avoiding overlap. The final step is then to bring down the amount of nitrogen atoms and quaternary sites by replacing nitrogen atoms with carbon atoms until the experimentally found percentage of C is achieved in the nanotube; this process is performed randomly, and applied only in quaternary-dominated regions away from the pyridinic sites.

The wall atoms are equilibrated before being filled with water, using the reactive force field: ReaxFF [242], which has the benefit of providing an equilibrated nanotube structure, and the unknown charges on all wall atoms using the charge equilibration technique [243]. In these pre-simulations, the total charge on the tubes was always zero. A timestep of 0.25 fs is only used for these LAMMPS pre-calculations. The wall atoms are then kept rigid for the water flow simulations that follow.

The remaining LJ potential parameters between the wall atoms and the water molecules were then obtained by calibration studies with our experiments. In the water-CNNT simulations, the oxygen-carbon potential parameters ϵ_{OC}= 0.102 Kcal/mol and σ_{OC} = 3.19 Å were already obtained from previous MD simulations [244] of water droplets on graphite surfaces, calibrated from an experimental contact angle of 86° [245], and are used also for the CNNT in this work. We fix these oxygen-carbon parameters, and determine the missing nitrogen-oxygen parameters by calibrating a sessile nanodroplet using the experimental contact angle of 53° measured in this work. To do this, we construct a double-layered sheet of carbon-nitride, with similar structures as the CNNT and equilibrate a water droplet of 17.5k water molecules at 298 K on the surface as shown in Figure 4-9a. The size of the droplet was chosen large enough to be much bigger than the lengthscale of the biggest pyridinic structure on the surface, as well as to minimise line-tension effects. The length scale parameter for oxygen-nitrogen interaction was fixed and calculated from the Lorentz-Berthelot mixing rules, to be σ_{ON} = 3.234 Å. In each simulation, the oxygen-nitrogen energy parameter ϵ_{ON} is varied, and the equilibrium contact angle was measured as demonstrated in Figure 4-9b. From results in Figure 4-9 the energy parameter ϵ_{ON} = 0.1304 Kcal/mol is chosen to match the experimental 53° contact angle. These LJ parameters are then fixed for future flow simulations through the CNNTs.

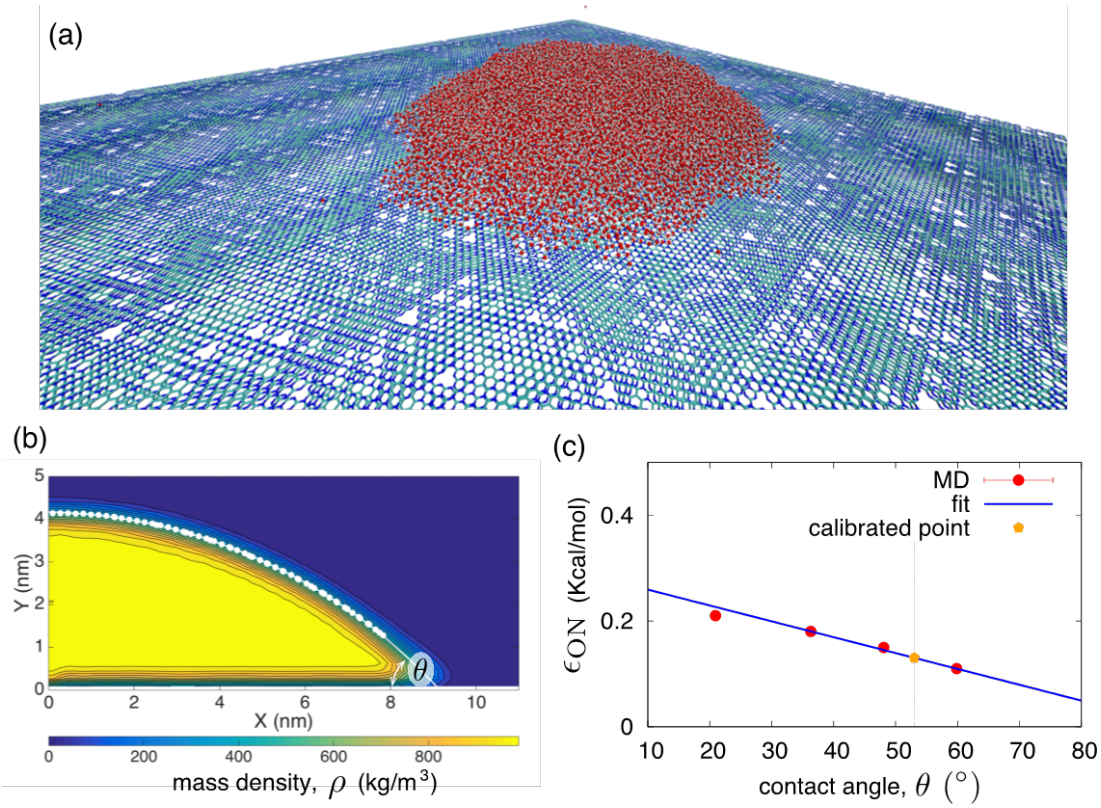

Figure 4-9: (a) MD case of a water droplet on a carbon nitride surface used for calibrating the Lennard-Jones energy parameter; (b) a density contour plot demonstrating how the contact angle is measured from the steady-state solution; (c) results of different MD simulations with varying ϵ_{ON}.

In the water-CNT simulations we use the same oxygen-carbon potential parameters as above, i.e. ϵ_{OC}=0.102 Kcal/mol and σ_{OC}=3.19 Å. For the turbostratic CNTs, however, we have modified the surface chemistry to contain ∼8.8% point defects that matches the experiments, and recalibrated the oxygen-carbon potential parameters using the same method as described above now with a target experimental contact angle of 61°, obtained as the lowest value from previous experimental data [18] giving: ϵ_{OC}=0.1162 Kcal/mol and σ_{OC}=3.19 Å.

All nanotubes are filled starting from reservoir filling simulations [246], and the density of ∼1000 kg/m^3 is measured in the nanotubes. The periodic nanotubes are then set at the same density and equilibrated at 298 K using a Berendsen thermostat. The main simulation then consisted of applying a body force $F_{\mathrm{x}} = \Delta P/\rho_{\mathrm{n}} L$ (in the x-direction) to all water molecules, where ρ_{n} is the number density, and $\Delta P/L$ is the pressure gradient. The length of the nanotubes were all fixed at L=15.74 nm. The steady-state

average mass flow rate was measured using $\langle\dot{\omega}\rangle = \omega_{\mathrm{i}}/L\sum_i v_{(\mathrm{x,i})}$ over ∼10 ns of MD simulation time, where $v_{(\mathrm{x,i})}$ is the x-component velocity of a water molecule of mass ω_{i}=2.99 10^{-26} kg.

The nanotube flow resistance per unit length ϱ was calculated using the linear flow relationship between pressure gradient and mass flow rate, i.e. $\Delta P/L = \varrho\langle\dot{\omega}\rangle$, which is used to calculate the slip length for a particular nanotube (geometry and surface chemistry) by rearranging the Hagen-Poiseuille equation as follows:

$$L_s = \left(\frac{128\mu}{\varrho\rho\pi D^4} - 1\right)\frac{D}{8}, \tag{4.13}$$

where D is the nanotube diameter, μ is the viscosity, and ρ is the mass density. The full-membrane permeance can be predicted by the theoretical model in Eq.4.14, where all terms are known from the experiments, except the slip length L_{s}, which is calculated from the MD simulations, using Eq.4.13.

$$K = \frac{\phi D^2}{32\mu L}\left(1 + \frac{8L_s}{D}\right), \tag{4.14}$$

Note that this approach only includes Poiseuille pressure losses (i.e. due to the flow in the nanotube). However, entrance/exit pressure losses can be included in this equation [247–249] when the following constraint is true [250]:

$$L > \frac{3\pi D}{16\epsilon}\left(1 + \frac{8L_{\mathrm{s}}}{D}\right), \tag{4.15}$$

where ϵ=0.01 is the error in the prediction. For example a typical experiment CNNT membrane carried out in this work has $L_{\mathrm{s}} < 1$ nm, $D = 80$ nm and $L = 50$ μm; the RHS of Eq. 4.15 is ∼5 μm. This means that CNNT membranes with nanotubes smaller than 5 μm require end losses to be incorporated in the flow prediction model of the Hagen Poiseuille equation. As our membranes thicknesses (which correspond to L) are 10 times larger, we ignore end losses from our theoretical analysis. The work of adhesion, viscosity and self-diffusion coefficient were obtained from equilibrium MD simulations of the $D = 4$ nm cases, but which contain no pressure-gradient forcing and so, no flow. The work of adhesion was computed by summing all potential energy interactions between wall and water molecules only, using Eq.4.16, and then dividing over the wetted area of the nanotube (πDL).

$$\epsilon = 1 + \frac{8L_s}{D}. \tag{4.16}$$

The viscosity, μ and the self-diffusion coefficient, D_s were then calculated using the Stokes-Einstein and Green-Kubo expressions, respectively [251], in radial bins:

$$\mu = \frac{k_B T}{3\pi\alpha D_s}, \tag{4.17}$$

$$D_s = \frac{1}{N}\int_0^\infty \sum_i^N \langle v_{i,x}(t) \cdot v_{i,x}(t+t')\rangle dt', \tag{4.18}$$

where T is the fluid temperature, k_B is Boltzmann's constant, α=1.7 Å is the effective hydrodynamic diameter of one water molecule, N are the number of molecules in the bins and $v_{i,x}$ is the streamwise velocity of the ith water molecule.

4.8 Computational Methodology for Particle Rejection

The LAMMPS [252] Molecular Dynamics (MD) software was used to simulate ionic nanoparticles near the entrance of BNNT and CNT membranes.

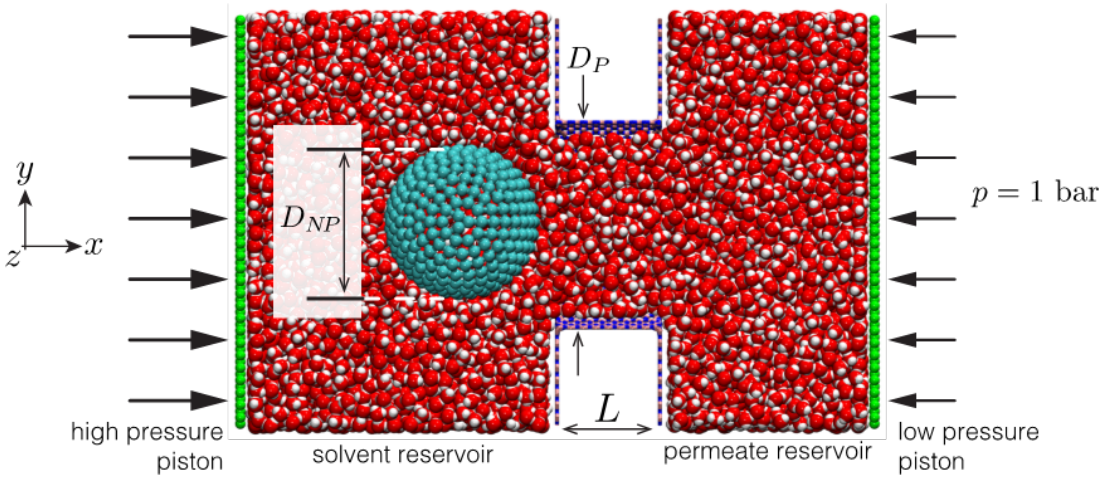

Figure 4-10: MD snapshot of case setup for BNNT membrane with particle placed in the solvent reservoir (left); a slice is taken at the xy plane of the domain for a better visual of the system.

The aim of using MD was to understand the behaviour of nanoparticles at a scale

that is inaccessible by experiments, which offered a means of explaining and verifying the experimental observations. We anticipate that the event of particle selection is very short in comparison with the overall timescales of the experiment. There are also fewer instances of particles crossing the membrane, when considering the large number of existing pores. As MD can only be used to study nanometres and nanoseconds of problem scales, we focus on what happens in the instant when a particle is located at a pore.

4.8.1 Geometry

Our MD setups were designed to be as close as possible to the experiments, within the computational limitations of MD. Figure 4-10 shows a snapshot of the MD case setup for the BNNT membrane. Both types of nanotubes of diameter $D_P = 40.68$ $\mathring{A}$ and length $L = 20.40$ $\mathring{A}$ used a pristine hexagonal structure and were embedded within a membrane surface of the same material. The nanotube length was kept short to reduce computational cost, as our interest lies in the particle dynamics at the pore entrance. The diameter was made as large as possible to ensure predominant bulk-like fluid in the nanotube [246].

Two reservoirs were filled with water and placed on either end of the nanotube membrane. The solvent (left) reservoir has dimensions 60 $\times$ 81.1 $\times$ 80.9 $\mathring{A}$, while the permeate (right) reservoir is 40 $\times$ 81.1 $\times$ 80.9 $\mathring{A}$; water of density 1000 kg m^{-3} was initialised in each reservoir and the nanotube pore. The left reservoir was purposely made much larger than the right to allow unimpeded Brownian motion of the particle, and allow enough time to take measurements (˜8 ns) as water depleted from the left reservoir during steady flow conditions.

Pistons on either side of the membrane maintained steady pressures (permeate side was always set at 1 bar). Various pressures were set to the solvent side: 5 bar, 20 bar, 60 bar, 100 bar and 1000 bar, in order to generate different pressure drops across the membrane. The force on each piston was transmitted to a rigid surface by setting the force on each atom to $F = p\ A/N$, where p is the applied pressure, $A = 66$ nm^2 is the area of the piston, and $N = 2508$ is the number of atoms on each piston. The direction of the force for the left piston was in the positive x direction, while the right piston was given a force in the negative x direction.

The particle was modelled as a hollow spherical shell made of one layer of rigid atoms distributed evenly across the sphere circumference. The *effective* diameter of the

nanoparticles D_{NP}, were chosen in line with the experimental observations, i.e. slightly smaller than the nanotube diameter D_P such that $0.6 < D_{NP}/D_P < 1$, where D_{NP} includes the actual diameter of the nanoparticle and the water-particle intermolecular lengthscale $\sigma \approx 3$ $\mathring{A}$. Specifically, 5 cases were considered: $D_{NP}/D_P = 1.0$, 0.9, 0.8, 0.7, 0.6, which represent *actual* particle diameters of 32.544 $\mathring{A}$, 28.476 $\mathring{A}$, 24.408 $\mathring{A}$, 20.34 and,16.272, respectively. All particles were initially placed 5 $\mathring{A}$ away from the pore, as measured between the entrance pore centre and the surface of the particle.

4.8.2 Force Fields

A hybrid pair-wise Lennard-Jones (LJ) and electrostatic Coulombic potentials were used for all atoms in the flow simulations (Eq. 4.12). The TIP4P/2005 model [253] along with the SHAKE algorithm [254] is used for modelling water molecules, which consist of two hydrogen (H) atoms (0.5564 e), one LJ oxygen (O) atom and one massless (M) site (-1.1128 e). The Coulombic interactions were modelled using the Particle-Particle Particle-Mesh (PPPM) method [255]. All short-range LJ interactions are shifted and truncated by a cut-off of 13.0 $\mathring{A}$. The LJ parameters used for the interactions between all the atoms are given in Table 4.3.

The surface partial charges of the BNNT and CNT were determined using charge equilibration in LAMMPS using the $\text{ReaxFF}_{\text{HBN}}$ force field [256]; this produced an equilibrated nanotube structure with a net neutral charge on the surface. The boron atoms on average were found to have a 0.9 e charge, nitrogen atoms a -0.9 e charge, and no charge for carbon atoms on the CNT.

Oxygen-boron, oxygen-nitrogen and oxygen-carbon potentials (see Table 4.3) were obtained using calibration studies with our experiments of water droplet contact angle measurements on surfaces of the same materials as the membranes, a method we describe in [257]. For BN surfaces we used a macroscopic contact angle of 78 ° from experiments, while for graphene we use 86 ° [238].

We modelled the zeta potential of the hydrated surfaces to be equal to that measured near the membranes in the experiments by subtracting charges from the boron atoms to produce a semi-hydrogenated surface with an overall negative surface charge density of -1.28 $\times$ 10^{-20} C nm^{-2}, which resulted in a change of -0.005 e per atom. The zeta potential near the CNT surface was found to be close to zero so no changes were applied to the partial charges. The particle charge density was set to -6.99 $\times$ 10^{-21} C nm^{-2} (also measured from experiments), which resulted in -0.003 e per atom.

Table 4.3: Lennard Jones force field parameters used in this work. No potential was applied between piston-piston, B-B, B-N, N-N, H-ALL and C-C pairs. [exp calib.] = calibrated from our experiments in this work; [est.] = estimated potential only required for transmitting pressure between piston and water; * the Si-O potential for particle-oxygen interactions is obtained from Lorentz-Berthelot mixing rules between O-O [253] and Si-Si [258] for σ, and calibration of ϵ from 20 ° experimentally-measured contact angle [259]; ** the Si-C particle-surface interactions were obtained from Lorentz-Berthelot mixing rules of Si-Si [258] and C-C [260]

Pair	ϵ **(kcal/mol)**	σ (**Å**)
O-O [3]	0.1852	3.159
O-B	0.0981 [exp calib.]	3.322 [7]
O-N	0.1213 [6]	3.278 [7]
O-Particle*	0.1912	3.433
O-Piston [est.]	0.3000	3.000
B/N/C-Particle**	0.0004	3.706
C-O [8]	0.1020	3.190

4.8.3 MD simulations

A NVT MD ensemble was adopted in all flow cases, using the velocity Verlet algorithm with an integration time-step of 2 fs. A streamwise-velocity unbiased Berendsen thermostat was used to maintain the temperature of the water at 300 K for the duration of the simulation. After initialising the cases as discussed above, an equilibration simulation was run to allow the pistons to set the target pressures in their respective reservoirs, while the particle was kept rigid, until a steady flow was generated ($\sim$ 0.5 ns). After this equilibration period, the particle was released and the production MD simulations were run for around 8 ns, during which all Lagrangian data was output every 1000 timesteps for further post-processing.

All our simulations were run on the UK's National Supercomputer Facility (ARCHER), using 96 processors for each case.

4.9 CFD for Nanotubes Rejection

4.9.1 Numerical Simulations

The conservation of mass and momentum equations, and particle tracing model for steady state and laminar flow conditions were solved by using a commercial Computational Fluid Dynamics (CFD) software COMSOL Multiphysics^{TM} v5.4. In all the

numerical models presented in this study, the flowing fluid was assumed to be Newtonian and incompressible. The overall domain size was 40 nm × 84 mnm (height × length) and is reported in Figure 4-11a. The domain was discretised into 8112 unstructured triangular elements, respectively, using finite element method (Figure 4-11b). For the computation of isoforce lines, the domain was considered symmetrical for x=42 nm.

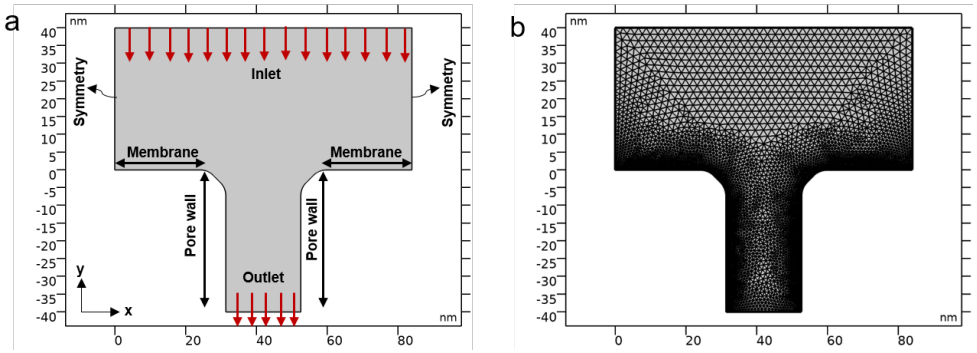

Figure 4-11: (a) Geometry and (b) mesh discretisations used in the CFD simulations.

4.9.2 Governing Equations and Boundary Conditions

Continuous phase

The continuous phase was assumed to be water with density, $\rho = 1000$ kg m^{-3} and dynamic viscosity, $\mu = 0.001$ kg m^{-1} s^{-1}. The hydrodynamics was modelled by solving the continuity and Navier-Stokes equations:

$$\nabla \cdot \mathbf{u} = 0, \tag{4.19}$$

$$\rho\,(\mathbf{u} \cdot \nabla \mathbf{u}) = -\nabla p + \mu \nabla^2 \mathbf{u}, \tag{4.20}$$

where $\mathbf{u}$ is the velocity (u,v,w) and p is the pressure. The boundary conditions were:

- *Inlet*: Pressure i.e. when y= 40 nm,0 < x < 84 nm.
- *Left wall*: Symmetry i.e. when x= 0 nm, 0 < y < 40 nm; $\mathbf{u}$=0.
- *Right wall*: Symmetry i.e. when x= 84 nm, 0 < y < 40 nm; $\mathbf{u}$=0.
- *Membrane*: No-slip and impermeable i.e. when y= 0 nm, 0 < x < 26 nm and 58 < x < 84 nm.

- *Pore wall*: No-slip and impermeable i.e. when $0 < y < 40$ nm, $26 < x < 31$ nm and $53 < x < 58$ nm.
- *Outlet*: Normal outflow velocity i.e. when y= 40 nm, $31 < x < 53$ nm. The outlet velocity was obtained by dividing the experimental flow through the membrane by the number of pores at the designated pressure.

Particles

The particle was assumed to be spherical with density, $\rho_p = 2650$ kg m^{-3}, and diameter, $D_{NP} = 19.2$ nm from the experimental value for a particle. The forces acting on the particles were described in Eq. 2.12. It was further assumed that there were no particle-particle interactions. The boundary conditions were: Inlet: Four particles were randomly released at the inlet between 0 s and 10^{-4} s with time interval 10^{-7} s.

- *Left wall*: Impermeable, the particles were set to bounce off when they contact the wall.
- *Right wall*: Impermeable, the particles were set to bounce off when they contact the wall.
- *Membrane*: Impermeable, the particles were set to bounce off when they contact the wall.
- *Pore wall*: Impermeable, the particles were set to bounce off when they contact the wall.
- *Outlet*: The particles were set to freeze once they exit through the outlet.

4.10 Error Analysis

All templated membranes for which permeance or rejection is reported in this work were analysed with SEM for the anaysis of pore size with the methodology described in Section 4.2.1. Error bars were drawn using the standard deviation of at least 20 repeats for the calculation of D_P. The error bars related to permeance K in each templated membrane were attributed to the standard deviation of at least three values, computed using the internal functions of Microsoft Excel. The error bars for the data in this work have been explained within the captions.

The quality of the fit of models was evaluated by the coefficient of correlation (R^2). The significance of the prediction of theoretical and MD models of experimental values is done by assessing whether the p-value (computed with Microsoft Excel) was lower than 0.05.

UV-vis calibration curves were prepared by diluting a starting suspension at the highest concentration five times. Predictions using the prepared calibration curve were associated to errors so calculated [261]:

$$s_{\mathrm{X}_0} = \frac{s(r)}{m}\sqrt{\frac{1}{N} + \frac{1}{n_P} + \frac{(\overline{y_0} - \overline{y})^2}{m^2 \sum_{i=1}^{n_P}(x_{\mathrm{i}} - \overline{x})_2}}, \tag{4.21}$$

where $s(r) = \sqrt{\sum_{i=1}^{n_P}(y_{\mathrm{i}} - \hat{x_{\mathrm{i}}})_2/(n_P/2)}$ is the residual standard deviation with y_{i} as the observed value of absorbance for a given concentration value of x_{i}; $\hat{y}_{\mathrm{i}}$ is the value of absorbance predicted by the plotted calibration line (with gradient m) for a given value of concentration x_{i}, and n_P is the number of paired calibration points; N is the number of repeat measurements made on the sample, which was three in all the samples collected; $\overline{y_0}$ is the mean of N repeat measurements of absorbance for the sample, while $\overline{y}$ is the mean of the absorbance values for the calibration standards; $\overline{x}$ is the mean of the concentration values [261].

4.11 Laboratory Safety and Waste Management

In compliance with the regulation, a Risk Assessment (RA) was prepared for every experimental procedure reported in this thesis, to assess hazard severity and likelihood of occurrence and therefore take precautionary measures for safe operations.

The synthesis procedures reported in Sections 4.1.1-4.1.5 were performed in a ventilated box, which served as a first containment for irritant and explosive gases, as well as a measure to avoid touching the furnace's hot components. To minimize the chance of leaking of gases in the laboratory, the gas lines were checked for leaks prior to each synthesis. Additionally, the laboratory was equipped with a NH_3 detector and an O_2 depletion alarm located outside of the ventilated box where the reactions took place. For explosive gases, such as H_2, the flow rate was always chosen so that the vol% of H_2 in the ventilated box would always fall well below the detonation limit, and the outlet gas cooled down at the furnace's exit. Additionally, an emergency isolation valve was located after the hydrogen cylinder, to provide an automatic means for stopping the hydrogen flow in an emergency. The box was purged with N_2 when reactions with H_2

took place. Ammonia was neutralised with a sulphuric acid scrubber at the outlet of the tube reactor in the synthesis of CNNTs. In case of a computer failure, the gas flows were switched off manually at the cylinders regulators.

Nanomaterials were handled in a fume hood equipped with HEPA filters. To quickly clean any considerable spillage, a wet tissue paper was always kept at hand. Nanomaterial waste in liquid or solid form was disposed as hazardous special waste. Nanomaterial was handled out of the fumehood only in liquid dispersions, or properly sealed. Dyes and foulants used in this work were disposed of in the non-halogenated waste bottles. If spilled in considerable amounts, these solutions were mopped up with blue tissue, which was then disposed of in the general bin. NaOCl, HCl and NaOH were handled in fumehoods and disposed of in the sink after being neutralised. Concentrated sulphuric acid was disposed of as a special waste. Acid spillages were cleaned up with dry inert material in provided spill kits. The compatibility between gloves in use and the material was confirmed before handling, assuring the breakthrough time of the solvent through the glove material would be longer than the experiment duration. The method for producing polyamide membranes detailed in Section 4.1.6 was carried out in a fumehood, and the produced membranes disposed as hazardous nanomaterial after use.

Chapter 5

Surface-controlled water flow in nanotube membranes

S. Casanova, M. K. Borg, Y. M. J. Chew and D. Mattia

This declaration concerns the article entitled: Surface-Controlled Water Flow in Nanotube Membranes	
Satus	Published
Publication details	ACS Appl. Mater. Interfaces 2019, 11, 1689 - 1698
Candidate's contributions to the paper (detailed, and also given as a percentage)	The candidate contributed to/ considerably contributed to/ executed the ... • *Formulation of Ideas* The initial idea was formulated by SC and DM based on preliminary observations conducted by DM. 80% • *Design of Methodology* The experimental work and data analysis was conducted by SC with supervision from DM and YMJC. 90% • *Molecular Dynamics* MKB is the author of the MD simulations presented in this paper. SC heavily contributed to the set-up of the MD model. 20% • *Presentation of Data in Journal Format* The first draft was written by SC with contribution from all authors. Subsequent drafts were reworked by all authors. 70%
Statement from candidate	This paper reports on original research I conducted during the period of my Higher Degree by Research Candidature.
Signed	, 23/12/2019

5.1 Introduction

The high water flow enhancement observed in carbon nanotubes (CNTs) [28] has, over the years, been attributed to a variety of causes [25, 262], from confinement effects at the nanoscale to the nature of the physical and chemical interactions between the liquid and the tubes' wall, to less likely explanations such as air gaps or depletion layers at the interface between the two. As nanotubes, and now 2D materials, are incorporated in mixed matrix membranes or fabricated as stand-alone membranes, elucidating the origin of the flow enhancement phenomenon is crucial to tailor these materials for specific applications, ranging from seawater desalination [263], to removal of pollutants in nanofiltration [264].

The effect of confinement has been well-researched and is now well understood [265], including a threshold below which continuum fluid mechanics no longer applies [251], the presence of slip, i.e. low resistance to liquid flow [47], and how both are affected by the curvature of the tube [14].

The picture regarding the effect of physico-chemical interactions on flow is less clear. Flow enhancement is generally attributed to the 'hydrophobic nature' of carbon. However, the contact angle of water on pristine graphite surfaces is just below 90 degrees [262], a key aspect explaining why water naturally imbibes into CNTs [8, 266]. Furthermore, water flow enhancement has been shown to occur – to varying degrees – in materials much more 'hydrophilic' than carbon (i.e. with lower water contact angle) [48, 267], for example silicon carbide [268]. The above results have been obtained via molecular dynamics (MD) alone. However, modest flow enhancement has also been observed experimentally in silica [7], and alumina [269] nanochannels and in turbostratic carbon nanotube membranes [18]. To further complicate the picture, recent experiments showed little to no water flow enhancement in boron nitride tubes (BNNTs) [14], a material that has a very similar water contact angle to graphite [270], while MD simulations of water flow in BNNTs showed significant enhancement, though still less than CNTs [30]. It has long been hypothesised, via simulations, that hydrophilic nanochannels or nanotubes, with either larger surface-liquid energy [35], or/and surface polarity [271], have the effect of decreasing flow, which translates to small [272] or zero hydrodynamic slip length [42]. MD studies imposing more hydrophilic potentials (e.g. that of silicon) on the sp2 carbon structure showed a drastic decrease of the water flow rate [273]. Furthermore, MD simulations have also shown that creating defects in the carbon structure (i.e. missing carbon atoms) leads to a decrease in flow rates [274], as did the addition of functional groups on the wall's surface [247, 57]. In all these

instances, however, it is difficult to separate the effect on flow arising from changes in the structure (e.g. defects, roughness) from those occurring in the surface chemistry (e.g. presence of functional groups) of the nanotube wall materials.

Several theoretical models have been developed to explain these effects [47, 271] with most focusing on the slip length, L_s, as defined in the Hagen-Poiseuille equation with Navier slip at the nanotube walls:

$$q = \frac{\pi D^4 \Delta P}{128 \mu L} \left(1 + \frac{8 L_s}{D}\right), \tag{5.1}$$

where ΔP is the applied pressure, μ is the fluid viscosity, and q is the volume flow rate through one nanotube of diameter D and length L. It should be noted that while the above equation is strictly valid only for continuum transport (i.e. when no confinement occurs) it has also been used to provide insight into non-continuum transport phenomena [265, 31, 274, 275]. The ratio of Equation 5.1 to the no-slip case yields the flow enhancement:

$$\epsilon = 1 + \frac{8 L_s}{D}. \tag{5.2}$$

Equation 5.2 can be transposed to a membrane (i.e. a structure containing a large number of aligned nanotubes) if the tubes' size distribution and membrane porosity are known [18]. Under the assumption that all n nanotubes in the membrane have a narrow size distribution, one obtains the following expression for the permeance, K, which is of relevance to membrane scientists:

$$K = \frac{Q}{\Delta P A_{mem}} = \frac{\phi D^2}{32 \mu L} \left(1 + \frac{8 L_s}{D}\right), \tag{5.3}$$

where A_{mem} is the membrane's area, ϕ is the porosity and $Q = q \times n$ is the total flow rate through the membrane. The derivation of this equation is highlighted by Equations 2.8 and 2.9 in Section 2.2.4. In this manuscript, the effect on water flow enhancement caused by modifying the surface chemistry and structure of carbon nanotubes independently, is demonstrated for the first time through a combination of experiments and MD. This has been achieved by fabricating novel carbon nitride nanotube (CNNT) membranes. Carbon nitride nanotubes have a similar surface structure to carbon nanotubes but with the presence of C-N bonds, which significantly change their surface chemistry [66], without significantly altering their structure (i.e. sp2 net-

work) [76]. The CNNT membranes have been prepared via CVD inside anodic alumina membranes, modifying a previously developed pyrolisation process [67]. This approach does not use the toxic reagents previously employed [66], and, more relevant to this work, produces CNNTs with lower carbon to nitrogen ratios [78]. This allows a direct comparison with published experimental data for carbon nanotube membranes produced inside anodic alumina membranes (AAMs) [18]. The experimental and MD results presented in this chapter show that changes to the carbon nanotubes' structure (i.e. transition from graphitic to turbostratic) and surface chemistry (i.e. carbon to carbon nitride) affect water flow enhancement. The approach proposed here allows decoupling these two effects, opening new ways to tailor the nanotubes' surface chemistry and structure for specific applications.

5.2 Results and Discussion

This work aims at testing the flow of pure water in carbon nitride nanotubes and, in conjunction with MD, assess the extent of the effect of differences in surface chemistry and structure on flow enhancement, when compared to carbon nanotubes.

5.2.1 CNNT Membrane Synthesis and Characterisation

After synthesis, CNNT membranes appeared yellow (Figure 5-1), a recurrent colouring for carbon nitride nanomaterials [276].

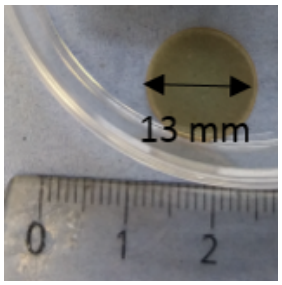

Figure 5-1: Picture of a CNNT membrane after casting.

The surface was clean with open pores (Figure 5-2a), ranging from 11.4 ± 2.1 nm to 76.1 ± 4.7 nm in diameter, depending on the starting AAM used and synthesis conditions. When the AAM were partially dissolved in H_3PO_4, the CNNTs stick out from the pores, presenting open ends (Figure 5-2b and c). The CNNTs outer surface resembles the rough inner pore surface of the ceramic template [277], as shown in the

magnified micrograph in Figure5-2d. The CNNTs look detached from the template in Figure5-2d because the template has been partially dissolved with the aim of imaging the nanotubes.

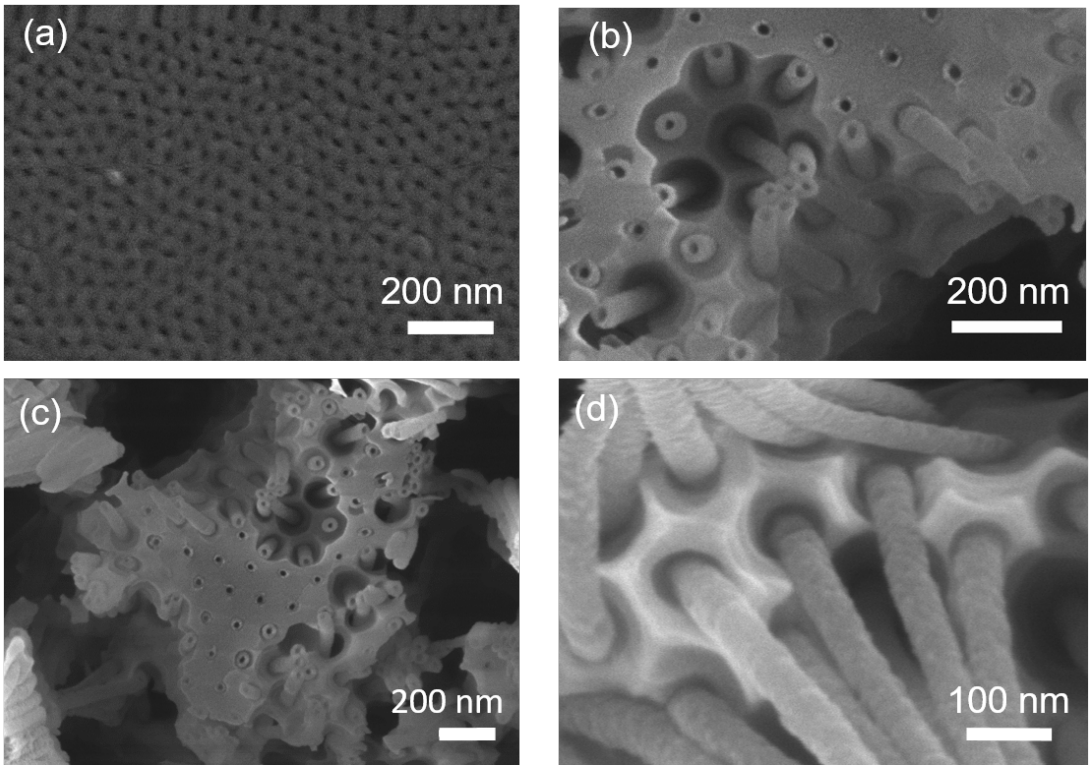

Figure 5-2: FESEM micrographs of (a) a CNNT membrane surface and (b,c,d) CNNTs protruding from an AAM partially dissolved in H_3PO_4 for 45 minutes.

TEM micrographs of CNNTs released from the AAM (Figure 5-3b and c), also confirm tubular features with a turbostratic structure (Figure 5-3d), similar to that of CNT membranes produced using the same CVD process [18]. We can observe that by identifying possible supramolecular structures (scale 1 to 100 nm) as being either graphitic, turbostratic or amorphous, both experimental CNTs and CNNTs are turbostratic but differ in chemical composition, while the modelled CNTs that give us high slip lengths are graphitic and have the same chemical composition as our turbostratic CNTs. This change in the surface chemistry with the introduction of N implies a variation in atomic structure and bonding, but not in the supramolecular turbostratic structure of the nanotubes. The CNNTs have outer tube diameters comparable to the size of the membrane pores.

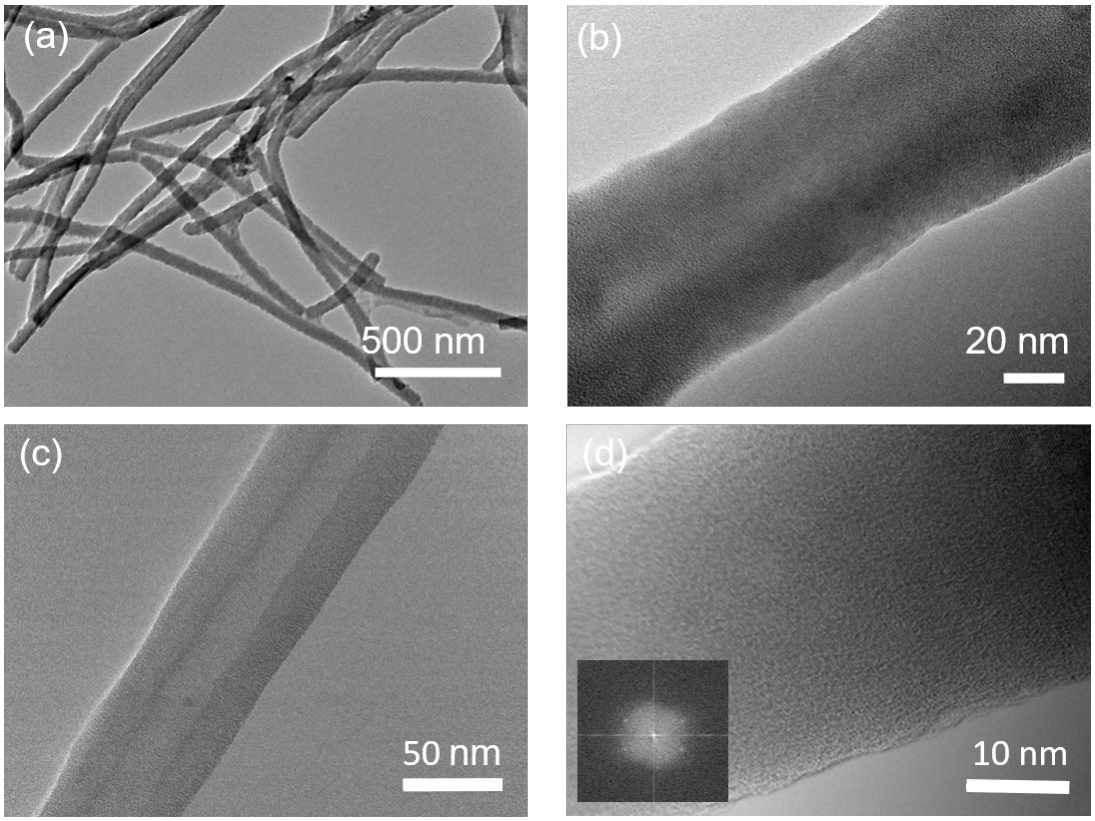

Figure 5-3: (a)TEM micrographs of CNNTs released from the AAM template, showing (b,c) their hollow, smooth inside and (d) turbostratic nature.

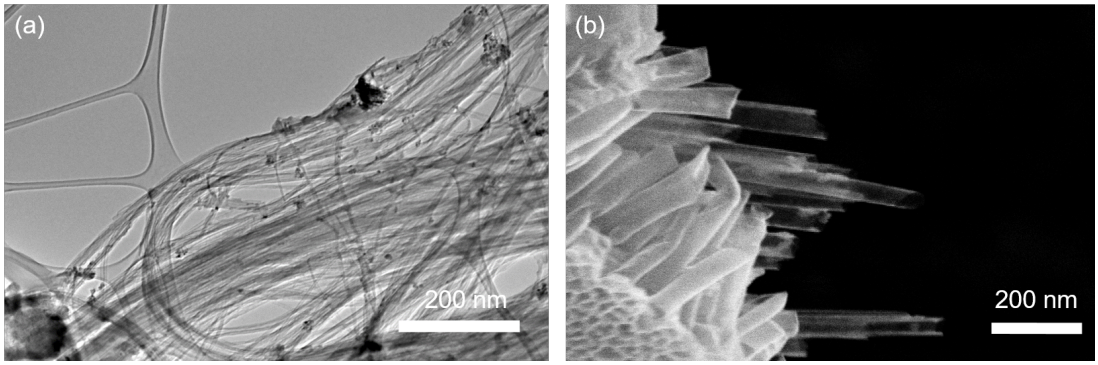

Figure 5-4: (a)TEM micrographs of CNTs released from the AAM template and (b) 100k magnification FESEM micrograph of CNTs sticking out of the template (WD= 10.0 mm).

It is observed that a side-effect of the process employed to release the CNNTs from the AAM templates is that the resulting tubes are partially covered by the by-products of the dissolution process (Figure 5-3c). These side-effects are not present in those membranes used for flow testing as they were not subjected to this procedure, as described in the Materials and Methods section. While the external walls of the deposited CNNTs had a high degree of roughness (Figure 5-2d), caused by the patterning from the alumina template surface, the inner surface of the analysed tubes was shown in the TEM to be smooth and lacked this same pronounced roughness (Figure 5-3c).

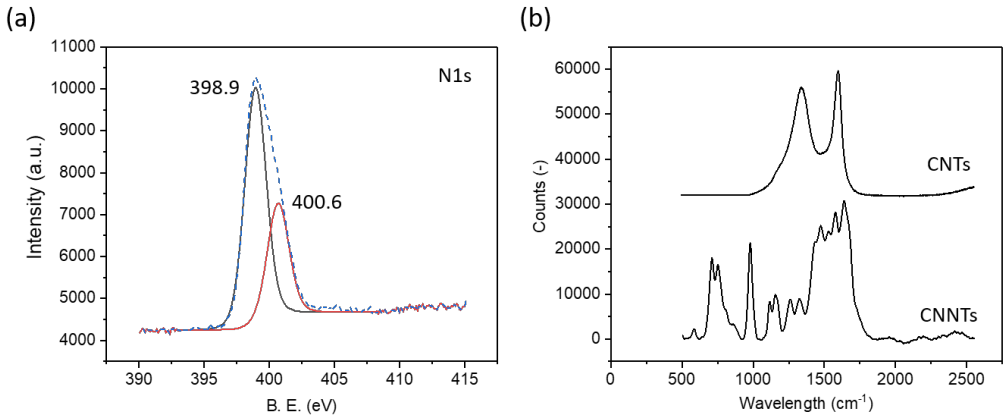

Figure 5-5: (a) CNNTs high-resolution XPS spectra of the N1s region showing the graphitic species (black line) and the pyridinic species (red line); (b) Raman spectra for CNNTs and CNTs.

X-ray photoelectron spectroscopy (XPS) analysis of CNNTs reveals a C:N atomic ratio of 1.47 and allows identifying the percentage of pyridinic and quaternary nitrogen based

on their binding energies at 398.9 eV and 400.6 eV respectively [278, 279], as shown in Figure 5-5a.

The structure of the CNNTs was compared to that of turbostratic CNTs prepared via a similar non-catalytic CVD process inside the pores of AAMs [18]. A well-established method was used to quantify the C=C sp2 bonding in the carbon structure and that of different functional groups (i.e. COH, C-O-C, C=O) and vacancies [280]. This method allowed quantifying the percentage of defects, relating it to the broadening of the C1s line shape in the XPS spectra. For CNTs, carbon in the graphitic sp2 form was found to account for 91.2 atomic % (± 0.6%) of the sample, while defects accounted for the remaining 8.6% ± 0.6%. CNNTs had a comparable amount of carbon defects that accounted for the 11.6% ± 1.3%. High resolution XPS spectra of C1s for CNNTs and CNTs with peaks identification is shown in Figure 5-6.

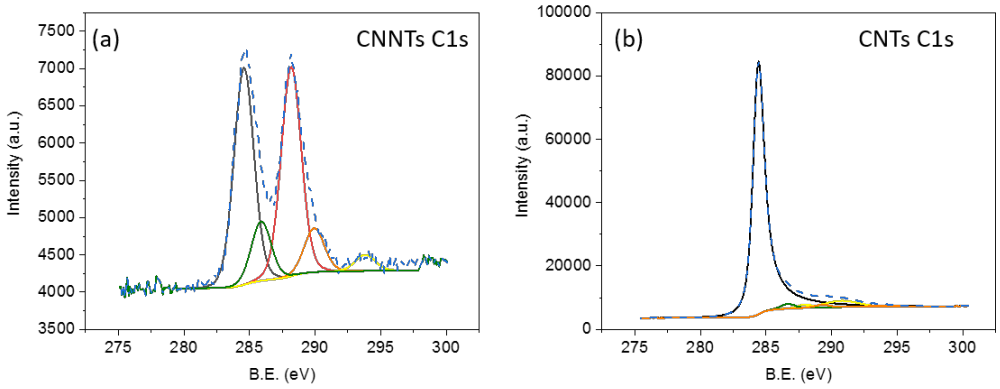

Figure 5-6: High-resolution XPS spectra of the C1s in (a) CNNTs and (b) CNTs showing C-C species (black line) at 284.5 eV, C-N (red line) at 288.2 eV, O-C=O (orange line) at 289 eV, C-O (green line) at 286 eV and vacancies (yellow line) at 290.7 eV and 293.8 eV. While XPS analysis of the produced CNNTs gives a C:N ratio of 1.47, XPS of the starting melamine precursor reveals a 0.76 C:N atomic ratio.

Figure 5-5b compares the Raman spectra of CNNTs membranes in this work and turbostratic CNTs membranes previously synthesized [18], showing the characteristic D- and G-bands. For the CNNT spectra, additional Raman bands at 700 cm^{-1} and 900 cm^{-1} are identified as the N-breathing and bending vibrations of heterocyclic molecules containing the triazine ring species [281]. Bands between 1200 cm^{-1} and 1700 cm^{-1} are attributed to the G- and D-band with disordered graphitic carbon and observable also in carbon-nitride materials [282].

The CNNTs membranes surface zeta potential at pH =6.0 was -14.6 ± 3.37 (R^2=0.87).

Fourier Transform Infrared Spectroscopy/ Attenuated Total Reflection (FTIR/ATR) was performed on the AAMs surface (Figure 5-7). The bands from 1250 to 1700 cm^{-1} are attributed to C-N and C-C bonds characteristic of the material [274, 282]. A large and short –OH vibration cantered at 3400 cm^{-1} is observed, showing a low amount of –OH groups adsorbed from the atmosphere onto the surface.

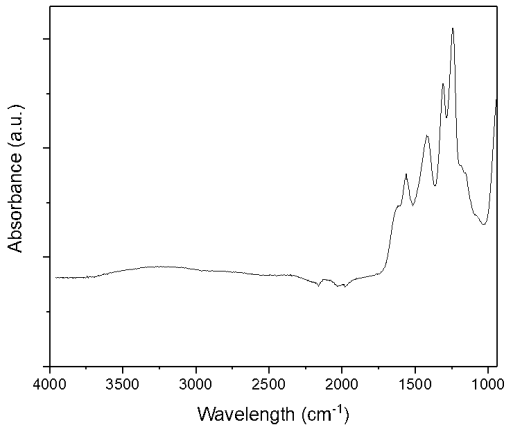

Figure 5-7: FTIR-ATR spectra of CNNTs membrane surface.

5.2.2 Molecular Surface Model of CNTs and CNNTs

The XPS data was used to build the CNT and CNNTs used in the MD simulations. An example of the MD surface for a (60,60) CNNT with diameter D = 8.14 nm is shown in Figure 5-8a.

The amount of carbon and nitrogen atoms of the nanotube is 60% and 40%, respectively, with pyridinic ($\sim$ 13%) and quaternary ($\sim$ 27%) microscopic structures, obtained from the XPS results, randomly distributed on the surface of the tubes. Figure 5-8b shows the point charge distribution on a small section of a CNNT surface. Using charge-equilibration calculations on these CNNT configurations, it was found that the nitrogen atoms are negatively charged (-0.4 e to -0.7 e), while the carbon atoms are positively charged when surrounded by nitrogen atoms or with zero charge in carbon-only areas. More information about constructing the CNNTs and obtaining point charges, including the MD methodology, can be found in Chapter 4.

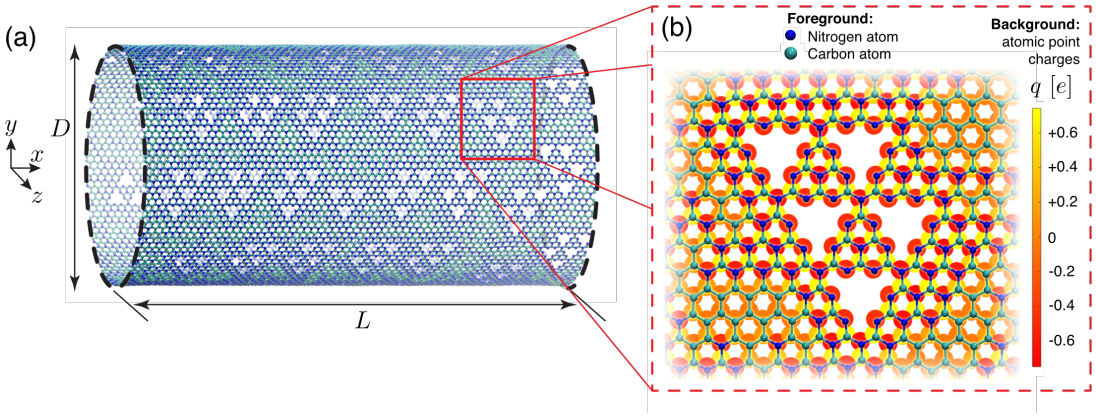

Figure 5-8: (a) Molecular dynamics setup of a CNNT (showing only the inner tube of a double-wall CNNT) of diameter D = 8.14 nm, chirality (60,60), and length L=15.74 nm (blue atoms are nitrogen, and cyan atoms are carbon); (b) point charges on a representative small sample of the CNNT surface.

5.2.3 Wettability Measurements

Literature reports contact angles values for turbostratic CNTs produced by CVD in the range between 61° and 90° [18], whereas the contact angles for highly graphitic CNTs have been found to be 82 - 86° [238]. The contact angle of the CNNTs in this work was measured to be in the range 43 - 67°, after being adjusted for roughness with the Wenzel equation, with an average of 53°. This is in agreement with results for flat films in the literature [282].

5.2.4 Permeance in CNNT Membranes

Experimental results of pure water permeance through CNNTs with inner diameter ranging from 11.4 ± 2.1 nm to 76.1 ± 4.7 nm showed an expected quadratic dependence of water permeance on pore diameter reported as permeance K, with units LMH @ 1 bar ($\mathrm{Lm^{-2}hr^{-1}bar^{-1}}$) [283]. All the data collected for the study are reported in Figure 5-9 as $[KL\mu/\phi]^{0.5}$ vs. D to enable comparing results between different materials and sets of experiments. Each experimental data point is the average of 2 to 6 measurements on the same membrane for different transmembrane pressures. The scatter in experimental data can be associated to non-evident partial cracks, imperfections in the starting templates or potential pore clogging. The validity of the MD model is also verified by the permeance values for defected CNTs in literature [18] and is shown in Figure 5-10. All MD simulations in this work have been constructed to be as close as possible

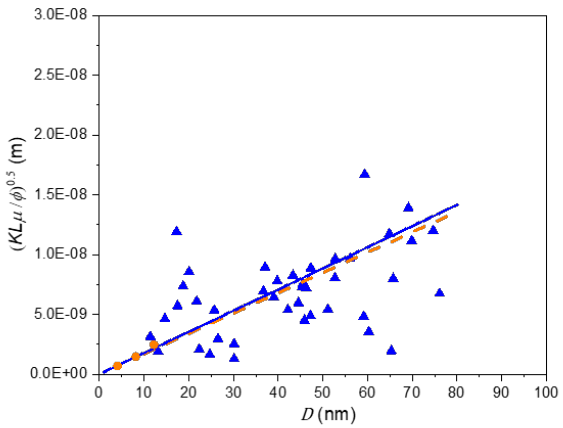

Figure 5-9: Comparison of permeance measurements between experiments (▲) and molecular dynamics simulations (●). The MD results are obtained by measuring flow rate in three CNNTs of different diameters. The dashed orange line (-) extrapolates the measurements of flow resistance R from these MD simulations using only the assumption that flow rate $q \sim D^4$, as predicted in Eq.5.1, while the straight blue line (-) uses directly Eq. 5.3 for flow rate derived from the H-P relationship, with slip length calculated from MD. The comparison between experimental and the independent MD prediction shows coefficients of correlation of 0.63. Data is plotted as the square root of $KL\mu/\phi$ (m) versus pore diameter D (nm).

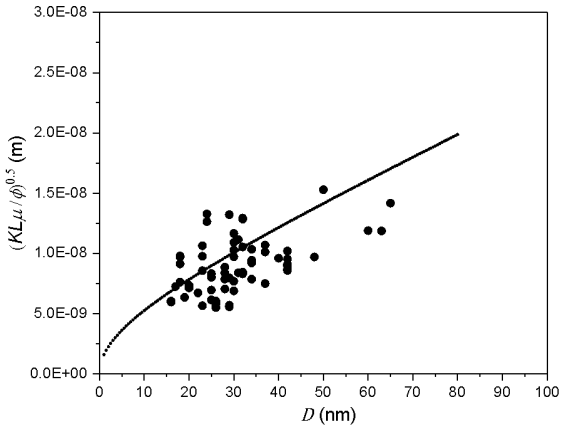

Figure 5-10: Comparison of experimental (•) and molecular dynamics (straight line) permeance for CNTs plotted as the square root of $KL\mu/\phi$ (m) versus pore diameter D (nm). The correlation between MD and experimental data is 0.88.

to experimental conditions, including having the same surface structure and surface chemistry as those measured from the experiments, as well as using a realistic water model that models accurately the condensed phase of water (detailed in Section 4.7 in Chapter 4).

All results from these MD simulations are provided in Table 5.1. MD simulations of water flow through CNNTs show good agreement with the experimental data. The orange circle symbols in Figure 5-9 are MD simulations of water transport through different CNNT diameters (4 nm, 8 nm, 12 nm). Note that the scope of using the term $\mathrm{KL}\mu/\phi$ on the y-axis of Figures 5-9 and 5-10 is also to normalise permeance with membrane geometry, thereby allowing MD simulations in single nanotubes to be compared directly with membrane experiments. Furthermore, as the experimental membranes have much larger CNNT diameters D than what can be tractably simulated using MD, the solid and dashed lines in Figure 5-9 indicate theoretical predictions using input from the MD flow measurements. The solid blue line uses Eq. 5.1 with slip length ($L_s < 1$ nm) computed from the MD, while the dashed orange line assumes that the flow rate has a relationship that depends on D^4, as per Eq. 5.1. It is important to highlight that the MD data and predictions are independent of permeance or membrane parameters (such as length or porosity) measured in the experiments; i.e. solid and dashed lines in Figure 5-9 are not fits of the experimental data points. MD simulations also confirmed that nanotube end losses are negligible for these membrane thicknesses, and so do not need to be incorporated in Eq.5.1 [250].

Table 5.1: Water flow measurements from CNNT and CNT nanotubes of constant length. Standard errors (SE) are already multiplied by 1.96, which means they represent upper and lower 95% confidence limits.

Case name	D (nm)	F (10^{-15}N)	N (-)	dP/dL (Nm^{-3})	$\dot{m}$ (10^{-14}kgs^{-1})	R (10^{27}kg s^{-1})	L_s (nm)
CNNT D4$_i$	4.068	48.758	5865	1.644×10^{15}	1.042 ± 0.105	161.000 ± 3.234	0.041 ± 0.01
CNNT D4$_{ii}$		97.515		3.288×10^{15}	2.070 ± 0.171		
CNNT D4$_{iii}$		390.061		1.315×10^{16}	8.179 ± 0.174		
CNNT D8	8.136	24.379	27301	8.133×10^{14}	8.985 ± 0.483	9.052 ± 0.488	-0.121 ± 0.05
CNNT D12	12.204	6.965	61573	2.329×10^{14}	16.532 ± 2.890	1.409 ± 0.255	0.175 ± 0.31
CNT$_{\text{pristine}}$	4.068	3.420	5865	1.153×10^{14}	7.502 ± 0.737	1.540 ± 0.153	52.778 ± 5.29
CNT$_{\text{defects}}$		6.965		2.349×10^{14}	2.923 ± 0.328	8.040 ± 0.915	9.716 ± 1.16

The comparison between experimental and the independent MD predictions (solid blue line) shows coefficients of correlation of 0.63. This indicates a strong relationship between MD results and experimental data, while p-values lower than 0.05 (1×10^{-5} for CNNTs) indicate a very significant prediction, where changes in the predictors'

value are strongly related to changes in the response value [284]. This serves as further validation of the usefulness of this MD model for the description of flow in nanosized channels. The same process was repeated for the turbostratic CNT membranes previously published [18], with correlation of 0.88 between MD and experimental data and p-value of 2×10^{-22} (Figure 5-10). The very good correlation between experimental and MD data, allows to go a step further and compare the permeance of graphitic and turbostratic CNTs with CNNTs (Figure 5-10). As experimental data for graphitic CNT membranes (i.e. pristine rolled graphene sheets) are rare, especially for these large diameters, in Figure 5-10 predictions using Eq. 5.1 are plotted, with slip length derived from MD simulations of flow through CNTs.

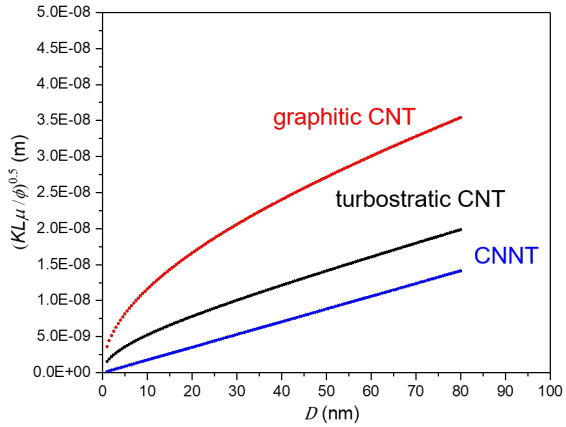

Figure 5-11: Comparison of permeance, Eq.5.1, using slip lengths derived from MD simulations (see Table 5.1) plotted as the square root of $KL\mu/\phi$ (m) versus pore diameter D (nm). The CNNTs line also corresponds to the condition L_s=0.

The comparison clearly shows a decrease in water permeance from the graphitic to the turbostratic CNTs and a further decrease for water permeating through CNNTs with the same diameter. The reduction in permeance between graphitic and turbostratic CNTs is attributed to a change in the sp2 surface structure of the carbon nanotubes [273, 274], where two carbon atoms form a sigma bond in the molecule by overlapping two sp2 orbitals, i.e. a decrease in graphitization, already measured in the turbostratic tubes [238] and higher surface wettability. In order to account for this less organised structure, the CNT used in the present MD simulations had a degree of defects set to match the XPS results and surface/liquid potentials calibrated from sessile droplet experiments. On the other hand, the transition in Figure 5-11 from turbostratic CNT to CNNT, is attributed primarily to a change in the surface chemistry due to the

hydrophilising effect on the sp2 carbon structure induced by the C-N bond. This is the first experimental observation of what postulated by previous MD work where a dependence of water permeance on an artificially imposed degree of hydrophobicity of the CNT structure was observed [35, 4]. The MD simulations also show that the presence of the C-N bonds dramatically changes the surface/liquid interfacial energy landscape of the CNNTs, compared to a pristine CNT. Inspecting the water ordering near the CNNTs from the radial density distribution measurements of water, reveals that the triazine rings act as local 'potential energy wells' (Figure 5-12a for oxygen atoms). These wells - indicated by the small dark blue peak near the walls of the CNNT in the figure - force the water molecules to flow radially outwards in the cross-section of the nanotube by ~ 0.1 nm (almost one molecular diameter) more than when those rings are not present, such as for the pristine CNTs, which have a smoother potential energy landscape. This small molecular roughness induced by the triazine rings on the flow affects the local solid-liquid friction, and brings the local slip at the wall close to zero. The CNNT surface produces a mixed slip system, with high slip near smooth graphitic patches on the surface, no-slip near the triazine rings (or any hydroxylated areas in the experiments), and somewhere in between near the C-N quaternary structures; the net effect is dominated by the lowest slip regions and their concentration over the entirety of the nanotube. In the case of CNNTs, the triazine rings and quaternary structures dominate the overall structure, leading to a drop in the overall slip length to below 1 nm. Figure 5-12b shows the MD results for radial velocity profiles in pristine CNT, turbostratic CNTs and CNNTs, indicating the calculated slip length, L_S, values for the three cases. The Hagen-Poiseuille flow Eq.5.3 with MD-derived slip length is also shown, indicating reasonably good predictions for all cases.

A comparison of radial viscosity and self-diffusivity from the MD simulations also revealed an increased attraction of water near the surface of a CNNT, when compared to pristine and turbostratic CNTs, as shown in Figure 5-12c and Figure 5-12d, respectively. The water in the CNNT experiences an increased viscosity and a drop in self-diffusivity very close to the surface, whereas in the CNTs it retains the same values for viscosity and self-diffusivity near the surface as those in the bulk [285]. It is noted here that the measurements for bulk self-diffusivity are similar to those published for water on graphene in previous MD simulations (D_S = 2.6 x 10-9 m^2/s) [285]. This means that for CNNTs, the hydrophilisation caused by the nitrogen on the tube's surface, i.e. the increased surface/water potential energy (including the effect of partial charges) and also the increased levels of flow roughness near the surface, are causing the drop in transport of the water molecules near the surface.

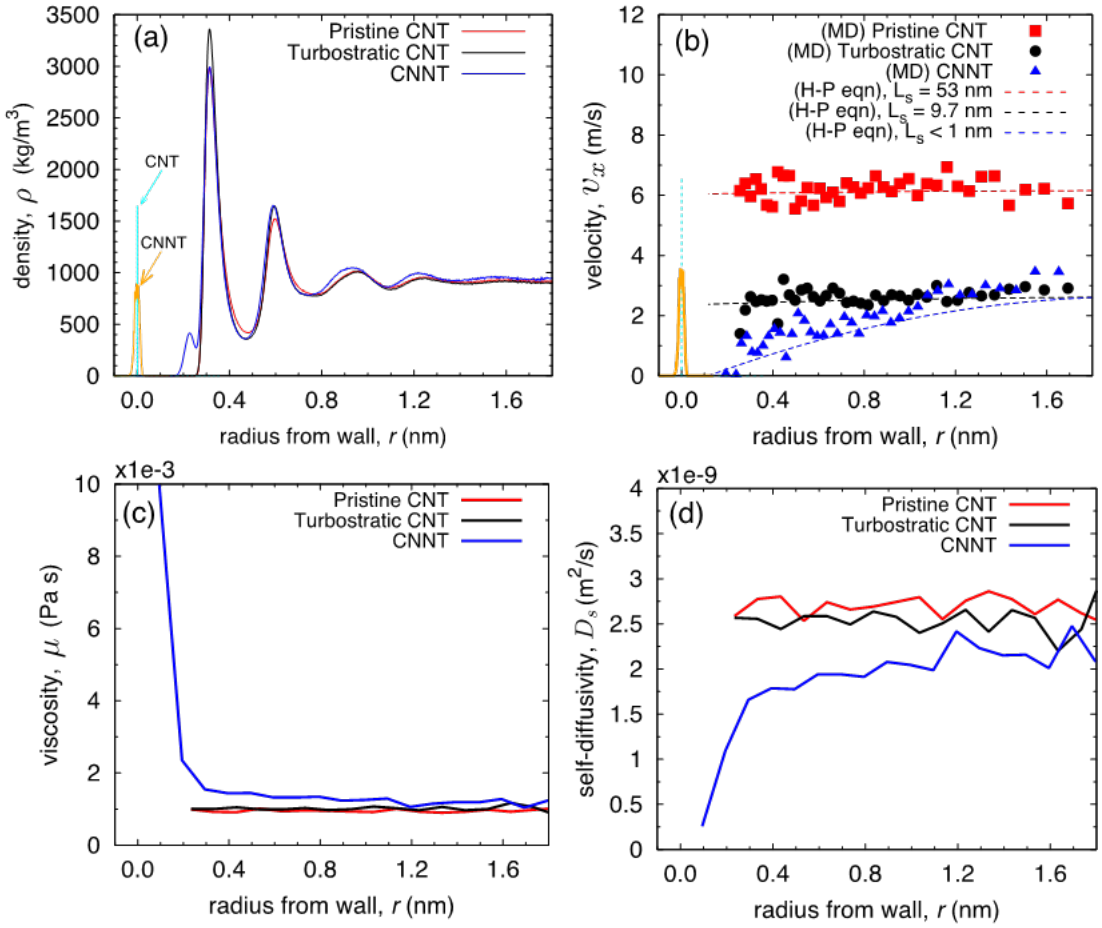

Figure 5-12: Radial profile measurements from the MD simulations of nanotube diameter $D = 4.071$ nm for (a) density, (b) velocity, (c) viscosity and (d) self-diffusivity, inside pristine CNTs (red), turbostratic CNTs, (black) and CNNTs (blue). The CNT and CNNT wall surfaces are indicated in cyan and orange, respectively, at $r = 0$, for visualisation purposes only; their density magnitudes have been scaled down to fit in the graph. In (a) oxygen atoms are only considered; similar results are obtained for the hydrogen atoms in the water molecule. In (b) comparisons are made with the Hagen-Poiseuille (H-P) flow Eq.5.3 using dashed lines; applied pressure gradients in the MD are 1.15 × 1014 Pa/m, 2.35 × 1014 Pa/m and, 1.32 × 1014 Pa/m for the pristine CNT, turbostratic CNT and CNNT, respectively.

Although the results clearly show that tube surface chemistry and structure do affect permeance, quantifying these effects is necessary to learn how to tailor the tubes' structure and chemistry for specific transport applications.

The potential energy between the surface and the fluid is an obvious quantity to achieve this goal, as it can be directly obtained from the MD data. However, the challenge is that while CNTs have just one interatomic potential between solid and water, with CNNTs there are now two potentials (oxygen-carbon and oxygen-nitrogen) to consider, making it difficult to decouple the effect of each component. The authors have previously proposed a model to interpret the effect of solid-liquid interactions on flow which uses the concept of work of adhesion W_A, defined as the amount of work needed to detach the liquid from the solid and create two new interfaces [286]. This quantity allows measuring the overall attraction, inclusive of both surface structuring (i.e. physical roughness) and chemistry (i.e. energy roughness). The values for W_A, which have been obtained from the MD simulations in this work as a sum of potential energy over a unit area, are reported in Table 5.2. Values for pristine and turbostratic CNTs are in good agreement with experimental data previously reported [47], giving further confidence about the value calculated here for CNNTs. Results in Table 5.2 clearly show an increase in the work of adhesion from pristine to turbostratic CNTs to CNNTs, in an inverse trend to contact angle. As $W_A = \pi_e + \gamma(1 + cos\theta)$ [286], this is not surprising. It should be noted, however, that the film pressure term, π_e, can be comparable in value to the surface tension for some materials including carbon [286], and, hence, cannot be ignored [47]. Therefore, the work of adhesion can effectively link the properties of the tubes' wall to permeance of a fluid through it. This is a superior approach to using the contact angle for the same purpose as, in fact, there is no contact angle in a tube full of liquid (as the third and necessary phase – air – is missing). In Table 5.2, the values for the slip length, L_s, calculated from MD are also reported. Similarly to the work of adhesion values, those obtained for the pristine and turbostratic CNTs are in agreement with literature values of 98×10^{-3} and 144×10^{-3} J m^{-2}, respectively [47, 30]. Green-Kubo measurements for surface viscosity and surface diffusion coefficients can be found in the Supplementary Information.

Table 5.2: Measured experimental and molecular dynamics data; Left: contact angles measured experimentally; Right: MD measurements for work of adhesion, slip length and the ratio of surface-diffusivity to work of adhesion.

Material	Contact angle (°)	Reference	W_A ($\mathrm{Jm^{-2}}$)	L_S (nm)	D_S/W_A ($\mathrm{m^3m^{-2}s^{-1}Pa^{-1}}$)
Graphitic CNTs	82-86	[238]	105×10^{-3}	53	2.5×10^{-8}
Turbostratic CNTs	61-90	[18]	137×10^{-3}	9.7	1.9×10^{-8}
CNNTs	43-67	this work	175×10^{-3}	< 1	$(0.2\text{-}1.0) \times 10^{-8}$

By comparing the values for W_A and L_S, a similar inverse relationship is observed, with the more hydrophilic materials, i.e. those having the strongest interaction with water, resulting in the smallest slip length. All of these results point to a relationship between the nanotube wall physico-chemical material properties, the strength of the interaction between the tube wall and the liquid flowing through it, the hydrodynamics of the flow, i.e. the slip length, L_S, and the permeance, K. The authors have previously proposed a model linking all of these properties [47], which can be summarised in the two equations below:

$$\epsilon = 1 + \frac{8L_S}{D} = \frac{K_{exp}}{K_{HP}}, \tag{5.4}$$

$$K_{exp} \approx \phi \frac{D_S}{W_A}, \tag{5.5}$$

where K_{HP} is the no-slip permeance (derived from Eq. 5.1 when L_S=0), K_{exp} is the permeance calculated from experimental data, and D_S is the surface diffusion arising from the chemical potential gradient present in pressure-driven flow. Eq. 5.5 is derived from first principles by replacing the Hagen-Poiseuille term and an expression linking L_S to D_S/W_A [47]. The last column in Table 5.2 reports the value for the D_S/W_A term obtained from MD data for the three materials investigated and Figure 5-9 shows how Eq.5.5 well compares with the experimental data for the CNNTs. A similar good agreement has already been shown with experimental data for turbostratic CNT membranes [18], and with MD simulations of SiCNT and BNNT nanotubes [30]. Here, the approach of the model in Eq.5.5 is further validated, representing a direct relation between permeance and solid-liquid interactions for a membrane of fixed porosity and nanotube material. This model can therefore be used to the design of aligned nanotube membranes that are tailored for specific applications, by controlling the transport of selected liquids using chemistry and structural changes inside the nanotubes.

5.3 Conclusions

Carbon nitride nanotubes were deposited in anodic alumina membranes using a non-catalytic CVD synthesis method and the type of C-N bonds formed were fully characterized. Pure water permeance measurements through CNNT membranes were compared to results obtained for CNTs in previous experimental work, which similarly used an AAM support with uniform and parallel nanopores, and with MD simulations. The latter were conducted on nanotube models built as a true reproduction of the structure of the synthesised materials, using the information gathered by their characterisation and wettability. This approach goes beyond traditional MD simulations conducted on perfect nanotubes (e.g. pristine CNTs). Both experiments and MD simulations showed that the presence of the C-N bonds hydrophilises the sp2 carbon structure of the nanotubes, resulting in a decrease of the pure water permeance compared to pristine and turbostratic carbon nanotube membranes. These results are explained in terms of the strength of the solid-liquid interactions occurring at the tubes' walls, with the water at the CNNT walls showing increased water viscosity and decreased surface diffusion compared to CNTs. The combination of experiments and MD simulations presented here has allowed, for the first time, to decouple the effect of nanotube wall structure and surface chemistry on the flow of water through a nanotube membrane. The model and results presented in this paper offer membrane scientists a unique capability to design novel membranes and separation processes by way of controlling the permeance within nanotube membranes through membrane surface chemistry and structural changes to the nanotubes.

Supplementary Information

The Supplementary Information contain detailed supporting results for this Chapter 5. A repository with the complete research data for this article can be found online [283].

Table 5.3: Measurements of Green-Kubo measurements for surface viscosity (μ_S) and surface diffusion coefficients ($D_{S,S}$). Bulk values for viscosity and self-diffusion coefficient are μ_B = 1.00 10^{-3} Pa s and $D_{S,S}$ = 2.34E-09 m^2s^{-1}, respectively.

Material	Inner tube diameter (nm)	μ_s/μ_b (-)	$D_{S,S}/D_{S,B}$ (-)
Graphitic CNTs	4.068	0.97	0.1.13
Turbostratic CNTs	4.068	1.01	1.09
CNNTs	4.068	1.55-10	0.7-0.1

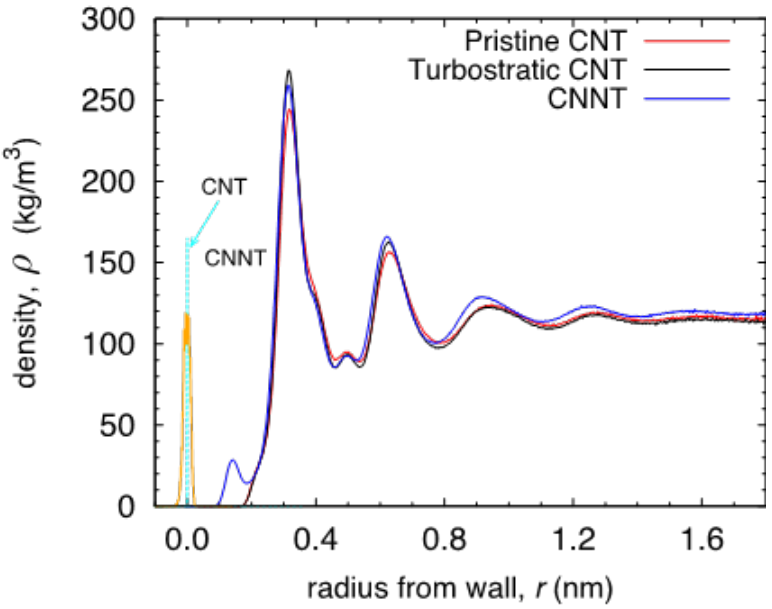

Figure 5-13: Radial density profiles for the hydrogen atoms measured from MD simulations for all three types of nanotubes considered in this work.

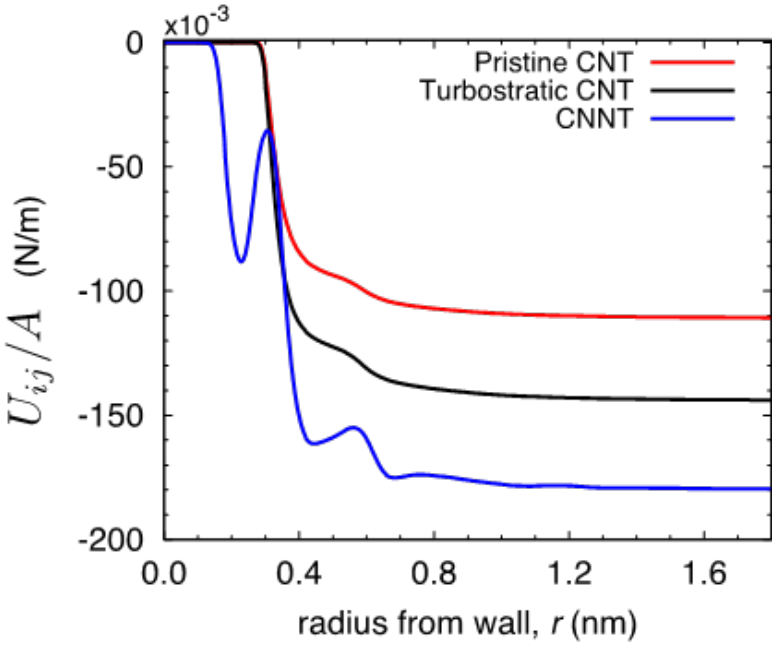

Figure 5-14: Potential energy per unit wetted area between all wall atoms (i) and all water atoms (j) as a function of radius for the three types of nanotubes considered in this work. The work of adhesion is obtained from the maximum peak at $r = 0.7$ nm (distance taken from the wall). Note, it is convention in MD that a negative value in potential energy indicates an attractive energy; we remove the minus sign from the work of adhesion to avoid confusion.

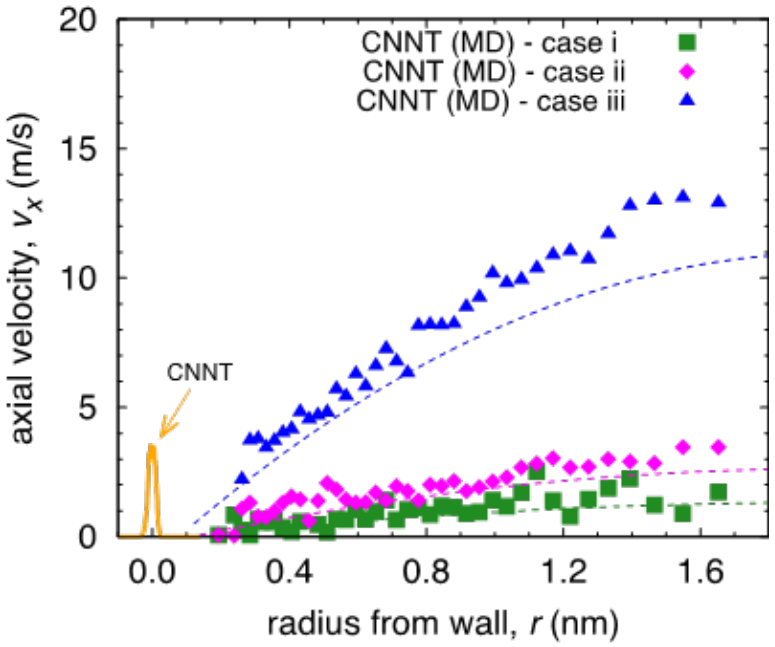

Figure 5-15: Steady velocity profiles measured from the MD simulations of water flow inside a CNNT of diameter $D = 4.068$ nm, for different pressure gradients. Symbols indicated MD results, dashed lines indicate predictions using the Hagen-Poiseuille flow equation.

Chapter 6

Enhanced Nanoparticle Rejection in Aligned Boron Nitride Nanotube Membranes

S. Casanova, S. Mistry, S. Mazinani, M. K. Borg, Y. M. J. Chew and D. Mattia

This declaration concerns the article entitled: Enhanced Nanoparticle Rejection in Aligned Boron Nitride Nanotube Membranes	
Satus	In Review
Publication details	-
Candidate's contributions to the paper (detailed, and also given as a percentage)	The candidate contributed to/ considerably contributed to/ executed the ... • *Formulation of Ideas* The initial idea was formulated by SC and DM based on preliminary observations conducted by DM. 80% • *Design of Methodology* The experimental work and data analysis was conducted by SC with supervision from DM and YMJC. 90% • *Molecular Dynamics* MKB and SM are the authors of the MD simulations presented in this paper.SM is the author of the CFD simulations. SC heavily contributed to the set-up of the MD and CFD models. 20% • *Presentation of Data in Journal Format* The first draft was written by SC with contribution from all authors. Subsequent drafts were reworked by all authors. 70%
Statement from candidate	This paper reports on original research I conducted during the period of my Higher Degree by Research Candidature.
Signed	, 23/12/2019

6.1 Introduction

Membrane filters capable of rejecting charged particles between 0.5 - 50 nm are crucial to a broad number of industrial applications, ranging from ion removal in wastewater treatment [287], to catalyst retrieval in heterogeneous reactions [288] to product recovery in biotech processes [289]. In commercial membranes, however, higher rejection is often associated with reduced water permeation [3], stimulating research in novel materials that could provide both. Carbon nanotubes (CNTs) showed promise, with high particle rejection [60] and high pure water flux [28, 29], leading to significant efforts towards developing membranes made of carbon nanotubes [6]. However, in CNTs, rejection is solely based on the relative size of a particle compared to the nanotubes' diameter [55], due to the neutral surface charge of the tubes. This necessitates the use of very narrow tubes to reject small ions, dyes and particles [57]. As a result, the amount of water that can flow through these nanotubes is limited, as flux scales with the square of a tube's diameter. Attempts to functionalise the tubes' entrance to improve rejection have been successful [57, 60], but at the cost of reducing water transport by 20-30% [61]. Molecular dynamics (MD) simulations have shown that depending on the functional groups used, the decrease in flux could be as high as 80% [57], thereby negating the very advantage of CNTs, i.e. their high flux. This aspect, coupled with significant challenges with scaling-up the manufacturing of CNT membranes [29, 28], has induced researchers to focus efforts on different materials types and structures to develop innovative membranes for separation applications [3].

Among these, boron nitride nanotubes (BNNTs) have shown significant promise, due to their high chemical stability, improved biocompatibility and thermal resistance [30, 73]. Boron nitride is iso-structural to graphitic carbon with a similar water contact angle [18, 270]. MD simulations of pure water flows in sub-nanometre BNNTs and CNTs showed larger enhancement for the former compared to the latter [13, 33]. However, this superior performance was not observed in experiments through individual tubes which reported significantly slower water flow in larger BNNTs (diameters ranging from 14 to 46 nm), compared to CNTs [14]. A potential explanation for this discrepancy is that in sub-nanometre tubes alone, the energy barriers for water transport at the entrance of and through the tubes are lower for BNNTs than CNTs [33], hence, the diffusion of water through the BN tubes is faster than CNTs [30]. This is the due to the different electrical landscapes between BN and graphitic carbon, with the electrons in the outer shell of the BN (insulating) material not contributing to quasi-frictionless transport as it is in the case of the carbon surface (semiconducting) [40]. This difference is reflected

in different water-nanotube wall interactions [30], which can be used to explain how water flows in nanotube membranes [30]. In terms of rejection, there is yet no molecular dynamics nor experimental evidence of BNNTs performance [33].

Here we show that boron nitride nanotubes can have the same particle rejection using a larger nanotube diameter than a CNT, thereby enabling 45% higher permeance and no requirement for surface functionalization. We report the fabrication of novel membranes of aligned boron nitride nanotubes and found that they reject negatively charged silica nanoparticles, with x 2.5 times higher rejection than positively charged hematite nanoparticles for the same nanotube diameter, with no reduction in permeance.

Our results provide the first experimental evidence of charged particle rejection in BNNTs. We anticipate our results will facilitate the design of more effective nanotube membranes, capable of high particle rejection and, at the same time, high water permeance, leading to significant reductions in the capital and operating costs of membrane filtration plants. Furthermore, our results are of direct relevance to the emerging area of 2D membranes, where both graphene and boron nitride nanosheets have been tested for ion and particle rejection for water purification [290, 30].

6.1.1 BNNT and CNT membrane fabrication and characterisation

CNTs and BNNTs were deposited in the pores of anodic alumina membranes (AAMs) by non-catalytic CVD as outlined in Figure 6-1a. While this process is well-known for CNTs [18], it has been demonstrated here for the first time for BNNTs via the decomposition of borazane at high temperature, previously used for deposition of planar BN on Cu [239] and Pt foils [158].

The membrane surface was left clean and with open pores after synthesis (Figure 6-1b) while the macrostructure changed colour from transparent to alabaster for BNNTs and black for CNTs. Individual nanotubes could be clearly seen protruding from the cracked surface of a membrane after CVD (Figure 6-1c). The water contact angle for the two materials was measured on an alumina support coated with BN and C, under the same deposition conditions for the respective nanotubes, and was 78 $\pm$ 2 $^{\circ}$ for both materials (Figure 6-1a), in agreement with literature [270, 18, 30]. The water contact angle for the initial alumina was 21 $\pm$ 2 $^{\circ}$. Computed Young contact angles are reported in the Supplementary Material.

High resolution XPS spectra revealed a B:N stoichiometry of 1.2 with the characteristic BN peak at 398.3 eV for N and 190.7 eV for B (Figure 6-1d) [291]. This value is close

to the theoretical B:N value of 1, with similar deviations observed in the literature for different synthesis methods, due to the presence of defects in the nanotubes produced experimentally [291]. BN was also directly observed on the AAMs via electron energy loss spectroscopy (EELS) (Figure 6-1b inset), with the boron and nitrogen K edges appearing near 200 and 400 eV, respectively [116]. The FTIR peak (Figure 1e) for the BN in-plane bond was identified on the produced BNNT membranes at 1375 cm^{-1}[292]. Additional peaks around 2000-2500 cm^{-1} in these spectra are associated to the background. Raman spectra were recorded on both sides of the support membranes after deposition showed the characteristic BN peaks at 1369 cm^{-1} in all the locations investigated (Figure 6-1f).

The surface zeta potential was close to zero for the bare AAMs, due to the absence of surface charged groups after thermal annealing (Figure 6-1g) [293]. For the CNT membranes, the value was -8.5 mV, due to residual functional groups arising from the non-catalytic CVD synthesis method [18], despite the use of post-synthesis hydrogen annealing [238] - which reduced the value from 20.8 mV. For the BNNT membranes, the surface zeta potential was -34.7 mV at pH 6, in excellent agreement with literature values (-34 $\pm$ 4 mV) on few layered BN [292]. The surface zeta potential as a function of pH for the 3 nanotube materials is reported in Figure 6-1g.

6.1.2 Permeance and rejection in BNNTs and CNTs membranes

Before performing permeance and rejection tests, the amount of silica and hematite adsorbed on the AAMs, CNTs-AAMs and BNNT-AAMs was determined. Silica presents low adsorption i.e. below 7% on all three membrane. For hematite, however, adsorption on BNNTs was as high as 22%, implying that some of the apparent rejection observed is to be ascribed to adsorption.

Pure water permeance tests (Figure 6-2a, b) show that the CNTs modestly outperform ($\sim$ 1.8x) BNNTs, with the difference between the CNTs and BNNTs membranes being comparable to what was previously observed for flow in single carbon and boron nitride nanotubes [14]. This difference is smaller than what we computed via MD, where the permeance of pristine CNTs is 3.3 times bigger than that in pristine BNNTs. The discrepancy is attributed to the synthesis method used here, non-catalytic CVD in the pores of AAMs, which results in nanotubes with a certain amount of defects [18], which, in turn, depresses permeance [274].

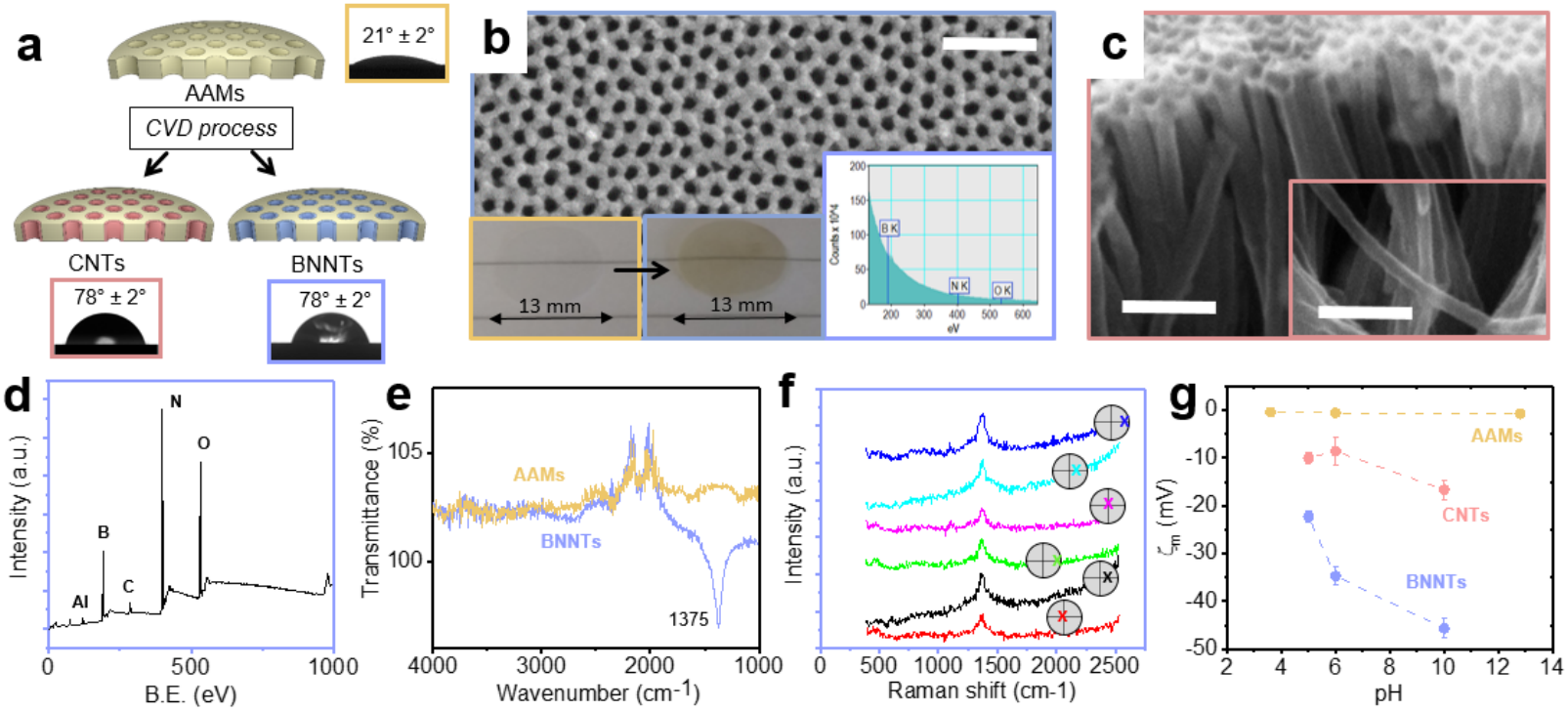

Figure 6-1: (a) Schematic of the deposition of CNTs and BNNTs in AAMs, with the insets containing an optical micrograph of a water droplet and associated contact angle for each material. (b) FESEM micrograph, photo of membrane before and after BN deposition (inset) and EELS of the BNNT membrane. (c) Individual nanotubes released from a cracked membrane after CVD. The scalebars in the FESEM micrographs are 200 nm. (d) XPS and (e) FTIR spectra of BNNTs. (f) Raman analysis of the BNNT membrane top and bottom surface at different locations on the sample. This is indicated by coloured crosses on the top (pink, light blue and blue) and bottom (red, black and light green) of the membrane. (g) Surface zeta potential (ζ_m) reported as a function of the tracer suspension pH for the 3 membrane materials.

The presence of defects in the BNNTs was confirmed by the oxidised BN species in the XPS spectrum (Supplementary Information), which generate a large charge on the surface when in contact with water [294].

BNNTs have higher rejection of negatively charged silica than bare AAMs and CNTs (Figure 6-2a) for average diameters of the nanoparticle (D_{NP}) smaller than the pore diameter (D_P) in the range $0.8 < D_{\mathrm{NP}}/D_P < 1$. In fact, AAMs and CNTs show appreciable rejections only when the particle diameter D_{NP} is larger than tube diameter D_P, whereas high rejection (up to $\sim 70\%$) is observed in BNNTs also when the particle is smaller than the tubes, $D_{\mathrm{NP}} \leq D_P$ (Figure 6-2a). This difference is not as marked for the positively charged hematite particles in Figure 6-2b, though rejection is still higher for BNNTs. In this case, the difference could also be due to adsorption as previously discussed. Improved rejection in BNNTs translates in the ability to notably increase permeance K, proportional to D_P^2, for set values of rejection (Figure 6-2c). Here, the effect on K is higher for lower rejection values, as this translates to the range $0.8 < D_{\mathrm{NP}}/D_P < 1$, where the enhanced particle rejection is observable.

Molecular dynamics and computational fluid dynamics (CFD) were employed to model the experimental phenomena with a theoretical model accounting for the main forces acting on the particle [51]. Details of both simulations, along with the force model used, are provided in the supporting information. In the MD simulations, negative-charged nanoparticles were released near the entrance of pores of BNNT and CNT membranes. Figure 6-2d shows that the dynamics of the nanoparticle for $D_{\mathrm{NP}}/D_P \sim 0.9$ at 20 bar pressure drop are very different between BNNT and CNT membranes. In the CNT, the particle approaches the pore and remains trapped at the centre of the pore entrance under the same applied pressure, whereas in the BNNT, the negative partial charges between pore and particle repels the nanoparticle away from the pore.

The pressure loss at the entrance of the membrane increases when the particle is partially blocking the entrance of the pore, which can be elucidated from the response of the mass flow rate in the MD simulations. At low applied pressures, there is a lower impact by the particle on the flow rate through the BNNT (e.g. -13% mass flow rate at 20 bar) than there is through the CNT (-40%), as seen in Figure 6-2e. At higher pressure drops ($\gtrsim$40 bar), however, the pressure force is large enough to also trap the particle near the BNNT pore, although with higher constrained dynamics. As such, the impact on flow rate becomes the same for both nanotube membrane materials for larger pressures.

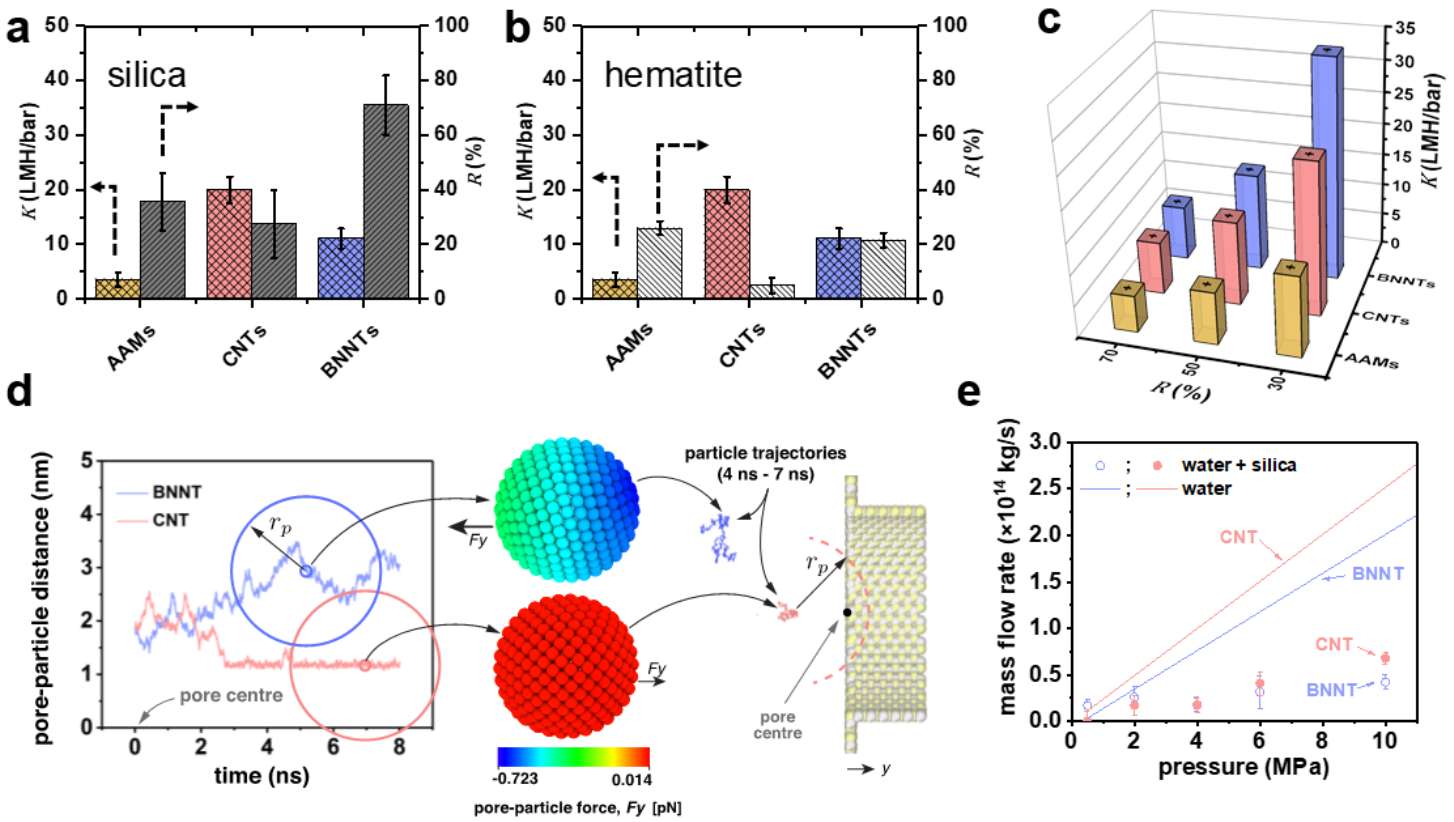

Figure 6-2: Experimental permeance K and rejection R for (a) negatively charged silica and (b) positively charged hematite nanoparticles are reported for particles with size smaller or equal to the diameter of the tubes ($D_{\mathrm{NP}} \leq D_P$). Full information on the particles and nanotubes, including sizes, can be found in the Supplementary Information. (c) 3D plot showing the calculated permeance of AAMs, CNTs and BNNTs membranes for set rejection percentages. (d) Pore-particle distance measured in MD simulations over time, with the size of the same simulated silica particle indicated by the coloured circles for CNTs and BNNTs. A repulsive pore-particle force acts on the particle introduced in the BNNT system, whilst weaker van der Waals forces attract the particle to the neutrally charged CNT. As a result, silica particles enter the CNT but are repelled from the BNNT, as shown by their particle trajectories plotted for the time interval 4ns – 7ns. (e) MD mass flow rate measurements through CNT and BNNT pores for $D_{\mathrm{NP}}/D_P \sim 0.9$, with varying pressure. Benchmark cases are simulations without particles. At lower pressures, flow rates through BNNT are less impacted, due to particles located further away from the pore than in the case of the CNT.

For CFD, particles were introduced from the top of the domain and particle tracing equations were solved via a time dependent solver using small time steps of 10^{-7} s, resulting in very small particle displacement but very high computational expense. Consequently, only one particle was introduced at the inlet. Figure 6-3a shows the trajectory of a negatively charged silica nanoparticle on the feed side of a BNNT (blue line) and of a CNT (red line) in presence of the forces (Brownian, drag and electrostatic) found in a cross-flow filtration apparatus such as the one used here, with an external pressure of 5 bar. The silica particle quickly reaches the CNT pore entrance and enters the tube, while it remained in the bulk of the feed for the BNNTs membrane, as observed in both MD simulations (Figure 6-2d) and experiments (Figure 6-2a).

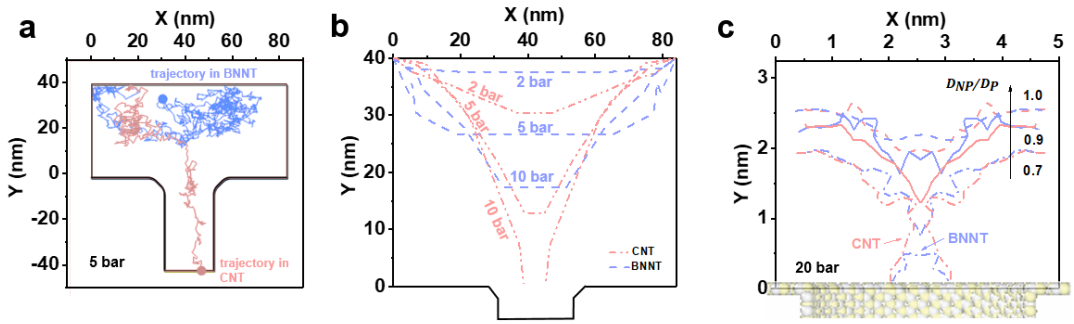

Figure 6-3: CFD trajectories after 10^{-4} s for particle tracing at 5 bar for applied electrostatic (F_{EL}), drag (F_D) and Brownian (F_B) forces. The silica nanoparticles enters the CNT and reaches its outlet, while the BNNT completely rejects it. (b) CFD isoforce lines for $F_D = F_{\mathrm{EL}}$ in the 2D domain for BNNTs and CNTs for different values of pressure, with $F_B = 0$. **(c)** MD isoforce lines for BNNTs and CNTs of same pressure but different values of D_{NP}/D_P.

The Brownian force was modelled as a Gaussian white noise process [51] and its direction is constantly changing. By taking out the randomness of Brownian force, whether a particle enters a tube or not, is the result of a balance between drag and electrostatic forces: $\Delta F = F_D - F_{\mathrm{EL}}$. The drag force is directly related to the externally applied pressure, whereas the electrostatic force is a function of the charge structure of the particles, the tubes and the electrolyte they are in contact with. Using the above force balance, it is possible to identify external pressure thresholds at which rejection would occur in the BNNT and CNT membranes. Figure 6-3b shows isoforce lines in a 2D geometry for which $\Delta F = 0$, where the particle effectively halts in the simulation in absence of Brownian forces. The pressure domain can be divided in three zones based on the particle behaviour when it reaches the pore entrance, in the absence of Brownian forces: one, below 6.6 bar, where both CNTs and BNNTs are able to reject the silica particle. A second zone between 6.6 bar and 29 bar where only BNNTs allow for the

rejection of the particle due to their higher electrostatic repulsion, and a final zone where no rejection occurs. In our experiments and in the CFD simulation in Figure 3a, we could also observe improved rejection for pressures below 6.6 bar for the BNNTs due of the presence of Brownian forces, which, as suggested by both MD and CFD, tend to draw the nanoparticles back in the bulk.

In the MD, the iso-force lines are measured directly from surface-particle and water-particle intermolecular forces. Figure 6-3c shows that when the nanoparticle/pore ratio D_{NP}/D_P is reduced below 1.0 at a fixed pressure of 20 bar, the particle always prefers being closer to the CNT entrance than to the BNNT, indicating the BNNT is more likely to reject particles than the CNT. At around $D_{\mathrm{NP}}/D_P \sim 0.6$-$0.7$ there is evidence of full particle passage through both membranes, which agrees well with observations in our experiments.

6.2 Conclusions

We have shown that the choice of boron nitride nanotubes over carbon nanotubes for the filtration of negatively charged nanoparticles results in a 45% higher permeance for the same rejection. Computational studies showed that this is due to charge-based rejection, enabled by the charged structured of the BNNTs as opposed to the neutrally charged CNTs. Both experiments and simulation show that BNNTs with size 21.2 $\pm$ 3.7 nm can reject nanoparticles down to 0.7 times smaller than their internal diameter and up to an external pressure of 6.6 bar. Thus, boron nitride nanotubes with larger diameters can be chosen to achieve similar rejection to carbon nanotubes, opening the way to significantly increasing the performance of commercial membranes in a variety of applications, from water treatment to bioprocessing.

6.3 Methods

6.3.1 Experimental

Boron nitride nanotubes were deposited via CVD in symmetric AAMs in a quartz holder located in the centre of a tube furnace. Firstly, the temperature was ramped up to 1000 °C under 150 sccm Ar flow. Borazane was sublimated at 80-100 °C and the synthesis was carried out for 40 min under a 15:135 sccm H_2:Ar flow. For the synthesis of CNTs membranes [18], AAMs were pre-annealed with a 1 °C/min ramp, up to 900

°C and then brought to 670 °C, when the feed was changed to ethylene and argon (CH_4:Ar 36:84 v/v%) for 4 hours. The membranes were then cured at 800 °C for 2 hours under a 50 sccm flow of H_2 [238]. Standard microscopy and spectroscopy were employed for the material characterisation. Surface zeta potential was analysed with a Malvern Zetasizer. The rejection was tested in tangential flow mode and assessed with UV-vis.

6.3.2 Molecular Dynamics

The LAMMPS [252] MD software was used to simulate pressure-driven flows of water containing a negative-charged particle through BNNT and CNT membranes. The MD setups consisted of solvent and permeate reservoirs filled with water, with a piston applied to each reservoir to control local pressure and pressure drop across the membrane. To obtain MD results as close to the experiments as possible, calibration studies of intermolecular potentials between water and BNNT were performed to match experimental contact angles [257]. Partial charges on BN atoms were calibrated using the ReaxFF force field [256], setting an experimental surface charge density of -1.28x10^{-20} C nm^{-2} for BNNT and -6.99x10^{-21} C nm^{-2} for the silica particles. The effective hydrated diameter D_{NP} of the particles was chosen to be smaller than the nanotube diameter D_P, such that $0.7 < D_{\mathrm{NP}}/D_P < 1$, in analogy to experimental data, and pressure drops varying between 5 and 1000 bar. Measurements were conducted for particle trajectories, particle-water force, particle-surface force and membrane mass flow rates.

Computational Fluid Dynamics

A system of equations describing the forces acting on single particles was solved using a commercial CFD software COMSOL MultiphysicsTM v5.4 in a two-dimensional domain in proximity to the entrance of a single pore for BNNTs and CNTs. Particle tracing was used in each simulation to track single particles (D_{NP}/D_P=0.85) subjected to combined drag, electrostatic and Brownian forces [51] for 0.0001 s. Further simulations that omitted Brownian forces with four particles were conducted for the same time step, to draw the isoforce $F_{\mathrm{EL}} = F_D$ lines.

Supplementary Information

This section contains detailed supporting results for this chapter. A repository with the complete research data for this article can be found online [295].

6.3.3 Particles Characterisation

Key parameters characterising the nanoparticles used in this work are reported in Table 6.1. TEM micrographs are collected in Figure 6-4 and Figure 6-5. These particles were chosen for the rejection tests because of sizes bigger and smaller than the membranes pore were chosen.

Table 6.1: Size, pH, colloids zeta potential (ζ_c) and ionic strength (I) of the nanoparticles used in this work. The particle diameter (D_{NP}) is computed form statistical analysis of TEM micrographs in Figure 6-4 and Figure 6-5.

Nanoparticle	Supplier	D_{NP} (nm)	pH	ζ_c (mV)	I (mol L^{-1})
S1	Sigma Aldrich	9.2 ± 1.8	9.2	- 12.7 ± 0.6	2.18×10^{-2}
S2	Sigma Aldrich	14.7 ± 1.8	8.6	- 27.4 ± 1.9	2.18×10^{-2}
S3	Fisher Scientific	19.2 ± 2.6	5.5	- 18.5 ± 1.9	2.18×10^{-2}
S4	Sigma Aldrich	27.1 ± 3.2	8.8	- 37.6 ± 4.1	2.18×10^{-2}
H1	BASF	15.8 ± 2.2	4.9	8.6 ± 1.5	6.30×10^{-6}
H2	BASF	17.2 ± 2.2	5.3	3.8 ± 1.6	2.51×10^{-6}
H3	Sigma Aldrich	37.3 ± 4.2	6.0	19.9 ± 0.2	5.05×10^{-7}

Nanotube membranes are always backflushed in between rejection tests, so that the membrane is cleaned from particle residuals as shown in Figure 6-6.

UV-Vis is used to link the light absorbance of nanoparticles to their concentration in a water suspension (Figure 6-7).

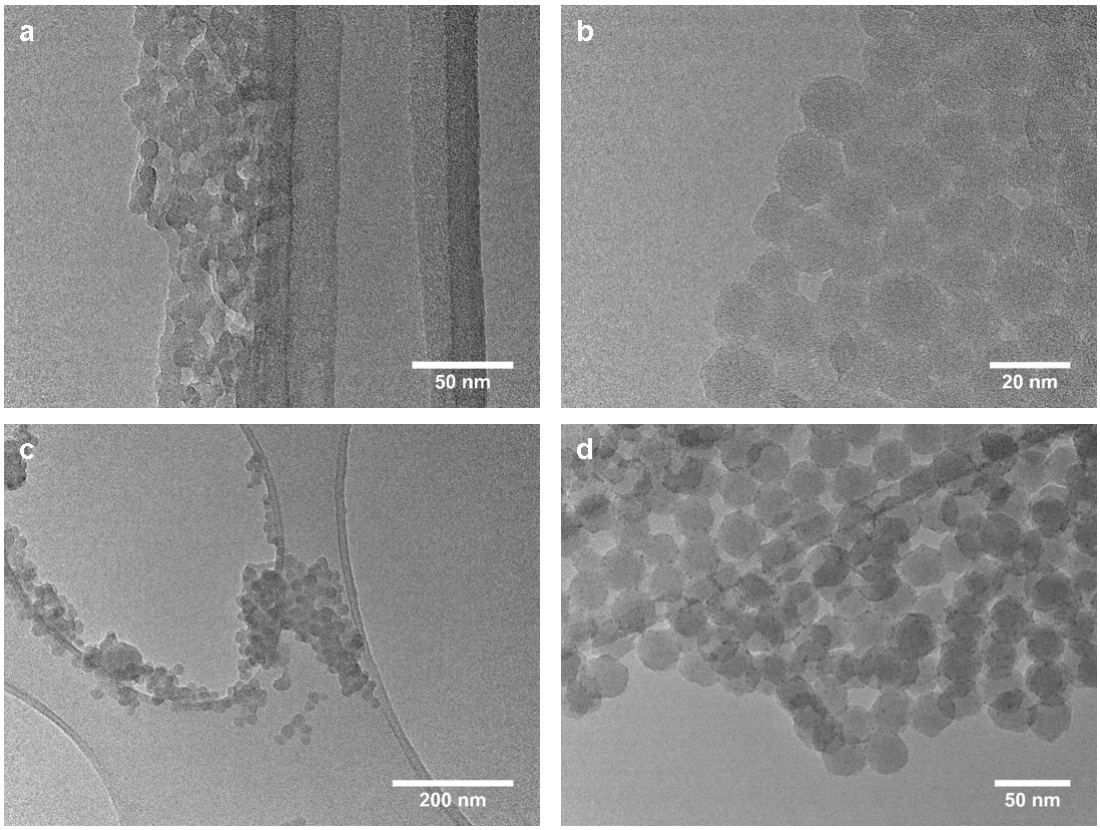

Figure 6-4: TEM micrographs of silica nanoparticles on Lacey carbon (a) S1, (b) S2, (c) S3 and (d) S4.

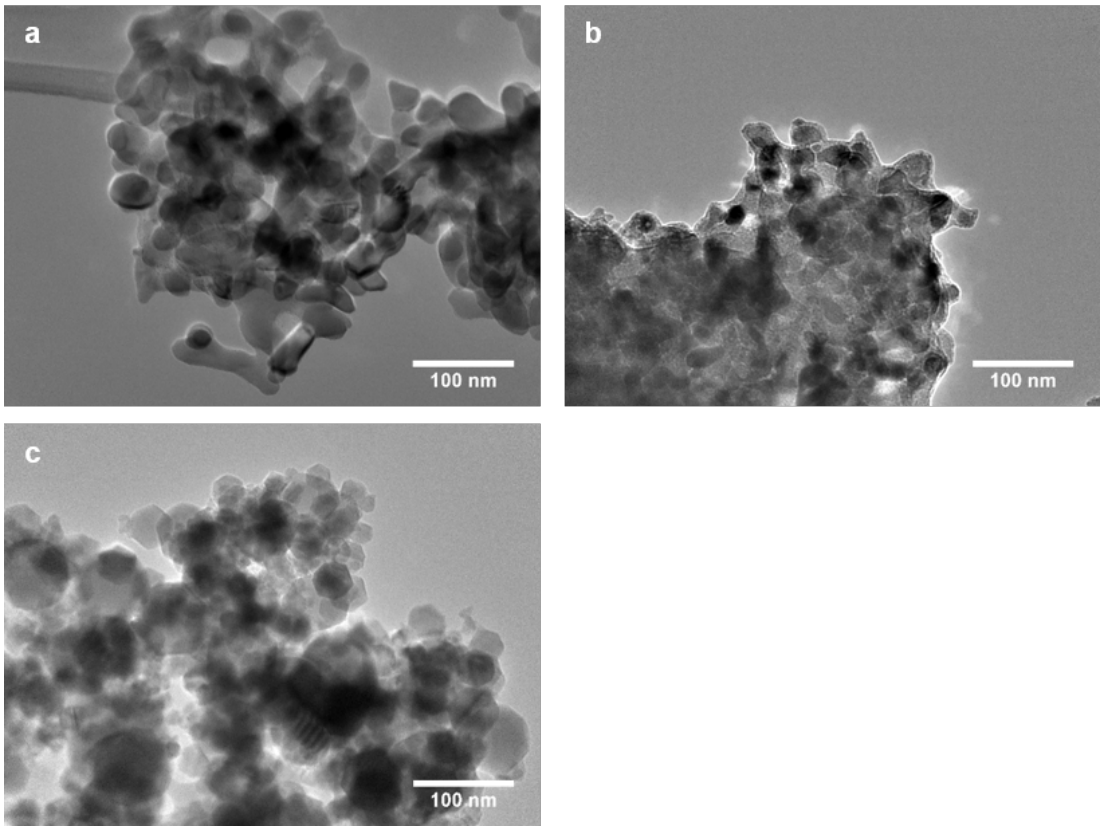

Figure 6-5: TEM micrographs of hematite nanoparticles on Lacey carbon (a) H1, (b) H2 and (e) H3.

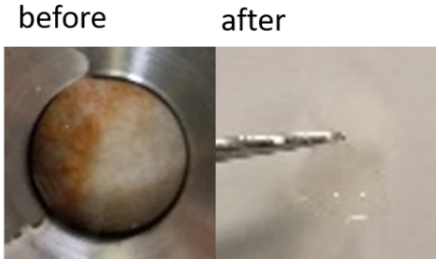

Figure 6-6: Image of the membrane before and after backflushing.

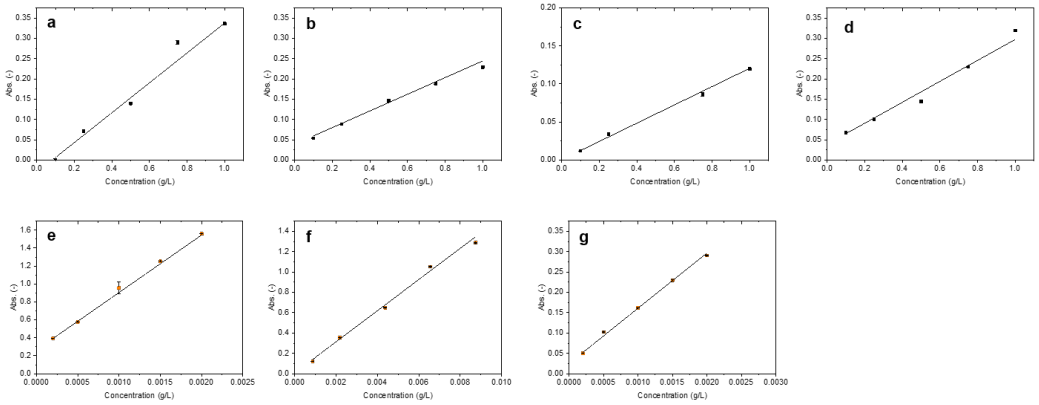

Figure 6-7: UV-vis calibration curves for (a) S1, (b) S2, (c) S3, (d) S4, (e) H1, (f) H2 and (g) H3. The acquisition time for each data point is 0.1 sec, and 3 repeats are performed for each concentration. Error bars are given as standard deviation from the average for each data point.

6.3.4 Membranes Characterisation

FESEMs of the BNNT-AAMs showed a clean surface with open pores after synthesis (Figure 6-8a), and EDX scans revealed the uniform deposition of B and N on the AAM (Figure 6-8b). The deposition of BN on Al_2O_3 is reported in these scans with atomic ratios around 50% higher than the theoretical value (B/N atomic ratio of 1).

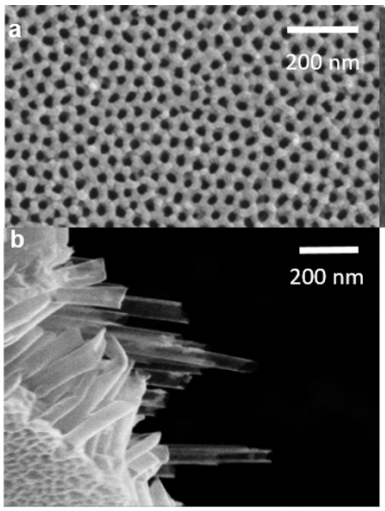

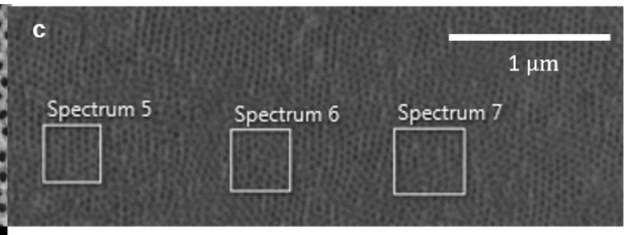

d

	Spectrum 5	Spectrum 6	Spectrum 7
Al (weight %)	47.6	45.6	45.0
O (weight %)	36.4	36.0	36.1
B (weight %)	7.9	8.3	8.6
N (weight %)	6.3	7.3	7.5
B:N atomic ratio	1.62	1.47	1.48

Figure 6-8: (a) FESEM of the surface of a BNNT-AAMs after synthesis and (b) nanotubes released from a cracked CNTs membrane. (c) EDX spectrum of an area on the membrane's surface, with (d) some examples spectra results showing a 1.62 (Spectrum 5), 1.47 (Spectrum 6) and 1.48 (Spectrum 7) B:N atomic ratio (details in Table 6.2).

After synthesis, the membranes changed colour slightly (Figure 6-9a-b), while retaining the open pore structure (Figure 6-8a). Since the synthesis happens in a reducing environment due to the presence of hydrogen gas, it is not advisable to choose alumina templates containing residual oxalic groups from the anodization process [23], as this might result in carbon impurities retained as carbonate or carboxyl groups after synthesis.

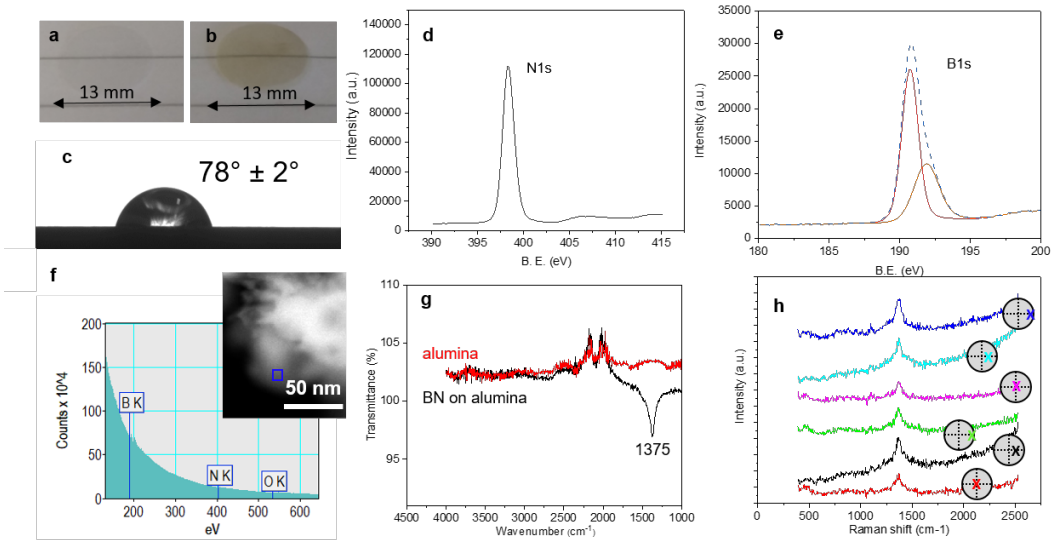

Figure 6-9: Picture of (a) bare AAM and (b) BNNT-AAM, (c) contact angle on BN-coated solid alumina disk, (d) N XPS spectrum, (e) B XPS spectrum, (f) EELS, (g) FTIR of BNNT-AAM, and (h) Raman analysis of the membrane top and bottom surface at different locations on the sample. This is indicated by coloured crosses on the top (pink, light blue and blue) and bottom (red, black and light green) of the membrane and detailed in Figure 6-13.

The contact angle measured (Figure 6-9c) on a BN-coated flat alumina support (Figure 6-9a) was 78° and the calculated Young contact angle using the Wenzel formula 80°, in good agreement with what found by molecular dynamics simulations [270]. The measured contact angle of water on dense alumina discs was 21° (Figure 6-10) in agreement with literature [296, 269]. When the roughness of the substrate was accounted for, the obtained Young contact angle was 41°.

High resolution XPS spectra revealed a B:N stoichiometry of 1.2 with the characteristic BN peak at 398.3 eV for N (Figure 6-9d) and 190.7 eV for B (Figure 6-9e) [291]. The 1.2 B:N ratio obtained with XPS is considered more reliable as B and N are close to the detection limit of EDX, thereby reducing the overall accuracy of the results obtained

with this technique. The XPS scan also identified a significant portion (14 atomic % of the analysed sample) of B at 192 eV, which can be associated to the presence of BN_YO_X species [297].

Table 6.2: XPS atomic percentage analysis and B: N atomic ratio on 7 different spots on the same membrane sample.

	B	**N**	**O**	**F**	**Na**	**Al**	**Si**	**S**	**Total**	**B:N**
Spectrum 1	14.51	9.04	41.8	2.12	0.16	32.07	0.29	0	100	1.61
Spectrum 2	14.49	9.12	42.03	2.42	0.2	31.1	0.4	0.23	100	1.59
Spectrum 3	15.57	9.2	41.84	2.36	0.17	30.2	0.34	0.31	100	1.69
Spectrum 5	13.74	8.5	42.89	1.03	0.13	33.27	0.44	0	100	1.62
Spectrum 6	14.4	9.78	41.99	1.45	0.17	31.52	0.48	0.21	100	1.47
Spectrum 7	14.71	9.95	41.99	1.44	0.14	31.01	0.55	0.21	100	1.48

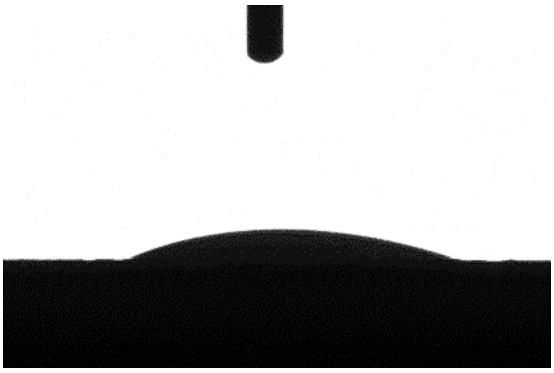

Figure 6-10: Uncoated alumina surfaces present a much more hydrophilic nature than BN-coated discs [296, 298].

BN on AAM was observed by EELS (Figure 6-9f, region indicated with a blue rectangle), showing the boron and nitrogen K edges near 200 eV and 400 eV respectively (Figure 6-9e). The FTIR peak for the BN in-plane bond was identified on the produced BNNT membranes at 1375 cm^{-1} (Figure 6-9g) [154]. Additional peaks around 2000-2500 cm^{-1} in these spectra are associated to the alumina support and machine background (Figure 6-12).

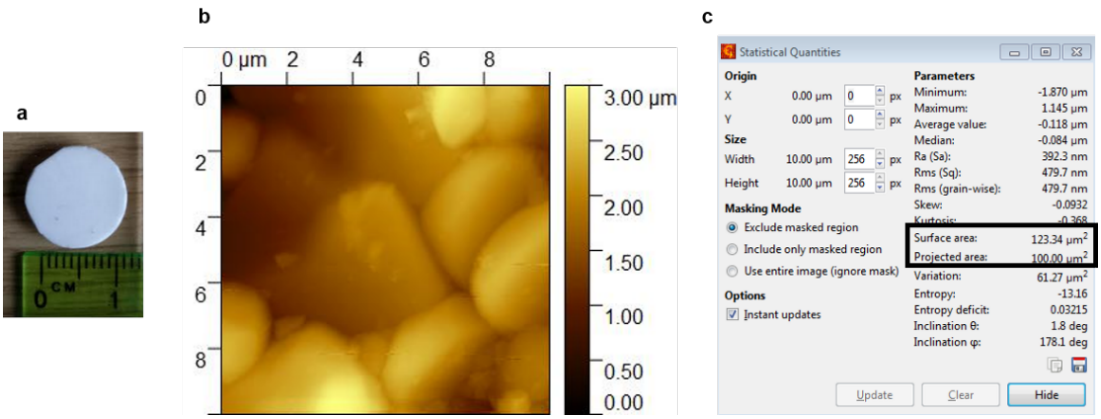

Figure 6-11: Alumina substrate used for BN contact angle measurements, (b) AFM used for roughness determination and correspondent (c) statistical analysis output showing the quantities used for the determination of the parameter r in Eq. 4.2.

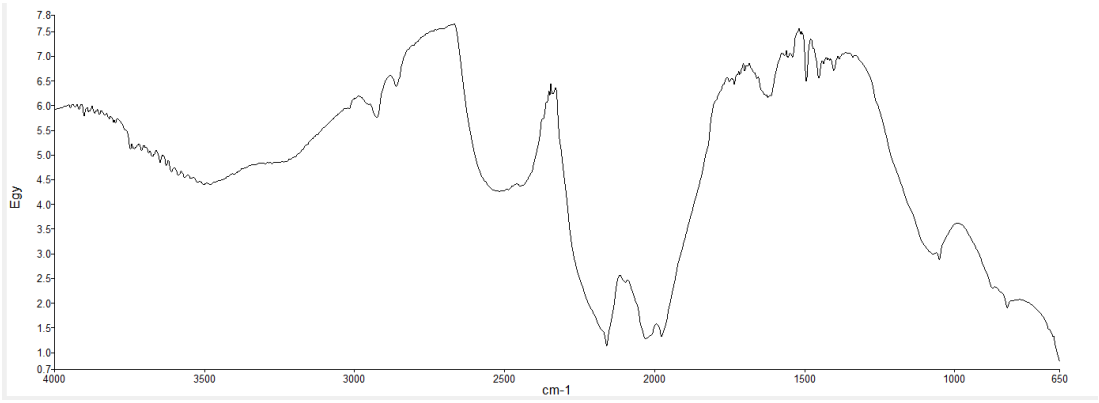

Figure 6-12: FTIR machine background.

Raman was used to confirm the deposition of boron nitride on both sides of the alumina membrane. Spectra were acquired on the top and bottom surface of a BNNT membrane, showing characteristic BN peaks at 1369 cm^{-1} in all the locations investigated (Figure 6-13). In fact, the gas flow at the centre of the furnace is laminar (Re ~1), and passage of the synthesis precursors across the pores is the only possible explanation for the uniform presence of BN on the membrane side facing the outlet of the reactor.

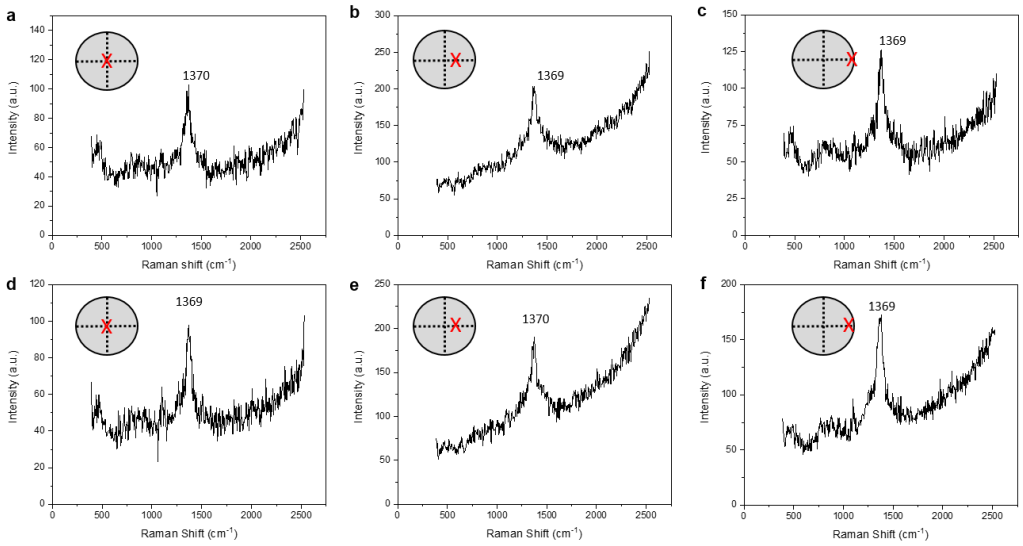

Figure 6-13: Raman spectra at different location on the (a, b, c) top and (d, e, f) bottom of the BN coated alumina membrane. The power used for these maps is 7.5 x 10^{-4} W.

The tracer used for the zeta potential analysis was tested in the absence of the membrane surface. For instance, at pH 6 it was found to have a zeta potential of -22.8 ± 0.8 mV (phase plot in Figure 6-15), leading to the calculation of a surface zeta potential of -34.7 ± 1.8 mV for BNNT-AAMs in agreement with literature values (-34 ± 4 mV) on few layered BN [292]. The zeta potential was very close to zero for the thermally treated, bare AAMs and this was associated to the absence of surface charged groups after annealing [293]. ζ_m as a function of pH is reported in Figure 6-1g. It can be noticed that BNNTs membranes maintain their negative charge over a wide range of pH solutions.

Characterisation results for Young contact angle computed with the Wenzel equation (Eq. 4.2), r values, zeta potential (ζ_m) at pH 6, average porosity (ϕ) and inner tube diameter D_P for the membranes under analysis are summarised in Table 6.3.

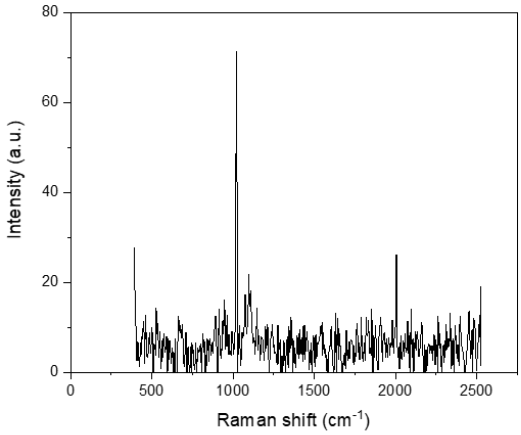

Figure 6-14: Raman blank spectrum (i.e. without sample) that was subtracted to the spectra presented in this work.

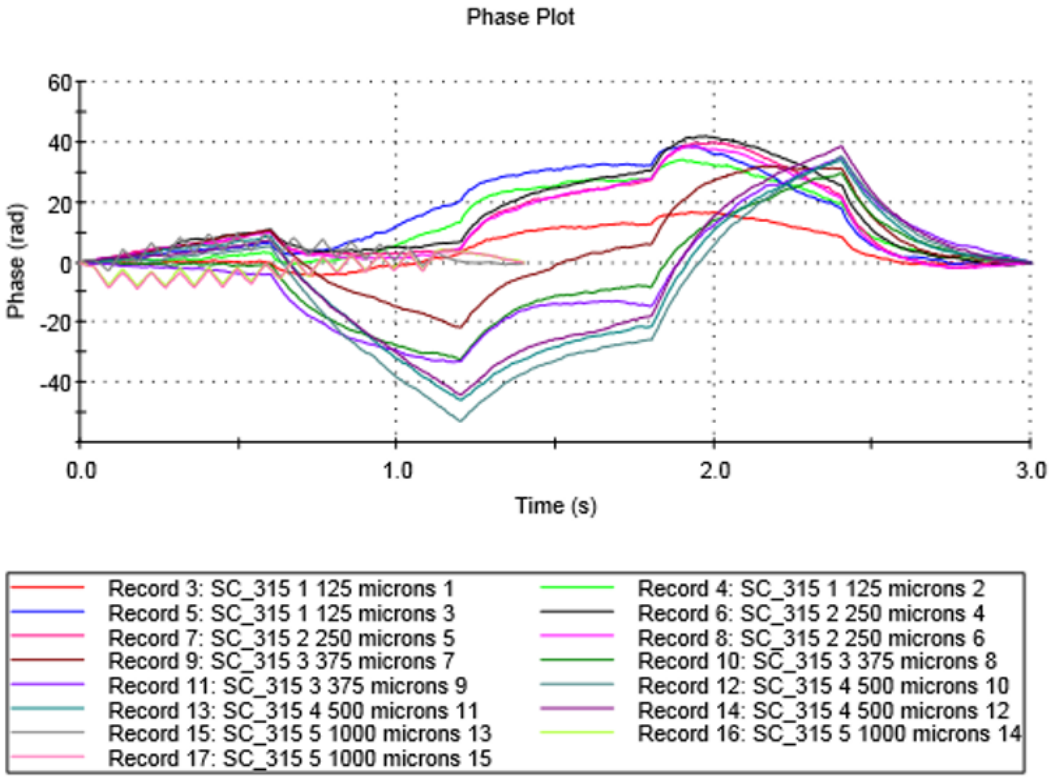

Figure 6-15: Phase plot for the analysis of ζ_m at different displacements from the analysed BN-AAM surface at pH 6.

Table 6.3: Physico-chemical average parameters for tested membranes and static adsorption tests results for the adsorption percentage ranges of silica (A_{silica} (%)) and hematite (A_{hematite} (%)) on AAMs, cured CNTs and BNNTs. Adsorption on sealing silicone gaskets is also investigated, and gives a range 0-8% for silica and 0-5% for hematite.

	θ		**r**	**Ra**	$\zeta_{\mathbf{m}}$	**A**		ϕ	$\mathbf{D_P}$	**K**	**R**
	W	Y				silica	hematite				
	deg ± 2°		-	nm	mV	%		-	nm	LMH/bar	%
AAMs	41	21			-0.6 ± 0.2	0-7	0-5	0.16	18 ± 3	7.5	35.6
CNTs	80	78	1.23	392	-8.55 ± 2.9	0	0-4	0.13	22.6 ± 4.4	19.6	27.5
BNNTs	80	78			-34.7 ± 1.8	0-6	0-22	0.14	21.2 ± 3.7	9.0	71.0

Static adsorption tests were performed to assess the degree of adsorption of silica and hematite on ANTs, CNTs and BNNT. As shown in Table 6.3, silica presents a similar adsorption degree on all membranes, with a reduced adsorption on carbon. However, the maximum degree of adsorption value of hematite on BN- coated alumina resulted 17% higher than on alumina and 16% bigger than on carbon.

6.3.5 Experimental Membrane Performance

Pure water tests are performed at different transmembrane pressures, as reported in [295]. In the ceramic membranes studied deformation of the matrix does not take place during testing [2]. Water viscosities are reported in [295] at the average experimental temperature for each membrane tested. Enhanced flow in nanotubes has classically been quantified in terms of flow enhancement ϵ, reported for the analysed membranes. This is defined as the ratio of the observed flow through a nanotube-based membrane system and the expected flow computable from the Hagen Poiseuille equation $q = \frac{\pi D^4 \Delta \mathrm{P}}{128\ \mu L}$, where ΔP is the transmembrane pressure, μ is the fluid viscosity at operating temperature, and q is the volume flow rate through one nanotube of diameter D and length L. BNNTs synthesized in this work present, flow enhancement factors ε in the range 0.2-4.0, while values reported for CNTs synthesized with a similar CVD method are in the range 1.1-9.8. Extrapolating values on flow enhancement from Secchi's experimental work on flow in BNNTs [14], leads to values around 1, which is comparable but slightly below to the findings of this work. The fact that some of the enhancement factors for BNNTs membranes were found to be less than one can be associated to possible membrane pore blocking, which would effectively render the membrane porosity value used in the Hagen Poiseuille equation different from the

one observed on the surface and therefore impact the flow enhancement factor. This drawback resulting from the fact that the flow through anodic alumina is averaged over millions of nanopores.

The source of error on the calculation of the average diameter in Figure 6-16 is given by the measured nanotube size distribution, which in turn depends on the alumina template pore size distribution and FESEM resolution. Results for membranes that suffered obvious cracks during handling are not reported in this work, but pinholes or non-evident pore clogging could be the source of errors in permeance recorded during the measurements.

The pure water permeance in BNNTs membranes ranged from ∼3 LMH/bar for the smallest pore size to ∼25 LMH/bar for the biggest pore size (Figure 6-16), values comparable to those of commercial membranes [18].

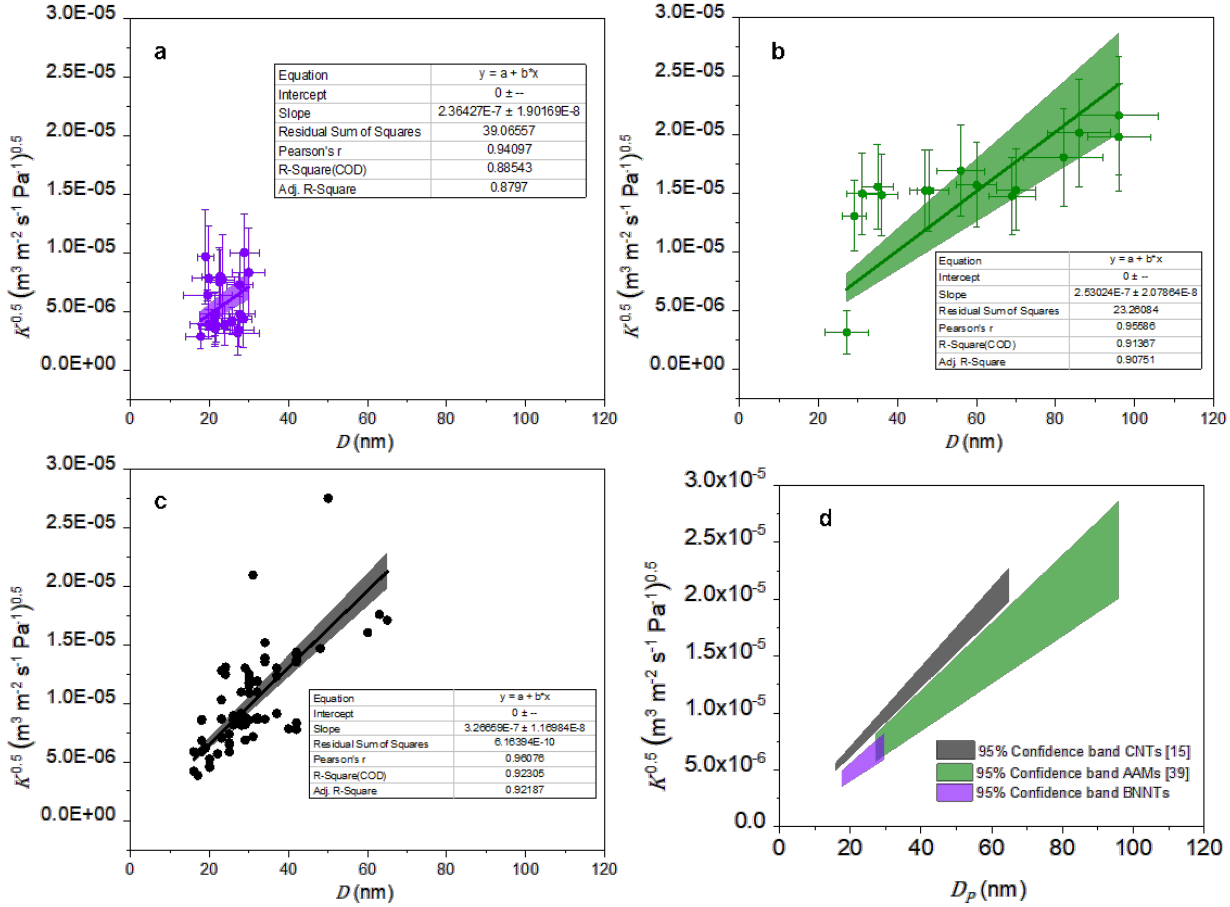

Figure 6-16: Linear fitting regressions for (a) BNNTs in this work, (b) AAMs [269] and (c) CNTs [18]. The inset tables report Pearson's r (a measure the strength of linear relationship between paired data), R^2 (a statistical measure of the linear regression) and Adj. R^2 (a modified version of R^2, adjusted for the number of predictor in the fitted line). Permeance 95 % confidence bands of regression on a set of BNNT-AAMs with D_P ranging from 17.8 to 28.9 nm are presented with the associated measurement error, and compared to the linear fitting of literature data for bare alumina [269] and CNTs [18] membrane. The dataset used to prepare these graphs can be found at [295].

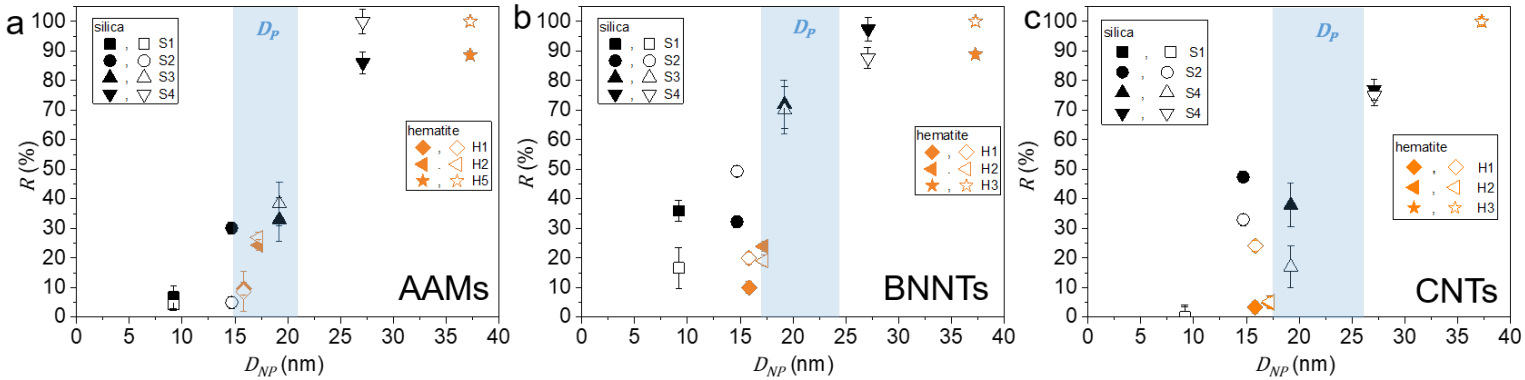

Figure 6-17: Rejection R reported as a function of the diameter of the particle tested D_{NP} on **(a)** two AAMs membranes (av. pore diameter 18 ± 3 nm for both); **(b)** two BNNT membranes (av. pore diameter 22.2 ± 2.2 nm in the first test (filled symbols, black for silica and orange for hematite) and 20.2 ± 2.9 nm in the second test (empty symbols, black for silica and orange for hematite) and **(c)** two CNTs membranes (av. pore diameter 21.1 ± 3.6 nm in the first test (filled symbols, black for silica and orange for hematite) and 24.1 ± 2.3 nm in the second test (empty symbols, black for silica and orange for hematite). The average pore diameter (D_P) is indicated by a blue band on the graph.

6.3.6 MD Simulation

The measurement of mass flow rate represents a way of probing the loss in pressure created by the impeding particle at the pore entrance. The flow rate was estimated by considering the total number of water molecules in the left and right reservoirs of Figure 4-10 and fitting a straight line through their variation with time, as shown in Figure 6-18 a and b for BNNT and CNT, respectively.

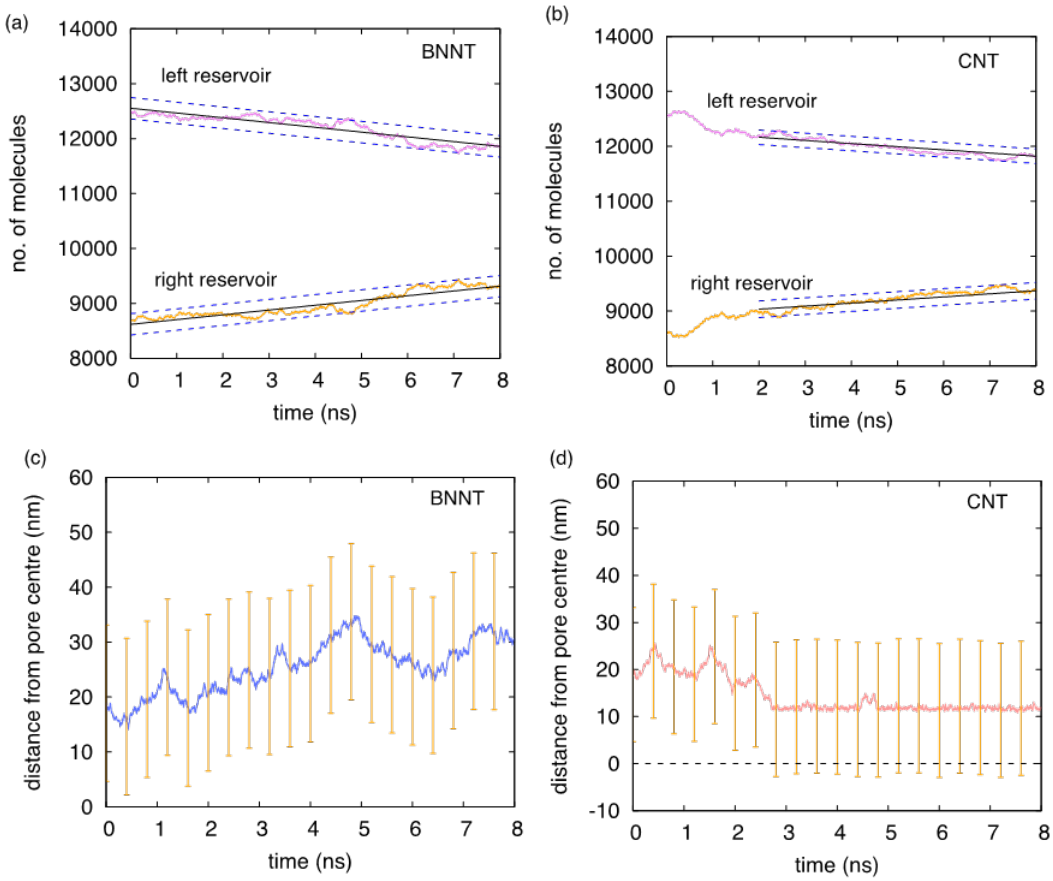

Figure 6-18: (a), (b) Number of molecules in the left and right reservoir as a function of time leads to the mass flow rate measurement; (c) (d) magnitude distance of particle from pore centre. In the top figures, black solid lines indicate fit through data, from which flow rate is the gradient of this line multiplied by the mass of one water molecule, while blue dotted lines indicate the uncertainty in the prediction. In the bottom figures, yellow vertical lines indicate the diameter of the particle (28.5 nm).

Figure 6-19 shows the flow rate with increasing pressure for three D_{NP}/D_P ratios. We also compare the results with benchmark cases, which are similar simulations, but which not include the particle. In these benchmark cases, we similarly measure flow

rate for increasing pressure and fit a line of best fit of the form $\Delta p = R\,\dot{m}$, where R is the gradient. For unimpeded particle flow, the CNT enables more water transport than the BNNT, which is understood due to the lower nanotube friction and slip length. For the pristine CNT, the measured slip length is 50 nm, while for the pristine BNNT the slip length is 13 nm. In previous work we found that defects decrease the slip length substantially, so we expect these values to be a maximum and larger than those seen in experiments [257, 274]. Given the length of the tubes in the experiments, we expect the pressure loss over the membrane to be dominant in the tube [257], so it is possible to predict the flow through the tube using the Hagen Poiseuille flow equation with slip, with slip lengths as mentioned above.

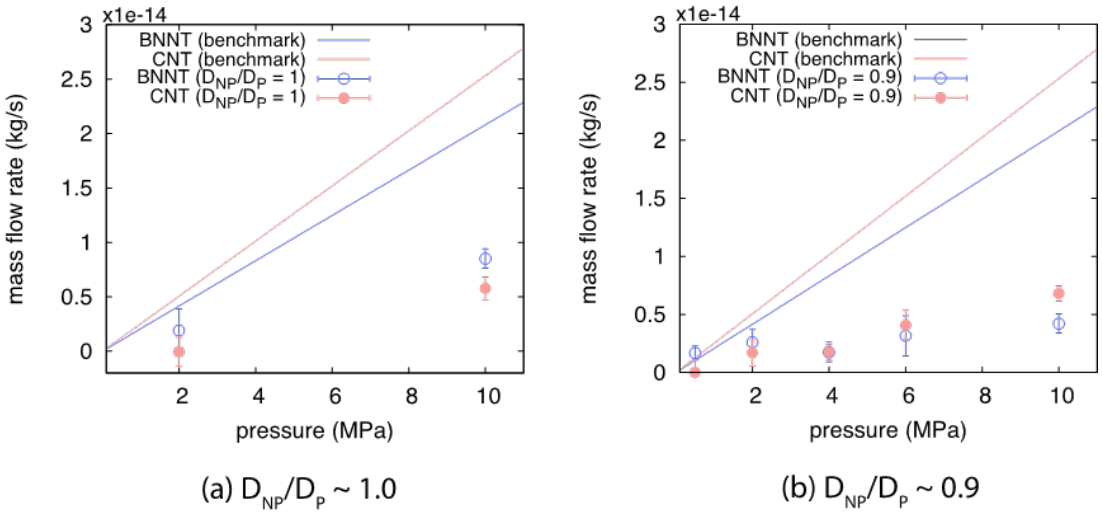

Figure 6-19: Mass flow rates against pressure drop for BNNT and CNT cases, and two D_{NP}/D_P ratios (a) 1.0 and (b) 0.9.

As expected, for the particle-impeded flow the transport is seen to drop below the benchmark for all cases because the particle blocks the mouth of the pore. We find that the drop in flow rate for the BNNT seems to be lower than that for the CNT. For example, for $D_{NP}/D_P \sim 0.9$ at pressure drop of 2 MPa, the drop in the flow rate is 13% for the BNNT and 40% for CNT, and at 6 MPa, the drop is 40% for BNNT and 70% for CNT. The reason for this difference in performance between BNNT and CNT lies in the positioning of the particle. In the BNNT, the particle is pushed further away from the pore due to the stronger interatomic charges, as we show in Figure 6-19d of the main paper. Figure 6-20 shows that below ~ 4 MPa, the particle ($D_{NP}/D_P \sim 0.9$) near the BNNT is still mobile, and has the tendency of moving back into the reservoir. For the CNT, the retreat of the particle back into the bulk is observed at lower pressures (i.e. < 2 MPa). Above 4 MPa of pressure, Figure 6-20 shows both particles are lodged

at the same distance away from the pore, and this is reflected in the further drop in flow rate by the BNNT. This observation lays the case for using BNNT surfaces for water filtration at pressures lower than 4 MPa; they are more likely to repel particles for this particle diameter ratio of $D_{NP}/D_P \sim 0.9$.

Evidence of differences in particle mobility are also measured using the Mean Squared Displacement [299], as shown in Figure 6-21. For the low pressures (Figure 6-21a), the particle near the BNNT is more mobile than the CNT. For larger pressures (Figure 6-21b), the BNNT however is more constrained at the pore, which we think is due to the larger repulsion in the surface-particle forces.

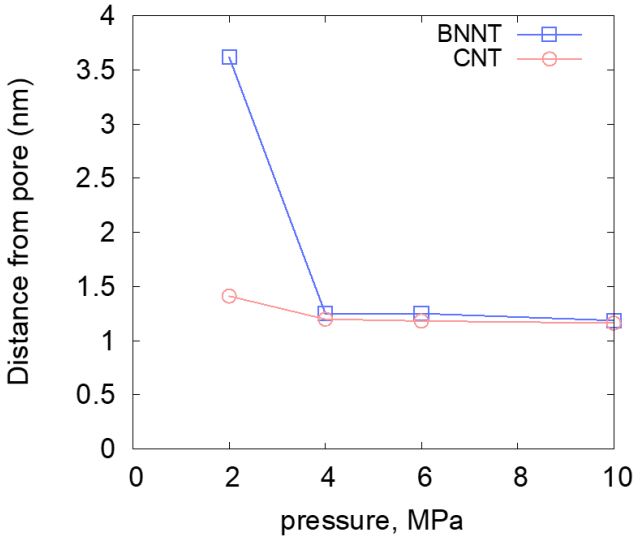

Figure 6-20: Distance between pore and particle against applied pressure for BNNT/CNT; $D_{NP}/D_P = 0.9$.

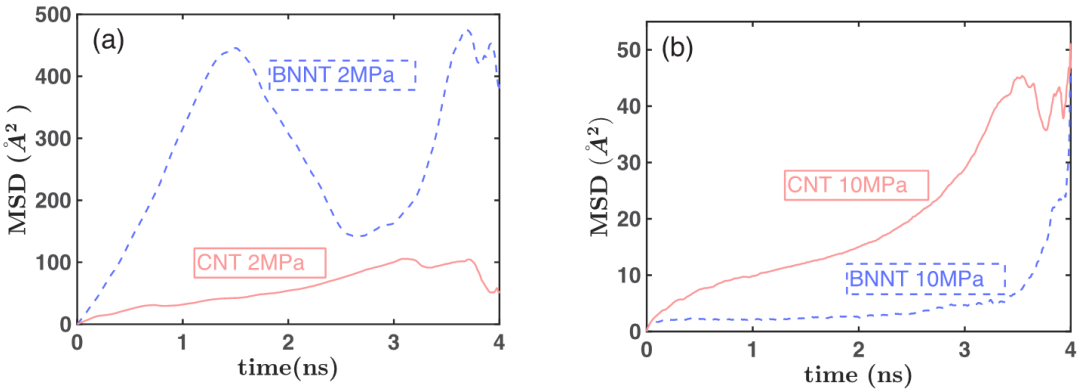

Figure 6-21: MSD plots for D_{NP}/D_P ~0.9 for (a) 2MPa and (b) 10MPa.

In order to investigate the equilibrium position of particles near the mouth of the BNNT

and CNT membranes, and therefore get an idea of probability of selection, we conduct a second independent set of MD simulations. Here the particles are displaced radially and axially to the pore at small increments; at each position the particle is frozen, and a pressure drop simulation of 20 bar was applied. In all cases, flow was allowed to reach a steady state around the fixed particle, before measurements are taken. We then determine the force balance on the particle due to intermolecular interactions between particle-membrane and particle-water.

The individual force contributions on the particle from the water and the wall atoms were calculated by switching off the unwanted interactions and recalculating the forces based on the position data. We measured the *particle-water* forces Δf_P and the *particle-surface* forces Δf_C. In our particle simulations we find that the particle-surface force has low noise (which makes sense), while particle-water forces has large thermal noise, indicating the dominant Brownian force component. We have produced graphs of distribution of the water-particles forces and have found the mean force (Figure 6-22). We compared these to the particle-surface forces. The particle-water forces are normally distributed, while the particle-surface force has a near constant value. When a particle is at a pore, and there is a steady flow, the mean of the forces balance out to almost zero. This is expected.

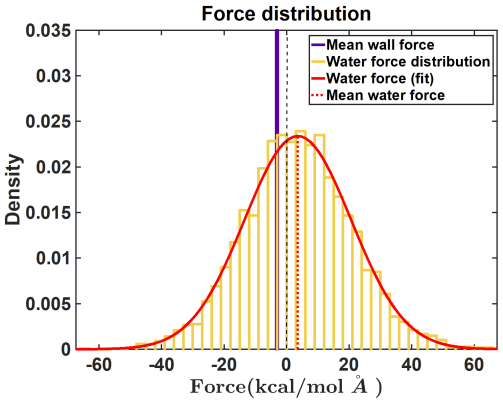

Figure 6-22: Distribution of forces on nanoparticle for D_{NP}/D_P ~0.9, BNNT membrane.

To produce contour plots of $\Delta f = \Delta f_C - \Delta f_P = 0$ vs D_{NP}/D_P (Figure 6-23), we ran simulations with the particles at fixed locations, and measure particle-water and particle-surface charges at those locations. This allows us to build a contour plot for Δf. The particle-liquid force which we measure is equal to $d\Delta f_P$. The negative value of df indicates repulsion from the pore, while a positive value indicates attraction.

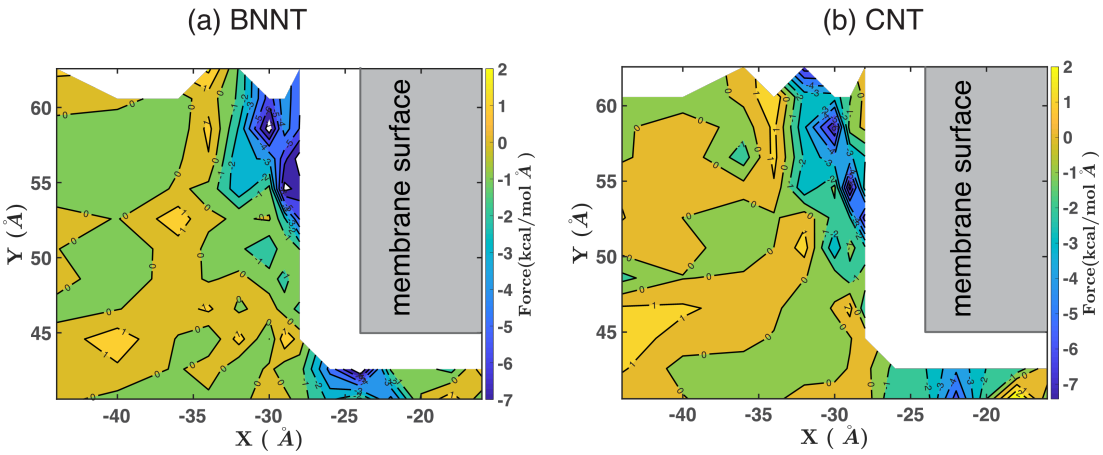

Figure 6-23: Contour plots for Δf for $D_{NP}/D_P \sim 0.9$, Δp = 20 bar: (a) BNNT and (b) CNT; The membrane surface has been displaced by the particle radius (14.2 nm) in these figures for better clarity.

The plots for Δf = 0 (Figure 6-24), extracted from the contour plots for Δf show that while smaller D_{NP}/D_P experience zero force at almost similar locations, this is not true for the larger values of D_{NP}/D_P, where the BNNT pushes the particle further away from the pore due to surface charges. This transition happens about $D_{NP}/D_P \sim 0.8$. This is due to the increasing contribution of the electrostatic repulsion as the particle size increases, creating a difference between the forces experienced due to the charge carrying BNNT surface and the uncharged CNT surface.

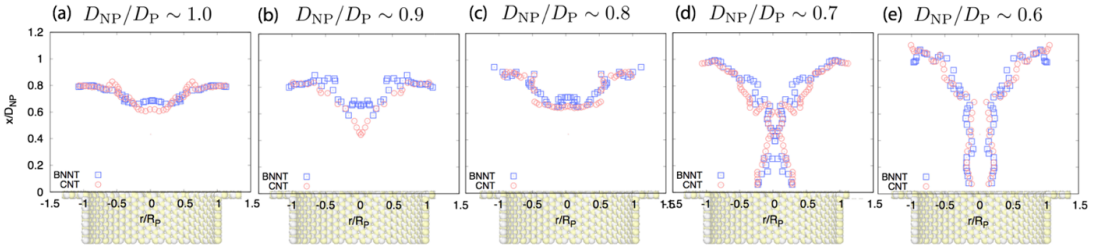

Figure 6-24: Iso-force graphs for BNNT/CNT membranes with particle/pore diameter ratios $0.6 < D_{NP}/D_P < 1$ and applied pressure drop Δp = 20 bar.

Chapter 7

Water Flow Enhancement in Polymer Nanotube Membranes

Z. Meng, S. Casanova, H. Mohamed, N. Kapil, X. Xiao, Y. Zhang, M. Coppens and D. Mattia

This declaration concerns the article entitled: Water Flow Enhancement in Polymer Nanotube Membranes	
Satus	Draft Manuscript
Publication details	-
Candidate's contributions to the paper (detailed, and also given as a percentage)	The candidate contributed to/ considerably contributed to/ executed the ... • *Formulation of Ideas* The initial idea was formulated by SC, JM, HM, MC and DM based on preliminary observations conducted by DM. 80% • *Design of Methodology* The experimental work and data analysis was conducted by JM, HM and SC with supervision from DM, MC and YMJC. 50% • *Presentation of Data in Journal Format* The first draft was written by SC with contribution from all authors. Subsequent drafts were reworked by all authors. 70%
Statement from candidate	This paper reports on original research I conducted during the period of my Higher Degree by Research Candidature.
Signed	, 23/12/2019

7.1 Introduction

Polymeric membranes are the cornerstone of large scale separation processes, from seawater desalination to CO_2 capture to the purification of drugs and chemicals [3]. However, fundamental problems to further improving these membranes remain, such as fouling, selectivity and stability, primarily related to constraints on the types of polymers and the micro-structures than can be obtained with current manufacturing methods, phase inversion, polymerisation, electrospinning, and sintering [300]. Polymeric membranes can be broadly classified according to their pore size, with ultrafiltration membranes, with have an irregular, highly tortuous porous structure [301]; and nanofiltration and reverse osmosis membranes which have a dense structure, without well-defined pores and transport occurring via the solution-diffusion model in the free volume between the polymer chains [172]. In all instances, these limitations result in increased transport resistance, which in turn requires more energy to force the liquid permeate through the membrane[2]. Considerable efforts to control the structure of transport pathways in polymeric membranes have been made over the years, with work ranging from copolymer self-assembly into isoporous membranes [163], to mimicking water channels found in biological membranes, such as aquaporins [302].

While these methods allow for fine control over pore size and tortuosity [164], they have not yet been able to obtain regular, cylindrical pores with a process that can be industrially scaled [165].

The first results showing high water flow rate in CNTs not only promised to offer higher performance compared to current polymeric membranes but also provided the availability of a well-defined and tuneable transport pathway ranging from ultrafiltration to reverse osmosis[28]. The former aspect was due to the low frictional losses associated with water flow through the tubes and related to the unfavourable energetic interaction between water and the sp2 graphitic structure of the CNTs [257, 14]. The effect of this interaction of flow can be quantified via the concept of slip length L_S in the Hagen-Poiseuille equation:

$$Q = \frac{\phi A_{mem} D^2 \Delta P}{32\ \mu L} \left(1 + \frac{8 L_S}{D}\right), \tag{7.1}$$

where ΔP is the applied pressure, μ is the fluid viscosity, ϕ is the porosity and Q is the volume flow rate through the membrane of area A_{mem} with nanopores of diameter D and length L.

The increase in flow over the non-slip case, i.e. for L_S =0, termed flow enhancement, ϵ, gives a measure of the theoretical improvement of CNT membranes (Eq. 2.4).

Values of ϵ of up to 10^5 were measured experimentally and predicted via molecular dynamics simulations [8]. Unfortunately, the challenge of aligning carbon nanotubes in the polymer matrix and the need to functionalise the nanotubes to obtain good adhesion with polymeric matrices have hindered any translation from the lab to practical use, so far [57, 303].

Transport studies in CNTs also showed that tuning the surface chemistry and structure of the nanotubes can have a significant effect on water flow, with a range of different nanotube materials tested [14, 269, 18].

Here, a fundamentally novel approach is proposed, creating straight, cylindrical polystyrene nanotubes, marrying the advantage of using a commonly used polymer with the formation of a well-defined and tuneable permeation pathway given by nanotubes. In this work, the synthesis of PNTs is performed from liquid deposition inside the pores of AAMs used as templates, resulting in the formation of polymer nanotube membranes, here called PNT-AAM (Figure 4-4).

This novel approach builds on previous work done on the deposition of polymers inside anodic aluminium oxide [304] and anodic alumina membranes [166, 168], the difference between the two being that the former has pores blocked at one end, while the latter's pores are open at both ends. These early works showed that a low starting polymer concentration led to unstable cylindrical structures, and only above predefined high concentrations could polymeric nanotubes be synthesized [304]. Moreover, low molecular weight polymers resulted in the formation of nanorods rather than nanotubes [170]. It was also found previously that the complete wetting of the template can be facilitated by adjusting the annealing temperature. This temperature is dependent on the polymers' glass transition temperature and thus, its molecular weight [169]. Indicatively, nanotubes were obtained for annealing temperatures around 100 °C above glass transition, to have sufficiently high polymer spreading onto the template, related to a spreading coefficient which increases for the polymer with increasing temperature [171]. The annealing time was also found to have an impact on the hollowness of the nanotubes, as this needed to be optimised to a minimum of 2 hours to avoid that the nanopores were fully blocked by polymer melts [169].

Herein, the AAM template was soaked in a polymer solution before drying and annealing steps, and the key parameters influencing the synthesis were systematically studied, including polymer concentration (1, 3 and 7 wt% in chloroform), polymer

molecular weight (90 and 200 kDa) and annealing time (2 and 12 hours). The annealing times investigated are the minimum and maximum lengths of times found in literature [305, 169]. The PNT membrane samples nomenclature is explained in Table 7.1.

Table 7.1: Definition of the samples used in this work. The parameters that are varied from the baseline sample (PNTs 3 wt%) are highlighted in bold.

Sample	Molecular Weight	Annealing Time	PS Concentration
PNTs 1wt%	90 kDa	2 h	**1wt%**
PNTs 3 wt%	90 kDa	2 h	3wt%
PNTs 7wt%	90 kDa	2 h	**7wt%**
PNTs 200kDa	**200 kDa**	2 h	3wt%
PNTs 12 h	90 kDa	**12 h**	3wt%

The influence of synthesis parameters on the tubes' morphology and length was clearly identified by the variation of one factor at a time. The frequently faced problem of pore clogging on the surfaces of AAMs [166] was successfully bypassed in this study by the introduction of optimised surface plasma etching (details in SI).

Fragments of the produced PNT-AAMs were coated with gold and positioned on carbon tape for FESEM analysis to image their top and bottom surfaces and assess their porosity via statistical image analysis using ImageJ, according to a known method [18]. All membranes appeared opaque and faintly yellow after synthesis (refer to the SI for images), and their top and bottom surface appeared clear of debris (Figure 7-1 and SI).

SEM cross-section micrographs show the PNTs released from the template and forming along the whole thickness of the AAM (Figure 7-2). The increase in the polymer molecular weight leads to the formation of more fragmented nanotube walls (Figure 7-2c) with increased roughness (Figure 7-2d). This was attributed to the fact that PS with lower molecular weight has a lower glass transition temperature (SI), which means it will form a better PNT structure under the same annealing condition, with better adherence to the substrate [169]. The annealing temperature was fixed as 220 °C as this was well above the polymer glass transition temperature. SEM analysis shows that a change in annealing time does not significantly impact the tubes' length (Figure 7-2g).

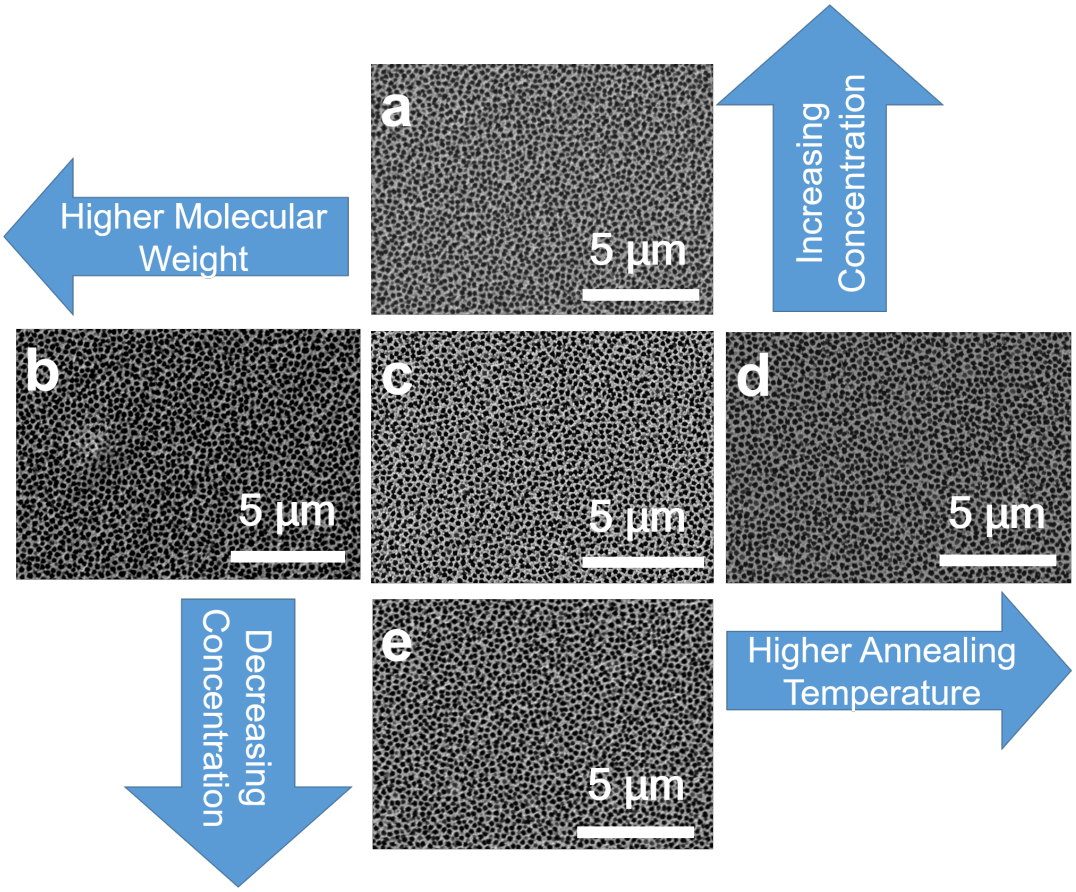

Figure 7-1: Top surfaces for (a) 7wt%, 90kDa, 2hrs; (b) 3 wt%, 200 kDa, 2hrs; (c) 3 wt%, 90 kDa, 2hrs (baseline); (d) 3 wt%, 90 kDa, 12h; (e) 1 wt%, 90 kDa, 2hrs respectively taken at x 5000 magnification. Plasma etching was optimised for a duration of 5 min for the baseline sample (3wt%, 90kDa, 2hrs), which was found to be enough to totally remove the polymer debris from the membrane top and bottom surfaces in the baseline sample (SI).

The hollowness of the PNTs is verified by the TEM in Figure 7-3. The produced PNTs-AAMs were tested for pure water permeance in a customised dead-end filtration setup with effective diameters of 10 mm [257]. The experimental permeance K_{EXP} in $m^3m^{-2}s^{-1}Pa^{-1}$ as an average of three measurements at different water flow rates per sample is defined in Eq. 2.5.

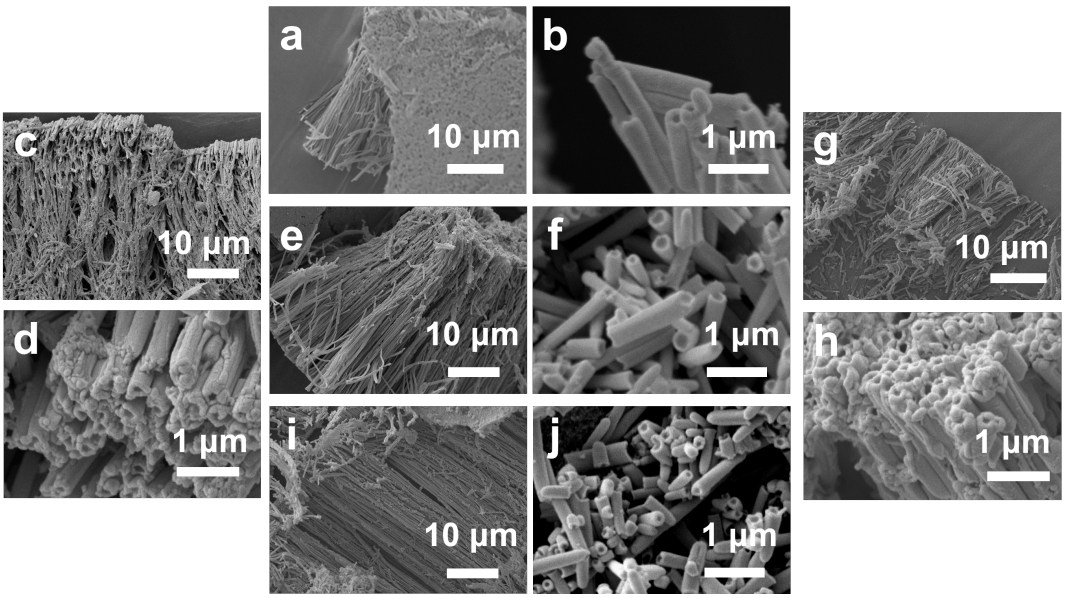

Figure 7-2: SEM micrographs of PNTs. Cross-section views: (a) 7wt%, (c) 200 kDa, (e) baseline (g) 12h and (i) 1wt% taken at x 2000 magnification. Opening views: (b) 7wt%, (d) 200 kDa, (f) baseline (h) 12h and (j) 1wt% taken at x 25000 magnification.

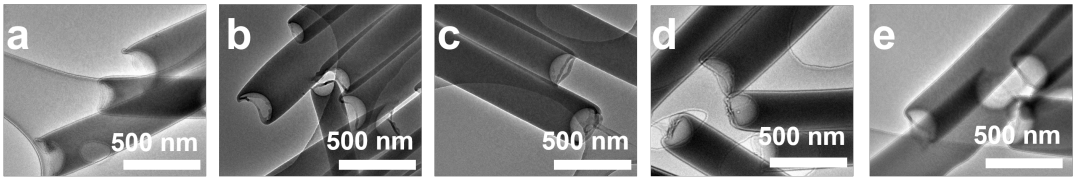

Figure 7-3: TEM micrographs of PNTs prepared with different PS concentration, molecular weight and annealing time: (a) 1wt%, (b) 3wt%, (c) 7 wt%, (d) 200 kDa and (e) 12h.

K_{EXP} was calculated on three membranes for each sample. The expected theoretical value for permeance K_{HP} can be calculated using Eq. 2.5 by inserting the value of Q obtained from Eq. 7.1 computed using the radius measured by Porolux for each nanotube membrane (Table 7.2).

1 wt% of PS (90 kDa) in the starting solution is enough to reduce the membranes' pore diameter from 200 nm of the template to 95 nm. A further increase in the concentration

to 3 wt% (the baseline) leads to a pore diameter of 45 nm. A further increase in concentration to 7 wt% did not produce any further reduction in pore size, possibly due to pore clogging (Figure 7-2a) and higher local tube thickness (Figure 7-2b). The Young contact angle of water (θ_Y) increases with increasing PS concentration from 65 ± 2° to 116 ± 2° (Table 7.2). The low contact angle for the lowest PS concentration is attributed to potentially incomplete coverage of the AAM's surface by the polymer.

Table 7.2: Pore size, porosity, theoretical ($L_s = 0$) and experimental permeance, average surface roughness of the membranes under analysis and Young contact angle.

AAM	D	ϕ	K_{HP}	K_{EXP}	R_a	θ_Y
	(nm)	(-)	(LMH/bar)	(LMH/bar)	(nm)	(°)
AAM	200 ± 8	0.35	3539	4210 ± 250	-	41 ± 2
1wt%	95 ± 2	0.38	865	2040 ± 240	62.9	65 ± 2
3 wt%	45 ± 1	0.23	119	513 ± 45	73.7	105 ± 2
7wt%	49 ± 1	0.29	176	97 ± 33	51.9	116 ± 2
200kDa	46 ± 1	0.31	164	282 ± 76	26.1	108 ± 2
12 h	53 ± 1	0.25	180	691.5 ± 33	70.1	114 ± 2

As the polymer coats the walls of the AMM, this also results in a reduction in porosity and permeance (Table 7.2), as expected [269]. However, the flow enhancement, ϵ, increases significantly, with a maximum of 4.5x for a starting PS concertation of 3 wt% (Figure 7-4). Using a higher molecular weight PS in the starting solution (3wt%) did not change the contact angle (Table 7.2) compared to the 90kDa PS at the same concentration but resulted in a significantly lower flow enhancement (Figure 7-4). This difference is attributed to slower surface diffusion of water on the 200 kDa PS than on the 90 kDa, due to the higher molecular weight [305]. This is in agreement with an investigation of the Rayleigh instability of PS films coated in the pores of AAMs, which found that, under the same annealing conditions, instability would occur more significantly when the molecular weight is higher, resulting in a change in the PNTs structure [306]. The Rayleigh instability is caused by the process in which a liquid in a cylindrical conformation tends to assume a configuration that leads to a minimum in its surface energy [305]. In the present work, the tubes formed using the 200 kDa PS are less regular than those prepared with the 90 kDa PS (cfr. Figure 7-2e with Figure 7-2d). The less regular structure effect is associated with the Rayleigh instability [305]. We hypothesize that the irregular shape of PNTs results in lower flow enhancement by reducing the surface diffusion of water on the tube wall. This is not reflected in the R_a

value, which was obtained for the membranes surface rather than inner walls.

An increase in annealing time from 2 to 12 hours did not produce any significant effect on the flow enhancement, despite a small increase in contact angle, attribute to chain rearrangement in the polystyrene [306].

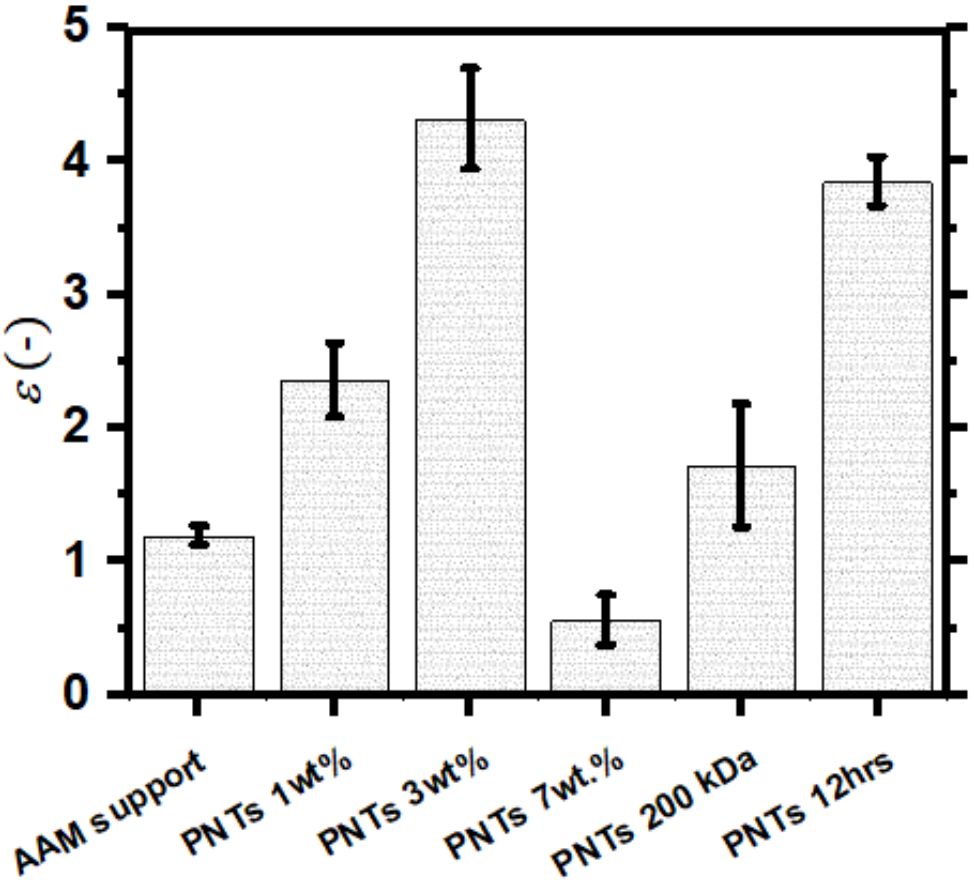

Figure 7-4: Flow enhancement factors for the membranes studied in this work, with the parameters varied from the baseline (3wt%, 90kDa, 2hrs) indicated on the x-axis. The error bars in this figure represent the data's standard deviation. The nomenclature used in this Figure is clarified in Table 7.1.

In summary, this chapter reports the formation of polystyrene nanotube membranes via soaking of anodic alumina membranes in polystyrene solutions. The effect of polystyrene concentration, molecular weight and annealing time on the structure of polystyrene nanotubes and on the pure water permeance through the membranes was investigated, showing that a flow enhancement as high as 4.5x the no-slip case was obtained for a 3 wt% concertation of 90kDa polystyrene in the starting solution followed

by 2h annealing in argon. Further increases in initial polymer concentration, polymer molecular weight and annealing time did not produce any significant increase in pure water permeance. These results open the way for creating polymeric nanotube membranes with well-defined pore structures and tunable surface properties, overcoming the limits of current polymeric membranes whose internal transport pathway cannot be controlled or defined as well as for the case of the polymer nanotubes presented here.

Supplementary Information

This section contains detailed supporting results for this Chapter. A repository with the complete research data for this article can be found online [307].

PNT samples were compared after performing plasma etching for different times (Figure 7-5). The produced membranes looked clear with a shade of yellow (Figure 7-6).

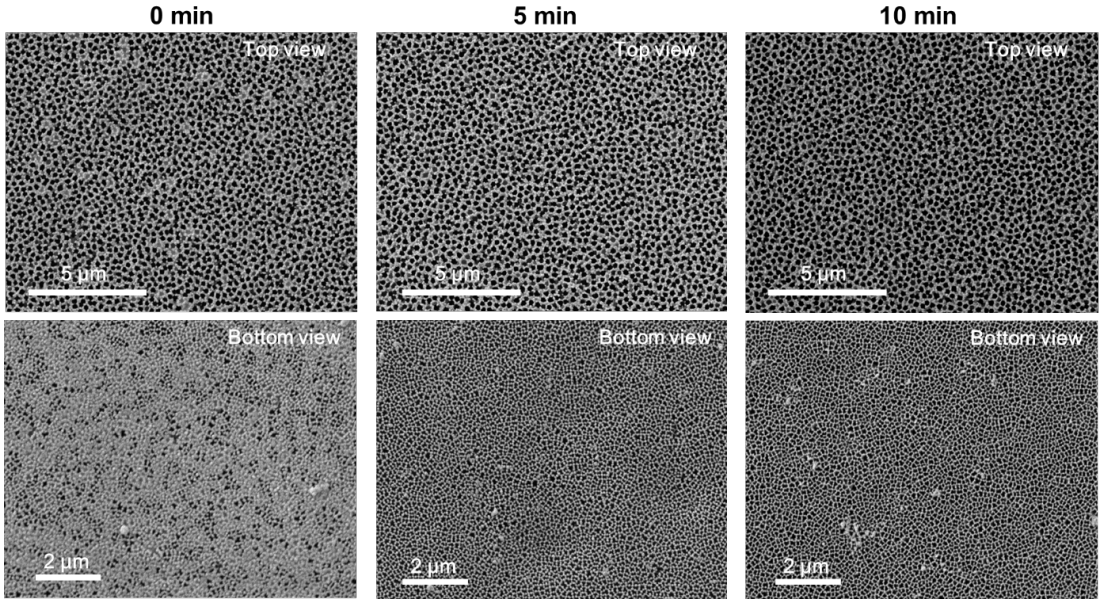

Figure 7-5: Comparison of PNT samples after performing plasma etching for different times. The top three images are the membrane's top view with a magnification of x5000, the bottom three images are the membrane's bottom view with a magnification of x10000.

Plasma etching was optimised for a duration of 5 min for the baseline sample (3wt%, 90kDa, 2hrs), which was found to be enough to totally remove the polymer debris from the membrane top and bottom surfaces in the baseline sample (Figure 7-7).

DSC was performed to assess polymers' glass transition temperatures, and is reported in Figure 7-8.

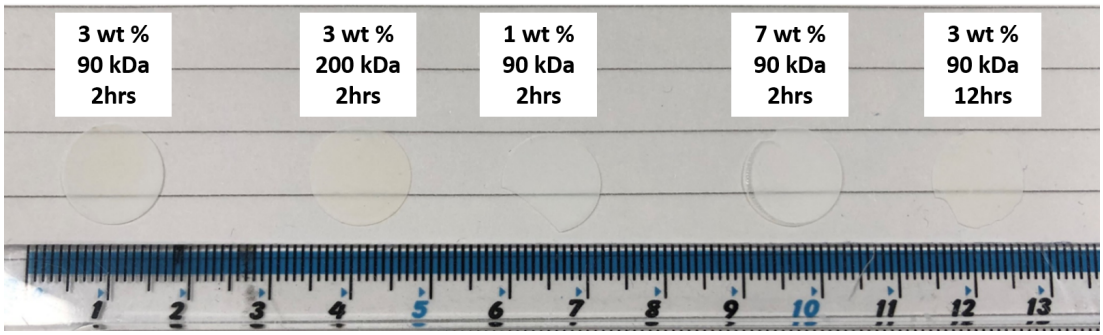

Figure 7-6: Comparison of PNT samples after performing plasma etching for different times. The top three images are the membrane's top view with a magnification of x5000, the bottom three images are the membrane's bottom view with a magnification of x10000.

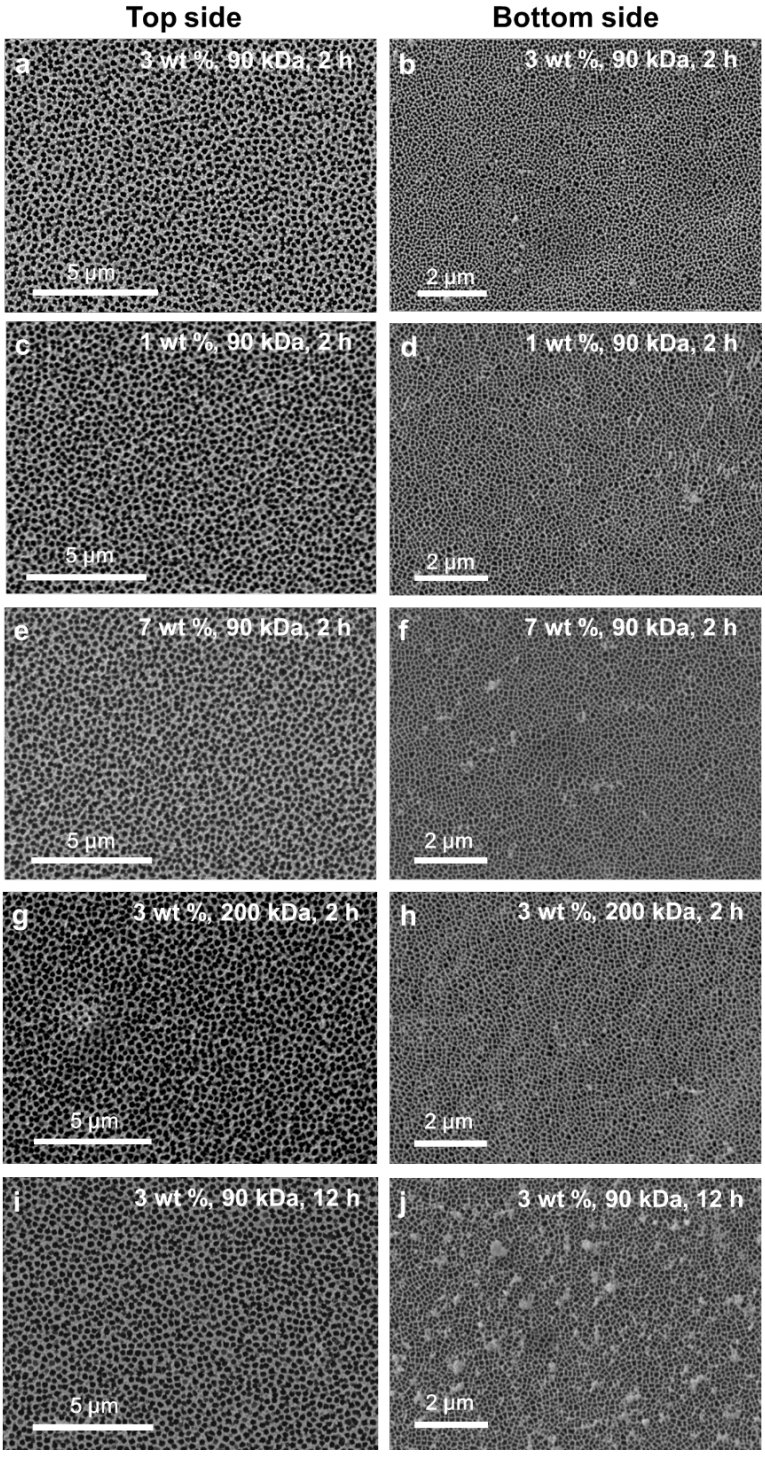

Figure 7-7: Top surfaces for (a,b) 3wt%, 90kDa, 2hrs; (c,d) 1 wt%, 90 kDa, 2hrs; (e,f) 7 wt%, 90 kDa, 2hrs; (g,h) 3 wt%, 200 kDa, 2hrs; (i,j) 3 wt%, 90 kDa, 12hrs respectively. Top sides are taken at x 5000 magnification. Bottom sides are taken at x 10000 magnification.

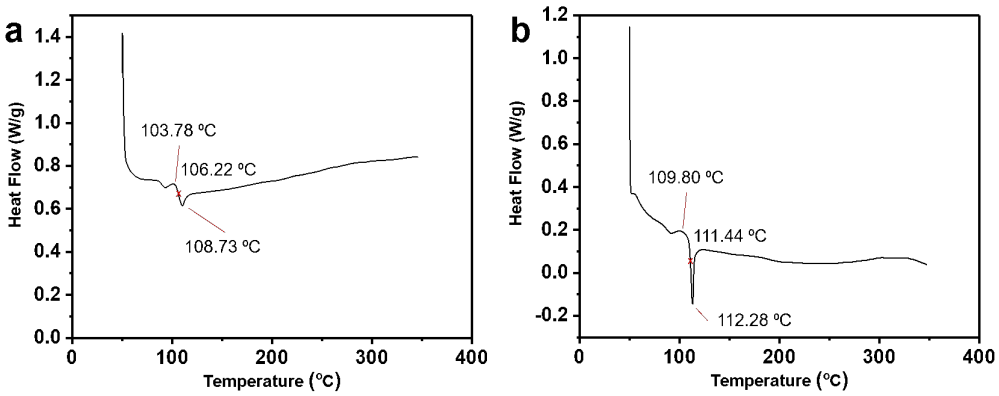

Figure 7-8: DSC of (a) 90 kDa and (b) 200 kDa polystyrene, presenting glass transition temperature mid-points of 106.22 °C and 111.44 °C respectively.

Chapter 8

High Flux Thin-Film Nanocomposites with Embedded Boron Nitride Nanotubes for Nanofiltration

S. Casanova, T. Liu, Y. M. J. Chew, A. Livingston and D. Mattia

This declaration concerns the article entitled: High Flux Thin-Film Nanocomposites with Embedded Boron Nitride Nanotubes for Nanofiltration	
Satus	Published
Publication details	Journal of Membrane Science, 2019, 117749, ISSN 0376-7388.
Candidate's contributions to the paper (detailed, and also given as a percentage)	The candidate contributed to/ considerably contributed to/ executed the ... • *Formulation of Ideas* The initial idea was formulated by SC and DM based on preliminary observations conducted by DM. 80% • *Design of Methodology* The experimental work and data analysis was conducted by SC and TYL with supervision from DM, AL and YMJC. 90% • *Presentation of Data in Journal Format* The first draft was written by SC with contribution from all authors. Subsequent drafts were reworked by all authors. 70%
Statement from candidate	This paper reports on original research I conducted during the period of my Higher Degree by Research Candidature.
Signed	[redacted], 23/12/2019

8.1 Introduction

Polymeric nanofiltration (NF) membranes have become a mainstay of water treatment processes, with high recovery rates [308], easy modular scale up [49] and economic viability across a broad range of feed [309]. NF membranes are particularly effective for the combinatorial rejection of salts, organic compounds, natural organic matter (NOM), and dyes. [301]. The industry, however, still faces challenges such as high energy costs per unit volume of water purified [1], handling of retentate waste [310], fouling and a fundamental understanding of the mechanisms underlying the purification of complex feeds [3].

Thin-film composite (TFC) membranes composed of a very thin, yet dense selective layer supported by a porous support combine high flux and rejection with mechanical stability. Although TFC membranes are successfully used commercially [311], there is still scope and need to increase efficiency, reduce energy consumption and extend the chemical stability of these membranes [188]. Many ways have been explored to improve the performance of TFCs, including diverse fabrication methods, and the tuning of precursors used to fabricate the membranes [183]. Another promising strategy is the incorporation of inorganic nanomaterials in the thin selective layer to form so-called thin-film nanocomposite (TFN) membranes [3]. These additions alter the structure of the selective layer by finely tuning properties such as hydrophilicity [312], porosity [313], surface zeta potential [314] and stability [315, 316]. Additionally, the fillers can introduce desired features such as antifouling [317], adsorption [318] and photocatalytic characteristics [319] into the membranes.

Amongst the wide range of inorganic fillers tested so far [49], carbon nanotubes (CNTs) have been considered for application in membrane technology due to their fast water transport and low tortuosity [34]. The reduced friction of water on the defect-free carbon surface in nanotube membranes results in very high water permeances through the tubes [257], translating in higher efficiency (i.e. higher flux) per applied pressure [320]. However, efforts to create membranes with the CNTs aligned perpendicularly to the membrane surface in systems fit for commercialisation have been, so far, unsuccessful [172, 8, 18], with the alignment of nanotubes in bulk bypassing the use of templates a yet unsolved challenge [172]. On the other hand, the incorporation of randomly aligned CNTs in polymer matrices led to the successful formation of selective membranes [321], but with only modest increases in water permeance and a decrease in selectivity [236]. While the former can be attributed to the small fraction of tubes directly connecting feed and permeate, the latter is attributed to the formation of uncontrolled permeation

pathways at the interface between the CNTs and the polymer, due to poor chemical compatibility [303]. This aspect has been addressed by introducing an additional functionalisation step with acid groups, to form hydroxyl and carboxyl groups on the tube surface [322]. The functionalised CNTs have been added in relatively large amounts (1 wt% - 10 wt%), with a parallel increase in rejection up to 5% to provide permeances up to 50% higher than the one of the starting polyamide membrane [323, 324]. CNTs have also been functionalised with more complex zwitterion groups that, however, penalised the water permeance when compared to pristine CNTs, improving the rejection of NaCl from 97.6% to 98.5% thanks to the steric hindrance of the zwitterion functional groups [325]. Despite the promising results, the permeance increase potential is minimised by the low critical amount of hydrophobic nanofiller that can be added in the membrane matrix before incurring in agglomeration issues, which cause the formation of pinholes, and the subsequent loss of performance [326].

Here, boron nitride nanotubes (BNNTs) are investigated as fillers for nanofiltration membranes, as their physico-chemical characteristic allow overcoming some of the limitation of CNT-based TFNs highlighted above. Hexagonal BNNTs (hBN) are isostructural to graphitic CNTs, but behave as electrical insulators and show higher resistance to oxidation [73]. Molecular dynamics simulations on BNNTs in the subcontinuum range, with diameters 0.8 nm, have shown faster pure water flux than in CNTs [33]. For such small diameters it was shown that increased van der Waals and electrostatic interactions between the nanotube walls and the water molecules contribute to an easier filling of the BNNTs pore than for CNTs [327]. However, when the diameters of the tubes studied were larger, CNTs outperformed BNNTs in terms of improved water fluxes [14]. This was ascribed to differences in the electronic landscape in the two nanotube walls for tubes with radii around tens of nanometers, given the semiconducting nature of CNTs and the insulating nature of BNNTs [40]. Simulations also showed that BNNTs have tunable cation and anion selective properties due to the partial charge on the boron and nitrogen atoms of the nanotube [13] and osmotic energy storage capabilities [44]. Additionally, when boron nitride nanosheets were recently embedded in mixed matrix membranes, they showed improved fouling resistance [236]. Boron nitride nanotubes have recently been used to fabricate ultrafiltration membranes with improved thermal resistance and mechanical stability [235]. Additionally, CNTs have been shown to have antioxidant capabilities that slow down chlorine attack on polymeric membranes [303], however this effect is as yet unreported for BNNTs. Using BNNTs as membrane nanofillers is motivated, together with its novelty, by the fact that materials with high negative zeta potentials allow for rejection of pollutants not only by size but also by charge [7].

Despite the many advantages of this material over CNTs, there has been notably less published research on BNNTs than on their carbon counterparts, attributed mainly to the lack of methods for the production of the material at scale [73]. This obstacle has been overcome in this work, by optimising a known technique [104] for the production of BNNTs by CVD as described in the Materials and Methods. The nanomaterial was then embedded in the selective phase of an interfacially polymerised polyamide (PA-BNNT) membrane. BN is negatively charged in water over a broad pH range [294] and can adsorb OH^- on its surface further increasing its negative charge [44].

8.2 Results and Discussion

8.2.1 BNNTs Synthesis

BNNTs were synthesized via chemical vapour deposition, resulting in a dense product (Figure 8-1a), with the BNNTs having open ends (Figure 8-1b) and homogenously grown over the entire substrate area (Figure 8-1c) with a vertical orientation (inset cross-sectional HRTEM).

The BNNTs powder was collected with a yield of $\sim$ 10 mg per run by simple scratching of the silicon wafer (W x L 14 x 70 mm) substrate. The diffraction pattern generated by a single tube (Figure 8-1d) confirmed the *h*BN (002) crystal structure of boron nitride multiwalled (wall thickness $\sim$4.5 nm) nanotubes [86], with a straight inner channel of *c.a.* 8 nm in diameter and an outer diameter of *c.a.* 17 nm (Figure 8-1e), where the interspace layer distance of *h*BN is 0.328 nm as expected from literature [73]. Combining the open ends and penetrating inner voids, the as-synthesized BNNTs are ideal candidates for creating nanoscale channels in TFN membranes [17]. The morphology of the BNNTs showed a relatively wide size distribution with outer diameters in the range of 5 to 105 nm and tube lengths in the range of 1 to 5 μm, as statistically counted by 200 tubes in TEM micrographs (Figure 8-1f).

The BNNTs powder samples present the typical Raman *h*BN peak at 1369 cm^{-1} (Figure 8-2a). The XRD spectra in Figure 8-2b shows four main BN peaks at $2\theta = 10.5^o$ (*h*BN 001), 29^o (*h*BN 002), 40^o (*h*BN 100) and 53^o (*h*BN 004) [328], alongside some iron and MgO peaks in the region $20^o < 2\theta < 4\theta^o$, identified as catalyst impurities. Boron nitride FTIR peaks are identified in Figure 8-2c for the vibration mode along the tubes' longitudinal axis at 1367 cm^{-1}, in the tangential direction at 1537 cm^{-1} and the out of plane buckling mode at 795 cm^{-1} [104].

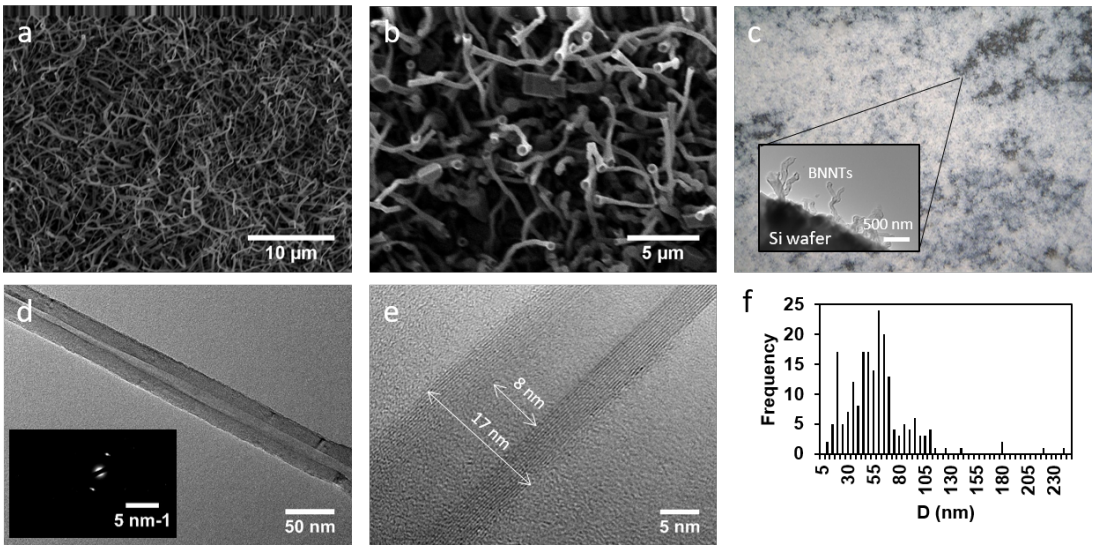

Figure 8-1: (a) FESEM micrograph of BNNTs on the Si wafer taken at 3000 x magnification and (b) collected from the alumina boat taken at 5000 x magnification with 8 mm working distance. (c) Optical microscope image (500 x) with a TEM micrograph inset showing BNNTs grown on a piece of silicon wafer; TEM micrographs and (d) corresponding diffraction pattern and (e) measures for inner and outer tube diameter of a selectedtube where the *h*BN interlayer spacing can be observed. (f) Counts of outer diameter intervals for 200 tubes randomly imaged with TEM.

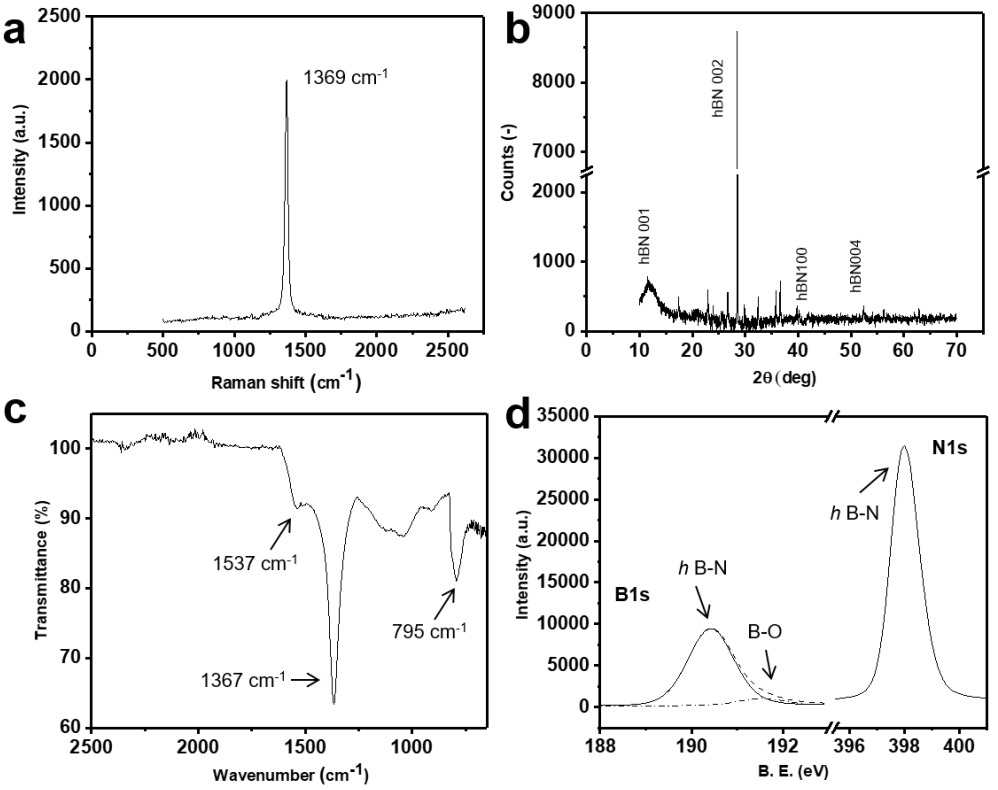

Figure 8-2: (a) Raman analysis of BNNTs with the characteristic *h*BN peak at 1369 cm^{-1} and (b) XRD pattern of the as produced BNNTs powder, showing four characteristic *h*BN peaks; (c) FTIR of BNNTs on silicon wafer; and (d) B1s and N1s high resolution XPS spectra of the BNNTs.

The spectra also presents peaks attributed to Si-O in the 1130-1000 cm^{-1} region and Si-H in the 850-900 cm^{-1} region, as the spectra was taken before the BNNTs material was scraped from the Si substrate. XPS results (Figure 8-2d) identify a B/N atomic ratio of 1.18 in the powder BNNT sample, very close to the theoretical value of 1. Peaks for hBN are identified at 190.41 eV and 398.00 eV for B and N respectively, and a 3.75 at.% of N-B-O bonds can be observed in the B high resolution spectra [329].

8.2.2 Characterisation of PA-BNNTs membranes

The surface and cross-sectional morphologies of the produced polyamide membranes are shown in Figure 8-3. The irregular morphology increased with BNNTs loading, which is consistent with an increase in the average surface roughness (R_a, nm) in Table 8.1, and therefore the ratio between the membrane surface area and the projected area, r, and morphological changes measured by AFM (Figure 8-4). The crumpled areas observed in the PA-BNNTs membranes showed similar material stiffness as the rest of the membrane (see phase plot analysis in Figure 8-11), indicating that no BNNTs protrude out of the membrane from the top surface.

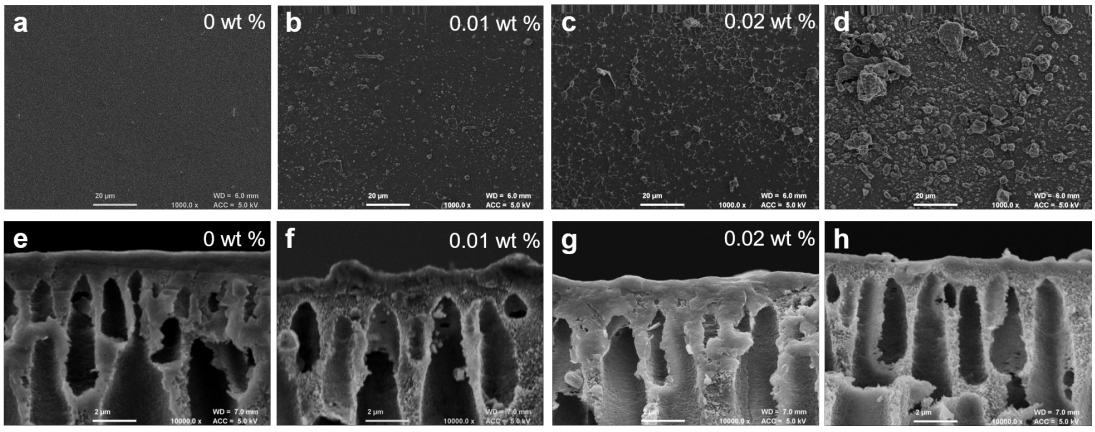

Figure 8-3: FESEM top and cross section of membranes prepared from solutions containing different percentages of nanofiller: (a,e) bare, (b,f) 0.01 wt%, (c,g) 0.02 wt% and (d,h) 0.03 wt% PA-BNNTs membranes.

Measured contact angle varies as a function of BNNTs concentration (Table 8.1). Water contact angle increased by approximately 20^o from PA-BARE to PA-BNNTs0.03, in agreement with both the increase in roughness R_a already observed in Figure 8-4 and an observed reduced material hydrophilicity. When the measured contact angle and roughness are used to calculate values for the Young contact angles *via* the Wenzel

equation [241], an observable although not drastic increase in material hydrophilicity is observed, with Young water contact angles increasing by 15-20% for each 0.01 wt% of BNNT added. In reverse, the non-polar diiodomethane contact angle ($\theta_{\text{Y\_DIM}}$) decreased over the four membranes tested, in line with the loss of hydrophilicity.

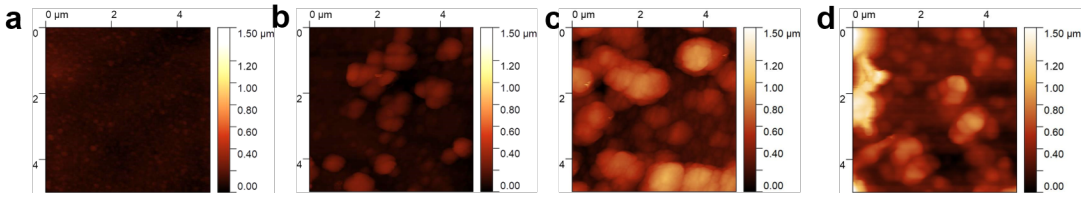

Figure 8-4: AFM maps of membranes (a) bare, (b) 0.01 wt%, (c) 0.02 wt% and (d) 0.03 wt% PA-BNNTs membranes.

Table 8.1: Measured water (θ_{WATER}) and diiodomehtane (θ_{DIM}) contact angles, Young water ($\theta_{\text{Y\_WATER}}$) and diiodomehtane ($\theta_{\text{Y\_DIM}}$) contact angles obtained applying the Wenzel equation, average surface roughness R_a results on PA-BARE and PA-BNNTs membranes and ratio r between the membrane surface area and the projected area, obtained by AFM.

Membrane	θ_{WATER}	θ_{DIM}	$\theta_{\text{Y\_WATER}}$	θ $_{\text{Y\_DIM}}$	R_a	r
PA-BARE	25° ± 2°	30° ± 2°	35° ± 2°	39° ± 2°	19 nm	1.11
PA-BNNTs0.01	32° ± 2°	29° ± 2°	40° ± 2°	38° ± 2°	49 nm	1.11
PA-BNNTs0.02	30° ± 2°	28° ± 2°	49° ± 2°	48° ± 2°	172 nm	1.32
PA-BNNTs0.03	45° ± 2°	10° ± 2°	59° ± 2°	44° ± 2°	181 nm	1.37

A free-standing film was placed in the TEM to observe the embedment of the BNNTs in the polyamide (Figure 8-5). Wrinkles in the thin layer are created when this is transferred to the TEM grid, but these formations can be clearly differentiated from the BNNTs as they show a hollow nature as previously shown in Figure 8-1b, e and in the inset of Figure 8-5a. Figure 8-5b shows a picture of the polyamide thin film formed at the interface between the PIP H_2O/ MeOH solution and TMC in hexane solution.

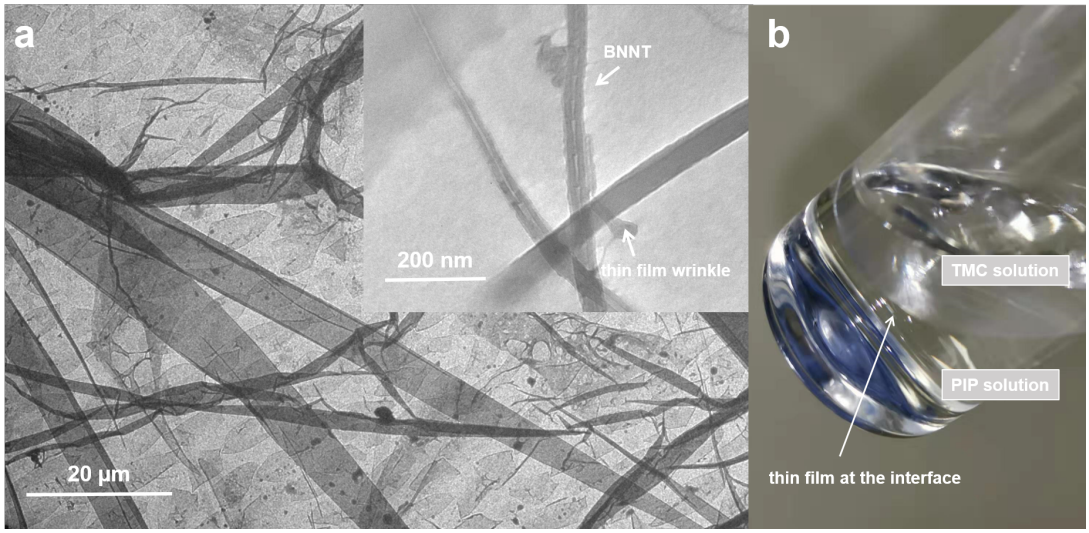

Figure 8-5: TEM micrograph of a free-standing film loaded with 0.01wt% BNNTs, observable in the magnified inset. Wrinkles generate in the film when it gets transferred to the TEM grid. (b) Picture of a thin film produced at the interface between the TMC and PIP solutions.

As expected, the introduction of a negatively charged material in the texture of the IP membrane slightly decreased its surface zeta potential (Figure 8-6). Although statistically significant (p-value=0.002), this change is not as dramatic as it might be expected by the introduction of negatively charged nanomaterial (literature reports a surface zeta potential of -34 $\pm$ 4 mV on few layered BN for pH 6 [292]), leading to the hypothesis that the vast majority of nanofillers are surrounded by the selective polymer layer, and do not protrude from the top surface, in agreement to the top layer stiffness results in Figure 8-11.

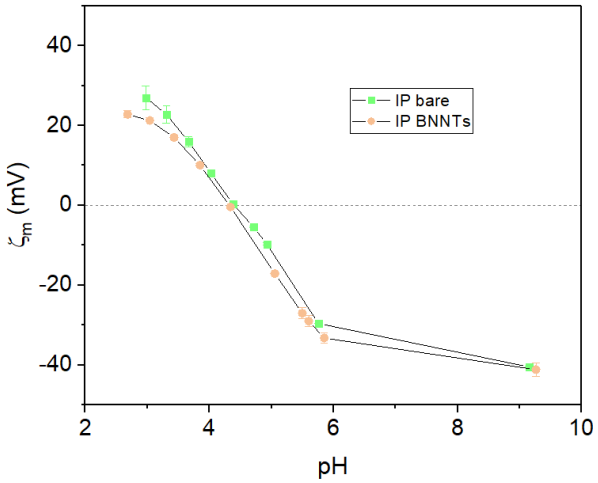

Figure 8-6: Surface zeta potential (ζ_m) vs. pH of a PA-BARE (IEP=4.40) and PA-BNNTs0.01 (IEP=4.32).

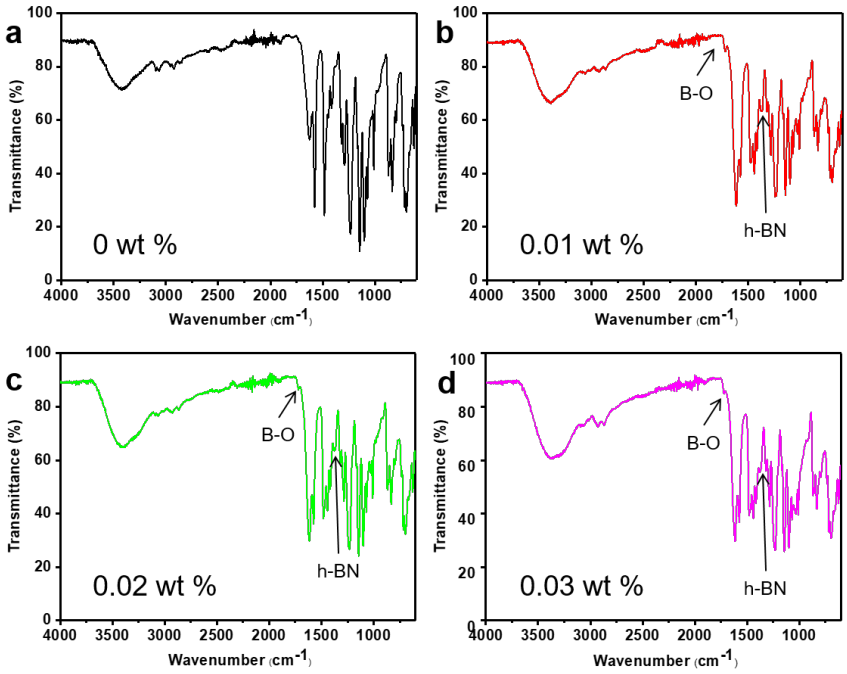

Figure 8-7: FTIR spectra for (a) bare, (b) 0.01 wt%, (c) 0.02 wt% and (d) 0.03 wt% PA-BNNTs membranes.

Figure 8-7a reports the FTIR-ATR spectra for the IP BARE membrane [330], and Figure 8-7b-c the scans for membranes with increasing BNNTs loading. The beam

penetrates the sample for 0.5 - 2 μm during testing [331], therefore representing the whole thickness of the membrane top layer and not just the very top surface. Thus, at the highest BNNTs concentration, the predominance of the 1375 cm^{-1} BNNTs' peak, corresponding to the longitudinal vibration mode of the tube, is observed [104, 332], together with a B-O functionalisation peak at 1721 cm^{-1} [333], showing a new bond not observable in the FTIR for the BNNTs in powder form (Figure 8-2c), potentially indicating some interaction between the boron nitride and the polymeric matrix already visible for BNNTs concentrations of 0.01wt.%. However, the intensity of the B-O bond is not increasing at increasing BNNTs concentrations.

The O/N ratio for each membrane is reported in Table 8.2. A fully cross-linked polyamide, $(O/N)_{fully\ cross-linked}$, has a O/N ratio of 1 and a theoretically fully linear polyamide, $(O/N)_{\text{fully linear}}$, has a O/N ratio of 2 [240]. From these values, the degree of crosslinking was calculated from XPS results using Eq. 4.1. While the addition of 0.01wt% BNNTs increases the degree of crosslinking from 0.7 to 1.0, this then declines moving to 0.02wt% and 0.03wt%, seemingly increasing the amount of transport pathways available in selective layer [334] by increasing polymer free volume. A consequence of this is identified in the lower intensity of B-O bonding observed in the FTIR in Figure 8-7 for high BNNTs concentrations, which could result from the change in the polymer structure.

Table 8.2: Experimental O/N from XPS and degree of crosslinking (Eq. 4.1).

Membrane	$(O/N)_{\text{XPS}}$	crosslinking (%)
PA-BARE	1.3	0.7
PA-BNNTs0.01	1.0	1.0
PA-BNNTs0.02	1.6	0.4
PA-BNNTs0.03	1.7	0.3

8.2.3 Performance of PA-BNNTs membranes

The permeance of the tested IP membranes increases with BNNTs loading (Figure 8-8a), from an average of 1.1 LMH/bar for the bare membrane to 2.7 LMH/bar for the PA-BNNTs0.01, 4.5 LMH/bar for the PA-BNNTs0.02 and 4.1 LMH/bar for PA-BNNTs0.03. The permeance values follow a convex profile often found in literature as a function of loading, as the initial addition of nanomaterial generates an initial increase in pore size, and then a decrease [322]. The former is ascribed to the higher free volume

provided by the BNNTs [174], whereas the latter is due to increasing agglomeration [335]. The increase in water flow pathways however does not impact the membrane's rejection performance up to 0.02 wt% loading, likely because the polyamide layer is still the main contribution to rejection up to that concentration value [174]. This suggests that the addition of the BNNT fillers might have created additional pathways for facile transport of water but not solutes [336, 337], and the slight increase in membrane surface charge might also have contributed to maintain a high rejection [49]. The slight decrease observed in the permeance value from PA-BNNTs0.02 to PA-BNNTs0.03 des not, however, show a statistically significant difference Student's t-test, p-value > 0.05).

Two batches of PA-BNNTs membranes (empty and filled symbols in Figure 8-8a) are tested for monovalent NaCl and divalent ($CaCl_2$, $MgSO_4$) salts rejection. Calibration curves for these measurements are reported in Figures 8-12, 8-13, 8-14, and ionic concentrations in Table 8.4. The rejection for NaCl remains low (20 – 40 %) for the whole concertation range investigated with 0.03 wt% BNNTs being the worst performing case. However the membranes perform well for divalent salts rejection, with the rejection for $MgSO_4$ is above 90 % for loading up to 0.02 wt% BNNTs, whilst it decreases to $\sim$ 80 % for PA-BNNTs0.03. $CaCl_2$ rejection raises from 75 – 80 % for the bare PA membrane to 97% for the PA-BNNTs0.01 and then decreases to around 40 % with further addition of nanofiller. The mass balance for the rejection of salts was $\geq$ 96% for $CaCl_2$ and NaCl, and $\geq$ 90% for $MgSO_4$. In all cases, the addition of 0.03 wt% of BNNTs notably penalises the membranes rejection, whilst the membranes show highly desirable performances for loadings $\leq$ 0.02 wt%, with PA-BNNTs0.02, in particular, combining the highest permeance (4.5 LMH/bar) with the highest divalent salt rejection. This is conceivably due to the additional free volume and thus water pathways offered by the presence of the BNNTs in the matrix, while the polyamide enveloping the nanomaterial provides salt rejection, effect also called sieve freefloating.

The observed behaviour showed little change in terms of recovering of their initial flux after two long fouling sequences in Figure 8-8b and c, with high FRR: 97%, 100%, 95%, 97 % for the first cycle and 100%, 100%, 96, 92% in the second cycle for PA-BARE, PA-BNNTs0.01, PA-BNNTs0.02 and PA-BNNTs0.03, respectively. The membranes, possessing a white, opaque colour at origin, could be cleaned completely by vigorous water flushing and no irreversible contamination could be observed visually after the test or by the FRR in the fouling cycles. The pump flow rate chosen in this study (175 ml/min) is a common setting for membrane fouling tests [236]. The membranes' behaviour might change if the test was carried out at higher flow rates, where some irreversible fouling might be observed.

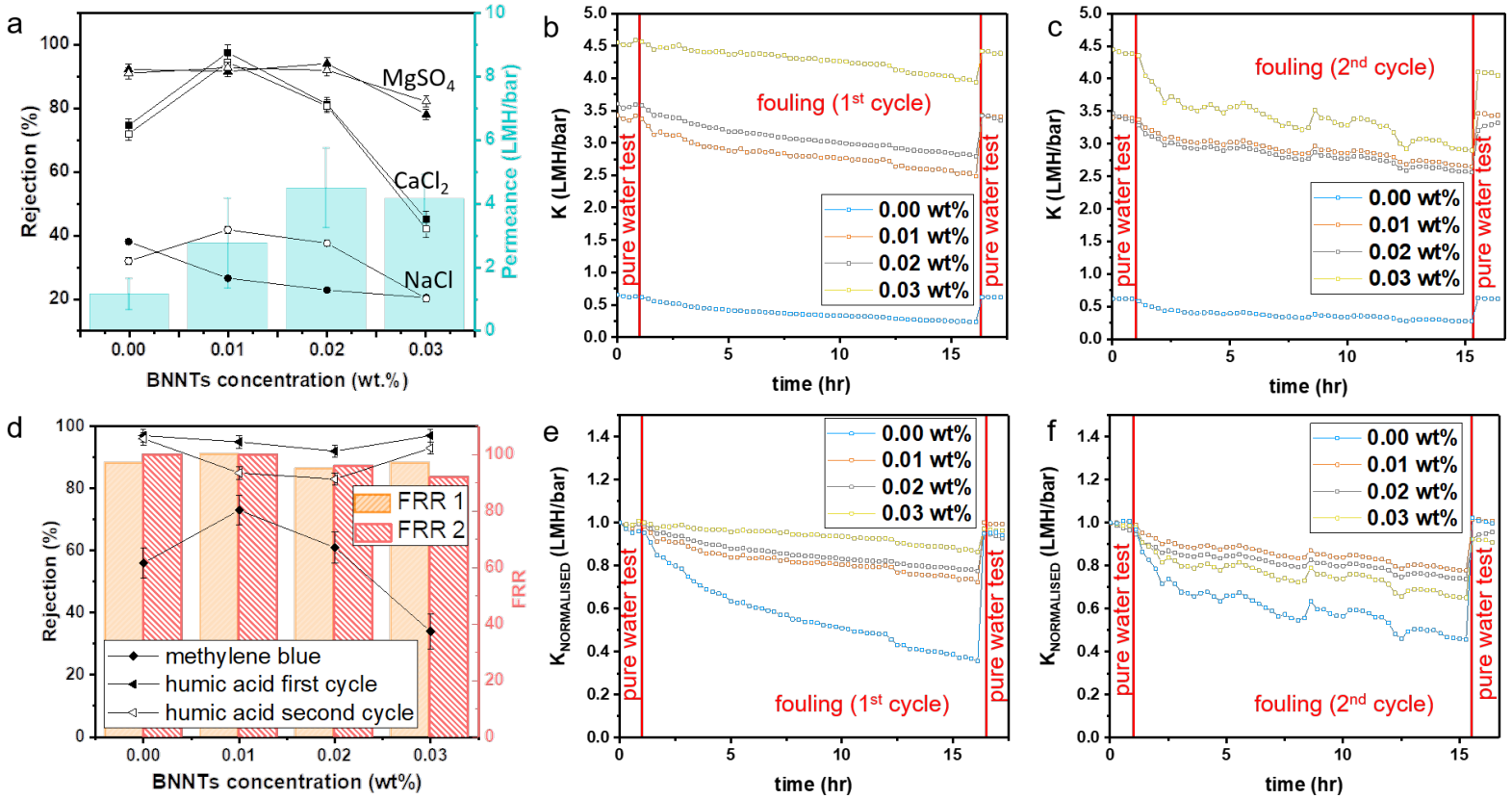

Figure 8-8: (a) Salt rejection (left axis) and permeance (right axis) of the bare and TFN membranes containing BNNTs; rejection tests have been repeated on two batches of membranes indicated with full and empty dots for $MgSO_4$, $CaCl_2$ and NaCl: (b) First and (c) second fouling cycle; (d) Rejection of methylene blue and humic acid together with flux recovery ratio (FRR) performances in the two fouling cycles in orange and red respectively; (e) first and (f) second fouling cycle, as displayed in the top panel, but normalised by initial pure water permeance for each membrane tested.

Figure 8-8e and f explicitly show that PA-BARE reversibly fouls to a greater extent, decreasing to 40% of the initial flux, compared to 80-90% for the TFN membranes. This is possibly due to the different repulsion between the fouling material and nanofiller, which may lead to a higher percentage flux decline during tests, even though this is eventually recovered after cleaning. Additionally, the different roughness as reported in Table 8.1 might play a role into this effect. The contribution to total resistance during fouling is reported in Table 8.3.

The fouling layer resistance contribution to the total resistance decreased with increased BNNT loading, as indicated by the decrease in value of the parameter $R_{\%}$ for the first fouling cycle from 60.5% for PA-BARE to 8.0% in Table 8.3. This can be observed in Table 8.5 for the second fouling cycle as well, where, however, the benefit in terms of lower fouling layer resistance at high BNNTs loading is attenuated by a slightly lower FRR in PA-BNNTs0.02 and PA-BNNTs0.03.

Table 8.3: Calculated membrane (R_m), irreversible (R_{ir}), reversible (R_r), total (R_t) and percentage ($R_{\%}$) resistances for the membranes under analysis during the first fouling cycle.

	PA-BARE	PA-BNNTs0.01	PA-BNNTs0.02	PA-BNNTs0.03
R_m	3.6 $\times 10^{+17}$ m^{-1}	6.5 $\times 10^{+16}$ m^{-1}	7.0 $\times 10^{+16}$ m^{-1}	5.5 $\times 10^{+16}$ m^{-1}
R_{ir}	7.7 $\times 10^{+15}$ m^{-1}	3.9 $\times 10^{+14}$ m^{-1}	4.6 $\times 10^{+14}$ m^{-1}	2.7 $\times 10^{+15}$ m^{-1}
R_r	5.6 $\times 10^{+17}$ m^{-1}	1.4 $\times 10^{+16}$ m^{-1}	1.5 $\times 10^{+16}$ m^{-1}	5.0 $\times 10^{+15}$ m^{-1}
R_t	9.3 $\times 10^{+17}$ m^{-1}	8.8 $\times 10^{+16}$ m^{-1}	8.9 $\times 10^{+16}$ m^{-1}	6.2 $\times 10^{+16}$ m^{-1}
$R_{\%}$	60.5 %	25.5 %	13.3 %	8.0 %

Figure 8-8d shows high rejection (80-90%) of humic acid in all the membranes tested (UV-vis calibration curve reported in Figure 8-15). In addition to being able to effectively reject the foulant, all membranes could recover $\geq$ 95% of their initial flux, with PA-BNNTs0.03 recovering $\geq$ 90% of its flux after physical cleaning, indicating that the increased membrane roughness can make harder the removal of the formed fouling layer [301].

Figure 8-8d also reports data on the rejection of methylene blue dye, with the addition of 0.01 wt% BNNTs improving rejection by 17% compared to PA-BARE, possibly to ascribe to an increased repulsion between the charged BNNTs and the dye. Rejection then decreased with increasing amounts of BNNTs added. As observed in the case of salts, the addition of 0.03 wt% of BNNTs to the thin film worsens rejection per-

formances. The mass balance for the rejection of methylene blue was always $\geq$ 96%. The rejection of methylene blue (319 Da) is lower than the one of humic acid (227 Da) due to the different feed concentrations and the formation of a fouling cake on the membrane during the fouling tests, which can also function as selective layer.

The relation between rejection and $CaCl_2$ concentration in the operational range 500 - 2000 ppm was also studied (Figure 8-9), with a relatively stable selectivity between 500 and 1500 ppm. Above this value, when Donnan type rejection becomes predominant [60], a decrease in rejection is observed for the PA-BARE and PA-BNNTs0.03, but not for the PA-BNNTs0.01 and PA-BNNTs0.02 for a concentration of $CaCl_2$ of 2000 ppm. When the PA layer is the major contributor to rejection, however, a constant rejection over different concentrations is expected [325]. We can therefore conclude that the PA layer is the major contributor to the rejection of the membranes analysed for all membranes but PA-BNNTs0.03, where hypothesized defects due to high loading demonstrate to have a detrimental effect at high concentrations (2000 ppm).

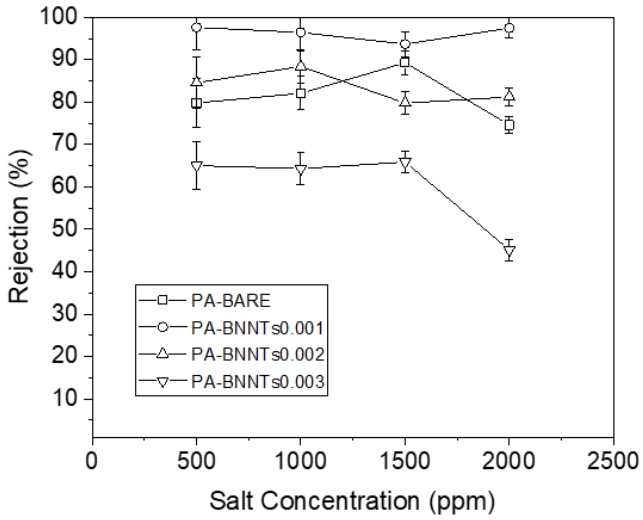

Figure 8-9: Dependence of $CaCl_2$ rejection on salt concentration for the membranes analysed in this work.

Membranes based on a polyamide linkage are prone to chlorine attacking the feed, as free chlorine radicals tend to be attracted by the N-H electron density [49]. Thus, NaOCl exposure is studied here for the membranes under analysis. As observed in Figure 8-10, the exposure to the chlorinating agent is more adverse to all PA-BNNTs membranes compared to the PA-BARE, indicating that the introduction of BNNTs in the polyamide structure exposes the amide bonds prone to chlorine attacks. Previously

it was found that increasing the density of amide bonds in the PA membrane is a successful strategy for increasing chlorine resistance [338], and this is consistent with the decrease in crosslinking in the PA-BNNTs membranes leading to premature failure in presence of NaOCl. In fact, at an exposure of 5000 ppm over 1 hr, while $CaCl_2$ rejection of PA-BARE decreased from 89% to 73%, PA-BNNT 0.01wt% plummeted from 97% to 32%. The permeance of PA-BNNTs 0.02wt% increased from 3.67 LMH/bar to 4.68 LMH/bar after 11000 ppm over 1 hr chlorine exposure. However, it remained fairly steady for the other membranes, indicating that the maximum exposure tested did not dissolve the PA layer, but was enough to perturb it and decrease notably its ion rejection.

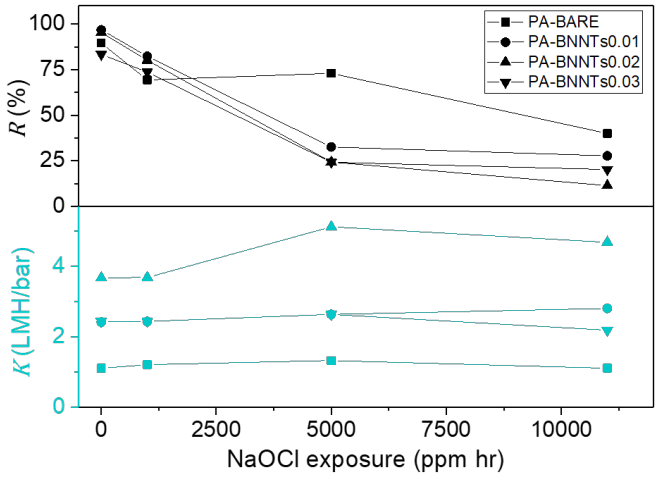

Figure 8-10: Rejection (R) of $CaCl_2$ and permeance (K) of PA-BARE, PA-BNNTs0.01, PA-BNNTs0.02 and PA-BNNTs0.03 as a function of the exposure to sodium hypochlorite.

The best performing PA-BNNTs membrane in this work could provide 4 times higher permeance than PA-BARE membranes with only 0.193 mg cm^{-2} of nanofiller on the membrane area. For their part, hydroxyl functionalised CNT membranes were reported to show 2 times higher pure water permeance than thin film polyamide membranes, but required 13.3 mg cm^{-2} of filler [19]. An increase of permeance up to 2.7 times was reported in PA-CNTs, but this required the use of 0.458 mg/cm^2 of modified MWCNTs. When compared with TFN membranes based on CNTs, the membranes in this work have therefore the capability to notably improve the permeance of pure polyamide using a limited amount of nanofiller (Table 8.6) without requiring functionalisation.

8.3 Conclusions

In this work, a known synthesis route for the production of boron nitride nanotubes was optimised and deployed for the production of large amounts of boron nitride nanotubes, which were then used as a nanofillers in nanofiltration thin film nanocomposite membranes prepared via interfacial polymerisation of PA. BNNTs homogeneously integrate in the polyamide layer, forming a B-O bond between the nanofiller and the polymer. Rejection of divalent and monovalent salts is not compromised for up to 0.02wt% BNNTs added to the aqueous phase in interfacial polymerisation, while the average permeance at this concentration goes up four times compared to the permeance of a membrane with no nanofiller. This is to be ascribed to an increase in water transport pathways given by the boron nitride nanochannels enveloped by the selective layer, with no appreciable loss of selectivity compared to the bare PA membrane. A permeance 4.5 times higher than in a bare PA membrane can be observed for low amounts of BNNTs, thus considerably limiting costs of adding nanofillers. Nonetheless, potential nanofiller leaking and recycling will have to be further investigated prior to large scale application, as BNNTs can be dangerous for the environment. In addition, the BNNTs membranes show a high resistance to irreversible fouling. This is a desirable condition for applications in, for example, the food industry, where standard operations take place in highly fouling environments.

Supplementary Information

This section contains detailed supporting results for this Chapter 8. A repository with the complete research data for this article can be found online [339].

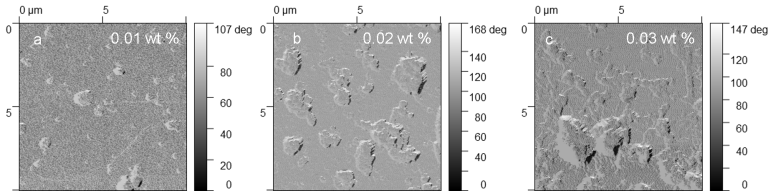

Figure 8-11: AFM phase plots of PA-BNNTs membranes with BNNTs loading of (a) 0.01 wt%, (b) 0.02 wt% and (c) 0.03 wt%.

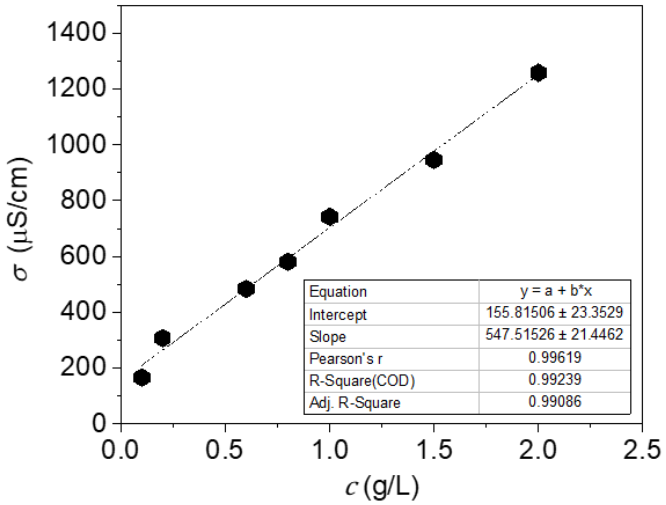

Figure 8-12: Conductivity σ (μS/cm) vs concentration c (g/L) calibration curve for $CaCl_2$. Each datapoint is repeated three times.

Table 8.4: Calculated ionic strengths (I) in mol/l for the solutions used for Figure 8-8.

	$CaCl_2$	$MgSO_4$	NaCl
I (mol/l)	7.2×10^{-2}	6.6×10^{-2}	2.6×10^{-2}

To assess the statistically significance difference between the two datasets in Figure 8-6, we can make a statistical comparison by noting that the green graph (PA bare) is uniformly higher than the orange graph (PA BNNTs) at each of its nine observed points.

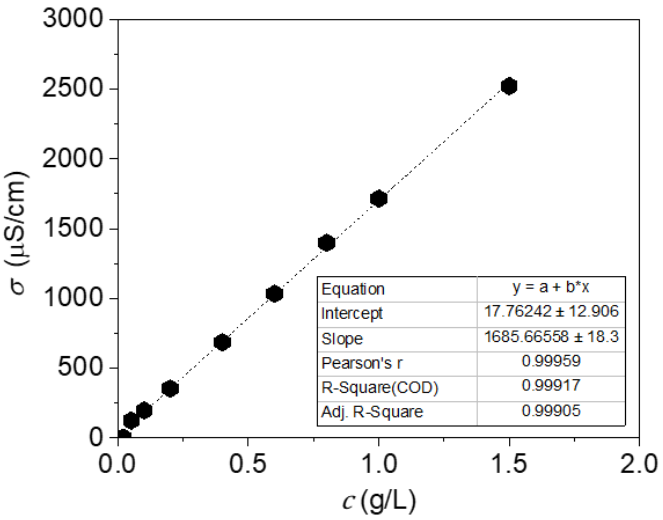

Figure 8-13: Conductivity σ (μS/cm) vs concentration c (g/L) calibration curve for NaCl. Each datapoint is repeated three times.

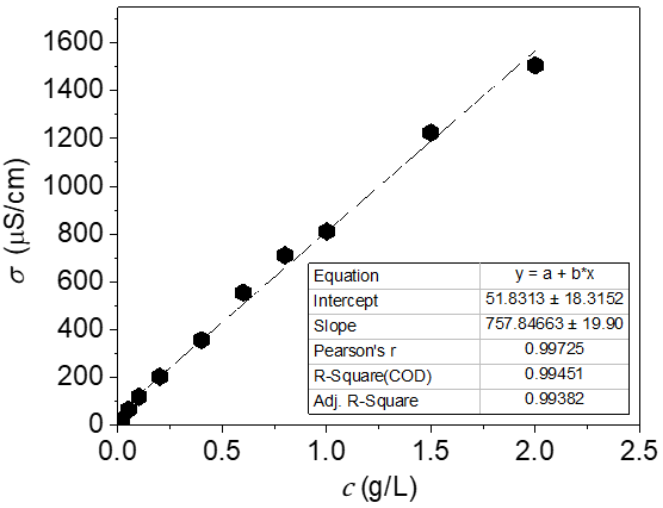

Figure 8-14: Conductivity σ (μS/cm) vs concentration c (g/L) calibration curve for $MgSO_4$. Each datapoint is repeated three times.

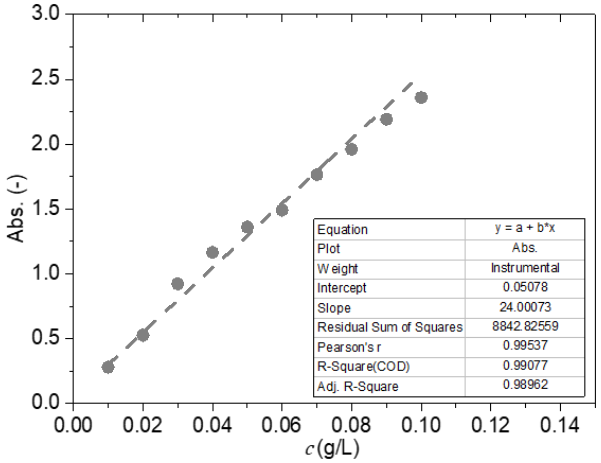

Figure 8-15: UV-vis light absorption (-) vs concentration c (g/L) calibration curve for humic acid. Each datapoint is repeated three times.

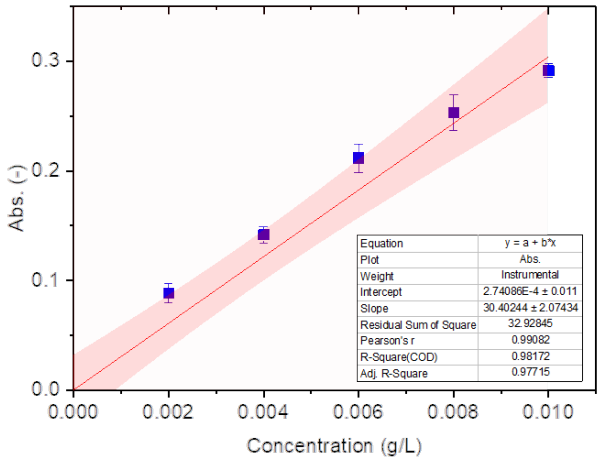

Figure 8-16: UV-vis light absorption (-) vs concentration c (g/L) calibration curve for methylene blue, with 95% confidence bands in the calibration. Each datapoint is repeated three times.

Table 8.5: Calculated membrane (R_m), irreversible (R_{ir}), reversible (R_r), total (R_t) and percentage ($R_{\%}$) resistances for the membranes under analysis during the second fouling cycle.

	PA-BARE	PA-BNNTs0.01	PA-BNNTs0.02	PA-BNNTs0.03
R_m	3.7 $\times 10^{+17}$ m^{-1}	6.5 $\times 10^{+16}$ m^{-1}	7.2 $\times 10^{+16}$ m^{-1}	5.6 $\times 10^{+16}$ m^{-1}
R_{ir}	2.8 $\times 10^{+15}$ m^{-1}	2.8 $\times 10^{+14}$ m^{-1}	3.7 $\times 10^{+15}$ m^{-1}	5.9 $\times 10^{+15}$ m^{-1}
R_r	4.3 $\times 10^{+17}$ m^{-1}	1.8 $\times 10^{+16}$ m^{-1}	2.1 $\times 10^{+16}$ m^{-1}	2.3 $\times 10^{+15}$ m^{-1}
R_t	8.0 $\times 10^{+17}$ m^{-1}	8.4 $\times 10^{+16}$ m^{-1}	9.8 $\times 10^{+16}$ m^{-1}	8.5 $\times 10^{+16}$ m^{-1}
$R_{\%}$	53.8 %	21.7 %	21.9 %	27.6 %

We will test the null hypothesis that there is really no difference between the data represented in the green and orange graphs.

If our null hypothesis is true then we would expect the green graph to have approximately half of its points above the orange graph and half below it. This means that, under the null hypothesis, the probability of a green point being above the orange graph would be 0.5.

We note that all nine green points are above the orange graph. The probability of this happening, under the null hypothesis, is 0.5 to the power 9 giving us a p-value of 0.0019. Therefore we have strong evidence to reject the null hypothesis of no difference between the data in the green and orange graphs, and adopt our alternative hypothesis that there is indeed a difference between the data represented in the two graphs.

Table 8.6: Comparison between the membranes analysed in this work and results in literature in terms of filler amount per unit membrane area (c_S), rejection R, permeance K and K/c_S.

ref.	**Nanofiller**	$\mathbf{c_S}$	R	K	$\mathbf{K/\ c_S}$
		(mg/cm^2)	%	LMH/bar	$LMH/bar/g/cm^2$
this work	BNNTs	0.096	97 % $CaCl_2$	2.7	28.02
		0.193	81 % $CaCl_2$	4.5	23.35
		0.289	45 % $CaCl_2$	4.1	14.19
[19]	PA bare	0.000	97% Na_2SO_4	3.5	-
	CNTs-COOH	13.333	94 % $MgSO_4$	6.2	0.47
	CNTs-OH	13.333	97 % $MgSO_4$	6.9	0.52
	CNTs-NH	13.333	95 % $MgSO_4$	5.3	0.40
[176]	PA bare	0.000	94 % $MgCl_2$	5.2	-
	CNTs	0.458	97 % $MgCl_2$	14.0	30.57
[324]	CNTs	1.931	75 % Na_2SO_4	0.7	3.61
[340]	PA bare	0.000	99 % Na_2SO_4	1.2	-
	CNTs	1.707	99 % Na_2SO_4	1.9	1.11

Chapter 9

Conclusions and Future Directions

9.1 Conclusions

The aim of this thesis was to investigate permeance, rejection and the scaling up potential of nanotube membranes based on materials other than carbon. Templated nanotubes made of boron nitride, carbon nitride and polystyrene were found ideal for performing fundamental studies. These allowed to meet the goal of better understanding of water flow and rejection in nanotube membranes. Specifically, the synthesis and testing of CNNTs and PNTs in anodic alumina allowed to decouple the effect of nanotube wall structure and surface chemistry on the flow of water. Templated BNNTs gave insights into charge-based rejection. Furthermore, the embedment of BNNTs in PA was tested to investigate the feasibility and potential of application of BNNTs membranes in commercial NF, evaluating these new composites as potentially beneficial for their improved water transport and antifouling properties.

9.1.1 Aligned NTs Synthesis, Characterisation and Modeling

In line with the objectives of this research, novel ways to produce nanotube membranes were developed. CNNTs and BNNTs were prepared by non catalytic CVD, and PNTs by solution soaking and annealing. The synthesis of CNNTs in the pores of AAMs was achieved from melamine in a simple degradation route which used confinement in the AAMs pores to form open nanotubes. This will open ways to simpler investigations of the potential of CNNTs membranes. BNNTs were produced with an analogous method in AAMs starting from borazane, and leading to a uniform distribution of boron nitride on both sides of AAMs with pore diameters $\sim$ 20 nm, and inside the pores. The surface charge of carbon nanotube membranes produced with an established CVD method - which however introduces a high amount of defects in the structure - was tuned by the implementation of a H_2 curing step. This was important to achieve and compare the performance of charged BNNTs with the one of CNTs with low surface charge. The synthesis of polystyrene nanotubes membranes by anodic alumina templates soaking in polymeric solutions was also performed. The membranes displayed a well-defined geometry and open pores, with thick NTs formed in the AAMs pores. This was achieved by means of a one-factor-at-a-time optimisation of key parameters impacting nanotube formation, and by adding a plasma etching step to bypass membrane surface clogging. NT membranes were characterised with Raman spectroscopy, FESEM and high resolution XPS amongst other techniques, to ascertain the structure and properties of the engineered materials. The detailed characterisation of the NTs material and their

defects allowed to build MD systems that truly reproduced their structure.

9.1.2 PA BNNTs Membranes Fabrication

Boron nitride nanomaterials previously showed improved antifouling capabilities and charge based rejection abilities that could overcome some of the CNTs limitations. Thus, one of the objectives of this thesis has been their application in TFN membranes. A known BNNT synthesis route was here optimised and deployed for their easy production in large amounts. BNNTs were then used as a nanofillers in membranes prepared via interfacial polymerisation of PA. A defect-free layer without the need for tubes' functionalisation was created for loading amounts up to 0.289 mg cm^{-2}. It was concluded that BNNTs homogeneously integrated in the PA layer, forming a B-O bond between the nanofiller and the polymer, and generating a membrane with improved performance.

9.1.3 Templated Nanotube Membranes Permeance

Experimental studies on water flow in nanotubes were found to be scarce, and mostly focused on CNTs. Thus, one of the objectives of this thesis was to compare pure water permeance through CNNT membranes to data obtained for CNTs in previous experimental work, which similarly used an AAM support with uniform and parallel nanopores, and with MD simulations. The latter were conducted on nanotube models built as a true reproduction of the structure of the synthesised materials, using the information gathered by their characterisation and wettability. This approach goes beyond traditional MD simulations conducted on perfect nanotubes (e.g. pristine CNTs). Both experiments and MD simulations showed that the presence of the C-N bonds hydrophilises the sp2 carbon structure of the nanotubes, resulting in a decrease of the pure water permeance compared to pristine and turbostratic CNTs membranes. These results are explained in terms of the strength of the solid-liquid interactions occurring at the tubes' walls, with the water at the CNNT walls showing increased water viscosity and decreased surface diffusion compared to CNTs. Therefore, the effect of nanotube wall structure and surface chemistry on the flow of water through a nanotube membrane could be decoupled. In line with the aims of this thesis, these models and results can offer membrane scientists a unique capability to design novel membranes and separation processes by way of controlling the permeance within nanotube membranes through membrane surface chemistry and structural changes to the nanotubes.

9.1.4 Templated Nanotube Membranes Rejection

A further objective of this thesis was the study of charge-based rejection in nanotube membranes. Using a custom made setup for testing, it was found that the choice of BNNTs over CNTs for the filtration of negatively charged nanoparticles results in a 45% higher permeance for the same rejection. MD and CFD studies showed that this is due to charge-based rejection, enabled by the charged structure of the BNNTs as opposed to the neutrally charged CNTs. With the purpose of better comprehending the phenomena, MD was used to analyse the impact of different nanoparticle to tube diameter ratios on rejection, while computational fluid dynamics investigated pressure. Both experiments and simulation show that BNNTs can reject nanoparticles down to 0.7 times smaller than their internal diameter and up to an external pressure of 6.6 bar. Thus, this work unravelled that BNNTs with larger diameters can be chosen to achieve similar rejection to carbon nanotubes, opening the way to significantly increasing the performance of commercial membranes in a variety of applications, from water treatment to bioprocessing.

9.1.5 PA BNNTs Membranes Performance

As CNTs have been used in interfacially polymerised membranes, we argued that BNNTs could serve as nanofillers enhancing water permeance in nanocomposite membranes. We found that rejection of divalent and monovalent salts is not compromised (within error) for up to 0.02wt% BNNTs added to the aqueous phase in interfacial polymerisation, while the average permeance at this concentration goes up four times compared to the permeance of a membrane with no nanofiller. This is to be ascribed to an increase in water transport pathways given by the boron nitride nanochannels enveloped by the selective layer, with no appreciable loss of selectivity compared to the bare PA membrane. A permeance 4.5 times higher than in a bare PA membrane can be observed for low amounts of BNNTs, thus considerably limiting costs of adding nanofillers and the membrane areas required to achieve set permeances. In addition, the BNNTs membranes show a high resistance to irreversible fouling. This is a desirable condition for applications in, for example, the food industry, where standard operations take place in highly fouling environments.

9.2 Proposed Future Work

This section recommends directions for future efforts in this area of research, based on the results achieved in this thesis.

9.2.1 Nanotube Membranes: Further Optimisation and Application

Once achieved the successful and repeatable synthesis of CNNTs, it was not within the scope of this thesis to develop synthesis routes to control for parameters such as tube diameter and degree of defects. A thorough study on synthesis parameters such as deposition time, precursor amount and furnace type could be further investigated. The choice of a different carrier, such as CO_2, could lead to lower C:N ratios producing CNNTs closer to the theoretical graphitic ratio. Increasing synthesis temperatures in the production of g- C_3N_4 was also found to improve the materials' visible light response for application in photocatalysis [341]. Furthermore, CNNTs membranes could be employed in applications such as CO_2 activation [342], metal-free catalysis [343] and sensing [344]. The production of BNNTs from borazane was adapted from the synthesis of BN on Cu and Pt foils [158, 239]. Porosimetry and FESEM analysis could be combined to have precise information on the percentage of blocked pores in AAM membranes.

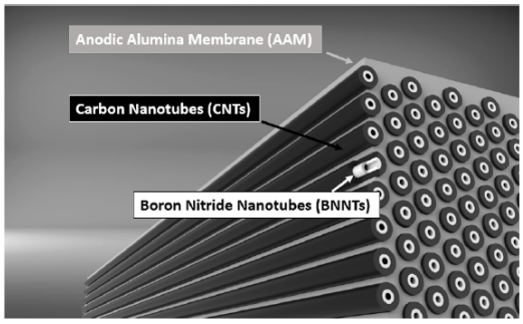

Figure 9-1: Schematic of the result of BNNTs coating in the pores of AAM with a substitution and growth type of synthesis.

This synthesis, on AAMs, is limited to a specific type of membrane not prepared from oxalic acid and that has to undergo a thermal treatment. This renders the procedure particularly costly, and not suitable for large scale utilisation. The process could be optimised by adding a low pressure step, to have a fine control on the thickness of the deposited layer [239], however tubes with smaller diameters can be also attained

by choosing templates with smaller pore sizes. A synthesis method based on a polymer thermolysis process that has been previously adopted at the microscale could be adapted to the nanoscale [345], however this choice would not address the limitations posed by the type of membrane that has to be chosen and the thermal treatment that membranes need to undergo. Another possible route for the formation of aligned BNNTs membranes was identified in the carbothermal substitution developed by Tay et al. [346], in a two step synthesis (substitution and growth), to form BNNTs on top of CNTs as schematised in Figure 9-1.

One evident extension of the work on PNT membranes would be the use of templates with smaller pore sizes to achieve tube inner diameters of $\sim$ 10 nm. Additionally, Porolux results could be coupled with molecular weight cut-off (MWCO) tests. MD could be used to compute values for D_S on the polymer tube walls as outlined in Section 4.7, and the water permeance could be modelled using the theoretical model amply discussed in this thesis and introduced in Section 2.2.4 that links tubes permeances to their geometry and surface-liquid interactions.

9.2.2 PA Membranes

One of the key factors limiting wider application of nanotubes in polymeric membranes is the difficulty of aligning them at the macroscale [347]. Thus, a major future effort should be focussed towards this goal.

Additionally, better techniques to study the distribution in the IP layer could be used, such as Raman mapping [236]. Additionally, mechanical testing of the produced membranes should be performed before larger scale adoption.

9.2.3 Nanofiller Leaking and Environmental and Health Risks

One of the issues that will eventually determine the large adoption of nanomaterial based membrane filters will be assessing whether the technology is safe. Specifically, nanotubes are high aspect-ratio nanomaterials that can have adverse health effects by irritating the respiratory track. Additionally, nanoparticles can be uptaken by living organisms, accumulate into organs as well as persist and bioaccumulate in the environment, entering the food chain [348].

Therefore, there is need for a standardised method to detect nanofiller leaking after long usage of TFN membranes, especially given the limited literature investigation

on the topic. There is still a gap in the hazard identification and characterisation that BNNTs and CNNTs pose to the human health and the environment [349, 350], although cytotoxicity (toxicity to living cells) was proved for BNNTs [226], CNTs [227] and CNNTs [228]. Established detailed risk assessment methodologies [351] could be extended to these novel nanomaterials as well. Lastly, further research should look into the production of nanotubes in a less energy intensive way, in the prospect of large applications in a carbon neutral era.

Bibliography

[1] Muhammad Wakil Shahzad, Muhammad Burhan, Li Ang, and Kim Choon Ng. Energy-water-environment nexus underpinning future desalination sustainability. *Desalination*, 413:52–64, 2017.

[2] J Mulder. *Basic principles of membrane technology*. Springer Science & Business Media, 2012.

[3] Ho Bum Park, Jovan Kamcev, Lloyd M Robeson, Menachem Elimelech, and Benny D Freeman. Maximizing the right stuff: The trade-off between membrane permeability and selectivity. *Science*, 356(6343):0530, 2017.

[4] Gerhard Hummer, Jayendran C Rasaiah, and Jerzy P Noworyta. Water conduction through the hydrophobic channel of a carbon nanotube. *Nature*, 414(6860): 188, 2001.

[5] RK Joshi, Paola Carbone, Feng Chao Wang, Vasyl G Kravets, Ying Su, Irina V Grigorieva, HA Wu, Andre K Geim, and Rahul Raveendran Nair. Precise and ultrafast molecular sieving through graphene oxide membranes. *science*, 343 (6172):752–754, 2014.

[6] Davide Mattia, Kah Peng Lee, and Francesco Calabrò. Water permeation in carbon nanotube membranes. *Current opinion in chemical engineering*, 4:32–37, 2014.

[7] Xingyu Lin, Qian Yang, Longhua Ding, and Bin Su. Ultrathin silica membranes with highly ordered and perpendicular nanochannels for precise and fast molecular separation. *ACS nano*, 9(11):11266–11277, 2015.

[8] Mainak Majumder, Nitin Chopra, and Bruce J Hinds. Effect of tip functionalization on transport through vertically oriented carbon nanotube membranes. *Journal of the American Chemical Society*, 127(25):9062–9070, 2005.

[9] G Che, BB Lakshmi, CR Martin, ER Fisher, and Rodney S Ruoff. Chemical vapor deposition based synthesis of carbon nanotubes and nanofibers using a template method. *Chemistry of Materials*, 10(1):260–267, 1998.

[10] Guangli Che, Brinda B Lakshmi, Ellen R Fisher, and Charles R Martin. Carbon nanotubule membranes for electrochemical energy storage and production. *Nature*, 393(6683):346, 1998.

[11] Yao Zheng, Jian Liu, Ji Liang, Mietek Jaroniec, and Shi Zhang Qiao. Graphitic carbon nitride materials: controllable synthesis and applications in fuel cells and photocatalysis. *Energy & Environmental Science*, 5(5):6717–6731, 2012.

[12] Ying Chen. *Nanotubes and Nanosheets: Functionalization and Applications of Boron Nitride and Other Nanomaterials*. CRC Press, 2015. ISBN 9781466598096.

[13] Tamsyn A Hilder, Daniel Gordon, and Shin-Ho Chung. Salt rejection and water transport through boron nitride nanotubes. *Small*, 5(19):2183–2190, 2009. ISSN 1613-6829.

[14] Eleonora Secchi, Sophie Marbach, Antoine Niguès, Derek Stein, Alessandro Siria, and Lydéric Bocquet. Massive radius-dependent flow slippage in carbon nanotubes. *Nature*, 537(7619):210, 2016.

[15] R Andrews, D Jacques, AM Rao, F Derbyshire, D Qian, X Fan, EC Dickey, and J Chen. Continuous production of aligned carbon nanotubes: a step closer to commercial realization. *Chemical physics letters*, 303(5-6):467–474, 1999.

[16] David B Hall, Patrick Underhill, and John M Torkelson. Spin coating of thin and ultrathin polymer films. *Polymer Engineering & Science*, 38(12):2039–2045, 1998.

[17] Bruce J Hinds, Nitin Chopra, Terry Rantell, Rodney Andrews, Vasilis Gavalas, and Leonidas G Bachas. Aligned multiwalled carbon nanotube membranes. *Science*, 303(5654):62–65, 2004.

[18] Davide Mattia, Hannah Leese, and Kah Peng Lee. Carbon nanotube membranes: from flow enhancement to permeability. *Journal of Membrane Science*, 475:266–272, 2015.

[19] Shuang-Mei Xue, Zhen-Liang Xu, Yong-Jian Tang, and Chen-Hao Ji. Polypiperazine-amide nanofiltration membrane modified by different functionalized multiwalled carbon nanotubes (MWCNTs). *ACS applied materials & interfaces*, 8(29):19135–19144, 2016.

[20] T.V. Ratto, J.K. Holt, and A.W. Szmodis. Membranes with embedded nanotubes for selective permeability, August 9 2011. URL `https://www.google.com/patents/US7993524`. US Patent 7,993,524.

[21] Maryam Amini, Mohsen Jahanshahi, and Ahmad Rahimpour. Synthesis of novel thin film nanocomposite (TFN) forward osmosis membranes using functionalized multi-walled carbon nanotubes. *Journal of Membrane Science*, 435:233–241, 2013.

[22] Takashi Kyotani, Li-fu Tsai, and Akira Tomita. Preparation of ultrafine carbon tubes in nanochannels of an anodic aluminum oxide film. *Chemistry of Materials*, 8(8):2109–2113, 1996.

[23] O Jessensky, F Müller, and U Gösele. Self-organized formation of hexagonal pore arrays in anodic alumina. *Applied physics letters*, 72(10):1173–1175, 1998.

[24] Mihail Gărăjeu, Henri Gouin, and Giuseppe Saccomandi. Scaling navier-stokes equation in nanotubes. *Physics of fluids*, 25(8):082003, 2013.

[25] M Whitby and N Quirke. Fluid flow in carbon nanotubes and nanopipes. *Nature nanotechnology*, 2(2):87, 2007.

[26] Brian Dean and Bharat Bhushan. Shark-skin surfaces for fluid-drag reduction in turbulent flow: a review. *Philosophical Transactions of the Royal Society of London A: Mathematical, Physical and Engineering Sciences*, 368(1929):4775–4806, 2010.

[27] Pfitzner. Poiseuille and his law. *Anaesthesia*, 31:273–275, 1976.

[28] Mainak Majumder, Nitin Chopra, Rodney Andrews, and Bruce J Hinds. Nanoscale hydrodynamics: enhanced flow in carbon nanotubes. *Nature*, 438 (7064):44, 2005.

[29] Jason K Holt, Hyung Gyu Park, Yinmin Wang, Michael Stadermann, Alexander B Artyukhin, Costas P Grigoropoulos, Aleksandr Noy, and Olgica Bakajin. Fast mass transport through sub-2-nanometer carbon nanotubes. *Science*, 312 (5776):1034–1037, 2006.

[30] Konstantinos Ritos, Davide Mattia, Francesco Calabrò, and Jason M Reese. Flow enhancement in nanotubes of different materials and lengths. *The Journal of chemical physics*, 140(1):014702, 2014.

[31] John A Thomas and Alan JH McGaughey. Reassessing fast water transport through carbon nanotubes. *Nano letters*, 8(9):2788–2793, 2008.

[32] Haiyang Yu, Youwei He, Peng Li, Shuang Li, Tiantian Zhang, Elena Rodriguez-Pin, Song Du, Chenglong Wang, Shiqing Cheng, Christopher W Bielawski, et al. Flow enhancement of water-based nanoparticle dispersion through microscale sedimentary rocks. *Scientific reports*, 5:8702, 2015.

[33] ME Suk, AV Raghunathan, and NR Aluru. Fast reverse osmosis using boron nitride and carbon nanotubes. *Applied Physics Letters*, 92(13):133120, 2008.

[34] Alexander Berezhkovskii and Gerhard Hummer. Single-file transport of water molecules through a carbon nanotube. *Physical review letters*, 89(6):064503, 2002.

[35] Matthew Melillo, Fangqiang Zhu, Mark A Snyder, and Jeetain Mittal. Water transport through nanotubes with varying interaction strength between tube wall and water. *The journal of physical chemistry letters*, 2(23):2978–2983, 2011.

[36] HK Lonsdale, Ulrich Merten, and RL Riley. Transport properties of cellulose acetate osmotic membranes. *Journal of Applied Polymer Science*, 9(4):1341–1362, 1965.

[37] Ludovic Garnier, Anthony Szymczyk, Patrice Malfreyt, and Aziz Ghoufi. Physics behind water transport through nanoporous boron nitride and graphene. *The journal of physical chemistry letters*, 7(17):3371–3376, 2016.

[38] Chongqin Zhu, Hui Li, and Sheng Meng. Transport behavior of water molecules through two-dimensional nanopores. *The Journal of chemical physics*, 141(18): 18C528, 2014.

[39] Gabriele Tocci, Laurent Joly, and Angelos Michaelides. Friction of water on graphene and hexagonal boron nitride from ab initio methods: very different slippage despite very similar interface structures. *Nano letters*, 14(12):6872–6877, 2014.

[40] JB Sokoloff. Enhancement of the water flow velocity through carbon nanotubes resulting from the radius dependence of the friction due to electron excitations. *Physical Review E*, 97(3):033107, 2018.

[41] John A Thomas, Alan JH McGaughey, and Ottoleo Kuter-Arnebeck. Pressure-driven water flow through carbon nanotubes: Insights from molecular dynamics simulation. *International journal of thermal sciences*, 49(2):281–289, 2010.

[42] Lydéric Bocquet and Elisabeth Charlaix. Nanofluidics, from bulk to interfaces. *Chemical Society Reviews*, 39(3):1073–1095, 2010.

[43] Kerstin Falk, Felix Sedlmeier, Laurent Joly, Roland R Netz, and Lydéric Bocquet. Molecular origin of fast water transport in carbon nanotube membranes: superlubricity versus curvature dependent friction. *Nano letters*, 10(10):4067–4073, 2010.

[44] Alessandro Siria, Philippe Poncharal, Anne-Laure Biance, Rémy Fulcrand, Xavier Blase, Stephen T Purcell, and Lydéric Bocquet. Giant osmotic energy conversion measured in a single transmembrane boron nitride nanotube. *Nature*, 494(7438): 455, 2013.

[45] Cécile Cottin-Bizonne, Jean-Louis Barrat, Lydéric Bocquet, and Elisabeth Charlaix. Low-friction flows of liquid at nanopatterned interfaces. *Nature materials*, 2(4):237–240, 2003.

[46] Lukas Schreiber and Jörg Schönherr. Permeance, diffusion and partition coefficients: Units and their conversion. *Water and Solute Permeability of Plant Cuticles: Measurement and Data Analysis*, pages 53–60, 2009.

[47] Davide Mattia and Francesco Calabrò. Explaining high flow rate of water in carbon nanotubes via solid–liquid molecular interactions. *Microfluidics and Nanofluidics*, 13(1):125–130, 2012.

[48] Francesco Calabrò. Modeling the effects of material chemistry on water flow enhancement in nanotube membranes. *MRS Bulletin*, 42(4):289–293, 2017.

[49] Jun Yin and Baolin Deng. Polymer-matrix nanocomposite membranes for water treatment. *Journal of membrane science*, 479:256–275, 2015.

[50] Tao Lin, Jianan Zhang, and Wei Chen. Recycling of activated carbon filter backwash water using ultrafiltration: Membrane fouling caused by different dominant interfacial forces. *Journal of Membrane Science*, 544:174–185, 2017.

[51] Myung-man Kim and Andrew L Zydney. Effect of electrostatic, hydrodynamic, and brownian forces on particle trajectories and sieving in normal flow filtration. *Journal of Colloid and Interface Science*, 269(2):425–431, 2004.

[52] Donald L Ermak and Helen Buckholz. Numerical integration of the langevin equation: Monte carlo simulation. *Journal of Computational Physics*, 35(2):169–182, 1980.

[53] W Richard Bowen, Anatoly N Filippov, Adel O Sharif, and Victor M Starov. A model of the interaction between a charged particle and a pore in a charged membrane surface. *Advances in Colloid and Interface Science*, 81(1):35–72, 1999.

[54] Amy Li and Goodarz Ahmadi. Dispersion and deposition of spherical particles from point sources in a turbulent channel flow. *Aerosol science and technology*, 16(4):209–226, 1992.

[55] Seung-Min Park, Jungwoo Jung, Sangho Lee, Youngbin Baek, Jeyong Yoon, Dong Kyun Seo, and Yong Hyup Kim. Fouling and rejection behavior of carbon nanotube membranes. *Desalination*, 343:180–186, 2014.

[56] Ben Corry. Designing carbon nanotube membranes for efficient water desalination. *The Journal of Physical Chemistry B*, 112(5):1427–1434, 2008.

[57] Ben Corry. Water and ion transport through functionalised carbon nanotubes: implications for desalination technology. *Energy & Environmental Science*, 4(3): 751–759, 2011.

[58] Amrit Kalra, Shekhar Garde, and Gerhard Hummer. Osmotic water transport through carbon nanotube membranes. *Proceedings of the National Academy of Sciences*, 100(18):10175–10180, 2003.

[59] Li Zhang, Lingjie Jia, Jing Zhang, Jiachen Li, Lijun Liang, Zhe Kong, Jia-Wei Shen, Xinping Wang, Wei Zhang, and Hongbo Wang. Understanding the effect of chemical modification on water desalination in boron nitride nanotubes via molecular dynamics simulation. *Desalination*, 464:84–93, 2019.

[60] Francesco Fornasiero, Hyung Gyu Park, Jason K Holt, Michael Stadermann, Costas P Grigoropoulos, Aleksandr Noy, and Olgica Bakajin. Ion exclusion by sub-2-nm carbon nanotube pores.

[61] Mainak Majumder and Ben Corry. Anomalous decline of water transport in covalently modified carbon nanotube membranes. *Chemical Communications*, 47 (27):7683–7685, 2011.

[62] Meijia Zhang, Bao-qiang Liao, Xiaoling Zhou, Yiming He, Huachang Hong, Hongjun Lin, and Jianrong Chen. Effects of hydrophilicity/hydrophobicity of

membrane on membrane fouling in a submerged membrane bioreactor. *Bioresource technology*, 175:59–67, 2015.

[63] Sumio Iijima and Toshinari Ichihashi. Single-shell carbon nanotubes of 1-nm diameter. *Nature*, 363(6430):603–605, 1993.

[64] O Stephan, PM Ajayan, C Colliex, Ph Redlich, et al. Doping graphitic and carbon nanotube structures with boron and nitrogen. *Science*, 266(5191):1683, 1994.

[65] Angel Rubio, Jennifer L Corkill, and Marvin L Cohen. Theory of graphitic boron nitride nanotubes. *Physical Review B*, 49(7):5081, 1994.

[66] Xifeng Lu, Hongjun Wang, Shuyong Zhang, Deliang Cui, and Qilong Wang. Synthesis, characterization and electrocatalytic properties of carbon nitride nanotubes for methanol electrooxidation. *Solid State Sciences*, 11(2):428–432, 2009.

[67] Shengping Wang, Changjiang Li, Tuo Wang, Peng Zhang, Ang Li, and Jinlong Gong. Controllable synthesis of nanotube-type graphitic c 3 n 4 and their visible-light photocatalytic and fluorescent properties. *Journal of Materials Chemistry A*, 2(9):2885–2890, 2014.

[68] N. G. Chopra and A. Zettl. *Solid State Commun*, 105, 1998. doi: 10.1016/s0038-1098(97)10125-9. URL `http://dx.doi.org/10.1016/S0038-1098(97)10125-9`.

[69] Jiesheng Wang, Chee Huei Lee, and Yoke Khin Yap. Recent advancements in boron nitride nanotubes. *Nanoscale*, 2(10):2028–2034, 2010.

[70] Wei-Qiang Han, W Mickelson, John Cumings, and A Zettl. Transformation of B x C y N z nanotubes to pure BN nanotubes. *Applied physics letters*, 81(6): 1110–1112, 2002.

[71] X Blase, A Rubio, SG Louie, and ML Cohen. Stability and band gap constancy of boron nitride nanotubes. *EPL (Europhysics Letters)*, 28(5):335, 1994. ISSN 0295-5075.

[72] Marvin L Cohen and Alex Zettl. The physics of boron nitride nanotubes. *Phys. Today*, 63(11):34–38, 2010.

[73] Dmitri Golberg, Yoshio Bando, Yang Huang, Takeshi Terao, Masanori Mitome, Chengchun Tang, and Chunyi Zhi. Boron nitride nanotubes and nanosheets. *ACS nano*, 4(6):2979–2993, 2010. ISSN 1936-0851.

[74] Xiaoming Chen, Liuyang Zhang, Cheol Park, Catharine C Fay, Xianqiao Wang, and Changhong Ke. Mechanical strength of boron nitride nanotube-polymer interfaces. *Applied Physics Letters*, 107(25):253105, 2015.

[75] Chunyi Zhi, Yoshio Bando, Chengchun Tang, Susumu Honda, Kazuhiko Sato, Hiroaki Kuwahara, and Dmitri Golberg. Characteristics of boron nitride nanotube–polyaniline composites. *Angewandte Chemie International Edition*, 44(48):7929–7932, 2005.

[76] Yoshiyuki Miyamoto, Marvin L Cohen, and Steven G Louie. Theoretical investigation of graphitic carbon nitride and possible tubule forms. *Solid State Communications*, 102(8):605–608, 1997.

[77] Qixun Guo, Yi Xie, Xinjun Wang, Shuyuan Zhang, Tao Hou, and Shichang Lv. Synthesis of carbon nitride nanotubes with the c 3 n 4 stoichiometry via a benzene-thermal process at low temperatures. *Chemical communications*, (1): 26–27, 2004.

[78] Shao-Wei Bian, Zhuo Ma, and Wei-Guo Song. Preparation and characterization of carbon nitride nanotubes and their applications as catalyst supporter. *The Journal of Physical Chemistry C*, 113(20):8668–8672, 2009.

[79] Sonja Tragl, Katharina Gibson, Jochen Glaser, Viola Duppel, Arndt Simon, and H-Jürgen Meyer. Template assisted formation of micro-and nanotubular carbon nitride materials. *Solid state communications*, 141(9):529–534, 2007.

[80] Mehmet Lütfi Yola, Tanju Eren, and Necip Atar. A molecular imprinted voltammetric sensor based on carbon nitride nanotubes: Application to determination of melamine. *Journal of The Electrochemical Society*, 163(13):B588–B593, 2016.

[81] Hui Pan, Yong-Wei Zhang, Vivek B Shenoy, and Huajian Gao. Ab initio study on a novel photocatalyst: functionalized graphitic carbon nitride nanotube. *Acs Catalysis*, 1(2):99–104, 2011.

[82] Zhenxing Zeng, Kexin Li, Liushui Yan, Yuhua Dai, Huiqin Guo, Mingxin Huo, and Yihang Guo. Fabrication of carbon nitride nanotubes by a simple water-induced morphological transformation process and their efficient visible-light photocatalytic activity. *RSC Advances*, 4(103):59513–59518, 2014.

[83] SH Lai, YL Chen, LH Chan, YM Pan, XW Liu, and HC Shih. The crystalline properties of carbon nitride nanotubes synthesized by electron cyclotron resonance plasma. *Thin Solid Films*, 444(1):38–43, 2003.

[84] Xiaojuan Bai, Li Wang, Ruilong Zong, and Yongfa Zhu. Photocatalytic activity enhanced via g-c3n4 nanoplates to nanorods. *The Journal of Physical Chemistry C*, 117(19):9952–9961, 2013.

[85] Mitesh B Panchal and SH Upadhyay. Doubly-clamped single walled boron nitride nanotube based nanomechanical resonators: A computational investigation of their behavior. *Journal of Nanotechnology in Engineering and Medicine*, 3(4): 044501, 2012. ISSN 1949-2944.

[86] Ayten Celik-Aktas, J-M Zuo, James F Stubbins, Chengchun Tang, and Yoshio Bando. Double-helix structure in multiwall boron nitride nanotubes. *Acta Crystallographica Section A: Foundations of Crystallography*, 61(6):533–541, 2005.

[87] Xiaoji G Xu, Leonid Gilburd, Yoshio Bando, Dmitri Golberg, and Gilbert C Walker. Defects and deformation of boron nitride nanotubes studied by joint nanoscale mechanical and infrared near-field microscopy. *The Journal of Physical Chemistry C*, 120(3):1945–1951, 2016. ISSN 1932-7447.

[88] Thang Pham, Ashley L Gibb, Zhenglu Li, S Matt Gilbert, Chengyu Song, Steven G Louie, and Alex Zettl. Formation and dynamics of electron-irradiation-induced defects in hexagonal boron nitride at elevated temperatures. *Nano Letters*, 16(11):7142–7147, 2016. ISSN 1530-6984.

[89] Nasreen G Chopra, RJ Luyken, K Cherrey, and Vincent H Crespi. Boron nitride nanotubes. *Science*, 269(5226):966, 1995. ISSN 0036-8075.

[90] Michael W Smith, Kevin C Jordan, Cheol Park, Jae-Woo Kim, Peter T Lillehei, Roy Crooks, and Joycelyn S Harrison. Very long single-and few-walled boron nitride nanotubes via the pressurized vapor/condenser method. *Nanotechnology*, 20(50):505604, 2009. ISSN 0957-4484.

[91] Chee Huei Lee, Shiva Bhandari, Bishnu Tiwari, Nazmiye Yapici, Dongyan Zhang, and Yoke Khin Yap. Boron nitride nanotubes: Recent advances in their synthesis, functionalization, and applications. *Molecules*, 21(7):922, 2016.

[92] Jiesheng Wang, Vijaya K Kayastha, Yoke Khin Yap, Zhiyong Fan, Jia G Lu, Zhengwei Pan, Ilia N Ivanov, Alex A Puretzky, and David B Geohegan. Low temperature growth of boron nitride nanotubes on substrates. *Nano letters*, 5 (12):2528–2532, 2005. ISSN 1530-6984.

[93] FL Deepak, CP Vinod, K Mukhopadhyay, A Govindaraj, and CNR Rao. Boron nitride nanotubes and nanowires. *Chemical Physics Letters*, 353(5):345–352, 2002. ISSN 0009-2614.

[94] Roland Yingjie Tay, Hongling Li, Siu Hon Tsang, Lin Jing, Dunlin Tan, Mingwei Wei, and Edwin Hang Tong Teo. Facile synthesis of millimeter-scale vertically aligned boron nitride nanotube forests by template-assisted chemical vapor deposition. *Chemistry of Materials*, 27(20):7156–7163, 2015. ISSN 0897-4756.

[95] Dmitri Golberg, Yoshio Bando, CC Tang, and CY Zhi. Boron nitride nanotubes. *Advanced Materials*, 19(18):2413–2432, 2007. ISSN 1521-4095.

[96] Oleg R Lourie, Carolyn R Jones, Bart M Bartlett, Patrick C Gibbons, Rodney S Ruoff, and William E Buhro. CVD growth of boron nitride nanotubes. *Chemistry of materials*, 12(7):1808–1810, 2000. ISSN 0897-4756.

[97] M Terauchi, M Tanaka, K Suzuki, A Ogino, and K Kimura. Production of zigzag-type BN nanotubes and BN cones by thermal annealing. *Chemical Physics Letters*, 324(5):359–364, 2000. ISSN 0009-2614.

[98] CC Tang, SS Fan, P Li, M Lamy de la Chapelle, and HY Dang. In situ catalytic growth of Al 2 O 3 and Si nanowires. *Journal of crystal growth*, 224(1):117–121, 2001.

[99] CC Tang, XX Ding, XT Huang, ZW Gan, SR Qi, W Liu, and SS Fan. Effective growth of boron nitride nanotubes. *Chemical physics letters*, 356(3):254–258, 2002. ISSN 0009-2614.

[100] Chengchun Tang, Yoshio Bando, Tadao Sato, and Keiji Kurashima. A novel precursor for synthesis of pure boron nitride nanotubes. *Chemical Communications*, (12):1290–1291, 2002. ISSN 1364-548X.

[101] Chengchun Tang, Yoshio Bando, and Dmitri Golberg. Multi-walled BN nanotubes synthesized by carbon-free method. *Journal of Solid State Chemistry*, 177 (8):2670–2674, 2004. ISSN 0022-4596.

[102] C.C. Tang, Y. Bando, and T. Sato. Synthesis and morphology of boron nitride nanotubes and nanohorns. *Applied Physics A*, 75(6):681–685, 2002. ISSN 1432-0630. doi: 10.1007/s00339-002-1498-1. URL `http://dx.doi.org/10.1007/s00339-002-1498-1`.

[103] Chunyi Zhi, Yoshio Bando, Chengchun Tan, and Dmitri Golberg. Effective precursor for high yield synthesis of pure BN nanotubes. *Solid state communications*, 135(1):67–70, 2005. ISSN 0038-1098.

[104] C. H. Lee, J. S. Wang, V. K. Kayatsha, J. Y. Huang, and Y. K. Yap. *Nanotechnology*, 19, 2008. doi: 10.1088/0957-4484/19/45/455605. URL `http://dx.doi.org/10.1088/0957-4484/19/45/455605`.

[105] Samuel L Mensah, Vijaya K Kayastha, Ilia N Ivanov, David B Geohegan, and Yoke Khin Yap. Formation of single crystalline ZnO nanotubes without catalysts and templates. *Applied physics letters*, 90(11):113108, 2007.

[106] JM Blakely and KA Jackson. Growth of crystal whiskers. *The Journal of Chemical Physics*, 37(2):428–430, 1962.

[107] W-K_ Burton, N Cabrera, and FC Frank. The growth of crystals and the equilibrium structure of their surfaces. *Philosophical Transactions of the Royal Society of London A: Mathematical, Physical and Engineering Sciences*, 243(866):299–358, 1951.

[108] Pervaiz Ahmad, Mayeen Uddin Khandaker, Yusoff Mohd Amin, and Ziaul Raza Khan. Influence of growth duration on size and morphology of boron nitride nanotubes grown via chemical vapor deposition technique. *Journal of Physics and Chemistry of Solids*, 85:226–232, 2015. ISSN 0022-3697.

[109] Pervaiz Ahmad, Mayeen Uddin Khandaker, and Yusoff Mohd Amin. Synthesis of boron nitride nanotubes by argon supported thermal chemical vapor deposition. *Physica E: Low-dimensional Systems and Nanostructures*, 67:33–37, 2015. ISSN 1386-9477.

[110] Yang Huang, Jing Lin, Chengchun Tang, Yoshio Bando, Chunyi Zhi, Tianyou Zhai, Benjamin Dierre, Takashi Sekiguchi, and Dmitri Golberg. Bulk synthesis, growth mechanism and properties of highly pure ultrafine boron nitride nanotubes with diameters of sub-10 nm. *Nanotechnology*, 22(14):145602, 2011. ISSN 0957-4484.

[111] Andrei T Matveev, Konstantin L Firestein, Alexander E Steinman, Andrey M Kovalskii, Oleg I Lebedev, Dmitry V Shtansky, and Dmitri Golberg. Boron nitride nanotube growth via boron oxide assisted chemical vapor transport-deposition process using lino3 as a promoter. *Nano Research*, 8(6):2063–2072, 2015. ISSN 1998-0124.

[112] Wei Li, Huan Yang, Shuaifeng Chen, Qing Chen, Lijie Luo, Jianbao Li, Yongjun Chen, and Changjiu Li. Temperature-dependent morphology evolution of boron nitride and boron carbonitride nanostructures. *Journal of Nanomaterials*, 2019, 2019.

[113] Chee Huei Lee, Ming Xie, Vijaya Kayastha, Jiesheng Wang, and Yoke Khin Yap. Patterned growth of boron nitride nanotubes by catalytic chemical vapor deposition. *Chemistry of Materials*, 22(5):1782–1787, 2010.

[114] Myung Jong Kim, Shahana Chatterjee, Seung Min Kim, Eric A Stach, Mark G Bradley, Mark J Pender, Larry G Sneddon, and Benji Maruyama. Double-walled boron nitride nanotubes grown by floating catalyst chemical vapor deposition. *Nano letters*, 8(10):3298–3302, 2008. ISSN 1530-6984.

[115] Ling Li, Lu Hua Li, Ying Chen, Xiujuan J Dai, Peter R Lamb, Bing-Ming Cheng, Meng-Yeh Lin, and Xiaowei Liu. High-quality boron nitride nanoribbons: unzipping during nanotube synthesis. *Angewandte Chemie International Edition*, 52 (15):4212–4216, 2013.

[116] Amir Pakdel, Chunyi Zhi, Yoshio Bando, Tomonobu Nakayama, and Dmitri Golberg. A comprehensive analysis of the CVD growth of boron nitride nanotubes. *Nanotechnology*, 23(21):215601, 2012. ISSN 0957-4484.

[117] Vijayesh Kumar, Palash Chandra Maity, Debrupa Lahiri, and Indranil Lahiri. Copper catalyzed growth of hexagonal boron nitride nanotubes on a tungsten substrate. *CrystEngComm*, 20(19):2713–2719, 2018.

[118] Wanseop Jeong, Jaewoo Kim, and Jaeyong Kim. Synthesis and physical properties of boron nitride nanotubes. *Science of Advanced Materials*, 9(2):276–279, 2017.

[119] Md Mokhlesur Rahman, Srikanth Mateti, Qiran Cai, Irin Sultana, Ye Fan, Xinwei Wang, Chunping Hou, and Ying Chen. High temperature and high rate lithium-ion batteries with boron nitride nanotubes coated polypropylene separators. *Energy Storage Materials*, 2019.

[120] Ben McLean, Clothilde A Eveleens, Izaac Mitchell, Grant B Webber, and Alister J Page. Catalytic CVD synthesis of boron nitride and carbon nanomaterials–synergies between experiment and theory. *Physical Chemistry Chemical Physics*, 19(39):26466–26494, 2017.

[121] Yao-Wen Yeh, Yevgeny Raitses, Bruce E Koel, and Nan Yao. Stable synthesis of few-layered boron nitride nanotubes by anodic arc discharge. *Scientific reports*, 7(1):3075, 2017.

[122] Biswajit Santra, Hsin-Yu Ko, Yao-Wen Yeh, Fausto Martelli, Igor Kaganovich, Yevgeny Raitses, and Roberto Car. Root-growth of boron nitride nanotubes: experiments and ab initio simulations. *Nanoscale*, 10(47):22223–22230, 2018.

[123] John Cumings and A Zettl. Mass-production of boron nitride double-wall nanotubes and nanococoons. *Chemical Physics Letters*, 316(3):211–216, 2000. ISSN 0009-2614.

[124] Chan Min Lee, SI Choi, SS Choi, and Sang Hee Hong. Synthesis of boron nitride nanotubes by arc-jet plasma. *Current Applied Physics*, 6(2):166–170, 2006. ISSN 1567-1739.

[125] D Golberg, A Rode, Y Bando, M Mitome, E Gamaly, and Barry Luther-Davies. Boron nitride nanostructures formed by ultra-high-repetition rate laser ablation. *Diamond and related materials*, 12(8):1269–1274, 2003. ISSN 0925-9635.

[126] Dmitri Golberg, Yoshio Bando, Mikhail Eremets, Keiji Kurashima, Takashi Tamiya, Kenichi Takemura, and Hitoshi Yusa. High–resolution analytical electron microscopy of boron nitrides laser heated at high pressure. *Journal of electron microscopy*, 46(4):281–292, 1997. ISSN 2050-5698.

[127] DP Yu, XS Sun, CS Lee, I Bello, ST Lee, HD Gu, KM Leung, GW Zhou, ZF Dong, and Z Zhang. Synthesis of boron nitride nanotubes by means of excimer laser ablation at high temperature. *Applied Physics Letters*, 72(16):1966–1968, 1998. ISSN 0003-6951.

[128] R Arenal, AC Ferrari, S Reich, Ludger Wirtz, J-Y Mevellec, S Lefrant, A Rubio, and A Loiseau. Raman spectroscopy of single-wall boron nitride nanotubes. *Nano letters*, 6(8):1812–1816, 2006. ISSN 1530-6984.

[129] M Cau, N Dorval, B Attal-Trétout, JL Cochon, B Cao, L Bresson, P Jaffrennou, M Silly, A Loiseau, and ED Obraztsova. Laser-based diagnostics applied to the study of BN nanotubes synthesis. *Journal of nanoscience and nanotechnology*, 8 (11):6129–6140, 2008. ISSN 1533-4880.

[130] VG Naumov, FK Kosyrev, VG Vostrikov, NR Arutyunyan, ED Obraztsova, VI Konov, Hua Jiang, A Nasibulin, and E Kauppinen. Synthesis of boron ni-

tride multi-walled nanotubes by laser ablation technique. *Laser physics*, 19(5): 1198–1200, 2009. ISSN 1054-660X.

[131] Peter A Gnoffo and Catharine C Fay. Laser vaporization and plume chemistry in a boron nitride nanotube production rig. *Journal of Thermophysics and Heat Transfer*, 27(3):369–381, 2013. ISSN 0887-8722.

[132] Aidin Fathalizadeh, Thang Pham, William Mickelson, and Alex Zettl. Scaled synthesis of boron nitride nanotubes, nanoribbons, and nanococoons using direct feedstock injection into an extended-pressure, inductively-coupled thermal plasma. *Nano letters*, 14(8):4881–4886, 2014. ISSN 1530-6984.

[133] Keun Su Kim, Christopher T Kingston, Amy Hrdina, Michael B Jakubinek, Jingwen Guan, Mark Plunkett, and Benoit Simard. Hydrogen-catalyzed, pilot-scale production of small-diameter boron nitride nanotubes and their macroscopic assemblies. *ACS nano*, 8(6):6211–6220, 2014. ISSN 1936-0851.

[134] Amanda L Tiano, Cheol Park, Joseph W Lee, Hoa H Luong, Luke J Gibbons, Sang-Hyon Chu, Samantha Applin, Peter Gnoffo, Sharon Lowther, and Hyun Jung Kim. Boron nitride nanotube: Synthesis and applications. In *SPIE Smart Structures and Materials+ Nondestructive Evaluation and Health Monitoring*, pages 906006–906006–19. International Society for Optics and Photonics.

[135] Stephen J Hales, Joel A Alexa, Brian J Jensen, and Donald L Thomsen. Radio frequency plasma synthesis of boron nitride nanotubes (BNNTs) for structural applications: Part i. 2016.

[136] Muhammad Sajjad, Vladimir Makarov, Ali Aldalbahi, Peter X Feng, Brad R Weiner, and Gerardo Morell. Synthesis micro-scale boron nitride nanotubes at low substrate temperature. *AIP Advances*, 6(7):075110, 2016. ISSN 2158-3226.

[137] D Golberg, Y Bando, M Eremets, K Takemura, K Kurashima, and H Yusa. Nanotubes in boron nitride laser heated at high pressure. *Applied Physics Letters*, 69(14):2045–2047, 1996. ISSN 0003-6951.

[138] RS Lee, J Gavillet, M Lamy de La Chapelle, A Loiseau, J-L Cochon, D Pigache, J Thibault, and F Willaime. Catalyst-free synthesis of boron nitride single-wall nanotubes with a preferred zig-zag configuration. *Physical Review B*, 64(12): 121405, 2001.

[139] Guang Wen Zhou, Ze Zhang, and Zhi Gang Bai. Catalyst effects on formation of boron nitride nano-tubules synthesized by laser ablation. *Solid state communications*, 109(8):555–559, 1999. ISSN 0038-1098.

[140] T. Laude, Y. Matsui, A. Marraud, and B. Jouffrey. *Appl Phys Lett*, 76, 2000. doi: 10.1063/1.126593. URL `http://dx.doi.org/10.1063/1.126593`.

[141] R. Arenal, O. Stephan, J. . L. Cochon, and A. Loiseau. *J Am Chem Soc*, 129, 2007. doi: 10.1021/ja076135n. URL `http://dx.doi.org/10.1021/ja076135n`.

[142] Jerry Augustine, Timonthy Cheung, Valerie Gies, Jennifer Boughton, Maohui Chen, Zygmunt Jakubek, Steven Walker, Yadienka Martinez-Rubi, Benoit Simard, and Shan Zou. Assessing size-dependent cytotoxicity of boron nitride nanotubes using a novel cardiomyocyte afm assay. *Nanoscale Advances*, 2019.

[143] Keun Su Kim, Martin Couillard, Homin Shin, Mark Plunkett, Dean Ruth, Christopher T Kingston, and Benoit Simard. Role of hydrogen in high-yield growth of boron nitride nanotubes at atmospheric pressure by induction thermal plasma. *ACS nano*, 12(1):884–893, 2018.

[144] B Zhong, L Song, XX Huang, GW Wen, and L Xia. Synthesis of boron nitride nanotubes with sic nanowire as template. *Materials Research Bulletin*, 46(9): 1521–1523, 2011. ISSN 0025-5408.

[145] Saban Kalay, Zehra Yilmaz, and Mustafa Çulha. Synthesis of boron nitride nanotubes from unprocessed colemanite. *Beilstein journal of nanotechnology*, 4 (1):843–851, 2013. ISSN 2190-4286.

[146] Weiqiang Han, Yoshio Bando, Keiji Kurashima, and Tadao Sato. Synthesis of boron nitride nanotubes from carbon nanotubes by a substitution reaction. *Applied Physics Letters*, 73(21):3085–3087, 1998. ISSN 0003-6951.

[147] D Golberg, Y Bando, W Han, K Kurashima, and T Sato. Single-walled b-doped carbon, B/N-doped carbon and BN nanotubes synthesized from single-walled carbon nanotubes through a substitution reaction. *Chemical Physics Letters*, 308(3):337–342, 1999. ISSN 0009-2614.

[148] D Golberg, Y Bando, K Kurashima, and T Sato. Moo 3-promoted synthesis of multi-walled BN nanotubes from c nanotube templates. *Chemical Physics Letters*, 323(1):185–191, 2000. ISSN 0009-2614.

[149] Qiang Zhang, Jia-Qi Huang, Meng-Qiang Zhao, Wei-Zhong Qian, and Fei Wei. Carbon nanotube mass production: principles and processes. *ChemSusChem*, 4 (7):864–889, 2011. ISSN 1864-564X.

[150] Kaili Jiang, Jiaping Wang, Qunqing Li, Liang Liu, Changhong Liu, and Shoushan Fan. Superaligned carbon nanotube arrays, films, and yarns: a road to applications. *Advanced Materials*, 23(9):1154–1161, 2011. ISSN 1521-4095.

[151] Konstantin B Shelimov and Martin Moskovits. Composite nanostructures based on template-grown boron nitride nanotubules. *Chemistry of Materials*, 12(1): 250–254, 2000. ISSN 0897-4756.

[152] Mikhael Bechelany, Samuel Bernard, Arnaud Brioude, David Cornu, Pierre Stadelmann, Catherine Charcosset, Koffi Fiaty, and Philippe Miele. Synthesis of boron nitride nanotubes by a template-assisted polymer thermolysis process. *The Journal of Physical Chemistry C*, 111(36):13378–13384, 2007. ISSN 1932-7447.

[153] XZ Wang, Q Wu, Z Hu, and Y Chen. Template-directed synthesis of boron nitride nanotube arrays by microwave plasma chemical reaction. *Electrochimica acta*, 52(8):2841–2844, 2007. ISSN 0013-4686.

[154] Matthieu Weber, Boonprakrong Koonkaew, Sebastien Balme, Ivo Utke, Fabien Picaud, Igor Iatsunskyi, Emerson Coy, Philippe Miele, and Mikhael Bechelany. Boron nitride nanoporous membranes with high surface charge by atomic layer deposition. *ACS applied materials & interfaces*, 9(19):16669–16678, 2017.

[155] Wei-Qiang Han, Peter J Todd, and Myron Strongin. Formation and growth mechanism of 10BN nanotubes via a carbon nanotube-substitution reaction. *Applied physics letters*, 89(17):3103, 2006. ISSN 0003-6951.

[156] CC Tang, M Lamy de la Chapelle, P Li, YM Liu, HY Dang, and SS Fan. Catalytic growth of nanotube and nanobamboo structures of boron nitride. *Chemical physics letters*, 342(5):492–496, 2001. ISSN 0009-2614.

[157] Yuting Wang, Shiro Shimada, Yasunori Yamamoto, and Norio Miyaura. Preparation of h-BN nano-tubes,-bamboos, and-fibers from borazine oligomer with alumina porous template. *Materials Research Bulletin*, 43(2):251–256, 2008. ISSN 0025-5408.

[158] Ki Kang Kim, Allen Hsu, Xiaoting Jia, Soo Min Kim, Yumeng Shi, Mario Hofmann, Daniel Nezich, Joaquin F Rodriguez-Nieva, Mildred Dresselhaus, Tomas

Palacios, et al. Synthesis of monolayer hexagonal boron nitride on cu foil using chemical vapor deposition. *Nano letters*, 12(1):161–166, 2011.

[159] Ji-Hoon Park, Jin Cheol Park, Seok Joon Yun, Hyun Kim, Dinh Hoa Luong, Soo Min Kim, Soo Ho Choi, Woochul Yang, Jing Kong, Ki Kang Kim, et al. Large-area monolayer hexagonal boron nitride on pt foil. *Acs Nano*, 8(8):8520–8528, 2014.

[160] Carlo M Orofeo, Satoru Suzuki, Hiroyuki Kageshima, and Hiroki Hibino. Growth and low-energy electron microscopy characterization of monolayer hexagonal boron nitride on epitaxial cobalt. *Nano Research*, 6(5):335–347, 2013.

[161] Chenping Wu, Abdul Majid Soomro, Feipeng Sun, Huachun Wang, Youyang Huang, Jiejun Wu, Chuan Liu, Xiaodong Yang, Na Gao, Xiaohong Chen, et al. Large-roll growth of 25-inch hexagonal BN monolayer film for self-release buffer layer of free-standing gan wafer. *Scientific reports*, 6:34766, 2016.

[162] Guangyuan Lu, Tianru Wu, Qinghong Yuan, Huishan Wang, Haomin Wang, Feng Ding, Xiaoming Xie, and Mianheng Jiang. Synthesis of large single-crystal hexagonal boron nitride grains on cu–ni alloy. *Nature communications*, 6:6160, 2015.

[163] Klaus-Viktor Peinemann, Volker Abetz, and Peter FW Simon. Asymmetric superstructure formed in a block copolymer via phase separation. *Nature materials*, 6(12):992, 2007.

[164] Juliana Isabel Clodt, Volkan Filiz, Sofia Rangou, Kristian Buhr, Clarissa Abetz, Daniel Höche, Janina Hahn, Adina Jung, and Volker Abetz. Double stimuli-responsive isoporous membranes via post-modification of ph-sensitive self-assembled diblock copolymer membranes. *Advanced Functional Materials*, 23(6): 731–738, 2013.

[165] Thomas Bucher, Volkan Filiz, Clarissa Abetz, and Volker Abetz. Formation of thin, isoporous block copolymer membranes by an upscalable profile roller coating process—a promising way to save block copolymer. *Membranes*, 8(3):57, 2018.

[166] Martin Steinhart, Ralf B Wehrspohn, Ulrich Gösele, and Joachim H Wendorff. Nanotubes by template wetting: a modular assembly system. *Angewandte Chemie International Edition*, 43(11):1334–1344, 2004.

[167] Hui Wu, Yuji Higaki, and Atsushi Takahara. Molecular self-assembly of one-dimensional polymer nanostructures in nanopores of anodic alumina oxide templates. *Progress in Polymer Science*, 77:95–117, 2018.

[168] Martin Steinhart, Stephan Senz, Ralf B Wehrspohn, Ulrich Gösele, and Joachim H Wendorff. Curvature-directed crystallization of poly (vinylidene difluoride) in nanotube walls. *Macromolecules*, 36(10):3646–3651, 2003.

[169] Mingfu Zhang, Priyanka Dobriyal, Jiun-Tai Chen, Thomas P Russell, Jessica Olmo, and Aurora Merry. Wetting transition in cylindrical alumina nanopores with polymer melts. *Nano letters*, 6(5):1075–1079, 2006.

[170] Stefanie Schlitt, Andreas Greiner, and Joachim H Wendorff. Cylindrical polymer nanostructures by solution template wetting. *Macromolecules*, 41(9):3228–3234, 2008.

[171] Shin-Ya Akatsuka, Hiroshi Yoshigiwa, and Yasuhiko H Mori. Temperature dependencies of spreading coefficients of hydrocarbons on water. *Journal of colloid and interface science*, 172(2):335–340, 1995.

[172] Kah Peng Lee, Tom C. Arnot, and Davide Mattia. A review of reverse osmosis membrane materials for desalination—development to date and future potential. *Journal of Membrane Science*, 370(1–2):1 – 22, 2011. ISSN 0376-7388. doi: https://doi.org/10.1016/j.memsci.2010.12.036. URL `http://www.sciencedirect.com/science/article/pii/S0376738810010045`.

[173] Babak Rajaeian, Ahmad Rahimpour, Moses O Tade, and Shaomin Liu. Fabrication and characterization of polyamide thin film nanocomposite (tfn) nanofiltration membrane impregnated with tio2 nanoparticles. *Desalination*, 313:176–188, 2013.

[174] Sagar Roy, Susana Addo Ntim, Somenath Mitra, and Kamalesh K Sirkar. Facile fabrication of superior nanofiltration membranes from interfacially polymerized cnt-polymer composites. *Journal of membrane science*, 375(1-2):81–87, 2011.

[175] Ludovic Dumée, Judy Lee, Kallista Sears, Blaise Tardy, Mikel Duke, and Stephen Gray. Fabrication of thin film composite poly (amide)-carbon-nanotube supported membranes for enhanced performance in osmotically driven desalination systems. *Journal of membrane science*, 427:422–430, 2013.

[176] Hai-Zhen Zhang, Zhen-Liang Xu, Hao Ding, and Yong-Jian Tang. Positively charged capillary nanofiltration membrane with high rejection for Mg2+ and Ca2+ and good separation for Mg2+ and li+. *Desalination*, 420:158–166, 2017.

[177] Guo-dong Kang and Yi-ming Cao. Development of antifouling reverse osmosis membranes for water treatment: a review. *Water research*, 46(3):584–600, 2012.

[178] Zviel Gal and Avi Efraty. Ccd series no. 18: record low energy in closed-circuit desalination of ocean seawater with nanoh2o elements without erd. *Desalination and Water Treatment*, 57(20):9180–9189, 2016.

[179] Emerson L Wittbecker and Paul W Morgan. Interfacial polycondensation. i. *Journal of Polymer Science*, 40(137):289–297, 1959.

[180] Dan Li and Huanting Wang. Recent developments in reverse osmosis desalination membranes. *Journal of Materials Chemistry*, 20(22):4551–4566, 2010.

[181] Jane Kucera. *Desalination: water from water*. John Wiley & Sons, 2019.

[182] Yongyang Song, Jun-Bing Fan, and Shutao Wang. Recent progress in interfacial polymerization. *Materials Chemistry Frontiers*, 1(6):1028–1040, 2017.

[183] Sanne Hermans, Roy Bernstein, Alexander Volodin, and Ivo FJ Vankelecom. Study of synthesis parameters and active layer morphology of interfacially polymerized polyamide–polysulfone membranes. *Reactive and Functional Polymers*, 86:199–208, 2015.

[184] Kaihua Shen, Debang Qi, Ying Li, Xinglin Zhao, and Yang Li. Amphiphilic tertiary amine n-oxides: a mediated radical emulsion polymerization with non-formation of alkoxyamine dormant chains. *Chemical Communications*, 51(50): 10166–10169, 2015.

[185] Santanu Karan, Zhiwei Jiang, and Andrew G Livingston. Sub–10 nm polyamide nanofilms with ultrafast solvent transport for molecular separation. *Science*, 348 (6241):1347–1351, 2015.

[186] Nathalie C Mougin, Patrick Van Rijn, Hyunji Park, Axel HE Müller, and Alexander Böker. Hybrid capsules via self-assembly of thermoresponsive and interfacially active bionanoparticle–polymer conjugates. *Advanced Functional Materials*, 21 (13):2470–2476, 2011.

[187] Victor V Yashin and Anna C Balazs. Theoretical model of interfacial polymerization. *The Journal of chemical physics*, 121(22):11440–11454, 2004.

[188] WJ Lau, AF Ismail, N Misdan, and MA Kassim. A recent progress in thin film composite membrane: a review. *Desalination*, 287:190–199, 2012.

[189] B-X Yang, Kumari Pallathadka Pramoda, Guo Qin Xu, and Suat Hong Goh. Mechanical reinforcement of polyethylene using polyethylene-grafted multiwalled carbon nanotubes. *Advanced Functional Materials*, 17(13):2062–2069, 2007.

[190] Keun-Young Shin, Sunghun Cho, and Jyongsik Jang. Graphene/polyaniline/poly (4-styrenesulfonate) hybrid film with uniform surface resistance and its flexible dipole tag antenna application. *small*, 9(22):3792–3798, 2013.

[191] Wansuk Choi, Joung-Eun Gu, Sang-Hee Park, Seyong Kim, Joona Bang, Kyung-Youl Baek, Byoungnam Park, Jong Suk Lee, Edwin P Chan, and Jung-Hyun Lee. Tailor-made polyamide membranes for water desalination. *ACS nano*, 9(1): 345–355, 2015.

[192] Xin-Gui Li, Yaozu Liao, Mei-Rong Huang, and Richard B Kaner. Interfacial chemical oxidative synthesis of multifunctional polyfluoranthene. *Chemical science*, 6(3):2087–2101, 2015.

[193] Kah P Lee, Jumeng Zheng, Gerrald Bargeman, Antoine JB Kemperman, and Nieck E Benes. ph stable thin film composite polyamine nanofiltration membranes by interfacial polymerisation. *Journal of membrane science*, 478:75–84, 2015.

[194] F MacRitchie. Mechanism of interfacial polymerization. *Transactions of the Faraday Society*, 65:2503–2507, 1969.

[195] Chunfang Zhang, Kaifang Wei, Wenhai Zhang, Yunxiang Bai, Yuping Sun, and Jin Gu. Graphene oxide quantum dots incorporated into a thin film nanocomposite membrane with high flux and antifouling properties for low-pressure nanofiltration. *ACS applied materials & interfaces*, 9(12):11082–11094, 2017.

[196] Pravin G Ingole, Muhammad Irshad Baig, Won Kil Choi, and Hyung Keun Lee. Synthesis and characterization of polyamide/polyester thin-film nanocomposite membranes achieved by functionalized tio 2 nanoparticles for water vapor separation. *Journal of Materials Chemistry A*, 4(15):5592–5604, 2016.

[197] WJ Lau, Stephen Gray, T Matsuura, D Emadzadeh, J Paul Chen, and AF Ismail. A review on polyamide thin film nanocomposite (tfn) membranes: history, applications, challenges and approaches. *Water research*, 80:306–324, 2015.

[198] Mary L Lind, Asim K Ghosh, Anna Jawor, Xiaofei Huang, William Hou, Yang Yang, and Eric MV Hoek. Influence of zeolite crystal size on zeolite-polyamide thin film nanocomposite membranes. *Langmuir*, 25(17):10139–10145, 2009.

[199] Dangchen Ma, Shing Bo Peh, Gang Han, and Shing Bor Chen. Thin-film nanocomposite (tfn) membranes incorporated with super-hydrophilic metal–organic framework (mof) uio-66: toward enhancement of water flux and salt rejection. *ACS applied materials & interfaces*, 9(8):7523–7534, 2017.

[200] T Sirinupong, W Youravong, D Tirawat, WJ Lau, GS Lai, and AF Ismail. Synthesis and characterization of thin film composite membranes made of psf-tio2/go nanocomposite substrate for forward osmosis applications. *Arabian Journal of Chemistry*, 11(7):1144–1153, 2018.

[201] Luying Wang, Manquan Fang, Jing Liu, Jing He, Jiding Li, and Jiandu Lei. Layer-by-layer fabrication of high-performance polyamide/zif-8 nanocomposite membrane for nanofiltration applications. *ACS applied materials & interfaces*, 7 (43):24082–24093, 2015.

[202] Daryoush Emadzadeh, Woei Jye Lau, T Matsuura, Ahmad Fauzi Ismail, and M Rahbari-Sisakht. Synthesis and characterization of thin film nanocomposite forward osmosis membrane with hydrophilic nanocomposite support to reduce internal concentration polarization. *Journal of membrane science*, 449:74–85, 2014.

[203] WJ Lau, AF Ismail, PS Goh, Nidal Hilal, and BS Ooi. Characterization methods of thin film composite nanofiltration membranes. *Separation & Purification Reviews*, 44(2):135–156, 2015.

[204] Hyun Soo Lee, Se Joon Im, Jong Hak Kim, Hee Jin Kim, Jong Pyo Kim, and Byoung Ryul Min. Polyamide thin-film nanofiltration membranes containing tio2 nanoparticles. *Desalination*, 219(1-3):48–56, 2008.

[205] Seung Yun Lee, Hee Jin Kim, Rajkumar Patel, Se Joon Im, Jong Hak Kim, and Byoung Ryul Min. Silver nanoparticles immobilized on thin film composite polyamide membrane: characterization, nanofiltration, antifouling properties. *Polymers for Advanced Technologies*, 18(7):562–568, 2007.

[206] Qiang Li, Yihua Wang, Jie Song, Yipeng Guan, Hui Yu, Xianhui Pan, Feiyang Wu, and Meng Zhang. Influence of silica nanospheres on the separation performance of thin film composite poly (piperazine-amide) nanofiltration membranes. *Applied Surface Science*, 324:757–764, 2015.

[207] Junfeng Zheng, Meng Li, Yujian Yao, Xuan Zhang, and Lianjun Wang. Zwitterionic carbon nanotube assisted thin-film nanocomposite membranes with excellent efficiency for separation of mono/divalent ions from brackish water. *Journal of Materials Chemistry A*, 5(26):13730–13739, 2017.

[208] M Ghanbari, D Emadzadeh, WJ Lau, SO Lai, T Matsuura, and AF Ismail. Synthesis and characterization of novel thin film nanocomposite (tfn) membranes embedded with halloysite nanotubes (hnts) for water desalination. *Desalination*, 358:33–41, 2015.

[209] GS Lai, WJ Lau, PS Goh, YH Tan, BC Ng, and AF Ismail. A novel interfacial polymerization approach towards synthesis of graphene oxide-incorporated thin film nanocomposite membrane with improved surface properties. *Arabian journal of chemistry*, 2017.

[210] Yafei Li, Yanlei Su, Yanan Dong, Xueting Zhao, Zhongyi Jiang, Runnan Zhang, and Jiaojiao Zhao. Separation performance of thin-film composite nanofiltration membrane through interfacial polymerization using different amine monomers. *Desalination*, 333(1):59–65, 2014.

[211] MN Abu Seman, M Khayet, and Nidal Hilal. Nanofiltration thin-film composite polyester polyethersulfone-based membranes prepared by interfacial polymerization. *Journal of membrane science*, 348(1-2):109–116, 2010.

[212] Yan Zhang, Yanlei Su, Jinming Peng, Xueting Zhao, Jiazhan Liu, Jiaojiao Zhao, and Zhongyi Jiang. Composite nanofiltration membranes prepared by interfacial polymerization with natural material tannic acid and trimesoyl chloride. *Journal of membrane science*, 429:235–242, 2013.

[213] Adel Soroush, Jalal Barzin, Mahdi Barikani, and Mahdi Fathizadeh. Interfacially polymerized polyamide thin film composite membranes: Preparation, characterization and performance evaluation. *Desalination*, 287:310–316, 2012.

[214] Jintang Duan, Eric Litwiller, and Ingo Pinnau. Preparation and water desalination properties of poss-polyamide nanocomposite reverse osmosis membranes. *Journal of membrane science*, 473:157–164, 2015.

[215] Hai Huang, Xinying Qu, Xiaosheng Ji, Xin Gao, Lin Zhang, Huanlin Chen, and Lian Hou. Acid and multivalent ion resistance of thin film nanocomposite ro membranes loaded with silicalite-1 nanozeolites. *Journal of Materials Chemistry A*, 1(37):11343–11349, 2013.

[216] Fan Xiao, Biao Wang, Xiaoyu Hu, Sankar Nair, and Yingbo Chen. Thin film nanocomposite membrane containing zeolitic imidazolate framework-8 via interfacial polymerization for highly permeable nanofiltration. *Journal of the Taiwan Institute of Chemical Engineers*, 83:159–167, 2018.

[217] Sara Sorribas, Patricia Gorgojo, Carlos Teellez, Joaquin Coronas, and Andrew G Livingston. High flux thin film nanocomposite membranes based on metal organic frameworks for organic solvent nanofiltration. *Journal of the American Chemical Society*, 135(40):15201–15208, 2013.

[218] Eun-Sik Kim, Geelsu Hwang, Mohamed Gamal El-Din, and Yang Liu. Development of nanosilver and multi-walled carbon nanotubes thin-film nanocomposite membrane for enhanced water treatment. *Journal of membrane science*, 394: 37–48, 2012.

[219] Behnam Khorshidi, Ishita Biswas, Tanushree Ghosh, Thomas Thundat, and Mohtada Sadrzadeh. Robust fabrication of thin film polyamide-tio 2 nanocomposite membranes with enhanced thermal stability and anti-biofouling propensity. *Scientific reports*, 8(1):784, 2018.

[220] CY Tang, Y Zhao, R Wang, C Hélix-Nielsen, and AG Fane. Desalination by biomimetic aquaporin membranes: Review of status and prospects. *Desalination*, 308:34–40, 2013.

[221] Yang Zhao, Changquan Qiu, Xuesong Li, Ardcharaporn Vararattanavech, Wenming Shen, Jaume Torres, Claus Helix-Nielsen, Rong Wang, Xiao Hu, Anthony G Fane, et al. Synthesis of robust and high-performance aquaporin-based biomimetic membranes by interfacial polymerization-membrane preparation and ro performance characterization. *Journal of Membrane Science*, 423:422–428, 2012.

[222] PS Goh, AF Ismail, and Nidal Hilal. Nano-enabled membranes technology: sustainable and revolutionary solutions for membrane desalination? *Desalination*, 380:100–104, 2016.

[223] Joachim Habel, Michael Hansen, Søren Kynde, Nanna Larsen, Søren Midtgaard, Grethe Jensen, Julie Bomholt, Anayo Ogbonna, Kristoffer Almdal, Alexander Schulz, et al. Aquaporin-based biomimetic polymeric membranes: approaches and challenges. *Membranes*, 5(3):307–351, 2015.

[224] Chiu-wing Lam, John T James, Richard McCluskey, Sivaram Arepalli, and Robert L Hunter. A review of carbon nanotube toxicity and assessment of potential occupational and environmental health risks. *Critical reviews in toxicology*, 36(3):189–217, 2006.

[225] Michael Fischman, Eileen Storey, Robert J McCunney, and Michael Kosnett. National institute for occupational safety and health nanomaterials and worker health conference—medical surveillance session summary report. *Journal of occupational and environmental medicine*, 53:S35–S37, 2011.

[226] Lenke Horvath, Arnaud Magrez, Dmitri Golberg, Chunyi Zhi, Yoshio Bando, Rita Smajda, Endre Horvath, Laszlo Forro, and Beat Schwaller. In vitro investigation of the cellular toxicity of boron nitride nanotubes. *ACS nano*, 5(5):3800–3810, 2011.

[227] Guang Jia, Haifang Wang, Lei Yan, Xiang Wang, Rongjuan Pei, Tao Yan, Yuliang Zhao, and Xinbiao Guo. Cytotoxicity of carbon nanomaterials: single-wall nanotube, multi-wall nanotube, and fullerene. *Environmental science & technology*, 39(5):1378–1383, 2005.

[228] ML Zhao, DJ Li, L Yuan, YC Yue, H Liu, and X Sun. Differences in cytocompatibility and hemocompatibility between carbon nanotubes and nitrogen-doped carbon nanotubes. *Carbon*, 49(9):3125–3133, 2011.

[229] Kazuma Higashisaka, Yasuo Yoshioka, Kohei Yamashita, Yuki Morishita, Maho Fujimura, Hiromi Nabeshi, Kazuya Nagano, Yasuhiro Abe, Haruhiko Kamada, Shin-ichi Tsunoda, et al. Acute phase proteins as biomarkers for predicting the exposure and toxicity of nanomaterials. *Biomaterials*, 32(1):3–9, 2011.

[230] Padmavati Manchikanti and Tapas K Bandopadhyay. Nanomaterials and effects on biological systems: development of effective regulatory norms. *Nanoethics*, 4 (1):77–83, 2010.

[231] Charles-François de Lannoy, Elif Soyer, and Mark R Wiesner. Optimizing carbon nanotube-reinforced polysulfone ultrafiltration membranes through carboxylic acid functionalization. *Journal of membrane science*, 447:395–402, 2013.

[232] Farhad Asempour, Somaye Akbari, Du Bai, Daryoush Emadzadeh, Takeshi Matsuura, and Boguslaw Kruczek. Improvement of stability and performance of functionalized halloysite nano tubes-based thin film nanocomposite membranes. *Journal of membrane science*, 563:470–480, 2018.

[233] Douglas L Gin and Richard D Noble. Designing the next generation of chemical separation membranes. *Science*, 332(6030):674–676, 2011.

[234] Christopher Bellona and Jörg E Drewes. The role of membrane surface charge and solute physico-chemical properties in the rejection of organic acids by nf membranes. *Journal of Membrane Science*, 249(1-2):227–234, 2005.

[235] Hongjin Lim, Bong Lim Suh, Myung Jong Kim, Hongseok Yun, Jihan Kim, Bumjoon J Kim, and Se Gyu Jang. High-performance, recyclable ultrafiltration membranes from p4vp-assisted dispersion of flame-resistive boron nitride nanotubes. *Journal of membrane science*, 551:172–179, 2018.

[236] Ze-Xian Low, Jing Ji, David Blumenstock, Yong-Min Chew, Daniel Wolverson, and Davide Mattia. Fouling resistant 2d boron nitride nanosheet–pes nanofiltration membranes. *Journal of membrane science*, 563:949–956, 2018.

[237] Lindsey R Bornhoeft, Aida C Castillo, Preston R Smalley, Carter Kittrell, Dustin K James, Bruce E Brinson, Thomas R Rybolt, Bruce R Johnson, Tonya K Cherukuri, and Paul Cherukuri. Teslaphoresis of carbon nanotubes. *ACS nano*, 10(4):4873–4881, 2016.

[238] D Mattia, MP Rossi, BM Kim, G Korneva, HH Bau, and Y Gogotsi. Effect of graphitization on the wettability and electrical conductivity of CVD-carbon nanotubes and films. *The Journal of Physical Chemistry B*, 110(20):9850–9855, 2006.

[239] Gwangwoo Kim, A-Rang Jang, Hu Young Jeong, Zonghoon Lee, Dae Joon Kang, and Hyeon Suk Shin. Growth of high-crystalline, single-layer hexagonal boron nitride on recyclable platinum foil. *Nano letters*, 13(4):1834–1839, 2013.

[240] Chuyang Y Tang, Young-Nam Kwon, and James O Leckie. Probing the nano-and micro-scales of reverse osmosis membranes—a comprehensive characterization of physiochemical properties of uncoated and coated membranes by xps, tem, atr-ftir, and streaming potential measurements. *Journal of Membrane Science*, 287 (1):146–156, 2007.

[241] Robert N Wenzel. Surface roughness and contact angle. *The Journal of Physical Chemistry*, 53(9):1466–1467, 1949.

[242] Adri CT Van Duin, Siddharth Dasgupta, Francois Lorant, and William A Goddard. ReaxFF: a reactive force field for hydrocarbons. *The Journal of Physical Chemistry A*, 105(41):9396–9409, 2001.

[243] Anthony K Rappe and William A Goddard III. Charge equilibration for molecular dynamics simulations. *The Journal of Physical Chemistry*, 95(8):3358–3363, 1991.

[244] Konstantinos Ritos, Nishanth Dongari, Matthew K Borg, Yonghao Zhang, and Jason M Reese. Dynamics of nanoscale droplets on moving surfaces. *Langmuir*, 29(23):6936–6943, 2013.

[245] Frederick M Fowkes and William D Harkins. The state of monolayers adsorbed at the interface solid—aqueous solution. *Journal of the American Chemical Society*, 62(12):3377–3386, 1940.

[246] Matthew K Borg, Duncan A Lockerby, Konstantinos Ritos, and Jason M Reese. Multiscale simulation of water flow through laboratory-scale nanotube membranes. *Journal of membrane science*, 567:115–126, 2018.

[247] Jens Honore Walther, T Werder, RL Jaffe, P Gonnet, M Bergdorf, U Zimmerli, and P Koumoutsakos. Water–carbon interactions iii: the influence of surface and fluid impurities. *Physical Chemistry Chemical Physics*, 6(8):1988–1995, 2004.

[248] Konstantinos Ritos, Matthew K Borg, Duncan A Lockerby, David R Emerson, and Jason M Reese. Hybrid molecular-continuum simulations of water flow through carbon nanotube membranes of realistic thickness. *Microfluidics and Nanofluidics*, 19(5):997–1010, 2015.

[249] Matthew K Borg and Jason M Reese. Multiscale simulation of enhanced water flow in nanotubes. *MRS Bulletin*, 42(4):294–299, 2017.

[250] Harold L Weissberg. End correction for slow viscous flow through long tubes. *The Physics of Fluids*, 5(9):1033–1036, 1962.

[251] John A Thomas and Alan JH McGaughey. Water flow in carbon nanotubes: transition to subcontinuum transport. *Physical Review Letters*, 102(18):184502, 2009.

[252] Steve Plimpton. Fast parallel algorithms for short-range molecular dynamics. *Journal of computational physics*, 117(1):1–19, 1995.

[253] Jose LF Abascal and Carlos Vega. A general purpose model for the condensed phases of water: Tip4p/2005. *The Journal of chemical physics*, 123(23):234505, 2005.

[254] Jean-Paul Ryckaert, Giovanni Ciccotti, and Herman JC Berendsen. Numerical integration of the cartesian equations of motion of a system with constraints:

molecular dynamics of n-alkanes. *Journal of computational physics*, 23(3):327–341, 1977.

[255] Roger W Hockney and James W Eastwood. *Computer simulation using particles*. crc Press, 1988.

[256] Sang Soo Han, Jeung Ku Kang, Hyuck Mo Lee, Adri CT Van Duin, and William A Goddard III. The theoretical study on interaction of hydrogen with single-walled boron nitride nanotubes. i. the reactive force field reaxff hbn development. *The Journal of chemical physics*, 123(11):114703, 2005.

[257] Serena Casanova, Matthew K Borg, YM John Chew, and Davide Mattia. Surface-controlled water flow in nanotube membranes. *ACS applied materials & interfaces*, 11(1):1689–1698, 2018.

[258] Randall T Cygan, Jian-Jie Liang, and Andrey G Kalinichev. Molecular models of hydroxide, oxyhydroxide, and clay phases and the development of a general force field. *The Journal of Physical Chemistry B*, 108(4):1255–1266, 2004.

[259] HA Zambrano, Jens Honore Walther, and RL Jaffe. Molecular dynamics simulations of water on a hydrophilic silica surface at high air pressures. *Journal of Molecular Liquids*, 198:107–113, 2014.

[260] Jens Honore Walther, Richard L Jaffe, EM Kotsalis, Thomas Werder, Timur Halicioglu, and Petros Koumoutsakos. Hydrophobic hydration of c60 and carbon nanotubes in water. *Carbon*, 42(5-6):1185–1194, 2004.

[261] V. Barwick. Preparation of calibration curves: A guide to best practice. *National Measurement System Valid Analytical Measurement (VAM) Programme*, 2003.

[262] Davide Mattia and Yury Gogotsi. Static and dynamic behavior of liquids inside carbon nanotubes. *Microfluidics and Nanofluidics*, 5(3):289–305, 2008.

[263] Rasel Das, Md Eaqub Ali, Sharifah Bee Abd Hamid, Seeram Ramakrishna, and Zaira Zaman Chowdhury. Carbon nanotube membranes for water purification: a bright future in water desalination. *Desalination*, 336:97–109, 2014.

[264] Xiangju Song, Li Wang, Lili Mao, and Zhining Wang. Nanocomposite membrane with different carbon nanotubes location for nanofiltration and forward osmosis applications. *ACS Sustainable Chemistry & Engineering*, 4(6):2990–2997, 2016.

[265] Truong Quoc Vo and BoHung Kim. Transport phenomena of water in molecular fluidic channels. *Scientific reports*, 6:33881, 2016.

[266] Shashank Sinha, Maria Pia Rossi, D Mattia, Yury Gogotsi, and Haim H Bau. Induction and measurement of minute flow rates through nanopipes. *Physics of Fluids*, 19(1):013603, 2007.

[267] Jacob N Israelachvili and Richard M Pashley. Molecular layering of water at surfaces and origin of repulsive hydration forces. *Nature*, 306(5940):249, 1983.

[268] Mahdi Khademi and Muhammad Sahimi. Molecular dynamics simulation of pressure-driven water flow in silicon-carbide nanotubes. *The Journal of chemical physics*, 135(20):204509, 2011.

[269] Kah Peng Lee, Hannah Leese, and Davide Mattia. Water flow enhancement in hydrophilic nanochannels. *Nanoscale*, 4(8):2621–2627, 2012.

[270] Hui Li and Xiao Cheng Zeng. Wetting and interfacial properties of water nanodroplets in contact with graphene and monolayer boron–nitride sheets. *ACS Nano*, 6(3):2401–2409, 2012.

[271] Christian Sendner, Dominik Horinek, Lyderic Bocquet, and Roland R Netz. Interfacial water at hydrophobic and hydrophilic surfaces: Slip, viscosity, and diffusion. *Langmuir*, 25(18):10768–10781, 2009.

[272] Tuan Anh Ho, Dimitrios V Papavassiliou, Lloyd L Lee, and Alberto Striolo. Liquid water can slip on a hydrophilic surface. *Proceedings of the National Academy of Sciences*, 108(39):16170–16175, 2011.

[273] Sony Joseph and NR Aluru. Why are carbon nanotubes fast transporters of water? *Nano letters*, 8(2):452–458, 2008.

[274] WD Nicholls, Matthew Karl Borg, Duncan A Lockerby, and JM Reese. Water transport through carbon nanotubes with defects. *Molecular Simulation*, 38(10): 781–785, 2012.

[275] Jens H Walther, Konstantinos Ritos, Eduardo R Cruz-Chu, Constantine M Megaridis, and Petros Koumoutsakos. Barriers to superfast water transport in carbon nanotube membranes. *Nano letters*, 13(5):1910–1914, 2013.

[276] Bo Yuan, Zengyong Chu, Gongyi Li, Zhenhua Jiang, Tianjiao Hu, Qinghua Wang, and Chunhua Wang. Water-soluble ribbon-like graphitic carbon nitride (gc 3 n 4): green synthesis, self-assembly and unique optical properties. *Journal of Materials Chemistry C*, 2(39), 2014.

[277] Hannah Leese. *Electroosmosis in nanoporous membranes: connecting material properties to flow behaviour*. Thesis, 2013.

[278] Jiao Wu, Xiangjun Zheng, Chao Jin, Jinghua Tian, and Ruizhi Yang. Ternary doping of phosphorus, nitrogen, and sulfur into porous carbon for enhancing electrocatalytic oxygen reduction. *Carbon*, 92:327–338, 2015.

[279] Qiao Liu, Youxin Duan, Qiuping Zhao, Fuping Pan, Bin Zhang, and Junyan Zhang. Direct synthesis of nitrogen-doped carbon nanosheets with high surface area and excellent oxygen reduction performance. *Langmuir*, 30(27):8238–8245, 2014.

[280] K Ganesan, Subrata Ghosh, Nanda Gopala Krishna, S Ilango, M Kamruddin, and AK Tyagi. A comparative study on defect estimation using XPS and Raman spectroscopy in few layer nanographitic structures. *Physical Chemistry Chemical Physics*, 18(32):22160–22167, 2016.

[281] A Belen Jorge, David James Martin, Mandeep TS Dhanoa, Aisha S Rahman, Neel Makwana, Junwang Tang, Andrea Sella, Furio Coraa, Steven Firth, Jawwad A Darr, et al. H2 and O2 evolution from water half-splitting reactions by graphitic carbon nitride materials. *The Journal of Physical Chemistry C*, 117(14):7178–7185, 2013.

[282] Yiou Wang, Mustafa K Bayazit, Savio JA Moniz, Qiushi Ruan, Chi Ching Lau, Natalia Martsinovich, and Junwang Tang. Linker-controlled polymeric photocatalyst for highly efficient hydrogen evolution from water. *Energy & Environmental Science*, 10(7):1643–1651, 2017.

[283] Borg M. Chew J. Mattia D. Casanova, S. Dataset for "Surface-controlled water flow in nanotube membranes", 2019. URL `https://doi.org/10.15125/BATH-00613`.

[284] Andy Field. *Discovering statistics using IBM SPSS statistics*. sage, 2013.

[285] Jae Hyun Park and NR Aluru. Ordering-induced fast diffusion of nanoscale water film on graphene. *The Journal of Physical Chemistry C*, 114(6):2595–2599, 2010.

[286] A. W. Adamson and A. P. Gast. Adsorption of gases and vapors on solids. *Physical Chemistry of Surfaces*, 1997.

[287] Mark A Shannon, Paul W Bohn, Menachem Elimelech, John G Georgiadis, Benito J Marinas, and Anne M Mayes. Science and technology for water purification in the coming decades. *Nature*, 452(7185):301–310, 2008.

[288] Patrizia Marchetti, Maria F Jimenez Solomon, Gyorgy Szekely, and Andrew G Livingston. Molecular separation with organic solvent nanofiltration: a critical review. *Chemical reviews*, 114(21):10735–10806, 2014.

[289] John A Howell, V Sanchez, and Robert W Field. *Membranes in bioprocessing: theory and applications*. Springer Science & Business Media, 2012.

[290] RR Nair, HA Wu, PN Jayaram, IV Grigorieva, and AK Geim. Unimpeded permeation of water through helium-leak–tight graphene-based membranes. *Science*, 335(6067):442–444, 2012.

[291] Xiujuan J Dai, Ying Chen, Zhiqiang Chen, Peter R Lamb, Lu H Li, Johan du Plessis, Dougal G McCulloch, and Xungai Wang. Controlled surface modification of boron nitride nanotubes. *Nanotechnology*, 22(24):245301, 2011.

[292] Weiwei Lei, Vadym N Mochalin, Dan Liu, Si Qin, Yury Gogotsi, and Ying Chen. Boron nitride colloidal solutions, ultralight aerogels and freestanding membranes through one-step exfoliation and functionalization. *Nature communications*, 6: 8849, 2015.

[293] Ryszard Sprycha. Electrical double layer at alumina/electrolyte interface: I. surface charge and zeta potential. *Journal of colloid and interface science*, 127 (1):1–11, 1989.

[294] MJ Crimp, DA Oppermann, and K Krehbiel. Suspension properties of hexagonal bn powders: effect of ph and oxygen content. *Journal of materials science*, 34 (11):2621–2625, 1999.

[295] Mistry S. Mazinani S. Borg M. Chew J. Mattia D. Casanova, S. Dataset for "Enhanced nanoparticle rejection in aligned boron nitride nanotube membranes". URL `https://researchdata.bath.ac.uk`.

[296] David Megias-Alguacil, Elena Tervoort, Cyrill Cattin, and Ludwig J Gauckler. Contact angle and adsorption behavior of carboxylic acids on α-Al2O3 surfaces. *Journal of colloid and interface science*, 353(2):512–518, 2011.

[297] Michael S Bresnehan, Matthew J Hollander, Maxwell Wetherington, Ke Wang, Takahira Miyagi, Gregory Pastir, David W Snyder, Jamie J Gengler, Andrey A Voevodin, William C Mitchel, et al. Prospects of direct growth boron nitride films as substrates for graphene electronics. *Journal of Materials Research*, 29 (3):459–471, 2014.

[298] Kah Peng Lee and Davide Mattia. Monolithic nanoporous alumina membranes for ultrafiltration applications: Characterization, selectivity–permeability analysis and fouling studies. *Journal of membrane science*, 435:52–61, 2013.

[299] Nadine Tarantino, Jean-Yves Tinevez, Elizabeth Faris Crowell, Bertrand Boisson, Ricardo Henriques, Musa Mhlanga, Fabrice Agou, Alain Israël, and Emmanuel Laplantine. Tnf and il-1 exhibit distinct ubiquitin requirements for inducing nemo–ikk supramolecular structures. *J Cell Biol*, 204(2):231–245, 2014.

[300] XueMei Tan and Denis Rodrigue. A review on porous polymeric membrane preparation. part i: Production techniques with polysulfone and poly (vinylidene fluoride). *Polymers*, 11(7):1160, 2019.

[301] Bart Van der Bruggen and Carlo Vandecasteele. Removal of pollutants from surface water and groundwater by nanofiltration: overview of possible applications in the drinking water industry. *Environmental pollution*, 122(3):435–445, 2003.

[302] Simon Gravelle, Laurent Joly, François Detcheverry, Christophe Ybert, Cécile Cottin-Bizonne, and Lydéric Bocquet. Optimizing water permeability through the hourglass shape of aquaporins. *Proceedings of the National Academy of Sciences*, 110(41):16367–16372, 2013.

[303] Haiyang Zhao, Shi Qiu, Liguang Wu, Lin Zhang, Huanlin Chen, and Congjie Gao. Improving the performance of polyamide reverse osmosis membrane by incorporation of modified multi-walled carbon nanotubes. *Journal of Membrane Science*, 450:249–256, 2014.

[304] Hui Wu, Yan Cao, Ryohei Ishige, Yuji Higaki, Taiki Hoshino, Noboru Ohta, and Atsushi Takahara. Confinement-induced crystal growth in one-dimensional isotactic polystyrene nanorod arrays. *ACS Macro Letters*, 2(5):414–418, 2013.

[305] Chia-Chan Tsai and Jiun-Tai Chen. Rayleigh instability in polymer thin films coated in the nanopores of anodic aluminum oxide templates. *Langmuir*, 30(1): 387–393, 2013.

[306] Go Matsuba, Keisuke Kaji, Koji Nishida, Toshiji Kanaya, and Masayuki Imai. Conformational change and orientation fluctuations prior to the crystallization of syndiotactic polystyrene. *Macromolecules*, 32(26):8932–8937, 1999.

[307] Casanova S. Mohamed H. Kapil N. Xiao X. Zhang Y. Coppens M. Mattia D. Meng, Z. Dataset for "Water flow enhancement in polymer nanotube membranes", 2019. URL `https://doi.org/10.15125/BATH-00721`.

[308] Pei Xu, Tzahi Y Cath, Alexander P Robertson, Martin Reinhard, James O Leckie, and Jörg E Drewes. Critical review of desalination concentrate management, treatment and beneficial use. *Environmental Engineering Science*, 30 (8):502–514, 2013.

[309] Edward Jones, Manzoor Qadir, Michelle TH van Vliet, Vladimir Smakhtin, and Seong-mu Kang. The state of desalination and brine production: A global outlook. *Science of the Total Environment*, 2018.

[310] Sangho Lee, Juneseok Choi, Yong-Gyun Park, Hokyong Shon, Chang Hoon Ahn, and Seung-Hyun Kim. Hybrid desalination processes for beneficial use of reverse osmosis brine: Current status and future prospects. *Desalination*, 454:104–111, 2019.

[311] Law Yong Ng, Abdul Wahab Mohammad, Choe Peng Leo, and Nidal Hilal. Polymeric membranes incorporated with metal/metal oxide nanoparticles: a comprehensive review. *Desalination*, 308:15–33, 2013.

[312] Zhifeng Fan, Zhi Wang, Ning Sun, Jixiao Wang, and Shichang Wang. Performance improvement of polysulfone ultrafiltration membrane by blending with polyaniline nanofibers. *Journal of Membrane Science*, 320(1-2):363–371, 2008.

[313] Y Mansourpanah, SS Madaeni, A Rahimpour, M Adeli, MY Hashemi, and MR Moradian. Fabrication new pes-based mixed matrix nanocomposite membranes using polycaprolactone modified carbon nanotubes as the additive: property changes and morphological studies. *Desalination*, 277(1-3):171–177, 2011.

[314] Haiyang Zhao, Liguang Wu, Zhijun Zhou, Lin Zhang, and Huanlin Chen. Improving the antifouling property of polysulfone ultrafiltration membrane by incorporation of isocyanate-treated graphene oxide. *Physical Chemistry Chemical Physics*, 15(23):9084–9092, 2013.

[315] Eric MV Hoek, Asim K Ghosh, Xiaofei Huang, Monty Liong, and Jeffrey I Zink. Physical–chemical properties, separation performance, and fouling resistance of mixed-matrix ultrafiltration membranes. *Desalination*, 283:89–99, 2011.

[316] Song Zhao, Zhi Wang, Xin Wei, Xinxia Tian, Jixiao Wang, Shangbao Yang, and Shichang Wang. Comparison study of the effect of PVP and PANI nanofibers additives on membrane formation mechanism, structure and performance. *Journal of membrane science*, 385:110–122, 2011.

[317] Jesús María Arsuaga, Arcadio Sotto, Gilberto del Rosario, Ana Martínez, Serena Molina, Shivanand B Teli, and Javier de Abajo. Influence of the type, size, and distribution of metal oxide particles on the properties of nanocomposite ultrafiltration membranes. *Journal of membrane science*, 428:131–141, 2013.

[318] Parisa Daraei, Sayed Siavash Madaeni, Negin Ghaemi, Ehsan Salehi, Mohammad Ali Khadivi, Rostam Moradian, and Bandar Astinchap. Novel polyethersulfone nanocomposite membrane prepared by PANI/Fe3O4 nanoparticles with enhanced performance for Cu (ii) removal from water. *Journal of Membrane Science*, 415:250–259, 2012.

[319] A Rahimpour, SS Madaeni, AH Taheri, and Y Mansourpanah. Coupling TiO2 nanoparticles with UV irradiation for modification of polyethersulfone ultrafiltration membranes. *Journal of Membrane Science*, 313(1-2):158–169, 2008.

[320] Menachem Elimelech and William A Phillip. The future of seawater desalination: energy, technology, and the environment. *science*, 333(6043):712–717, 2011.

[321] Mohammadali Baghbanzadeh, Dipak Rana, Christopher Q Lan, and Takeshi Matsuura. Effects of inorganic nano-additives on properties and performance of polymeric membranes in water treatment. *Separation & Purification Reviews*, 45(2):141–167, 2016.

[322] Jun Yin, Guocheng Zhu, and Baolin Deng. Multi-walled carbon nanotubes (MWNTs)/polysulfone (PSU) mixed matrix hollow fiber membranes for enhanced water treatment. *Journal of membrane science*, 437:237–248, 2013.

[323] Huiqing Wu, Beibei Tang, and Peiyi Wu. MWNTs/polyester thin film nanocomposite membrane: an approach to overcome the trade-off effect between permeability and selectivity. *The Journal of Physical Chemistry C*, 114(39):16395–16400, 2010.

[324] Chang Chao Yu, Hong Wei Yu, Yue Xia Chu, Hui Min Ruan, and Jiang Nan Shen. Preparation thin film nanocomposite membrane incorporating PMMA modified MWNT for nanofiltration. In *Key Engineering Materials*, volume 562, pages 882–886. Trans Tech Publ, 2013.

[325] Wai-Fong Chan, Hang-yan Chen, Anil Surapathi, Michael G Taylor, Xiaohong Shao, Eva Marand, and J Karl Johnson. Zwitterion functionalized carbon nanotube/polyamide nanocomposite membranes for water desalination. *Acs Nano*, 7(6):5308–5319, 2013.

[326] Junwoo Park, Wansuk Choi, Sung Hyun Kim, Byung Hee Chun, Joona Bang, and Ki Bong Lee. Enhancement of chlorine resistance in carbon nanotube based nanocomposite reverse osmosis membranes. *Desalination and Water Treatment*, 15(1-3):198–204, 2010.

[327] Chang Y Won and Narayana R Aluru. Water permeation through a subnanometer boron nitride nanotube. *Journal of the American Chemical Society*, 129(10): 2748–2749, 2007.

[328] TM Chen, J Xiao, and GW Yang. Cubic boron nitride with an intrinsic peroxidase-like activity. *RSC Advances*, 6(74):70124–70132, 2016.

[329] Bingping Liu, Shihai Yan, Zhongqian Song, Mengli Liu, Xuqiang Ji, Wenrong Yang, and Jingquan Liu. One-step synthesis of boron nitride quantum dots: Simple chemistry meets delicate nanotechnology. *Chemistry–A European Journal*, 22(52):18899–18907, 2016.

[330] NK Saha and SV Joshi. Performance evaluation of thin film composite polyamide nanofiltration membrane with variation in monomer type. *Journal of Membrane Science*, 342(1-2):60–69, 2009.

[331] FM Mirablella. Internal reflection spectroscopy: Theory and applications. practical spectroscopy series, 1993.

[332] Bo Zhong, Xiaoxiao Huang, Guangwu Wen, Hongming Yu, Xiaodong Zhang, Tao Zhang, and Hongwei Bai. Large-scale fabrication of boron nitride nanotubes via a facile chemical vapor reaction route and their cathodoluminescence properties. *Nanoscale Res Lett*, 6(1):36, 2010. ISSN 1556-276X. doi: 10.1007/s11671-010-9794-8. URL `http://dx.doi.org/10.1007/s11671-010-9794-8`.

[333] Witita Laosamathikul, Toshiki Sawada, and Takeshi Serizawa. Alcoholysis-assisted exfoliation of boron nitride nanosheets from hexagonal boron nitride. *Transactions of the Materials Research Society of Japan*, 42(5):135–138, 2017.

[334] Mary Laura Lind, Daniel Eumine Suk, The-Vinh Nguyen, and Eric MV Hoek. Tailoring the structure of thin film nanocomposite membranes to achieve seawater ro membrane performance. *Environmental science & technology*, 44(21):8230–8235, 2010.

[335] Julian S Taurozzi, Christopher A Crock, and Volodymyr V Tarabara. C60-polysulfone nanocomposite membranes: entropic and enthalpic determinants of

c60 aggregation and its effects on membrane properties. *Desalination*, 269(1-3): 111–119, 2011.

[336] Byeong-Heon Jeong, Eric MV Hoek, Yushan Yan, Arun Subramani, Xiaofei Huang, Gil Hurwitz, Asim K Ghosh, and Anna Jawor. Interfacial polymerization of thin film nanocomposites: a new concept for reverse osmosis membranes. *Journal of membrane science*, 294(1-2):1–7, 2007.

[337] Jun Yin, Eun-Sik Kim, John Yang, and Baolin Deng. Fabrication of a novel thin-film nanocomposite (TFN) membrane containing MCM-41 silica nanoparticles (NPs) for water purification. *Journal of membrane science*, 423:238–246, 2012.

[338] Sang Gon Kim, Dong Hun Hyeon, Jeong Hwan Chun, Byung-Hee Chun, and Sung Hyun Kim. Nanocomposite poly (arylene ether sulfone) reverse osmosis membrane containing functional zeolite nanoparticles for seawater desalination. *Journal of membrane science*, 443:10–18, 2013.

[339] Liu T. Chew J. Livingston A. Mattia D. Casanova, S. Dataset for "High flux thin-film nanocomposites with embedded boron nitride nanotubes for nanofiltration", 2019. URL `https://doi.org/10.15125/BATH-00686`.

[340] Jiang nan Shen, Chang chao Yu, Hui min Ruan, Cong jie Gao, and Bart Van der Bruggen. Preparation and characterization of thin-film nanocomposite membranes embedded with poly (methyl methacrylate) hydrophobic modified multiwalled carbon nanotubes by interfacial polymerization. *Journal of membrane science*, 442:18–26, 2013.

[341] Jinghai Liu, Tiekai Zhang, Zhichao Wang, Graham Dawson, and Wei Chen. Simple pyrolysis of urea into graphitic carbon nitride with recyclable adsorption and photocatalytic activity. *Journal of Materials Chemistry*, 21(38):14398–14401, 2011.

[342] Frédéric Goettmann, Arne Thomas, and Markus Antonietti. Metal-free activation of co2 by mesoporous graphitic carbon nitride. *Angewandte Chemie International Edition*, 46(15):2717–2720, 2007.

[343] Arne Thomas, Anna Fischer, Frederic Goettmann, Markus Antonietti, Jens-Oliver Müller, Robert Schlögl, and Johan M Carlsson. Graphitic carbon nitride materials: variation of structure and morphology and their use as metal-free catalysts. *Journal of Materials Chemistry*, 18(41):4893–4908, 2008.

[344] Jian Liu, Hongqiang Wang, and Markus Antonietti. Graphitic carbon nitride "reloaded": emerging applications beyond (photo) catalysis. *Chemical Society Reviews*, 45(8):2308–2326, 2016.

[345] Mikhael Bechelany, Samuel Bernard, Arnaud Brioude, David Cornu, Pierre Stadelmann, Catherine Charcosset, Koffi Fiaty, and Philippe Miele. Synthesis of boron nitride nanotubes by a template-assisted polymer thermolysis process. *The Journal of Physical Chemistry C*, 111(36):13378–13384, 2007.

[346] Roland Tay, Hongling Li, Siu Hon Tsang, Lin Jing, Dunlin Tan, and Edwin Hang Tong Teo. Synthesis and investigation of millimeter-scale vertically aligned boron nitride nanotube arrays. In *APS Meeting Abstracts*.

[347] Konstantin Iakoubovskii. Techniques of aligning carbon nanotubes. *Central European Journal of Physics*, 7(4):645–653, 2009.

[348] Katrin Ostertag and Bärbel Hüsing. Identification of starting points for exposure assessment in the post-use phase of nanomaterial-containing products. *Journal of Cleaner Production*, 16(8-9):938–948, 2008.

[349] CL Tran, K Donaldson, V Stones, T Fernandez, Alex Ford, N Christofi, J Ayres, M Steiner, J Hurley, R Aitken, et al. A scoping study to identify hazard data needs for addressing the risks presented by nanoparticles and nanotubes. *Institute of Occupational Medicine*, pages 1–48, 2005.

[350] Norris Alderson, Catherine Alexander, Celia Merzbacher, William Chernicoff, Paul Middendorf, Nancy Beck, Flora Chow, Dianne Poster, Mary Ann Danello, and Enriqueta Barrera. Environmental, health, and safety research needs for engineered nanoscale materials. Technical report, EXECUTIVE OFFICE OF THE PRESIDENT WASHINGTON DC NATIONAL SCIENCE AND ..., 2006.

[351] Mark Crane, Richard D Handy, John Garrod, and Richard Owen. Ecotoxicity test methods and environmental hazard assessment for engineered nanoparticles. *Ecotoxicology*, 17(5):421, 2008.